ANALYTICAL AND EXPERIMENTAL INVESTIGATION ON THE FATIGUE BEHAVIOUR OF TUBULAR JOINTS FOR OFFSHORE MONOPOD STRUCTURES

CENTRE FOR NEWFOUNDLAND STUDIES

TOTAL OF 10 PAGES ONLY
MAY BE XEROXED

(Without Author's Permission)

SIDDAPPA SHANKARE GOWDA

CANADIAN THESES ON MICROFICHE

I.S.B.N.

THESES CANADIENNES SUR MICROFICHE

National Library of Canada
Collections Development Branch,

Canadian Theses on
Microfiche Service

Ottawa, Canada
K1A 0N4

Bibliothèque nationale du Canada
Direction du développement des collections

Service des thèses canadiennes
sur microfiche

NOTICE

The quality of this microfiche is heavily dependent upon the quality of the original thesis submitted for microfilming. Every effort has been made to ensure the highest quality of reproduction possible.

If pages are missing, contact the university which granted the degree.

Some pages may have indistinct print especially if the original pages were typed with a poor typewriter ribbon or if the university sent us a poor photocopy.

Previously copyrighted materials (journal articles, published tests, etc.) are not filmed.

Reproduction in full or in part of this film is governed by the Canadian Copyright Act, R.S.C. 1970, c. C-30. Please read the authorization forms which accompany this thesis.

THIS DISSERTATION
HAS BEEN MICROFILMED
EXACTLY AS RECEIVED

AVIS

La qualité de cette microfiche dépend grandement de la qualité de la thèse soumise au microfilmage. Nous avons tout fait pour assurer une qualité supérieure de reproduction.

S'il manque des pages, veuillez communiquer avec l'université qui a conféré le grade.

La qualité d'impression de certaines pages peut laisser à désirer, surtout si les pages originales ont été dactylographiées à l'aide d'un ruban usé ou si l'université nous a fait parvenir une photocopie de mauvaise qualité.

Les documents qui font déjà l'objet d'un droit d'auteur (articles de revue, examens publiés, etc.) ne sont pas microfilmés.

La reproduction, même partielle, de ce microfilm est soumise à la Loi canadienne sur le droit d'auteur, SRC 1970, c. C-30. Veuillez prendre connaissance des formules d'autorisation qui accompagnent cette thèse.

LA THÈSE A ÉTÉ
MICROFILMÉE TELLE QUE
NOUS L'AVONS REÇUE

NL-339 (r. 82/08)

Canada

ANALYTICAL AND EXPERIMENTAL INVESTIGATION ON THE FATIGUE BEHAVIOUR OF TUBULAR JOINTS FOR OFFSHORE MONOPOD STRUCTURES

BY

© Siddappa Shankare Gowda, B.E., M.E.

A thesis submitted to the School of Graduate Studies in partial fulfillment of the requirements for the degree of Doctor of Philosophy

Faculty of Engineering and Applied Science
Memorial University of Newfoundland

October 1983

St. John's Newfoundland Canada

DEDICATION

To My Mother and Brothers.

ABSTRACT

This study is concerned with the analytical and experimental investigation of fatigue behaviour of monopod tubular joints in air and cold seawater environments. A total of seven joints were tested under cyclic loading. Two specimens - one in air and the other in water were subjected to pseudo-random loadings. The remaining five specimens - two in air and three in sea water were tested under constant amplitude sinusoidal loadings. The joints were tested both in as-welded and weld toe ground conditions. The corrosion tests were carried out in natural seawater at 0°C to simulate the cold ocean environment.

From the measured strains during static loading at critical hot spot locations, strain and stress concentration factors were determined and compared with the finite element analysis. The MSC/NASTRAN finite element computer code was used using triangular and quadrilateral flat shell elements. Each element has five degrees of freedom consisting of two in-plane displacements, a normal displacement and bending rotations.

The effect of seawater, weld toe grinding, the nature of applied loads and crack growth characteristics are studied in detail. The fatigue lives of the joints for crack initiation, propagation and final failure are determined and compared with those of T or Y-joints from the published

literature. For the three joints tested in seawater, the fatigue life for wall penetration are compared with the analytical life estimation using fracture mechanics approach. The fatigue results of all the joints tested are compared with the relevant U.K. DD 55 Q and AWS-XX S-N curves.

ACKNOWLEDGEMENT

The author wishes to express his sincere gratitude to his supervisor Professor M. Arockiasamy and co-supervisor Professor D.B. Muggeridge for their guidance, encouragement and indispensable help in the completion of this thesis. Grateful acknowledgements are due to Professor D.V. Reddy, who initiated the project during his stay at Memorial University.

The author would also like to gratefully acknowledge the following persons and organizations for their help and contributions:

- Dean Ross Peters, Faculty of Engineering and Applied Science for his interest and encouragement in the completion of the thesis.
- Dr. F.A. Aldrich, Dean of Graduate Studies for the award of Memorial University Fellowship.
- Dr. T.R. Chari, Associate Dean, Faculty of Engineering and Applied Science, for providing two work term students, Mr. S. Warren and Mr. L.S. Poh to assist during experiment.
- Professor H. Snyder, former Director, Center for Cold Ocean Resources and Engineering (C-CORE) for financial support to two work term students Mr. G. Yeo and Mr. I. McCloy for assistance in testing.
- National Research Council of Canada Grant No. A8119 and Imperial Oil Ltd., for their partial funding of the project.

- Mr. J.A. Cran of Steel Company of Canada (Stelco) for donating the steel specimens and partial financial support.
- Canada Center for Mineral and Energy Technology (CANMET), Department of Energy, Mines and Resources, Ottawa for the generous financial support for the corrosion fatigue tests and Dr. J.B. Gilmour and Dr. O. Vosikovsky for their interest and constructive criticisms in the preparation of the final report of Contract No. 20SU.23440-1-9090, which has been freely used in the preparation of the thesis.
- Dr. K. Munaswamy, Post-Doctoral Fellow for his time and effort in the finite element modelling of the joint and computer work.
- Mr. P.S. Cheema for useful discussions and fellow graduate students for their help and pleasant company.
- Mr. T. Duarte, Supervisor of Laboratories, and Mr. D. Tilley, Mr. A. Bursey, Mr. C. Gries, Mr. C. Ward and Mr. T. Lanning, staff of the Structures Laboratory, and Mr. T.N.N. Murthy for their help in the set up and testing of specimens.
- Mr. J. Andrews, Supervisor, Welding Section and Mr. P. Robinson, Supervisor, Machine Shop and their technical staff for their cooperation in fabrication of specimens and erection of loading frame.

- Peoples Educational Society College of Engineering, Mandya, Karnataka, India, for having granted the leave of absence for carrying out this work.
- Mrs. Mary Brown for typing the first draft and Mrs. Marilyn Warren for subsequent and final typing of the manuscript in a very short notice with considerable care and patience.

I also wish to express my fondest thanks to my wife Saroja for having freed me of all my domestic responsibilities, thus enabling me to devote time for the research work; and to my sons Ramachandra and Umeshchandra for their forbearance throughout the period of study.

Last, but not the least I thank The Almighty for making my desires come true.

CONTENTS

	Page
DEDICATION	i
ABSTRACT	ii
ACKNOWLEDGEMENT	iv
CONTENTS	vii
LIST OF RELATED PUBLICATIONS	x
LIST OF TABLES	xi
LIST OF ILLUSTRATIONS	xiii
NOMENCLATURE	xviii
CHAPTER 1 INTRODUCTION	1
1.1 General	1
1.2 Advantages of Tubular Members	2
1.3 Choice of Joint Model	3
1.4 Significance of the Study	3
1.5 Objectives and Scope	4
CHAPTER 2 REVIEW OF LITERATURE	6
2.1 General	6
2.2 Theoretical Analysis	6
2.3 Experimental and Analytical Investigations	10
2.3.1 Dry Fatigue Tests	10
2.3.2 Corrosion Fatigue Tests	23
2.4 Design Considerations	27
CHAPTER 3 ANALYTICAL PROCEDURE	30
3.1 General	30
3.2 Stress Analysis Methods	31
3.2.1 Parametric Equations	31
3.2.2 Finite Element Approach	34
3.2.3 Welded Steel Tubular Models	34
3.3 Hot Spot Strain or Stress Range	35
3.4 Fracture Mechanics Approach	37
3.4.1 Linear Elastic Fracture Mechanics	38
3.4.2 Determination Stress Intensity Factors	38
3.4.3 Fatigue Crack Growth Model	40
3.5 Fatigue Failure Criteria	41
CHAPTER 4 FINITE ELEMENT ANALYSIS	42
4.1 General	42

		Page
4.2	Flat Shell Elements - QUAD4 and TRIA3	43
4.3	Discretization of the Joint	46
4.4	Element Stresses and Strains	47
CHAPTER 5	EXPERIMENTAL PROGRAMME	48
5.1	General	48
5.2	Test Hardware and Loading Devices	48
5.3	Design of Typical Joints	50
5.4	Specimen Fabrication and Welding Details	52
5.5	Design and Installation of Cooling System for Seawater Circulation	53
5.6	Weld Surface Profiling	54
CHAPTER 6	TESTING PROGRAMME	56
6.1	General	56
6.2	Stress-Coat Application and Analysis	56
6.3	Test Set-Up and Instrumentation	62
6.4	Automatic Data Acquisition System	64
6.5	Measurement of Environmental Parameters	66
6.6	Static Tests	66
6.7	Fatigue Tests	67
6.8	Compact Tension Specimen Tests in Seawater	71
CHAPTER 7	FATIGUE FRACTURE MECHANICS ANALYSIS	73
7.1	Crack Growth Data and Material Constants, C and m	73
7.2	Crack Growth Data and Stress Intensity Factors for Tubular Joints	74
7.3	Fatigue Life Estimation	77
CHAPTER 8	TEST RESULTS, OBSERVATION AND DISCUSSION	80
8.1	Stress and Strain Distributions	80
8.2	Hot Spot Stress and Strain Range	81
8.3	Crack Initiation and Crack Growth Behaviour	85
8.4	Effect of Cold Seawater Environment	87
8.5	Effect of Weld Toe Grinding	88
8.6	Joint Stiffness Measurements	89
8.7	Fatigue Lives	90
8.8	Life Estimation Using Fracture Mechanics	92
CHAPTER 9	CONCLUSIONS AND RECOMMENDATIONS	94
9.1	Conclusions	94
9.2	Recommendations for Further Research	95
REFERENCES		97

Page

APPENDICES

Appendix A: Strain Gauge Installation 229
Appendix B: Measurement of Seawater Properties 233
Appendix C: Calculation of Maximum Principal Strains and Stresses 239
Appendix D: Generation of Pseudo-Random Load 241
Appendix E: Fatigue Testing Machine 246

LIST OF RELATED PUBLICATIONS

1. S.S. Gowda, D.V. Reddy, D.B. Muggeridge and M. Arockiasamy, "Corrosion Fatigue Behaviour of Tubular Joints in Offshore Structures - State of the Art", Presented at the First Indian Conference in Ocean Engineering, Indian Institute of Technology, Madras, India, February 1981.

2. S.S. Gowda, D.V. Reddy, M. Arockiasamy, D.B. Muggeridge and P.S. Cheema, "Experimental and Analytical Studies on Fatigue Behaviour of Monopod Tubular Joints", Presented at the Third International Conference on Behaviour of Offshore Structures (BOSS'82), M.I.T., Massachusetts, August 1982.

3. S.S. Gowda, M. Arockiasamy and D.V. Reddy, "Fatigue Crack Growth and Life Prediction of Tubular Joints in Offshore Monopod Structures", Presented at the Second Pan American Congress on Oceanic Engineering, UPADI-82, San Juan, Puerto Rico, August 1982.

4. S.S. Gowda, D.V. Reddy, M. Arockiasamy and D.B. Muggeridge, "Fatigue Strength of Welded Monopod Tubular Joints", Presented at the Second International Conference on Offshore Welded Structures, The Welding Institute, Cambridge, U.K., November 1982.

5. S.S. Gowda, M. Arockiasamy, D.B. Muggeridge and D.V. Reddy, "Corrosion Fatigue Strength of Offshore Monopod Tubular Joints in Cold Ocean Environment", Presented at the Offshore Technology Conference, Houston, Texas, May 1983.

6. S.S. Gowda, M. Arockiasamy, D.B. Muggeridge and D.V. Reddy, "Experimental and Analytical Investigation of Corrosion Fatigue Behaviour of Monopod Tubular Joints", ASCE EMD Specialty Conference, Purdue University, Indiana, May 1983.

7. S.S. Gowda, M. Arockiasamy and D.B. Muggeridge, "Fatigue Behaviour of Tripod Tower Type Platform Models", Presented at the 1983 Canadian Society for Civil Engineers Annual Conference, Ottawa, June 1983.

LIST OF TABLES

Table No.	Title	Page No.
1.	Monopod Tubular Joint Parameters	109
2a)	Validity Limits of Different Parametric Formulae	109
2b)	Stress Concentration Factors by Parametric Equations - Main Chord	110
3.	Mechanical Properties of Steel	111
4.	Chemical Composition of Steel	111
5.	Mechanical Properties of Electrodes	111
6.	Welding Details	112
7.	Strain Gauge Properties	113
8.	Range of Seawater Parameters	114
9.	Testing and Loading Details of Joints	115
10.	Static Strain Readings: Joint - Dry 1	116
11.	Static Strain Readings: Joint - Dry 2	117
12.	Static Strain Readings: Joint - Dry 3	118
13.	Static Strain Readings: Joint - Corr. 1	119
14.	Static Strain Readings: Joint - Corr. 2	120
15.	Static Strain Readings: Joint - Corr. 3	121
16.	Static Strain Readings: Joint - Corr. 4	122
17a)	Hot Spot Strain Range and Strain Concentration Factor - Main Chord	123
17b)	Hot Spot Strain Range and Strain Concentration Factor (SNCF) - Branch Tube	124
18.	Hot Spot Stress Range and Stress Concentration Factor (SCF) - Main Chord	125

Table No.	Title	Page No.
19.	Fatigue Test Results	126
20.	Comparison of Fatigue Lives with Fracture Mechanics	127
21.	Summary of Crack Growth Data: Joint - Dry 1 (Right of Centre Line)	128
22.	Summary of Crack Growth Data: Joint - Dry 2 (Right of Centre Line)	129
23.	Summary of Crack Growth Data: Joint - Dry 3 (Right of Centre Line)	130
24.	Summary of Crack Growth Data: Joint - Corr. 1 (Right of Centre Line)	131
25.	Summary of Crack Growth Data: Joint - Corr. 2 (Right of Centre Line)	132
26.	Summary of Crack Growth Data: Joint - Corr. 3 (Right of Centre Line)	133
27.	Summary of Crack Growth Data: Joint - Corr. 4 (Right of Centre Line)	134
28.	Summary of Crack Growth Data: Joint - Dry 1 (Left of Centre Line)	135
29.	Summary of Crack Growth Data: Joint - Dry 2 (Left of Centre Line)	136
30.	Summary of Crack Growth Data: Joint - Dry 3 (Left of Centre Line)	137
31.	Summary of Crack Growth Data: Joint - Corr. 1 (Left of Centre Line)	138
32.	Summary of Crack Growth Data: Joint - Corr. 2 (Left of Centre Line)	139
33.	Summary of Crack Growth Data: Joint - Corr. 3 (Left of Centre Line)	140
34.	Summary of Crack Growth Data: Joint - Corr. 4 (Left of Centre Line)	141
35.	Comparison of Fatigue Test Results with Relevant Published Data	142

LIST OF ILLUSTRATIONS

Figure No.	Title	Page No.
1.	Jacket-Type Steel Structure	143
2.	Cook Inlet Alaska Monopod Platform	144
3.	Monocone Drilling Unit	145
4.	Arctic Marine Drilling Structure	146
5.	Tripod Tower Platform	147
6.	Major Platform Loads and Corrosion Zones	148
7.	Weight-Strength Comparison of Common Structural Shapes	149
8.	Types of Simple Planar Joints	149
9.	Joint With Stiffening Rings	150
10.	Joint Without Stiffening Rings	151
11.	Monopod Joint Nomenclature	152
12.	Diagrammatic Representation Defining Idealized Hot Spot Stress	153
13.	Structural Integrity Parameters	154
14.	Schematic Representation of Fatigue Crack Growth in Steel	154
15.	Flat Shell Element Coordinates	155
16.	Force and Moment Resultants	156
17.	Discretization of the Developed Surface - Branch Tube 1	157
18.	Discretization of the Developed Surface - Branch Tube 2	158
19.	Discretization of the Developed Surface Branch Tube 3	159
20.	Discretization of the Developed Surface - Main Tube	160

Figure No.	Title	Page No.
21.	Finite Element Mesh Generation for the Joint	161
22.	Comparison of Strain Distributions: Joint Dry 2	162
23.	Comparison of Strain Distribution: Joint - Corr. 1	163
24.	Comparison of Strain Distributions: Joint - Corr. 2 and Dry 1	164
25.	Comparison of Strain Distributions: Joint - Corr. 3	165
26.	Comparison of Strain Distributions: Joint - Corr. 4	166
27.	Plan of Test Assembly	167
28.	Test Assembly for Fatigue Loading	168
29.	Connection Unit for Vertical Loading	169
30.	Connection Unit for Horizontal Loading	170
31.	Details of Monopod Joint With Stiffening Rings	171
32.	Details of Monopod Joint Without Stiffening Rings	172
33.	Directions of Applied Loads and Reactive Forces	173
34.	Tube Weld Connection Elevation	174
35.	Welding Details	175
36.	Details of Ring-to-Tube Welds for Stiffened Joint	176
37.	Schematic of Seawater Cooling and Circulation Systems	177
38.	Test Set-up With Test-Cell and Cooling Unit	178
39.	Weld Toe Grinding Profile	179
40.	Brittle Lacquer Coating for Joint Intersection	180

Figure No.	Title	Page No.
41.	Brittle Lacquer Coating for Stiffened Joint	180
42.a)	Brittle Coating Cracks Due to Tensile Load (Critical Region - Branch Tube 1)	181
42.b)	Brittle Coating Cracks Due to Tensile Load (Branch Tube 1)	181
43.a)	Brittle Coating Cracks Due to Compressive Load (Critical Region - Branch Tube 1)	182
43.b)	Brittle Coating Cracks Due to Compressive Load (Branch Tubes 2 and 3)	182
44.a)	Brittle Coating Cracks Due to Tensile Load (Branch Tubes 2 and 3)	183
44.b)	Brittle Coating Cracks Due to Tensile Load (Branch Tube 2)	183
45.	Test Set-up for Dry Testing	184
46.	Cross-Sectional View of Protective Coatings for Strain Gauge Installations in Water	185
47.	Strain Gauge Locations for Joint - Dry 1	186
48.	Strain Gauge Locations for Joint - Dry 2	187
49.	Strain Gauge Locations for Joint - Dry 3	188
50.	Strain Gauge Locations for Joint - Corr. 1	189
51.	Strain Gauge Locations for Joint - Corr. 2	190
52.	Strain Gauge Locations for Joint - Corr. 3	191
53.	Strain Gauge Locations for Joint - Corr. 4	192
54.	Computer Controlled Automatic Data Acquisition System	193
55.	Block Diagram of Data Acquisition System	194
56.a)	Standard Compact Tension Specimen	195
56.b)	Test Set-up of CTS Specimen with Container	196

Figure No.	Title	Page No.
56.c)	Fatigue Crack Growth Data of Compact Tension Specimens	197
57.	Summary of Fatigue Crack Growth Rate Data for A36 Steel	198
58.	Fatigue Crack Growth Data for Tubular Joints	198
59.	Assumed Geometry of Bowed Crack in Tubular Joints	199
60.	Variation of Correction Factor Y with Crack Depth for Tubular Joints	199
61.	Schematic of Circumferential Stress Distribution Above Joint Intersection	200
62.a)	Strain Distribution near Weld Toe: Joint - Dry 2	201
62.b)	Strain Distribution near Weld Toe: Joint - Dry 3	202
62.c)	Strain Distribution near Weld Toe: Joint - Corr. 1	203
62.d)	Strain Distribution near Weld Toe: Joint - Corr. 2 and Dry 1	204
62.e)	Strain Distribution near Weld Toe: Joint - Corr. 3	205
62.f)	Strain Distribution near Weld Toe: Joint - Corr. 4	206
63.	Surface Crack Growth Development: Joint - Dry 1	207
64.	Surface Crack Growth Development: Joint - Dry 2	208
65.	Surface Crack Growth Development: Joint - Dry 3	209
66.	Surface Crack Growth Development: Joint - Corr. 1	210

Figure No.	Title	Page No.
67.	Surface Crack Growth Development: Joint - Corr. 2	211
68.	Surface Crack Growth Development: Joint - Corr. 3	212
69.	Surface Crack Growth Development: Joint - Corr. 4	213
70.	Crack Growth Characteristics of Joints	214
71.	Overall Fatigue Crack Growth Rate of Joints (Left of Crack Initiation Point)	215
72.	Photograph of Joint Failure - Dry 1 (Pseudo-Random Load)	216
73.	Photograph of Joint Failure - Dry 2 (Harmonic Load)	217
74.	Photograph of Joint Failure - Dry 3 (Harmonic Load)	218
75.	Photograph of Joint Failure - Corr. 1 (Harmonic Load)	219
76.	Photograph of Joint Failure - Corr. 2 (Pseudo-Random Load)	220
77.	Photograph of Joint Failure - Corr. 3 (Harmonic Load)	221
78.	Photograph of Joint Failure - Corr. 4 (Harmonic Load)	222
79.	Specimen Tip Displacement: Joint - Corr. 1	223
80.	Specimen Tip Displacement: Joint - Corr. 2	224
81.	Specimen Tip Displacement: Joint - Corr. 3	225
82.	Specimen Tip Displacement: Joint - Corr. 4	226
83.	Comparison of Fatigue Test Results	227
84.	Basic S-N Curves for Tubular Joints	228

NOMENCLATURE

a	Crack depth
a_i	Initial crack depth
a_f	Final crack depth
B	Compact Tension Specimen thickness
C	Material constant
D	Mean diameter of chord
D_u	Usage factor
d	Mean diameter of brace
E	Young's modulus of elasticity
G_1, G_2, G_3 and G_4	Elastic constants
I	Second moment of area
K_I	Stress intensity factor for opening mode
K'	Constant
k	Constant
j	Total number of blocks
L	Length of chord member
M, N, Q	Force resultants
m	Material constant
N_y	Number of years
N	Number of life cycles
n	Slope of straight line
n_i	Exponents
P	Applied load
Q_x, Q_y	Transverse shear forces

R	Radius of chord
r	Radius of brace
T	Wall thickness of chord, Thickness of element
t	Wall thickness of brace
u_x, u_y, u_z	Displacements in x, y and z directions
W	Width of specimen
Y	Correction factor
ε_o	Nominal strain in the brace
ε_{HS}	Hot spot strain
σ_o	Nominal stress in the brace
σ_{HS}	Hot-spot stress
SCF	Stress concentration factor
SCNF	Strain concentration factor
ε''_{HS}	Extrapolated strain parallel to weld toe
ν	Poisson's ratio
σ_x	Normal stress in the x-direction
σ_y	Normal stress in the y-direction
σ_z	Normal stress in the z-direction
σ°	Membrane stress
τ_{xy}	Shear stress
$\Delta\sigma$	Stress range
ΔK	Stress intensity factor range
e°	Surface strain

θ_x, θ_y Rotational degrees of freedom in x and y directions

κ° Curvature of shell surface

$$\alpha = \frac{2 \times \text{Length of chord}}{\text{Mean dia. of chord}} = \frac{2L}{D}$$

$$\beta = \frac{\text{Mean radius of brace}}{\text{Mean radius of chord}} = \frac{r}{R}$$

$$\gamma = \frac{\text{Mean radius of chord}}{\text{Wall thickness of chord}} = \frac{R}{T}$$

$$\tau = \frac{\text{Wall thickness of brace}}{\text{Wall thickness of chord}} = \frac{t}{T}$$

CHAPTER 1

INTRODUCTION

1. INTRODUCTION

1.1 General

Research on fatigue of welded tubular joints has been heralded by the petroleum industry due to the increasing use of tubular members for offshore exploration and production platforms. The structural tubular members of offshore platforms consist exclusively of circular steel sections. During the last 20 years, the need for such members grew very rapidly and attention is being focussed on the unique problem of welded tubular intersections. The alternating loads in the web and bracing members due to random and repetitive nature of ocean waves, wind and ice floe result in fatigue of the members. The design of welded tubular connections has been complicated by the tube wall radial flexibility, which is a source of severe stress concentration at the joint intersections. This stress concentration causes an early fatigue failure of the joint. The main aim of the joint design is either to increase the radial stiffness of the column member or to limit the effect of flexibility using gusset plates, wing plates and ring stiffeners etc. Improper joint design, faulty welds during fabrication, and poorly placed non-structural attachments or holes can lead to high local stresses leading to early crack initiation.

Most of the exploration and production platforms are of the basic jacket type supporting a platform deck as shown in Fig. 1. The installation of the first template type steel structure in Gulf of Mexico marked the first use of welded tubular offshore platform. For shallower waters, such as Cook Inlet Alaska and the Beaufort Sea, monopod and monocone platforms have been in use for water depths up to 30 m (Figs. 2,3 and 4). Recently Heerema Engineering Company proposed a Tripod Tower Platform, Fig. 5, supported by three branch members for deep waters up to 350 m.

Offshore structures are subjected to large gravity loads and environmental forces besides corrosion and fouling. The pictorial summary of major loads, environmental forces and corrosion zones at different depths in a typical offshore structure is shown in Fig. 6. Several failures of tubular joints in offshore structures have triggered research interests for improved method of design. The advent of general purpose computer programmes, based on classical shell theory, makes it possible to analyze simplified tube sections by accurate representation of the complex connection of the members.

1.2 Advantages of Tubular Members

The tubular members have excellent strength properties, good resistance to primary and local bucklings

and offer minimum exposed area to wind and wave forces. They exhibit omni-directional strength with design flexibility, greater economy in mass and possess good hydrodynamic properties (1,2). The weight-strength comparison of common structural shapes is shown in Fig. 7.

1.3 Choice of Joint Model

Extensive literature review on analysis and design of tubular joints covers types of joints tested, theoretical and numerical studies, photo-elastic and brittle lacquer methods, and the effect of sea water environment on fatigue life. It is seen that extensive research has been carried out on T, K, Y, X, DK, DT, TK and DTK-type planar joints (Fig. 8). Very little information is available on the fatigue behaviour of spatial joints in which the main chord member is connected by three branch members representing a monopod platform. The present study considers a monopod-type joint, with and without stiffening rings (Figs. 9 and 10), where the three branch members are connected to the main chord at one-third of its height.

1.4 Significance of the Study

Recent discoveries of oil and gas fields in the eastern part of Canada have accelerated the research and development efforts in solving problems related to offshore

platforms, for deep waters and harsh ice infested environments. Particular attention needs to be given to the cold oceans in view of large dissolved oxygen content and the decrease in toughness of steel associated with lower temperatures.

The proposed study considers the fatigue behaviour of monopod tubular joints subjected to both constant and variable amplitude loadings, under dry and natural cold ocean environments.

1.5 Objectives and Scope

The objectives of the proposed research on spatial monopod type joints are the following:

(i) Study of the welded monopod joint behaviour with and without stiffening rings in as-welded and weld toe ground conditions under static and fluctuating loads,

(ii) Measurement of strains during static and fatigue loading at critical hot spots and comparison with the finite element analysis,

(iii) Prediction of fatigue lives using fracture mechanics principles,

(iv) Comparison of joint fatigue behaviour in air and cold seawater environments,

(v) Study the crack growth behaviour under constant amplitude and pseudo-random loadings, and

(vi) S-N relationship for spatial monopod type joints and comparison with the current published literature.

CHAPTER 2

REVIEW OF LITERATURE

2. REVIEW OF LITERATURE

2.1 General

Research carried out on symmetric planar tubular joints can be divided into three basic categories:

i) theoretical analysis,

ii) experimental and analytical investigations - 'dry' and 'wet' fatigue tests, and

iii) design considerations.

2.2 Theoretical Analysis

Bijlaard (3), carried out extensive theoretical studies on T-joints for the stress computations in a cylindrical shell and developed curves to determine the magnitude of localized stresses at the junction between larger and smaller diameter cylinders. The boom member was analyzed as a thin cylindrical shell using eighth-order differential equations, where the load was expressed as double Fourier series.

Dundrova (4) presented a theoretical solution for stress distribution in cross and T-joints. Experimental results were compared with theory. The differential equations were derived considering thin shell behaviour using the Kirchoff hypothesis.

Greste (5) and Greste and Clough (6) developed a computer programme with automatic mesh generation capability.

for the analysis of tubular joints, using both triangular and quadrilateral finite elements. The flexibility of the web members as well as the chord members was included in the analysis. Scordelis and Bouwkamp (7) presented the basic principles with the development of shell programmes. The ratio of the web and chord diameters and the wall thickness to diameter of the chord section were included in the study. Welded tubular connections were analyzed by Liaw, Litton and Reimer (8) using three-dimensional isoparametric elements. The elements provided more accurate modelling of joints than the commonly used flat plate shell elements. The results of PMBSHELL AND KJOINT programmes were compared for an ungrouted K-joint and found to agree well except for some differences in the hot spot stress regions.

The behaviour of joints with chord and web members, of hollow rectangular sections, was studied by Redwood (9). The analytical results are compared with experimental values for both axial load and bending in the branch member. The stiffness and the deformation varied with the thickness ratio of the branch and chord members.

Nolte and Hansford (10) derived closed form expressions for the fatigue damage of structures due to ocean waves. The relationships between wave height and stress range, stress range and number of cycles to failure, and

probability distribution for the occurrence of wave heights were derived for a single sea state/storm.

A finite element method for determining stresses, strains and deformations has been presented by Mehrotra (11). Empirical formulae were also developed for symmetrical rectangular tubes, to estimate the joint modulus. The results were checked with full-scale experiments with different loadings and boundary conditions. A non-conformable bending field was used in conjunction with the conformable constant strain membrane field which showed better performance than a conformable set of linear functions.

The effectiveness of higher order isoparametric solid finite elements for welded tubular joint analysis was studied by Morgan (12). The finite element model used a rezone technique to reduce the number of degrees of freedom. The plate elements at critical regions were redefined using higher order solid elements to provide for more accurate results. The rezone technique was efficient in reducing the computer costs.

Johnston (13) reviewed the available experimental data on welded tubular joints and compared with theoretical analysis based on three partial differential equations of the thin shell theory. The study indicated the inadequacy of the current design methods for structures in deeper waters.

Gurney and Maddox (14) carried out a statistical analysis of all available data on the fatigue design stresses and proposed changes in the existing design rules so as to be dependent on stress range only. Further research was suggested to investigate the influence of residual stresses. Marshall (15) reviewed the American Code of Practice on the design rules of tubular joint relative to static ultimate strength and fatigue, identified problems of high-cycle fatigue and cumulative damage and examined case histories of offshore failures in view of the proposed criteria and risk analysis.

Yoshida, Inui and Iida (16) studied the behaviour of tubular T-connections by hybridizing computer programmes based on non-linear shell and solid analyses. The computed strain distributions agreed well with the experimental values. Using a strain energy solution for a cylindrical shell, a stiffened T-joint with a gusset plate welded to a chord member has been analyzed by Frederick, Goldberg and Lewis (17). The cylindrical shell displacement field was compatible with that of the gusset plate, when subjected to radial tractions, obtained from the Fourier series representing a desired displacement field. Fracture mechanics technique for predicting fatigue life of non-overlapping tubular K-joints has been developed by Pan and Plummer (18), which was based on experimentally derived

stress intensity factor obtained from fatigue crack growth data. The predicted fatigue lives were compared with the results of eight sets of non-overlapping K-joint data.

The development of parametric equations and their validity ranges for T, Y, K and TK-joints was made by Kuang, et al (19), using thin shell finite element computer program "TKJOINT". The experimental hot spot stress concentrations compare reasonably well with the calculated values.

Van Delft (20), carried out a two dimensional analysis of the stresses at the vicinity of the weld toes of the welded tubular joints using finite element and photo-elastic methods. Different weld profiles without radii at the weld toe and the effect of the element mesh were investigated and the stress concentration due to weld profile was found to be independent of the stresses developed. The stress concentrations obtained from the finite element analysis are very sensitive to the accuracy of the element mesh.

2.3 Experimental and Analytical Investigations

2.3.1 Dry Fatigue Tests

Extensive experimental work on tubular joints with many configurations has been carried out by Bouwkamp (21-23). Tests included joints with and without ring stiffeners, wing-plates, gusset plates, inter-welded, non-interwelded cast-

steel seat-welded, flared joints and cement-grout filled joints under static and slow-cycle alternating loads. Buckling and post-buckling strength of circular joints have also been studied. Further studies were suggested to determine stress concentrations and the effect of over-strain on fatigue life of large scale tubular joints.

Toprac (24) and Beale, Toprac and Noel (25) studied the stress concentrations in tubular connections. Using the measured stresses, the contours of isostatics and isobars were constructed and the stress pattern and stress distributions plotted for the specimens tested.

Toprac, Johnston and Noel (26) suggested further research necessary to develop better methods for the design of welded joints, and the need for studies on three dimensional effects, cyclic loading, cumulative damage, testing of specimens with two or more members framing into the chord, and strengthening of joints.

Babikar (27) conducted tests on overlapping joints, partially intersecting and non-intersecting joints. The specimens were N-type truss joints with hollow rectangular chord and circular hollow web members. The vertical load on the specimens was introduced by prestressing. The cyclic speed varied from 5 to 30 cycles/min. It was found that the tests that the joints with 100% overlap exhibited satisfactory results when compared to partially intersecting

joints. The non-intersecting joints were found unsafe if designed according to class F joints.

Blockley (28) carried out tests on N-type circular hollow sections to determine deformation characteristics and stress distributions and the results compared with the theoretical values. The joints with intersection of the branch members resisted greater ultimate loads than those without intersection of the branch members. Tests on two tubular steel connections were performed by Kwan (29) for axial forces on the branches and compared the results with the finite element and the three-dimensional photoelastic solutions.

A method of analyzing a ring-stiffened tubular joint with multiple non-intersecting branch members was developed by Miller and Trammell (30). Model test results were compared with analytical results, for a three-way Y and K-joint. The full field distribution including the surface stresses on the shell was obtained by photoelastic coating at the joint intersection. Structural joints of N-girder type with rectangular hollow chord and circular or rectangular web sections were analyzed by Eastwood, Wardle, Osgorby, Wood and Shinoda (31). The deflections, bending moments, loads and stresses were calculated, based on assumed load and deflection patterns at the intersection. Eastwood, Osgerby, Wood and Blockley (32) computed the stresses and deformations

on hollow rectangular chord and circular hollow web members and compared with experimental data for T-joints. Also, for N-type joints, theoretical contours of load distributions, local deflections and stresses were obtained for different eccentricities.

Natarajan and Toprac (33) carried out fatigue tests on T-joints with different stress ranges and weld profiles and established S-N curves for crack initiation and complete failure of the joints. Kurobane, Natarajan and Toprac (34) studied the parameters including the ratios of i) chord length to mean chord radius, ii) mean radii of brace and chord, iii) mean chord radius to thickness, and iv) thickness of brace to chord. Stress concentration factors, initiation of fatigue cracks, failure of the joints under static and fatigue loads and the size effect were determined.

Static tests were conducted by Bryant (35) on full scale pipe joint connection with ring-reinforced and external band reinforced tubular joints. All the specimens were instrumented with a number of strain gauges to identify locations and compute maximum strains and stresses.

A large scale stiffened T-joint model has been tested by Hans, Visser and Zunderdorp (36) to determine local stresses close to the intersection of welds. The maximum stresses were found to occur at the outer surface of chord

and brace intersection and on the circumference of chord with the stiffening plates attachment inside the tube. The effects of alternating loads on tubular K-joints were investigated by Kurobane, Makino and Sagawa (37). For some of the specimens, fluctuating loads were applied till a certain predetermined number of cycles were reached. Then the specimens were removed from the loading rig, and heated to 230°C for 2 hours and again re-tested to failure under static loading. The failure of the joints were ductile.

Static tests on T and N-type joints were carried out by Mee (38) to study the efficiency and load deformation characteristics and compared the results of the values obtained from the finite difference technique.

Non-overlapping rectangular hollow booms and circular hollow branch members of tubular truss joints with 6 m span were tested by Dasgupta (39) and the results compared with the isolated joint tests. Failure loads were found to be about 25-30% lower than those of the isolated tests. The analytical results from the finite element method compared reasonably well with the experimental values.

Tests on N-type truss joints with hollow rectangular chord and circular brace members, were carried out by Shinouda (40). The joints were non-overlapping and stiffened with stiffening plate welded to the loaded face of the chord at the joint. The joints showed improvement in

ultimate load carrying capacity as a result of stiffening plates.

Mall and Zirn (41) investigated symmetrical K-joints with hollow circular members under static and dynamic loads. Among the overlapping and non-overlapping joints, it was found that the latter with negative eccentricity, showed increased load carrying capacity. Static and fatigue tests on full-scale in-plane tubular truss joints and stress analysis of welded tubular K-joints were carried out by Maeda, Uchino and Sakurai (42). The results indicated that increase in fatigue strength could be achieved in K-joints with increased chord thickness. Analytical results were compared with the axial stresses obtained from empirical formulae derived by Beale and Toprac (1). Correlation between specimen crack initiation location and geometrical parameters was made with those of Bouwkamp's (21). In the experiment reported by Ref. (21), all the cracks appeared in the brace of the weld toe in contrast to those appearing in the chords. The combination of butt and fillet welds and grinding welded beads in the vicinity of critically stressed areas improved the fatigue strength of K-joints considerably.

Tests on N-type joints in tubular frame works have been carried out by Eastwood, Wood and Shinouda (43) to investigate the strength and the reinforcing effect of the

three types of stiffening plates: in-plane gusset plates, diaphragm type plates and stiffening seat pieces. The parameters studied included the ratios of i) chord wall thickness to its width, ii) mean diameter of the web member to the chord width, and iii) stiffening plates to chord wall thickness.

Fatigue tests under random loading were carried out by Dover, Holdbrook, Hibberd and Charlesworth (44) on tubular T-joints subjected to in-plane and out-of-plane bending. Crack depth and length were measured and the results used to estimate the life of joints applying fracture mechanics principles.

Tests on N or V-type (Warren) girders were conducted by Delesques, Valbert and Sfintesco (45) to investigate the load carrying capacity and check the accuracy of current design methods. For all the four specimens tested stresses were computed using measured elastic deformations in the longitudinal directions.

Martin (46) tested small-scale T-joints to investigate the maximum stress concentrations. Fatigue data were used in the formulation of the design curves and the validity of Miner's rule checked for estimating cumulative damage calculations.

An experimental method to obtain hot spot stress concentrations for unstiffened tubular T and X-joints, have

been presented by Wordsworth (47). Strains were measured with brittle lacquer and resistance strain gauges in the joint scale models made up of acrylic tubing. Hlavacek (48) presented test results of 128 cruciform and K-type welded tubular joints, with and without gusset plates and negative eccentricities. The strength of joints with respect to inward buckling of the main tube member was correlated with the strength of tubular lattice girder and established a chord tube slenderness criterion and the shape factor for K-joints.

Investigation into the factors which affect the strength of tubular joints without gusset plates was presented by Sammet (49). The geometric configuration was changed to alter the rigidity and load carrying capacity at fracture.

Hauk (50) carried out tests on rectangular hollow structural joints including K and T-joints and measured joint strengths in terms of the ratio of 'yield joint' to 'yield tension member' and 'maximum joint' to 'maximum tension member'.

Static tests on 24 N and K-type circular member joints were conducted by Anderson (51) to investigate circumferential stresses in the chord member. The design procedures for welded attachment to tubes have been discussed by Melworm and Berman (52). The theoretical solutions based

on shell theory were compared with experimental values along with recommendations for alternative design procedure.

Gibstein (53) derived empirical relations for the failure strength of tubular joints under steady state loading conditions. Satake, Fujishima, Ishida, Kajimoto, Minami and Hirozane (54) studied the brittle fracture characteristics of tubular joints used in offshore structures. Parameters such as welding residual stress and weld defects introduced after the welding completion were successfully evaluated by measuring the crack opening displacement and improvements suggested in selecting materials for offshore structures.

Pan, Plummer and Kuang (55) carried out tests on K, T and X-type of joints and developed formulae for ultimate strengths. The strength behaviour and failure mechanism of platform tubular joints have been compared with those of other investigations.

Tests on 12 T-joints with rectangular steel tubes were carried out by the Austin Company (56) with emphasis on yield strength and elasticity or flexibility of the joint at the connection.

The International Committee for Study of Tubular Joints reported two case studies describing i) the behaviour of welded cruciform joints of tubular structures (57), and ii) load transmission in cruciform joints (58). The load carrying capacities of hollow circular sections and the load

distribution at the interaction of the tubes were investigated, which led to an empirical formula for predicting the collapse load.

Static and dynamic tensile tests on 6 welded steel tube node joints were conducted at the Technical University of Stuttgart (59) to estimate the load bearing capacity of such joints. The joints under static load failed by deformation of the chord members. In the dynamic tests, peak stresses were observed at the weld of the tie member.

An investigation on load-deformation characteristics of statically loaded joints of rectangular hollow sections was carried out by Eastwood, Osgerby, Wood and Mee (60). The specimens were of non-intersecting branches, partially intersecting branches and completely overlapping branches with one branch carrying compression and the other in tension. It was found from the experiments that an increase in overlap exhibits better load carrying capacity. The chances of failure of the chords by the collapse of the top face are more to occur when compared to the joints with overlap.

Eastwood and Wood (61) carried out tests on overlapping and welded gap joints in tubular structures involving rectangular and round sections. Three different analytical techniques, viz. finite element, finite difference and beam on elastic foundation analogy were used to

investigate the stress distribution and deformation characteristics around the joint.

Eastwood, Osgerby, Wood and Bakiker (62) carried out fatigue tests on joints consisting of rectangular chord members with circular branch members welded at 45° and 90°. Slow cyclic loading was applied with a stress ratio of 0.2. The overlapping joints exhibited significant load carrying capacity and transverse stiffness of the chord wall has little effect on fatigue performance.

A design procedure for low cycle fatigue life of tubular joints for offshore structures has been developed by Grigory (63). The analytical results using approaches, viz. Fracture Mechanics approach, The Naval Research Laboratory approach, and Notch Stress Analysis approach were compared with experimental values on large scale models of T and K-joints.

Pease (64) presented strain gauge test results for a T-joint, in which the branch was loaded in tension. The measured local stresses compared reasonably well with analytical values obtained from Bijlaards approach. The investigation was limited only to T-joint and one combination of member sizes. The orientation of the strain gauges was based on the stress coat analysis.

Smedley (65) reviewed the problems of fatigue analysis of offshore steel structures and the relevance of

existing methods and discussed the influence of size effect and residual stresses in the welds.

The structural behaviour of the connections between hollow sections subjected to static and dynamic loads have been studied by Mang (66). The theoretical investigation of the ultimate strength of hollow structural steel joints under static as well as dynamic loadings were studied using the spring simulation method. The results compared well with the experimental values.

Dutta (67) made assessment of recommendations on the construction of joints in which chord and branch members are welded to one another with gussets, diaphragms and stiffening rings, subjected to axial loads, with the member axes in the same plane. The fatigue analysis of a jack-up platform was carried out by Kwan (68) on the basis of the available drilling records from platforms in operation in the North Sea. For two different K-joints, stress concentration factors were obtained using finite element analysis. Fatigue lives of mobile and fixed platforms were compared with different S-N curves. The deterministic method of analysis was found to be more suitable than the power spectral density method which requires the transformation to be linear. Tests were carried out by Washio, Togo and Mitsui (69) to investigate the strength and stiffness of saddle type tubular truss joints and established empirical rules to calculate the

strength and stiffness of the joints as a function of the geometric parameters using least squares method.

Kurobane and Konomi (70) presented the experimental results on the fatigue strength of tubular K-joints in the form of a ratio of the fatigue strength to the static strength and found that the overlapping joints possessed greater fatigue strengths than the other types based on the S-N diagrams.

Maddox (71) discussed the design method using fracture mechanics approach, to predict the variable amplitude fatigue endurance (Miner's rule). Miner's linear cumulative damage rule was shown to be a special case of the fracture mechanics fatigue crack propagation analysis.

Graff (72) presented an analysis of the experimental data for the ultimate load carrying capacity, and the elastic stress distribution of chord in T, K, and Y-joints. Brink and Van der Krogt (73) carried out numerical and experimental investigations to study the local stress distribution in cross joints with specific weld sizes. The study indicated that the unstiffened cross-joint is poor in carrying alternating loads and can be improved by proper positioning of the seam weld relative to the attached brace.

For the first time, Holliday (74) investigated the stress distribution of tubular T-connections using photo-elastic models. Making use of three-dimensional

photoelasticity, stress distributions were obtained and the results compared with previous experimental results of steel models. The study indicated that the three-dimensional photoelasticity can be used more efficiently to study the high stress concentrations of more complex joints.

Holliday and Graff (75) extended the three-dimensional photoelastic model studies for T-joints and compared the results with similar joints of steel specimens. The photo-elastic study, as a new tool, proved to be more efficient for analyzing complex tubular intersections.

2.3.2 Corrosion Fatigue Tests

Dijkstra and de Back (76), presented the fatigue test results on forty tubular T and X-joints, carried out in The Netherlands. Most joints were tested in air and in axial loading. Four T-joints were tested in artificial sea water, three at free corrosion and one with cathodic protection. During the fatigue test, crack growth was monitored by visual inspection and strain measurements. The sea water tests had only 43% of the life that could be expected in air. The free corrosion and air fatigue tests showed relatively early crack initiation and slow crack growth compared to the cathodically protected joint. Hicks (77) described the United Kingdom Offshore Steel Research Programme (UKOSRP) fatigue programme designed to acquire information on the fatigue life of welded joints in seawater for compiling design rules for offshore

structures. The influence of a simulated seawater environment has been shown to be much less marked than would be expected and differences in stress history show small effects on performance. The characterisation of the stress histories on the basis of root mean square or higher order averaging offers a valuable method of comparing constant amplitude and variable amplitude test results.

Gibstein (78) presented the results obtained from fatigue tests carried out at Det Norske Veritas in the framework of the European Fatigue Research Programme. It was found that both the depth and length of cracks in tubular joints, are approximately linear functions of the number of cycles. Walker (79) has reported the Dutch results, which indicated that the fatigue endurance of T shaped joints in seawater at 20°C is equal to about 1/2 to 1/3 that of a similar test joint in air under constant amplitude loading conditions. On the contrary, the tests performed in Britain at stress ratios of R=0 and R=1 for joints freely corroding in seawater at 5°C showed that the fatigue strength was not significantly different from that obtained in air. Based on the measured strain drop in the hot spot, it was inferred that the fatigue crack growth rate in seawater was approximately three times that obtained in air. The rate of fatigue crack propagation in seawater in typical offshore steels at high stress ratios was considerably greater than

that observed from tests in air. The accelerated fatigue crack growth rate, however, occurred over a relatively narrow range of cyclic stress intensities. Schutz (80) presented general conclusions from the data accumulated within the frame of the European Coal and Steel Community (ECSC) offshore steels program. The effect of seawater corrosion on fatigue life is not significant (a factor of less than two on life) under realistic stress sequences and tests at constant amplitudes overestimate the effect (a factor of 2.5 on life). Further work has been suggested for i) prediction of crack propagation life of tubular joints in seawater and ii) study of effect of long exposure times to seawater on fatigue life under realistic stress amplitude. Tests on steels by Vosikovsky (81), over a frequency range of 0.01 and 10 Hz, under cathodic and free corrosion potential in aqueous environments, indicated that they were not susceptible to stress corrosion cracking in the environment used (3.5 percent NaCl solution).

Haagensen (82) presented a survey of research on fatigue strength improvement of welded cruciform and T-joints carried out within ECSC and Norway and compared the results with existing weld design codes. It has been shown that consistently high fatigue strengths in air were obtained for welds treated by grinding. Under free corrosion in sea water the increase in fatigue strength due to weld profile

improvement was less than in air. Mullen and Merwin (83) reported tests on full penetration butt welded T-joints and concluded that fatigue life improvement associated with toe grinding was significantly affected with greater beneficial effect at lower load levels. Increasing the toe radius improved the fatigue life by about 10 percent, even when the weld angle was kept constant. Further research has been recommended to quantify the magnitude and interaction of the effects of local geometry parameters such as weld angle, leg length, toe radius and plate thickness on crack propagation near the weld toe surface. Morgan (84) compared a fully ground profile with a 45° as welded profile for T butt welds in 38, 75 and 100 mm thick material. On the basis of experimental evidence, an increase of 30 percent on strength or 2.2 on life was recommended for toe ground welds. Zwaans, Jonkers and Overbeeke (85) performed fatigue tests on welded T-shaped plate specimens under random loading in air at a temperature of 17-26°C and sea water at 20 ± 1°C. It was found that seawater reduced the endurance by a factor of 2.2, which compared well with the German random load tests (factor ≅ 2). However, the lower reduction factor of 1.5 obtained from the British random tests was due to the lower temperature used (5°C versus 20°C).

2.4 Design Considerations

Offshore structures are designed considering self weight, installation equipment loads, wave, current, wind and ice forces. Typical joint failures may occur due to yielding, creep rupture, stress corrosion, fatigue and fracture. The present fatigue design considerations for fixed offshore platforms are reviewed in the following:

For template type structures with natural periods less than three seconds, the ductile steels and structural redundancy, the American Petroleum Institute (API) code (86) specifies the peak nominal stresses in the brace and discusses the limitation of the hot spot stress due to environmental loads for different types of joints. For structures with natural periods greater than 3 seconds, for different structural types, for higher design stresses or for areas where the long term distribution of cyclic loads is more severe than the Gulf of Mexico, a detailed analysis of cumulative fatigue damage analysis should be carried out.

The Palmgren-Miner cumulative damage fatigue rule is given by:

$$D_u = \sum_{i=1}^{j} \frac{n_i}{N_i} < 1 \qquad (1)$$

where

n_i = number of cycles within each block number i of the long-term stress-range distribution

N_i = number of cycles to failure at the same stress range, derived from the S-N curve

j = total number of blocks, and

D_u = usage factor.

After knowing the cumulative damage ratio, a planned life of N_y years will be assumed, based on the operational requirements and the oceanographic data, the fatigue life of joint will be estimated by:

$$\text{Life} = \frac{N_y}{D_u} \text{ (years)} \qquad (2)$$

The American Welding Society (AWS) structural welding code (87), suggests the use of AWS-XX S-N curve with hot spot stress or strain range for designing tubular members. This curve is based on the data obtained from joints tested in air. On the other hand, the API code recommends the use of X-curve for as-welded joints exposed to seawater environment. The hot spot strain range used can be obtained from i) measured data, ii) finite element analysis or iii) empirical equations.

The U.K. Draft for development DD 55, (88) suggests the use of Q curve for tubular joints. The new British code recommends the use of extrapolated hot spot strain range.

The Det Norske Veritas Code (89) suggests the fatigue design methods based on: a) fracture mechanics analysis, b) fatigue tests consisting of the following three main steps:

i) determination of long term distribution of stress range, using deterministic or spectral analysis;

ii) selection of appropriate S-N curve with a 95% confidence limit; and

iii) determination of accumulated damage, using Miner's rule.

The API code recommends checking the main chord member using K curve and the cyclic punching shear stress range Vpr, using

$$\text{Cyclic } V_{pr} = \tau \sin\theta \left[f_{akr} + 2 f_{aty} + \sqrt{(0.67\, f_{byr})^2 + (1.5\, f_{bzr})^2} \right] \quad (3)$$

where

τ = the joint parameter, $\frac{t}{T}$

f_{akr} = nominal stress range for that portion of the axial load which is reacted by adjacent braces in the same plane as in a K connection.

f_{atr} = the nominal stress range for that remaining portion of axial load which is reacted as in T, Y or X connections

f_{byr} = in-plane bending stress range,

and

f_{bzr} = out-of-plane bending stress range.

The literature review indicates that extensive research has been carried out by several investigators on planar joints viz. K, T, X and Y.

It is seen that very little work has been done on spatial type monopod tubular joints. Therefore the study on fatigue on monopod tye tubular joints was found to be quite relevant and hence proposed for investigation.

CHAPTER 3

ANALYTICAL PROCEDURE

3. ANALYTICAL PROCEDURE

3.1 General

The determination of the stress distribution in the components of a structure is very important in order to predict the fatigue strength. Accurate estimation of peak stresses around tubular joint intersection is complicated due to the presence of residual stresses, welding imperfections and joint configuration etc. When a tubular structure is subjected to external loads, the stress distribution includes: the basic structural response to applied loads (nominal stresses), geometrical stresses maintaining compatibility between the tubes, and 'notch' stresses resulting from the highly localized deformations in part of the tube wall near to the chord-brace intersection. Nominal stresses arising due to the tube behaviour as beam columns are determined by frame analysis; whereas geometric stresses result from the differences in deformation between the chord and brace under load (90). The differential deformations require the tube walls to bend so that the chord and brace maintain continuity at the weld. 'Notch' stresses arise because of the geometric discontinuity of the tube walls at the weld toes and do not extend far through the wall thickness. Sharper corners at the weld toes and greater angle of the overall weld profile to the tube wall cause higher notch stresses.

The use of small scale models have been very useful in the determination of stress distribution in elastic structures and its components. The most important factor affecting the fatigue life of tubular joint is the magnitude of the stresses at the intersection (91). Hence accurate determination of these stresses is important to obtain reliable results. The following are the stress analysis methods commonly employed for determining stress distribution in the models:

(1) Brittle lacquer techniques
(2) Strain gauged acrylic models
(3) Photoelastic methods
(4) Parametric equations
(5) Finite element approach
(6) Welded steel tubular models

In the present investigation the stress concentrations at the hot spot have been determined using parametric equations, the finite element analysis, and strain gauged steel tubular models.

3.2 Stress Analysis Methods

3.2.1 Parametric Equations

Semi-empirical equations are used for computing the magnitude of the stress concentrations in the hot spot region of the non-reinforced planar joints. The parametric

equations employ non-dimensional ratios of the geometric parameters viz. α, β, γ, τ and θ defined in Fig. 11 (19).

The semi-empirical parametric formulae for estimating the geometrical stress concentration factor (SCF) at the weld toe have the following general form (1,92)

$$SCF = K' \alpha^{n_1} \beta^{n_2} \gamma^{n_3} \tau^{n_4} (\sin\theta)^{n_5} \qquad (4)$$

where

$\alpha, \beta, \gamma, \tau$ = non-dimensional parameters

K' = constant

n_i = exponents

Among the formulae applicable to K, T and Y-joints, those with only in-plane bending mode have been considered. Beale and Toprac's equation derived from experimental data (1) is given by

$$SCF = 0.1873 \ \alpha^{0.56} \ \beta^{-0.022} \ \gamma^{0.746} \ \tau^{0.608} \qquad (5)$$

Visser's (93) equation obtained by generation of analytical data from finite element analysis applicable for T and K-joints is

$$SCF = \frac{t}{T} (10 + 0.15 \frac{D}{T}) \sin^2\theta \ (1.4 - 0.75 \frac{d}{D}) \qquad (6)$$

Kuang's (19) equations give the SCF at the location adjacent to the intersection line of the mid-surfaces of the branch and chord, and are given by

$$SCF_{T,Y_{chord}} = 0.702\beta^{-0.04}\ \gamma^{0.6}\ \tau^{0.86}\ \sin^{0.57}\theta \quad (7)$$

$$SCF_{T,Y_{Branch}} = 1.301\beta^{-0.38}\ \gamma^{0.23}\ \tau^{0.38}\ \sin^{0.21}\theta \quad (8)$$

$$SCF_{K_{chord}} = 1.822\beta^{0.06}\ \gamma^{0.38}\ \tau^{0.94}\ \sin^{0.9}\theta \quad (9)$$

Wordsworth's and Smedley's (94) equations for determination of SCF for in-plane bending for T, Y and X-joints are

$$SCF_{T,Y_{chord}} = 0.75\ \gamma^{0.6}\ \tau^{0.8}$$

$$(1.6\beta^{0.25} - 0.7\beta^{2})\ \sin^{1.5-1.6\beta}\theta \quad (10)$$

$$SCF_{T,Y_{branch}} = (1 + 0.63\ SCF_{chord}) \quad (11)$$

$$SCF_{K_{chord}} = 1.822\ \beta^{0.06}\ \gamma^{0.38}\ \tau^{0.94}\ \sin^{0.9}\theta \quad (12)$$

$$SCF_{K_{branch}} = 2.827\ \beta^{-0.35}\ \tau^{0.35}\ \sin^{0.5}\theta \quad (13)$$

The formulae proposed by Gibstein (95) are:

$$SCF_{T,Y_{chord}} = \gamma^{0.38}\ \tau^{1.05}[1.65 - 1.1(\beta - 0.42)^{2}] \quad (14)$$

$$SCF_{T,Y_{branch}} = \gamma^{0.38}\ \tau^{0.29}[0.95 - 0.65(\beta - 0.41)^{2}] \quad (15)$$

These equations are valid only for certain ranges of the dimensionless parameters. The joint parameters, given in Table 1, are within the validity range of the equations. For

unstiffened joints these ranges are given in Table 2(a). In deriving these parametric equations, the results of acrylic model tests or finite element analysis have been used, which estimate the peak stresses at the midthickness. The stress concentration factors obtained using above equations are given in Table 2(b).

3.2.2 Finite Element Approach

The stresses at the joint intersections can be determined accurately by the finite element method, provided the stress variation across the thickness of the shell element and the weld profile are included in the modelling. If the element stresses were to be computed from the middle surface of the shell, then some degree of variation will exist between the analysis and measurements. The finite element analysis for obtaining the hot spot stresses and stress concentration factors is used in chapter 4.

3.2.3 Welded Steel Tubular Models

The majority of fatigue tests have been carried out on steel joints, covering a wide range of parameters which are representative of joint intersections of offshore structures. The highest critical hot spot strain range is obtained by the linear extrapolation of the strain to the weld toe, from two strain gauges installed at the linear stress region. This method excludes strains due to residual and notch stresses. In the present study, the hot spot

strain range of the joints has been obtained using strain gauged steel tubular models.

3.3 Hot Spot Strain or Stress Range

The hot spot stress is the peak stress around the intersection of two or more members. The service life of tubular joints is generally calculated from S-N curve, where S is the hot spot stress range, and N is the number of cycles to failure.

According to AWS Structural Welding Code (87), the hot-spot stress or strain range is defined as: "Total range of worst hot-spot stress or strain on the outside surface of intersecting members of the toe of the weld joining them - measured after shakedown in model or prototype connection or calculated with best available theory". The British Code (88), uses the following definition for the hot-spot strain range: "Relationship Q (curve) applies to the main members of T, Y and K connections. The stress range corresponds to the peak range on the outer surface adjacent to the toe of the attachment weld between brace and chord members". The corresponding S-N curves for the above two definitions are AWS-X curve and DD 55-Q curve respectively.

The API Code RP2A (86), states "hot spot strain range may be defined as that which would be measured by a strain gauge element adjacent to and perpendicular to the toe

of the weld after stable strain cycles have been achieved". The proposed fatigue design rules (98), which is followed in the present study, suggest that the idealized hot spot strain range which is obtained by linear extrapolation of measured strains to the weld toe. The strains are measured by strain gauges at appropriate locations (A, B), indicated in Fig. 12, and defined by the following equations (137):

$$a_1 = 0.2\sqrt{rt} \text{ but} < 4 \text{ mm} \tag{16}$$

$$a_2 = 0.4\sqrt[4]{(rt)}\,(RT) \tag{17}$$

$$b_1 = 0.2\sqrt{rt} \text{ but} < 4 \text{ mm} \tag{18}$$

$$b_2 = 0.65\sqrt{rt} \tag{19}$$

The maximum hot spot strain range is obtained using the linear extrapolation to the weld toe through A and B, thus including the effects of the global geometry of the joint and the weld (76). The magnitude of the hot spot strain range, $\Delta\varepsilon$ for the random loading is given by an equivalent constant amplitude equal to the root mean square value (rms) of

$$\Delta\varepsilon = \frac{2\sigma_{rms}}{0.707} \tag{20}$$

where σ_{rms} = rms value of a random signal (139). In the American literature (15) the hot spot stress, σ_{HS} is defined as

$$\sigma_{HS} = E \cdot \varepsilon_{HS} \tag{21}$$

The strain concentration factor (SNCF) is the ratio of the hot spot strain, ε_{HS} and the nominal strain, ε_o in the

brace. The stress concentration factor (SCF) adopted in Europe is the ratio of maximum principal (hot spot) stress, σ_{HS} and the nominal stress σ_o in the brace (100,137). Thus,

$$SCF = \sigma_{HS}/\sigma_o \tag{22}$$

in which

$$\sigma_{HS} = \frac{E}{1-\nu^2}(\varepsilon_{HS} + \nu\varepsilon''_{HS}) \tag{23}$$

$$SNCF = \varepsilon_{HS}/\varepsilon_o \tag{24}$$

Eqn. (22) can be rewritten as

$$SCF = \frac{1}{(1-\nu^2)} \frac{\{\varepsilon_{HS}+\nu\varepsilon_{HS}''\}}{\varepsilon_o}$$

$$= \frac{\varepsilon_{HS}}{\varepsilon_o} \frac{1}{(1-\nu^2)} \{1+\nu \frac{\varepsilon_{HS}''}{\varepsilon_{HS}}\} \tag{25}$$

With $\nu = 0.3$ and $\frac{\varepsilon''_{HS}}{\varepsilon_{HS}}$ being small, the SCF > 1.1 SNCF. (100)

3.4 Fracture Mechanics Approach

The fracture mechanics provide a quantitative relationship between the applied stress, the size of the stress concentrator, such as a weld crack or similar flaw, and the toughness of the material and can be effectively used to establish the criteria for the design, inspection and repair of offshore platforms (101,102). The structural integrity parameters controlling fracture are shown in Fig. 13.

3.4.1 Linear elastic fracture mechanics (LEFM)

The application of linear elastic fracture mechanics to fatigue life prediction is based on the assumption of linear elastic material behaviour of the material. While the stress and strain distributions around the crack tip control its initiation and propagation, remote boundaries, the nature of applied loading and environment affect only the intensity of the local stress field (103). For any given interrelated parameter of fracture (Fig. 13),

viz. the applied stress/strain level, allowable defect size, or the material property, the unknown quantities governing the design can be estimated.

3.4.2 Determination of Fatigue Crack Growth Rate Curve

The stress intensity factor is of primary importance in the prediction of brittle failures using linear elastic fracture mechanics. Numerical determination of stress intensity distribution along the crack front is a difficult task and the stress intensity depends mainly on the boundary conditions away from the crack front.

Stress intensity factor K is a function of geometry, size and shape of the crack, and the loading conditions. The relationship among these parameters is given by

$$K = Y \sigma \sqrt{\pi a} \qquad (26)$$

where

a = half crack length (if it is an embedded crack)

= crack depth (for surface cracks)

σ = the remote stress,

Y = correction factor dependent on geometry

Since fatigue crack growth depends on the cyclic stress range, and the stress intensity factor varies directly with the applied load, it is appropriate to consider the range of stress intensity factor given by

$$\Delta K = Y \Delta\sigma \sqrt{\pi a} \tag{27}$$

For fracture mechanics prediction of fatigue life, knowledge of crack growth rate data for the material is essential. To determine the crack growth rate, a precracked specimen is subjected to constant amplitude cyclic loading. During the test, increments of crack length and the corresponding number of loading cycles are observed for a given load range. The resulting data of crack length, a, vs. number of cycles, N, are plotted. By performing experiments on identical specimens subjected to different stress ranges, crack length is plotted against number of cycles. da/dN for successive positions along the curves are determined graphically or numerically. The corresponding values of stress intensity factor ranges, ΔK, are computed from the known applied load range and mean crack length for each interval. The resulting data when displayed on a log-log plot of da/dN vs. ΔK reduces to a single curve as shown in

Fig. 14. This curve has a sigmoidal shape that can be divided into three major regions. Region I indicates a threshold value ΔK_{th}, below which no crack propagation takes place. Region III corresponds to the transition into the unstable regime of rapid crack extension. Region II shows essentially a linear relationship between log $\frac{da}{dN}$ and log ΔK defined by Paris equation (110).

3.4.3 Fatigue Crack Growth Model

In the present study, an analytical two dimensional crack model of an edge notch type is considered, to simulate the crack growth observed in the tubular monopod joints. The instantaneous crack growth rate was determined experimentally and then the stress intensity factor calculated from the relation given by Eqn. (28).

Paris (110), proposed that the growth rate of a crack under fatigue loading could be characterized by the stress intensity factor range, using the linear elastic fracture mechanics (LEFM) principles. In region II of the curve shown in Fig. 14, the fatigue crack growth rate $\frac{da}{dN}$ is related to the stress intensity factor range, ΔK, by

$$\frac{da}{dN} = C\,(\Delta K)^m \qquad (28)$$

in which

C and m are material constants

According to Gurney (111), C and m are not strictly material constants, since they vary with the mean cycling stress, test environment and the cyclic frequency. For a particular material and set of conditions, the values of C and m have to be determined. For more complicated configurations, such as tubular joints, the stress intensity factors have to be determined from the tubular joint fatigue test data and crack growth records. Substituting Eqn. (27) in Eqn. (28), we get

$$\frac{da}{dN} = C(Y \Delta\sigma \sqrt{\pi a})^m \qquad (29)$$

3.5 Fatigue Failure Criteria for Tubular Joint

The following fatigue lives defined by the extent of cracking are usually defined (140):

i) N_1 = 15% drop in the strain gauge measurement close to the point of crack initiation

ii) N_2 = First discernible surface cracking usually detected by visual inspection

iii) N_3 = First through thickness cracking

iv) N_4 = End of test, when the crack length becomes approximately equal to half the main chord circumference

CHAPTER 4

FINITE ELEMENT ANALYSIS

4. FINITE ELEMENT ANALYSIS

4.1 General

In welded tubular joints fatigue cracks are found to initiate at the weld toes at the hot spot. Many techniques have been in use to determine the stress concentrations in the hot spot region. In general this is done by strain gauge measurements or finite element calculations, or both. In both cases the effect of weld defects and weld profiles cannot be taken into consideration and hence do not provide information on the local effects. The high local stresses, usually characterized in terms of stress concentration factors, are especially important for fatigue considerations.

The monopod structure is analysed by the MSC/NASTRAN computer code (116,117) using flat shell elements. Because of the non-axisymmetric nature of the problem (structure being rotationally symmetric with the wave load antisymmetric), the nodal and element data were prepared for the three-dimensional structure and used to evaluate the stress distribution and structure deformation. The following section describes the basic theory related to the analysis using QUAD4 and TRIA3 finite elements.

4.2 Flat Shell Elements - QUAD4 and TRIA3

A three noded isoparametric flat element (TRIA3) and a four noded isoparametric flat element connecting three and four grid points respectively are shown in Fig. 15. The element formulation allows inplane, bending, and transverse shear deformations as well as coupling between inplane and bending behaviour. The grid point numbers associated with the fields G1, G2, G3 and G4 are unique for either element and must be ordered consecutively around the perimeter of the QUAD4 element such that all interior angles are less than 180 degrees. The element has five nodal degrees of freedom consisting of two inplane displacements, u_x, u_y and a normal displacement u_z, and two bending rotations θ_x, θ_y. No rotational degree of freedom is permitted about the normal for these elements so that there will be a row and a column of zeros in the six by six stiffness matrix associated with each connected grid point. The system stiffness matrix will thus be singular and constraint is imposed by the single point constraint (SPC) capability of NASTRAN computer code (117).

The constitutive matrix, which defines the stress-strain law for the shell element is as follows:

$$\begin{Bmatrix} \{N\} \\ \{M\} \\ \{Q\} \end{Bmatrix} = \begin{bmatrix} tG_1 & t^2G_4 & 0 \\ t^2G_4 & IG_2 & 0 \\ 0 & 0 & t_sG_3 \end{bmatrix} \begin{Bmatrix} e^\circ - e_1^\circ \\ \kappa^\circ - \kappa_1^\circ \\ \gamma^\circ \end{Bmatrix} \qquad (30)$$

where the matrices $\{M\}$ and $\{N\}$ are given as

$$\{M\} = \begin{Bmatrix} M_x \\ M_y \\ M_{xy} \end{Bmatrix} = - \int_{-t/2}^{t/2} z \, \{\sigma\} \, dz \tag{31}$$

$$\{N\} = \begin{Bmatrix} N_x \\ N_y \\ N_{xy} \end{Bmatrix} = - \int_{-t/2}^{t/2} \{\sigma\} \, dz \tag{32}$$

where t = thickness of the element and $\{\sigma\} = \begin{Bmatrix} \sigma_{xx} \\ \sigma_{yy} \\ \sigma_{xy} \end{Bmatrix}$

The terms e° are defined as surface strains and given as

$$\left\{e^{\circ}\right\} = \begin{Bmatrix} e^{\circ}_{xx} \\ e^{\circ}_{yy} \\ e^{\circ}_{xy} \end{Bmatrix} = \begin{Bmatrix} \partial u_x/\partial x \\ \partial u_y/\partial y \\ \dfrac{\partial u_x}{\partial y} + \dfrac{\partial u_y}{\partial x} \end{Bmatrix} \tag{33}$$

where u_x and u_y are the displacements of the natural surface in x and y directions. Similarly the reference surface curvatures are

$$\left\{\kappa^{\circ}\right\} = \begin{Bmatrix} \kappa^{\circ}_{xx} \\ \kappa^{\circ}_{yy} \\ \kappa^{\circ}_{xy} \end{Bmatrix} = \begin{Bmatrix} \dfrac{\partial^2 u_z}{\partial x^2} \\ \dfrac{\partial^2 u_z}{\partial y^2} \\ 2 \dfrac{\partial^2 u_z}{\partial x \partial y} \end{Bmatrix} \tag{34}$$

where u_z = the displacement in the z direction.

$e_1{}^\circ$ and κ° are the initial strain and curvature of the natural surface and $\{Q\}$ and $\{\gamma^\circ\}$ are defined as

$$\{Q\} = \begin{Bmatrix} Q_x \\ Q_y \end{Bmatrix} \tag{35}$$

$$\{\gamma^\circ\} = \begin{Bmatrix} \gamma_{xy}{}^\circ \\ \gamma_{yz}{}^\circ \end{Bmatrix} \tag{36}$$

Q_x and Q_y are the transverse shear forces in Fig. 16 and $\gamma_{xy}{}^\circ$ and $\gamma_{yz}{}^\circ$ are the corresponding transverse shear strains of the reference surface. The cross sectional properties of t, I and t_s are the membrane thickness, second area moment for the cross section and shear thickness respectively, referred to the reference surface.

The matrices G1, G2, G3 and G4 are elastic constants which are obtained from the continuum formulation. The term containing t^2G_4 in the Eqn. 30 represents the effect of coupling of bending and membrane behaviour.

The stresses are computed at distances z_1 and z_2 from the reference plane along a line perpendicular at the centroid of the element.

The stress state is given as:

$$\sigma^1 = -\frac{z_1}{I}\{M\} + \sigma^\circ + \{\Delta\sigma\} \tag{37}$$

where the membrane stress σ° is given by

$$\sigma^\circ = G_1\,(e^\circ - e_1{}^\circ) + t\,G_4\,(\kappa^\circ - \kappa_1{}^\circ) \tag{38}$$

and $\Delta\sigma$ results from thermal effects. In addition to these stresses, the force resultants M, N and Q are also computed at the node points.

The restraint provided by welds at the ends of the tubes with the base plate is simulated by restraining the translations and rotations of all the bottom nodes. The solution of the equilibrium yields the displacement components of the nodal points of the finite element system.

4.3 Discretization of the Joint

For discretization of the tubular connection, developed surfaces were drawn for the main chord, and three branch members with their lines of intersections. Both triangular and quadrilateral elements were used, with smaller size elements along the lines of intersection and larger size elements away from the intersection of the joint. Quadrilaterals are formed by connecting the points on two adjacent lines. Two triangles were formed from a quadrilateral by connecting its shorter diagonals. A smooth transition from smaller to larger elements was obtained and the elements and their node numbers were numbered consecutively. The developed surfaces, element patterns and their numbering for branch tubes and main chord are shown in Figs. 17-20. The bulk of the input data consisted of element numbers and surface coordinates of the nodal points. The generated mesh for the joint is shown in Fig. 21.

4.4 Element Stresses and Strains

The element surface strains and stresses obtained from the finite element analysis are compared with the values measured by strain gauges in Figs. 22 through 26 (137).

CHAPTER 5

EXPERIMENTAL PROGRAMME

5. EXPERIMENTAL PROCEDURES

5.1 General

The objective of the experimental work was to determine fatigue lives of monopod type tubular joints in i) air at room temperature and, ii) natural seawater at 0°C. Joint details, design of test frame and connections, specimen fabrication and cooling system for seawater circulation are described in the following sections:

5.2 Test Hardware and Loading Devices

The existing test frame was adapted to support the specimen and provide the necessary reactions for the hydraulic actuators. To avoid the lateral deflections of the frame additional inclined side braces were provided. The vertical hydraulic actuator was supported from the two channels which were bolted to the top of the two main columns. The horizontal hydraulic actuator was supported by the other two main columns approximately at one third of their height, with a box type unit with I-sections inside the unit at intervals to avoid the deformation of the unit during cyclic loading. The testing frame and the positions of loading actuators are shown in Figs. 27 and 28. To avoid any slight movement of the loading frame columns, due to the fluctuating load during testing, all the bolts were provided with steel bushings on either ends, so that the inner

diameter of the bushings were equal to the outer diameter of the bolts, so as to fit exactly. The bases of the columns were bolted to the heavy duty test floor with sufficient torque. The hydraulic rams were used to apply the loads both in vertical and horizontal directions. The base of the specimen was fixed to the 90 cm thick heavy duty test floor. The vertical and horizontal hydraulic actuators had capacities 220 KN and 670 KN respectively and were controlled by the MTS machine. The hydraulic power supply for the rams consisted of 40 H.P. electric motor with 1200 rpm and a hydraulic pump with a flow capacity of 65 litres per min. at an operating pressure of 20 MPa.

Special connection devices were designed to apply static vertical and cyclic horizontal loads to the specimens. Care was taken to achieve the verticality of the vertical load, to avoid any eccentric loading during testing. For the pin-jointed end of vertical ram, a square steel plate of 25 mm thick was connected. To the other side of this plate; a circular ring, with dimensions O.D. 375 mm x 50 mm high x 3.18 mm tk., was welded. The outside diameter of this tube was exactly equal to the inner diameter of the main chord of the specimen, so that it can easily slide. This was provided in order to avoid any slip of the vertical ram during cyclic loading. The vertical load connection unit is shown in Fig. 29. The concentricity of the vertical load was confirmed

from equal strains indicated by the four strain gauges spaced equally on the circumference of the main chord upon vertical load application.

For the cyclic load application in the horizontal direction, four semi-circular plates 12.7 mm tk. were welded to two end plates of 38 mm tk. at a distance of 250 mm apart. The semi-circular plates were fastened with two smaller plates on both top and bottom sides to make a monolithic connection. The end plates were interconnected using 25 mm diameter bolts on all the four corners, making the whole system to act as a single unit. One side of the unit in turn was welded to the end of the horizontal hydraulic ram as shown in Fig. 30.

Before the commencement of the actual testing program, a detailed loading frame analysis was carried out to ensure that the stresses and deflections at critical joints do not exceed the allowable values under the maximum expected loads. Also the load cells at the vertical and horizontal hydraulic rams were calibrated to check the linear relationship of load and the corresponding voltage levels.

5.3 Design of Typical Joints

Seven joints were fabricated to study the joint behaviour under static and cyclic loads (Table 9). One joint with stiffening rings (Fig. 31) and six without (Fig. 32).

stiffened joint stiffeners were provided at the main chord-branch tube intersection, to decrease the joint flexibility. The stiffening rings are circular in shape spaced at 100 mm apart with the dimensions of 75 mm wide by 6.25 mm thick. The directions of static and dynamic loads for the joints together with the reactive forces are shown in Fig. 33.

The material selected for the fabrication of specimens, was according to ASTM A36 Grade B steel for the wet tests and ASTM A53 Grade B specifications for the dry tests. The mechanical properties of the steels are given in Table 3, chemical compositions in Table 4.

All the three branch tubes, spaced at 120° to each other, intersect the main chord at one third of its height, with an inclination of 37° with the vertical axis. To avoid stress concentrations due to proximity, the axial and lateral loads were applied at distances of more than three times the diameter of the main tube from the joint intersection. The ends of all the branch tubes and the main chord were welded to a base plate of 25 mm thick, which was bolted to the heavy duty test floor of 760 mm thick. At a distance of 150 mm from the top of the main chord, a sleeve of 250 mm x 3.13 mm thick was provided to avoid any localized effects due to axial and dynamic loadings in the vertical and horizontal directions respectively.

5.4 Specimen Fabrication and Welding Details

The steel for the dry specimens was donated by STELCO (Steel Company of Canada) and the financial support for the wet specimens was provided by Department of Energy, Mines and Resources, Canada. The bevelling of ends of the tubes, cutting and trimming were carried out according to American Welding Society (AWS) Structural Welding Code (87) requirements.

Different weld thicknesses were used based on the design requirements. All welds were of the fillet type, with electrodes of AWS-ASTM E6011 and E7018 specifications to achieve full penetrations, economy in overall welding cost, and good weld quality. The welding of the specimens was done by a welder who was fully competent for the job with 15 years experience and qualified for this type of work. The weld sizes between i) intersecting branch tubes and main chord, ii) branch tube, main chord ends and base plate and iii) stiffening rings and the tubes are shown in Figs. 34 through 36.

In addition to normal visual inspection, all welds were subjected to 100% radiographic examination using gamma rays, to ensure that no cracks or major weld defects exist.

Faulty weld locations, indicated by radiography were removed and rewelded and reexamined to avoid all possible flaws. The mechanical properties of electrodes and welding details are shown in Tables 5 and 6. The welds for some joints were ground to enable comparison to be made with other joints tested in as-welded condition.

After welding of each specimen dimensional checks were carried out on all the models, to check the accuracy of the specimen positions and distortion due to manual metal arc welding. All the checks carried out were found to be within the acceptable tolerances in both linear and angular dimensions in comparison with the American Welding Code.

5.5 Design and Installation of Cooling System for Seawater Circulation

Two special tanks, one for cooling the water (dimensions: 1200 mm x 1200 mm x 1200 mm), and the other to house the test specimen (dimensions: 900 mm x 1050 mm x 1050 mm), were fabricated in the laboratory for carrying out tests in a simulated natural seawater environment. Natural seawater from the Atlantic Ocean was transported and cooled in the main tank and then circulated through the test cell containing the specimen. Two pumps, with a flow capacity of 11 litres/min., were used - one to pump the water to the test cell and the other to circulate the water from the test cell

back to the main tank. The water returning to the main tank was discharged with a free fall to maintain the oxygen concentration. A cooling unit was provided in the main tank with an automatic control system, and the water temperature was maintained between -1°C and -2°C. The seawater temperature around the specimen was maintained at 0°C throughout the testing period. The schematic view of the seawater circulation system with cooling arrangements is shown in Fig. 37. The sides and bottom of the sea water cooling tank were covered with a thick plastic sheet to minimize corrosion. However, the specimens and the inside surface of the test cell were free to corrode. The test set-up with test cell housing the specimen, and the main tank with cooling system are shown in Fig. 38.

5.6 Weld Surface Profiling

Fatigue strength of welded tubular joints depends on many factors, such as, weld imperfections, slag inclusions, notch geometry, crack-like defects and residual stress. Techniques have been developed to improve the fatigue strength of joints by reduction of the stress concentration factor and removal of intrusions at the weld toes.

One technique which has proved most promising, is

to grind the weld toes (82) with a disc grinder. Care was taken to produce a smooth concave profile at the weld toe. To achieve the maximum advantage, the grinding depth was kept approximately 1 mm, and it was extended little beyond the weld toe so as to remove the undercuts as can be seen in Section A, Fig. 39. Section B (Fig. 39) shows the profiling of the weld done on the joints tested in air.

CHAPTER 6

TESTING PROGRAMME

6. TESTING PROGRAMME

6.1 General

A total of seven joints were tested under constant amplitude and pseudo-random loadings. The three joints tested in air are denoted as 'Dry 1', 'Dry 2' and 'Dry 3'; and the four specimens tested in seawater are designated as 'Corr. 1', 'Corr. 2', 'Corr. 3' and 'Corr. 4'. The dry tests were carried out in air at room temperature, and corrosion tests were done in a simulated natural seawater environment. During testing, strains, specimen tip displacement and sea water properties were monitored. The fatigue life of joints for crack initiation, wall penetration and final failure were determined for all the specimens.

6.2 Stresscoat Application and Analysis

To determine the maximum strains and hence hot-spot stresses accurately, electric resistant strain gauges were used. The exact positions of the hot spots (the best strain gauge locations) can be obtained with the help of stresscoat application. Brittle lacquer coating cracks at threshold value which occur perpendicular to the maximum principal tensile strains. Since cracks initiate at the greatest strains, stress concentration points can be quickly identified. By knowing the direction of maximum strains at a point, orientation of the strain gauges can be made in order to obtain precise measurements (118).

Brittle lacquer coatings are very sensitive to changes in temperature and humidity. Depending on the prevailing conditions in the laboratory at the time of testing, the selection of the coating was made. For the laboratory temperature of 18°C and relative humidity of less than 50%, brittle lacquer TL-500-65 was selected.

The joint location was cleaned thoroughly to remove any oil, dirt, rust and loose paint if any, with the help of Tens-Lac brittle lacquer T-1 solvent. First of all, Tens-Lac brittle lacquer undercoat U-10, which consists of a mixture of aluminum powder and a carrier solvent, was sprayed on to the surface of the joint to obtain uniform reflectivity. Brittle lacquer was then applied over the undercoat, which was air-sprayed on to the joint portion of the monopod model, covering an area equal to about 1 1/2 times the diameter of the main tube and for the branch tubes this distance was almost equal to their diameter.

A uniform thickness of 0.15 mm was obtained by spraying about twelve layers, at intervals of 2 min. between each coating except the last one, which was applied after 20 min. Simultaneously, the coating was applied to four calibration beams of 206.25 mm x 18.75 mm x 3.125 mm standard

dimensions, of aluminum specimens, to measure the threshold cracking strain (sensitivity) of the brittle coating.

For the first test, the temperature during spraying was 65°F. The calibration beams and the model were cured at about 70° for 24 hours. The coated specimen is shown in Fig. 40. During curing, temperature was measured constantly with the help of a temperature sensor (thermo-couple) and the humidity was measured with relative humidity meter. After the curing time was completed, the temperature was brought down to the testing temperature of 65°F and the specimen was also allowed to attain the same temperature before the actual testing was started. The relative humidity was higher than that required during testing.

To start with, only vertical compressive load was applied at intervals of 10 kN and during each increment, the cracks were observed in the coating and the load was brought to zero each time before the next incremental load. This was followed for all load increments. At the same time, during incremental loading, the strain gauge readings from the four strain gauges, which were installed at four locations of the main tube were also recorded. 222 kN corresponding to the full load capacity of the vertical hydraulic actuator was applied to the model and no cracks were found in the coating. The maximum strain gauge readings during this load was about 300 με, but the sensitivity of the coating was 500 με and

hence no cracks were found in the coating. When the load was released, no cracks were observed. During testing, the sensitivity of the coating was measured using calibration beams with the aid of Tens-Lac calibrator Model C-220. This calibrator gives direct reading of brittle coating strains from the built-in strain scale when the free end of the cantilever specimen is pressed with the thumb pressure. The distance where the full length of the crack appear in the cantilever specimen, towards the free end gives the required coating strain. Details of the calibrator are shown in Fig. 42.

Next, using the horizontal hydraulic actuator, the load in the horizontal direction was applied by pulling the specimen towards the actuator. Load was applied at increments of 10 kN and cracks were observed. The first set of cracks appeared at 80 kN and these were marked with a felt-tipped pen. The load was raised to a maximum of 100 kN in increments and crack propagations marked on the coating. The photographs are shown in Fig. 43 for different locations of the joint. The crack distribution on the main tube, i.e. in the actuator side, was symmetrical on either side. The cracks in the other two branch tubes were almost similar to one another, on either side of the weld, both in the main tube as well as the branch tubes. This can be seen in Fig.

44(a). The coating and the undercoat were then removed using T-1 and T-2 brittle lacquer solvents respectively.

The second test was conducted to study the crack patterns in the coating, when the horizontal load was applied in the opposite direction by pushing the specimen away from the actuator. Again, coating was sprayed on the joint similar to first test. This time the coating selected was TL-500-70, which has a higher sensitivity than the previous coating. The coating was applied at 70°F and cured at 80°F for 24 hours. The relative humidity was 50% and was appropriate for the selected coating. After 24 hours, the temperature was brought down to ambient temperature of 70°F, and actual testing started. The load in the horizontal direction was increased in steps of 10 kN and each time the cracks were observed around the joint. The first set of cracks occurred in the main tube at the weld edge of the intersection of the main tube and the first leg which was in-line with the horizontal actuator for a load of 20 kN. A second set of cracks was found at a load of 40 kN at the edge of the weld in the branch tube. When the load was increased to 80 kN, many smaller cracks were found above the weld in the main tube. These cracks were marked on the specimen. As the loading was increased, the distribution of cracks spread out in the main tube but the cracks in the first branch tube were propagating along the weld instead of away from the weld

(Fig. 42). During this stage, small intermittent vertical cracks were observed in the main tube opposite to the first branch tube, in between the two other branch tubes intersection (Fig. 43(b)). No cracks were found in the remaining branch tubes until the load reached maximum at which the cracks were symmetrically distributed in the main tube and the branch tubes, as shown in Fig. 43(b). Cracks appeared during release of loading only on compression sides of the two branch tubes.

No cracks appeared beneath the lower portions of all branch tubes (lower crotches). All the cracks were marked on the specimen and photographs were taken before removing the coating. The spread of the lacquer cracks around the joint gave a vivid picture of the overall strain distribution and the severity of strains at critical locations, which were chosen for affixing the strain gauges around the joint to measure strains during static and fatigue loading.

The same procedure was followed for the joint with stiffening rings. The coated specimen and the coating crack patterns are shown in Figs. 41 and 42(b) respectively.

6.3 Test Set-Up and Instrumentation

Great care was taken to achieve the verticality of the static load with the vertical hydraulic actuator simulating the deck load, and the horizontality of the cyclic load with horizontal hydraulic actuator to simulate the wave loading. The base plate was secured to the test floor with the maximum allowable torque to the bolts. To avoid any lift of the base plate due to rocking of the specimen, two heavy angles were bolted on two sides of the plate. Finally, the vertical and horizontal load connection units were checked for smooth movements. To measure the specimen tip displacements during cyclic loading, a linear variable displacement transducer was placed at the top of the specimen (Fig. 38). The test assembly for dry-testing is shown in Fig. 45.

The direction of vertical and horizontal load applications and their reactive forces are shown in Fig. 33. Prior to the final assembly of the joint in the test rig, number of electrical resistance strain gauges were installed at important locations on the basis of the brittle lacquer testing. The strain gauges consisted of uniaxial, biaxial and rosette gauges. The properties of the gauges are given in Table 7. More gauges were placed near the critical region. All the uniaxial gauges were placed at locations where the direction of the maximum principal strains are

known. The rosette gauges were installed at locations of unknown directions of the principal strains. The strain gauges were connected to a wheatstone bridge in combination with a temperature-compensating dummy gauge.

For the joints tested in seawater, special protective coatings were applied on the gauges to protect them against chemical attack and moisture due to seawater and condensation around the joint. After the gauge was installed in position, M-coat G was applied to the terminal of the gauges where they are soldered to the lead wires. A thin coating of M-coat A/D was applied to the full width of the gauge and to all the exterior edges. After allowing to dry for about 24 hours at room temperature, an intermediate layer of metal foil such as M-coat FA or PTFE Teflon film was applied to produce a further vapour barrier. A final layer of M-coat G was applied after an elapse of a few hours (119). Fig. 46 shows the cross sectional view of protective coatings for strain gauge applications. This procedure was adopted for all the joints tested in seawater. The strain gauge locations and their directions for all the specimens tested are shown in Figs. 47 through 53. The procedure for strain gauge application to the metal surface is given in Appendix A.

6.4 Automatic Data Acquisition System

To measure strains under static and fatigue loadings, an automatic data acquisition system was employed with the following Hewlett-Packard units: 9825 Desktop Computer (controller), 9826A Plotter, 3455A Digital Voltmeter, 3437A System Voltmeter and 3495A Scanner. The units were connected via a Hewlett-Packard Interface Bus (HP-IB), which provides a link and communication between the components. All the strain gauges from the specimen were connected to BLH strain gauge switch and balancing units which in turn were interconnected to a B & K strain indicator unit. The change in the resistance of any strain gauge caused by the load could be read from the digital indicator display or through its remote analog output. The B & K strain indicator type 1526 gives instantaneous direct readings of strain levels on a digital display and has a hold function to permit the measurement of largest peak, regardless of sign and time. In cases where both static and dynamic strains are present the two components can be separated by the use of the hold function. The built-in set of low pass filters can also help to achieve this besides noise filtering. Because of the demodulator principle used in the strain indicator, resistive and capacitive unbalance on a strain gauge arrangement can be balanced out together by one potentiometer (120).

All the strain guages were connected in half-bridge configuration. To eliminate the temperature effects, compensating gauges were used along with the active strain gauges. The BLH switch and balancing units were modified internally by connecting a high and low wire from one of the input channels to the high and low output wires respectively, to facilitate automatic strain measurements and simultaneous data recording. This enables the scanner to pick up individual channels on the computer's command.

The strain gauges from the test specimen were connected to the strain indicator unit via the scanner and balancing units. An excitation voltage was applied across the simulated Wheatstone bridge and the variation in voltage drop recorded. The strain data was displayed in the indicator unit, while the analog signal was transmitted to the A/D converter i.e. the system voltmeter, where the signal was converted from analog to digital binary code and extended into the computer message storage. Similarly, the digital voltmeter interfaced with the computer received the load signal from the load cell of the hydraulic actuator. The computer was used to record simultaneously both the load and strain signals. The computer was programmed to collect data, store the maximum and minimum strain at any stage of testing, plot the stress-strain hysteresis loops for different gauges and record the data on paper. This automatic strain

measuring system helped to measure strains more efficiently and accurately during testing. The computer controlled data acquisition system is shown in Fig. 54, and the block diagram in Fig. 55.

6.5 Measurement of Environmental Parameters

Offshore structures are subjected to both corrosion and fatigue and the combined effect of an aggressive environment and fluctuating stress accelerates the fatigue damage. The corrosion fatigue life can be affected by environmental factors, such as dissolved oxygen content, salinity, temperature, velocity of the surrounding fluid and pH value. The normal temperatures in offshore Newfoundland vary from -2°C in midwinter to +10°C in midsummer. On the basis of this it was decided to maintain a temperature of 0°C throughout testing time simulating the natural seawater environment. In the present investigation, salinity, pH value, dissolved oxygen content, HCO_3^- concentration and temperature were measured once a day and the values shown in Table 8. The detailed measurement procedures are given in Appendix B.

6.6 Static Tests

The first stage in the testing procedure was the application of incremental static loading up to the peak

amplitudes of the prescribed fatigue loading in the vertical and horizontal directions. To measure strains during testing, each specimen was instrumented with sufficient number of electrical resistance strain gauges at important locations. The number of strain gauges and their positions for all the specimens are shown in Figs. 47 through 53. A shakedown of the instrumentation was performed by applying 4 to 5 cycles with a partial load before the commencement of the test, to ensure satisfactory performance of the gauges and eliminate drift.

After the calibration of the strain gauges, the joints were subjected to step-wise increasing and decreasing loads and strains recorded during each increment. The selected load levels for each joint in the vertical and horizontal directions, are given in Table 9. The static strains measured at the maximum and minimum peak loads for all the joints are given in Tables 10 through 16. From the measured strains, principal stresses and strains were calculated for the required gauges to obtain the stress and strain concentration factors (Tables 17 and 18). The details are given in Appendix C.

6.7 Fatigue Tests

Commencement of fatigue testing followed immediately after the completion of the static tests. The

maximum and minimum cyclic loads were selected to obtain a desired stress range. Five joints were tested under constant amplitude loading at stress ratio R = -1; four at a frequency of 0.20 Hz and one at 0.25 Hz. Two joints were tested under pseudo-random loading one in air and the other in water. The details of the test environment, weld conditions, and peak load levels for all the specimens are given in Table 9. The method of generation and application of random load time history and the constant amplitude sinusoidal signal are described in Appendix D. The number of cycles were counted as positive zero crossings. In both constant amplitude and pseudo-random load applications, the MTS testing system was employed. The details of the MTS capability and method of use are given in Appendix E. During fatigue loading, strains from all the strain gauges were recorded at appropriate intervals.

A linear variable displacement transducer (LVDT) was installed at the free end of the chord above the level of the horizontal hydraulic actuator (Fig. 38) to measure displacement of the specimen. Use of LVDT gave better accuracy in the displacement measurements of the joints than those based on the actuator stroke measurement.

Crack growth due to fatigue can be monitored by visual inspection, surface markings, measurement of the drop in strain level and non-destructive techniques (NDT). In the

present investigation, an attempt was made to detect the crack initiation and propagation using non-destructive testing methods. Krautkramer Ultrasonic Miniature Flaw Detector USK 5MR and Miniature Chart Recorder SR5 and a portable Magnetic Particle Testing unit were used to detect the cracks at the weld toes. The water level around the specimens was first lowered well below the joint intersection level and the locations near the expected crack initiation regions were cleaned and dried. The portion was then magnetized with individual contact prod sets. Immediately after magnetizing, magnaflux liquid was applied and the cracks were observed with a Magnaglo black light. The magnetic particles in suspension adhered to the crack openings indicating the presence of the crack.

Ultrasonic and magnetic particle testing methods were not successful for the wet tests in crack detection and as a result the reported surface crack lengths were measured visually using magnifying glass. The water level surrounding the test specimen was lowered for observing the crack initiation. The first crack initiation was noticed at crack lengths ranging from 2 mm - 10 mm. However, the detection of through-thickness-cracking of the chord was very successful. This was made feasible by the use of kerosene filled inside the chord to a predetermined height of 75 mm. As soon as the

through-cracking occurred, the kerosene oozed out during the crack opening in each cycle. This was immediately noticed not only by the smell but also by its floatation on the water surface. A fresh batch of natural sea water was then added within a time period of 2500 to 3000 cycles to replace the water polluted by kerosene. This procedure was followed for the stiffened and the four wet specimens and the crack growth measurements after wall penetration might have been affected due to the traces of kerosene. Total crack length was measured considering the main crack in the chord together with the secondary cracks branching off from the main crack along the weld toe. The specimens tested in weld toe ground conditions were Dry 2, Dry 3, Corr. 2 and Corr. 3, while Dry 1, Corr. 1 and Corr. 4 were tested in as-welded condition. Only Dry 1 and Corr. 2 were subjected to pseudo-random loading while the rest of the specimens tested under constant amplitude loading. The test parameters of the specimens are given in Table 9. The number of cycles corresponding to 15% strain drop in the hot spot region, first visual crack, crack initiation, through-thickness cracking and end of test for the joints were recorded and the results presented in Table 19.

6.8 Compact Tension Specimen Tests in Seawater

The crack growth data for ASTM A36 steel used for the tubular joints tested in sea water were obtained from compact tension specimen (CTS) tests. The typical details of CTS specimens fabricated according to ASTM Test Method E647-81 (135), are shown in Fig. 56(a). Fatigue tests were conducted under sinusoidal tension-tension load wave on an MTS hydraulically actuated, servo-controlled mechanical test system. The crack propagation was studied on specimens in natural sea water at 0°C, at a frequency of 0.2 Hz to simulate the environment in which the tubular joints were tested. The test set-up is shown in Fig. 56(b).

All the specimens were precracked in air from the machined notch tip to a distance of $\frac{a}{w} \approx 0.35$ (should not be less than 0.1B), prior to generating the crack growth data in seawater. The purpose of precracking was to produce a natural crack with a tip away from the effect of the notch. Precracking was carried out at a relatively high stress amplitude with a stress ratio R = 0.1. Load shedding was done during precracking. After precracking to the required length, the load was subsequently reduced to a new lower starting load level, with the reduction no greater than 20% (114,115).

Crack length measurements were made on either side using travelling microscopes and measuring scales with a

least count of 0.01 mm. Measurements were made when the crack tip passed over series of reference lines marked on the specimen. Crack growth rates, $\Delta a/\Delta N$, were calculated from crack length increments set at 0.25 to 0.5 mm divided by the corresponding number of cycles. Measured crack length versus elapsed number of cycle curves for the applied load ranges are shown in Fig. 56(c).

CHAPTER 7

FATIGUE FRACTURE MECHANICS ANALYSIS

7. FATIGUE FRACTURE MECHANICS ANALYSIS

7.1 Crack Growth Data and Material Constants C and M

From the crack growth data of CTS specimens, the stress intensity factor range corresponding to a given crack growth rate was calculated. The stress intensity factor equation that incorporates the important variables is given by:

$$\Delta K = \frac{\Delta P}{BW^{1/2}} f(a/w) \qquad (39)$$

where

a = average crack length, mm

P = applied load, MN

W = width of specimen, mm

B = thickness of specimen mm,

For the compact tension specimen, f(a/w) accurate within 0.25% for a/w between 0.3 and 0.7 is given by (111,134,138):

$$f(a/w) = 29.6 \left(\frac{a}{w}\right)^{1/2} - 185.5 \left(\frac{a}{w}\right)^{3/2} + 655.7 \left(\frac{a}{w}\right)^{5/2} - 1017.0 \left(\frac{a}{w}\right)^{7/2} + 638.9 \left(\frac{a}{w}\right)^{9/2} \qquad (40)$$

For the various applied load ranges, corresponding values of stress intensity factors and da/dN data were computed and plotted on a log-log scale (Fig. 57). Using the regression analysis, the material constants C and m in Eqn. 28 were determined to be 3.96×10^{-13} and 3.6 respectively.

7.2 Crack Growth Data and Stress Intensity Factors for Tubular Joints

The stress intensity factor K and the correction factor Y are determined from the experimental crack growth data of tubular joints. Since crack depth measurements could not be made during testing, the data were computed based on the measured circumferential crack lengths, and plotted against the number of cycles to wall penetration (Fig. 58). The growth rate appears to remain constant with increase in number of cycles, indicating a constant K during crack propagation stage. The following assumptions are made in computing the crack depth:

(1) The shape of crack surface is considered as segment of an arc of a circle.

(2) The transition from surface crack to through-thickness crack is considered to be smooth.

(3) The surface crack shape variation during crack propagation is the same for all the joints tested, and

(4) The initial crack depth a_i is assumed to be 0.1 mm. The final crack depth is taken equal to wall thickness of the chord.

The crack depth is computed based on assumed geometry of bowed crack in the tubular joints (Fig. 59).

The hot spot stress range, $\Delta\sigma$ vs. number of cycles of failure, N, for the tubular joints shown in Fig. 83 exhibits a linear relationship, which can be represented by:

$$\Delta\sigma = k\ N_f^n \tag{41}$$

where

$\Delta\sigma$ = stress range,

N_f = number of cycles to failure,

n = slope of the straight line,

and

k = constant.

Regression analysis of S-N data of tubular joints was carried out and the values of n and k, which provide a good fit of the test data were found to be -0.3001 and 9788.136 respectively.

The non-propagating fatigue crack region (Region I) of Fig. 14, corresponds to the endurance limit of the S-N curve. From the orthogonality assumption, the slope m of the $\frac{da}{dN}$ - ΔK plot (Fig. 14 and Eqn. 28), is related to the slope, n, of the log S-N curve (104,107) by

$$m = -\frac{1}{n} \tag{42}$$

For a known value of n = -0.3001, the corresponding value of the material constant m is 3.33, which differs from the value of 3.9 obtained from crack growth data of CTS specimens.

To determine the stress intensity factor for tubular joints, the correction factor Y is obtained using the following procedure (18):

Substitution of Eqn. 27 in Eqn. 28 gives

$$\frac{da}{dN} = C\,(Y\,\Delta\sigma\,\sqrt{\pi a})^m \qquad (43)$$

Multiplying both sides of Eqn. 43 by $N_{f/t}$, and substituting Eqn. 41 for $\Delta\sigma$, Eqn. 43 becomes

$$\frac{d(a/t)}{d(N/N_f)} = \frac{C}{t^{1-m/2}}\,(Y\,k\,\sqrt{\pi\,a/t})^m \qquad (44)$$

where

a = crack depth,

t = total thickness of the main tube,

N = number of cycles at crack depth a,

N_f = final life or number of cycles to through-thickness cracking (crack depth, a becomes equal to thickness, t)

and

Y = correction factor

Now the geometric correction factor Y will be of the form

$$Y = \left[\frac{d(a/t)}{d(N/N_f)}\right]^{1/m} \left[\frac{1}{\sqrt{\pi\,a/t}}\right] \left[\frac{t^{1/m - 1/2}}{k\,C^{1/m}}\right] \qquad (45)$$

Using Eqn. 45 the correction factor Y can be determined for any crack depth at a given number of cycles.

The range of values for the correction factor Y was found to be between 0.214 to 0.350. Knowing the values of correction factor Y, the crack tip stress intensity factor, K_I for the tubular joints is computed from Eqn. 27. Fig.

60 shows the variation of the correction factor, Y, with the corresponding crack depth to thickness ratio, a/t and it can be seen that the correction factor varies inversely proportional to $\sqrt{a}$ since K and σ remain constant during the crack growth.

7.3 Fatigue Life Estimation

The fracture mechanics approach to fatigue life estimation takes many parameters such as, the size and shape of the crack, the material properties etc. into consideration, compared to traditional S-N curve and Palmgren-Miner cumulative damage rule methods.

In the present study, fatigue life estimation of monopod tubular joints is made using fracture mechanics which considers the following factors:

(i) Initial defect size, a_i

(ii) Critical crack depth defining the failure of the joint, a_f

(iii) Calibration of stress intensity factor K for the cracks, and

(iv) The fatigue crack growth data for the material subjected to the service loading in the actual environment

The initial defect size, a_i, is normally considered as surface imperfection due to welding, and its value significantly affects the accuracy of final life. According

to the existing codes, it is assumed that the initial defects are always present along the weld toe. The AWS Structural Welding Code allows a maximum undercut of 0.25 mm, which would be an adequate initial defect for fatigue crack initiation. The DNV Code (106), allows an initial defect size, a_i equal to 0.1 mm. The critical crack size, a_f, will depend on the nature of crack growth. During experiment, if the crack penetrates the thickness of the tubes rapidly and then slowly propagates around the circumference, the critical crack size will be taken equal to half the brace diameter. Alternatively, if the crack is quickly established around the circumference and then propagates through the thickness slowly, the critical size will be taken equal to the tube wall thickness. This factor is specific to each particular type of joint and loading condition (101). In majority of tests, the time taken for a defect to grow to half the critical size is much higher than the remaining life. In the present case, following the DNV rules (89), the final critical crack depth, a_f, is taken equal to the thickness of the main chord wall (t = 9.525 mm).

With known values of the correction factor, Y, material constants, C and m, initial and final crack depths and the hot spot stress range, the number of cycles to failure is obtained by integrating Eqn. 43 and given by

$$N = \frac{1}{CY^m \pi^{m/2} (\Delta\sigma)^m} \left[\frac{a_f^{1-(m/2)} - a_i^{1-(m/2)}}{1 - m/2} \right] \qquad (46)$$

where a_i and a_f are initial and final crack lengths respectively.

The fatigue lives of the monopod tubular joints tested under constant and variable amplitude loadings in seawater were determined and the results tabulated in Table 20.

CHAPTER 8

TEST RESULTS, OBSERVATIONS AND DISCUSSION

8. TEST RESULTS, OBSERVATIONS AND DISCUSSION

8.1 Stress and Strain Distributions

The study of the stress analysis indicated that the stress and strain distribution around the joint intersection showed that the highest stress intensity exists in the hot spot region in the in-plane loading direction, at the junction between the first branch tube and the main chord. On the opposite side of the first branch tube, i.e. in between the branch tubes 2 and 3 the intensity was lower comparatively. The bending stress distribution is minimum towards the centerline of the bending axis, Fig. 61.

The stress analysis was carried out by finite element method and the results along the symmetry line with respect to bending loads are compared with the measured strains (Figs. 22 to 26). Generally the computed values compare reasonably well with the measurements, with the difference of only 10 to 15 percent. Neglecting the sixth degree of freedom in the thin shell element did not introduce any significant errors even when the bending effects are predominant. The maximum computed stresses occur at the midsurface intersection of the chord and brace. A more realistic estimate of the stress distribution can be determined if the weld dimensions are taken into account in the modelling. The difference between the numerical and experimental data would be decreased further if the influence

of the size of the weld is considered. In the vicinity of the weld and chord intersection, the secondary bending effects could be minimized by choosing the dimensions of the elements to be equal to one to two times the characteristic length, $\ell_c = \sqrt{TR}$, where T and R are the chord thickness and radius respectively (36,73).

8.2 Hot Spot Stress and Strain Range

The hot spot stress or strain ranges were determined from the maximum principal strains corresponding to peak static load ranges. The measured hot spot strain ranges are determined excluding the local weld effects.

The hot spot stress and SCF are computed using i) finite element method, ii) parametric equations (Eqns. 5 to 15) and equations suggested by iii) Marshall (15) (Eqn. 21) and iv) Radenkovic (100). The extrapolation method from the strain measurements to the weld toe as suggested by the European Working Group III and Department of Energy, U.K. (98) gives the hot spot strain range, which is consistent with the finite element method (Table 17, and Figs. 62(a) to 62(f)). For the joints with diameter ratio, $\beta = 0.428$ and wall thickness ratio, $\tau = 0.688$, this method can be applied

easily and the average SNCF at the hot spot is 8.65 for the six joints compared with 9.70 as obtained by the finite element method. For the brace the average maximum measured SNCF was 4.54 compared with 6.58 determined by FEM (Table 17(b)). Table 18, shows the comparison of stress concentration factors as obtained from the experiment and finite element method. The variation in the results can be due to i) absence of weld toe in the finite element discretization of the intersecting region and ii) limitations involved in obtaining consistent experimental data from the actual location with respect to the weld toe. The experimental uncertainty is compounded by the size and type of strain gauge used. Although the use of three gauge rosette ensures the measurement of the principal strains, the physical size of the rosette causes difficulties in obtaining measurements near the actual weld toe. Moreover, since the experimental SCF along the intersection weld is found at the weld toe, the numerical SCF is also calculated at that location. A relatively smaller uniaxial gauge will allow for the placement of the gauge closer to the weld toe, which requires a prior knowledge of the stress state to determine the maximum principal stress. The SCF computed by using Marshall's approach is lower than those determined by other methods, since it neglects the biaxiality of strains and the measured strain range (without extrapolation to the weld toe)

in a strain gauge perpendicular to and adjacent to the weld toe at the worst hot spot which is used in the hot spot stress computations. On the other hand SCF computations by Radenkovic's approach (100) which considers the biaxial strain field and takes into account the extrapolated strains, yield higher values than Marshall's. However the extrapolated strain compares reasonably well with the analytical results (Table 18). Figs. 62(a) through 62(f) show the distribution of strains near weld toe of main chord from which the extrapolated strains were obtained.

Although the finite element method constitutes a viable technique for predicting the hot spot stress in tubular joints, the parametric equations provide an alternate approach to estimate the relative magnitude of the hot spot stress with respect to the nominal branch stress. The thickness to diameter ratio of the chord and branch to chord diameter ratio are the parameters, which govern the stress distribution. The branch to chord thickness ratio influences only the relative bending stiffness of the branch and chord and hence governs the bending stress in the branch at the intersection. The measured and analytical strains on the branch tube and the main chord, in the in-plane bending direction were plotted graphically and are shown in Figs. 22 to 26. The computed strains in the elements very close to the branch-chord intersecting lines indicated high values of

bending stresses, which cannot be measured due to the presence of the weld.

From the finite element analysis, maximum hot spot strains, stresses and strain and stress concentration factors were determined for both main chord and branch members, which are given in Table 17 and 18. Although the parametric equations were developed for planar T-, Y-, and K-joints, their applicability to the spatial joint is examined in the present study. The stress concentration factors listed in Table 2 are based on the parametric equations derived by Kuang et al (Exxon), Gibstein (Dnv), and Wordsworth and Smedley (Lloyds). Among the equations used, only Kuang's, Visser's and Beale and Toprac's formulae yield 50% of the values obtained by FEM and experimental results. The stress concentration factors (Table 18) based on relationships proposed by i) Beale and Toprac (7), and ii) Visser (93) are low compared to those obtained by other methods although the parameters of the joints tested are within the range of applicability. Beale and Toprac's equation retains the chord length as a significant parameter while Visser's relationship has been developed mainly for modelling T- and K- joints. The original data, which form the basis of the parametric equations, were obtained from models, which did not simulate the presence of the weld or its influence on hot spot stress and this can cause under-estimation of the SCF.

8.3 Crack Initiation and Crack Growth Behaviour

The fatigue failure of the joints is a continuous process, which originates from small defects, that cannot be detected in their early stage of growth by ordinary nondestructive methods. The early indication of the development of the cracks is obtained from the observed drop in the strain output from the rosette gauge located at the critical hot spot (as close as 6 mm to the weld toe). The crack initiation life, N_1, is based on the laboratory observation of the reduction in the initial strain amplitude by 15 percent. The first visible crack length corresponding to N_2, ranges from 2.5 mm to 10.00 mm (Table 19). The crack propagation rates on the surface as well as in the through thickness directions are specific to tubular joints in planar components, where the propagation rates accelerate exponentially as the crack grows; the crack growth stage constitutes only a small part of the overall fatigue life (137). Although the tubular joints exhibit early crack initiation in view of the high SCF, it is compensated by the slow rate of propagation and the experimental fact indicates that the propagation stage constitutes the major span in the fatigue life (Table 19). All the joints tested in air and natural sea water failed in a similar fashion with the exception of a few additional secondary cracks in some

joints. In each case fatigue cracks initiated at the weld toe in the chord at the hot spot region within an arc covering approximately 30° on either side of the joint mid-plane. The cracks, always initiated at the weld toe in the hot spot region on the chord side close to the symmetry line in the plane of bending. In few cases multiple crack initiation was observed. The single cracks joined later into main crack which then propagated along the weld toe and then branched away from the weld toe into the chord wall. Figs. 63 through 69 and Tables 21 through 34, show the characteristic results from the measurements of crack propagation on the chord side. After the through thickness cracking, the crack on either side of the hot spot location propagated more or less symmetrically about the centerline. The crack length and growth rate for one side of symmetry line for all the joints are shown in Figs. 70 and 71. Half crack length vs N/N_4 indicates a linear relation until the occurrence of through thickness cracking Fig. 58. The crack growth rates on both sides of symmetry line at different stages of joint life vary from 1.05 to 158.82 x 10^{-4} mm per cycle depending on the used load range. The overall crack propagation rate for the joints Dry 1, Dry 2, Dry 3, Corr. 1, Corr. 2, Corr. 3 and Corr. 4 were respectively 4.29, 23.66, 10.93, 16.35, 5.81, 148.18, and 21.16 x 10^{-4} mm/cycle.

Increased crack growth rates correspond to higher hot spot stress ranges. When the main cracks started to grow into the chord surface, secondary cracks continued along the weld toe for a distance ranging from 10 to 25 mm. The photographs of failure pattern of joints Dry 1, Dry 2, Dry 3, Corr. 1, Corr. 2, Corr. 3 and Corr. 4 are shown in Figs. 72 to 78.

8.4 Effect of Cold Sea Water Environment

In this section, only test results of tubular joints tested in cold sea water are discussed and compared with the published literature. The fatigue strength under free corrosion has been studied by several investigators (79, 97, 121, 122). The Netherlands and Norwegian research programs have concluded that the free corrosion fatigue strength at water temperature of 20°C and 12°C is significantly lower than that in air. But the tests carried out in U.K. have found that sea water at 5°C has no significant effect on fatigue strength, since the corrosion effect at lower temperatures should be less than that for tests at higher water temperatures. Sea water tests have been reported (121) which had a lifetime of only 43 percent of that expected in air. The Dutch program concluded that fatigue crack growth rate in sea water is three times faster

than that in air. In the present study, the crack length of Joint Corr. 2 specimen, which was tested under variable amplitude loading in sea water at 0°C is compared with that of the companion specimen Dry 1 under identical loading conditions. For the same fatigue life (Fig. 83), the total crack lengths including the main and secondary cracks for the Joint Corr. 2 and Dry 1 are found to be 552 and 417 mm, respectively and the corresponding crack growth rates estimated at, 5.81×10^{-4} and 4.29×10^{-4} mm per cycle. The failure pattern for the two joints is shown in Figs. 72 and 75.

8.5 Effect of Weld Toe Grinding

The fatigue cracks tend to originate at the sharp defects left at the toe due to welding. Haagensen (82) and Mullen and Merwin (83) reviewed the advantages and limitations of several methods for improving the fatigue strength of welded joints. Weld toe grinding details of Dry. 1 and Corr. 2 joints are shown in Fig. 39. Toe radius in Corr. 2 joint (Section A, Fig. 39) is much larger than that of Dry 1 (Section B, Fig. 39). The onset of crack initiation occurred at 6.1×10^5 cycles and 2.38×10^5 cycles for Corr. 2 and Dry. 1 joints respectively. Possible increase in the toe radius, weld defect removal and surface finish have delayed considerably the crack initiation event. The

instantaneous crack growth rates for the two joints are approximately the same after the crack initiation. Similar findings have been reported for welded plate specimens and tubular joints (83,97,122). The stress ranges for the as welded joints Corr. 1 and Corr. 4 are different from those of toe ground specimens Corr. 2 and Corr. 3 and hence meaningful comparison of the effect of toe grinding cannot be made. However, it could be seen in Fig. 83 that the toe grinding did not improve the fatigue life in sea water. The thinning of the wall could have compensated for any benefits from the reduced stress concentration and the removal of weld toe defects.

8.6 Joint Stiffness Measurements

During fatigue testing, to monitor the change in stiffness of the specimens and to evaluate the degree of redundancy of the structure, before crack initiation, during its propagation and final failure, the tip displacement was recorded on a strip chart using a linear variable displacement transducer (LVDT). This was installed at the top of the specimen (Fig. 38). The use of LVDT gave a better monitoring of the displacement compared to the hydraulic actuator stroke measurements.

Little change in the stiffness was observed until crack initiation. During the crack propagation in the main

chord, a continuous increase in displacement was observed, However, neither crack initiation nor wall penetration is distinctly marked by a change of slope. When the crack length was approximately equal to about 50 percent of the main tube circumference, the displacement remained almost constant until the termination of the test. The specimens deflected more during opening of the crack i.e. during push cycle than during pull cycle when the closed crack transferred the compressive load. Monitoring the stiffness change during the service life becomes very significant in assessing the structural integrity of offshore structures.

The specimen tip displacements vs. number of cycles for the four joints are shown in Figs. 79 through 82.

8.7 Fatigue Lives

All the fatigue test results are given in Table 19 and Fig. 83. The extrapolated hot spot strain range is plotted against the number of cycles at the end of the test. The lives corresponding to the crack initiation and wall penetration are also shown in Fig. 83. The end of test lives fall above the AWS-XX and DD-55 Q curves. The full penetration lives of the Dry 1 and Corr. 1 joints tested under variable amplitude loading fall just short of DD-55Q curve. The measured hot spot stress ranges (defined by Radenkovic's SCF from Table 18) are plotted in the S-N diagram, (Fig. 84) using N_3, cycles to wall penetration as this is the preferred failure criteria used in the new

British Rules (98). The API-XX, AWS-XX, and DD-55 Q curves are widely used in offshore design as the basic curves for the hot spot strain or stress ranges. The AWS X-X curve is not based on a rigorous statistical analysis but was originally developed as a S_r-N and ε_r-N curve which maintained a consistent degree of conservatism with respect to the scatter band of data. This curve was intended for large tubular joints used in offshore installations, for 95% survival with 95% confidence limit (92). In Fig. 84, the experimental results are compared with the design T-curves for chord wall thicknesses of t<22 mm in air and sea water (unprotected), the basic T-curve application for t = 22 - 32 mm and the experimental data from model tubular joints on which the design curves are based (t = 16, 22 and 32 mm). All the measured lives are longer than the design lives defined by the T-curve for t<22 mm in sea water. With the exception of joint Corr. 3, tested at a rather high stress range, the measured lives exceed the design lives for joints in air, or cathodically protected in sea water.

The data presented in Refs. 97, 123, 124 and 125 showed a clear trend to reduced endurance as the thickness increases at the same hot spot stress range. However there is no obvious thickness effect in Japanese results. The present results fall just below the lower bound of the scatter (Fig. 84). The mean life of 6 mm (D-168) thick

joints was shown roughly three times longer than that of 16 mm thick joints by de Back (Ref. 124). The measured lives of monopod joints are thus seen to be shorter than those of T or Y joints of comparable dimensions. Table 19 shows the number of cycles corresponding to 15 percent strain drop, first visible crack, crack through chord wall and end of test and the ratio of fatigue lives. Surface cracks were as long as 50 percent of the circumference of the joints at the time of termination of the tests. Table 35 presents the comparison of results from available literature for the 'dry' and 'wet' tests. The selection of joints in Table 35 is based on comparable chord and brace dimensions and the hot spot stress levels close to those used in the present study. The variable amplitude test results, plotted on an rms basis (Eqn. 20) fit well in the S-N plot of the constant amplitude tests (Figs. 83 and 84).

The mode of loading has no effect on the fatigue strength of the joints, subjected to axial load in brace and in plane bending moment. However, a greater fatigue life was evidenced for joints tested with a compressive load in the chord.

8.8 Life Estimation Using Fracture Mechanics

Fatigue life prediction of monopod tubular joints tested in seawater environment is made using fracture

mechanics. Only three specimens, viz: Corr. 1, Corr. 2 and Corr. 4 are considered for illustration. The material constants C and m were determined from compact tension specimens under identical environmental test conditions in which tubular joints were tested. The fatigue crack growth data of the joints is used to determine the experimental stress intensity factor and the correction factor Y. Fatigue life is highly sensitive to initial crack depth, correction factor and material constants. The initial crack depth, a_i, is assumed on the basis of DNV and AWS guidelines. But the correction factor varies with increase in crack depth. Fatigue life predictions based on the intermediate value of Y, yields realistic estimates which compare reasonably well with the experimental results (Table 20).

CHAPTER 9

CONCLUSIONS AND RECOMMENDATIONS

9. CONCLUSIONS AND RECOMMENDATIONS

9.1 Conclusions

Based on the limited number of tests carried out on monopod tubular joints under constant amplitude and pseudo-random loadings in air and natural seawater the following conclusions can be drawn:

1) The fatigue crack initiation occurred in the joints (as welded and toe ground) close to but not necessarily at the highest critical hot-spot location. This could be due to the presence of possible weld defects and slag inclusions.
2) Weld toe grinding appears to have no beneficial effect on fatigue life in sea water.
3) Based on the tests on Corr. 2 and Dry 1 joints, the crack growth rates are approximately the same after crack initiation; for long cracks the growth rate is higher in the natural cold sea water than in air for the same fatigue life.
4) The crack-initiation phase consumes the major part of the joint lives. The number of cycles at which the visible crack initiation occurred ranges from 38.2 to 64.2 percent of the joint lives.

5) The measured lives of the spatial monopod joints are shorter than those of T or Y joints of comparable dimensions.

6) The joints resist the loads without large change in displacement, even when the crack length becomes equal to half the circumference of the main chord; further crack propagation does not take place in the main chord, since the branch members opposite to the horizontal hydraulic actuator resist the applied cyclic loads.

7) The use of linear elastic fracture mechanics principles leads to realistic estimation of the joint fatigue lives.

9.2 Recommendations for Further Research

Based on the tests carried out on monopod tubular joints in cold seawater environment at free corrosion potential, under constant amplitude and pseudo-random loading, the following recommendations are made:

1) More tests on similar joints with cathodic protection at normal potential, in the range of -800 mv to -1100 mv need be carried out to study the effect on fatigue life.

2) The main chord, branch tubes, base plate and the inside surface of the test-cell are affected by corrosion due to cold seawater which occurs after few days of wetting; the circulating sea water polluted with these impurities

may adversely affect the corrosion rate in the remainder of the testing. It is suggested that these areas be coated with an appropriate paint prior to the test except the region where the crack initiation and propagation are expected to occur. This precautionary measure will aid to establish a completely controlled corrosion test for better understanding of the corrosion effect in cold water.

3) The fatigue tests under wide and narrow band random load spectra with long return period, representative of those experienced in real offshore structures, would be more realistic.

4) Joint fatigue study for loads with a low cyclic frequency of 0.20 Hz - 1 Hz at low stress range levels may yield a high-cycle fatigue life in the range of 8.5×10^6 - 1.5×10^7 cycles.

5) A more realistic estimate of the stress and strain distributions in the vicinity of the weld and chord intersection need be made using the finite element method, considering the weld dimensions and an appropriate choice of the element sizes.

6) A probabilistic fatigue analysis of tubular joints, which takes into consideration the influence of loading, initial defect size characteristics may lead to better estimate of the fatigue life.

REFERENCES

1. Beale, L.A. and Toprac, A.A., "Analysis of In-plane T, Y, and K Welded Tubular Connections", Welding Research Council Journal, Vol. 125, October 1967.

2. "Tubular by Design", Committee of Steel Pipe Producers, American Iron and Steel Institute, Washington, D.C., U.S.A., 1976.

3. Bijlaard, P.P., "Additional Data on Stresses in Cylindrical Shells Under Local Loadings', Welding Research Council Bulletin, No. 50, May 1959.

4. Dundroya, V., "Stresses at Intersection of Tubes: Cross and T-Joints", S.F.R.L. Tech. Report, No. 550-5, University of Texas, Austin, Texas, August 1965.

5. Greste, O., "A Computer Programme for the Analysis of Tubular K-Joints", SEL Report No. 69-19, University of California, Berkeley, November 1969.

6. Greste, O., and Clough, R.W., "Finite Element Analysis of Tubular Joints: A Report on a Feasibility Study", SEL Report No. 67-7, University of California, Berkeley, April 1967.

7. Scordelis, A.C. and Bouwkamp, J.G., "Analytical Study of Tubular Tee-Joints", ASCE, J. Structural Division, Vol. 96, No. ST.1, January 1970.

8. Liaw, C.Y., Litton, R.W. and Reimer, R.B., "Improved Finite Elements for Analysis of Welded Tubular Joints", Offshore Technology Conference, Paper OTC 2642, Houston, Texas, May 1976.

9. Redwood, R.G., "The Behaviour of Joints Between Rectangular Hollow Structural Members", Civil Engineering and Public Works Review, Vol. 60, No. 711, October 1965.

10. Nolte, K.G. and Hansford, G.E., "Closed-Form Expressions for Determining the Fatigue Damage of Structures Due to Ocean Waves", Proceedings Offshore Technology Conference, Paper OTC 2606, Houston, Texas, May 1976.

11. Mehrotra, B.L., "Matrix Analysis of Welded Tubular Joints", Ph.D. Thesis, McGill University, December 1969.

12. Morgan, E.F., "Use of High Order Isoparametric Solid Finite Elements for the Stress Analysis of Welded Tubular Joints", SWRI Project Report No. 03-9217-001, Southwest Research Institute, Texas, February 1979.

13. Johnston, L.P., "The Welded Tubular Joint Problem in Offshore Oil Structures", Paper SPE 484, Society of Petroleum Engineers of AIME, Dallas, Texas, 1963.

14. Gurney, T.R. and Maddox, S.J., "Determination of Fatigue Design Stresses for Welded Structures from an Analysis of Data", Metal Construction and British Welding Journal, Volume 4, No. 11, November 1972.

15. Marshall, P.W., "General Considerations for Tubular Joint Design", International Conference Welding in Offshore Constructions, Volume 1, Newcastle, February 1974.

16. Yoshida, K., Inui, T. and Iida, K., "Behaviour Analysis and Crack Initiation Prediction of Tubular T-Connections", Offshore Technology Conference, Paper OTc 2854, Houston, Texas, May 1977.

17. Frederick, G.R., Goldberg, J.E. and Lewis, A.D.M., "Analysis of Stiffened Tubular Joints", Offshore Technology Conference, Paper OTC 2956, Houston, Texas, May 1977.

18. Pan, R.B. and F.B. Plummer, "A Fracture Mechanics Approach to Non-overlapping Tubular K-Joint Fatigue Life Prediction", Offshore Technology Conference, Paper OTc 2645, Houston, Texas, May 1976.

19. Kuang, J.G., Potvin, A.B. and Leick, R.D., "Stress Concentration in Tubular Joints", Paper OTC 2205, Offshore Technology Conference, Houston, Texas, May 1975.

20. Van Delft, D.R.V., "A Two Dimensional Analysis of the Stresses at the Vicinity of the Weld-Toes of Welded Tubular Joints", Report 6-81-8, Stevin Laboratory, Department of Civil Engineering, Delft University of Technology, Delft, The Netherlands, 1982.

21. Bouwkamp, J.G., "Tubular Joints Under Alternating Loads", Proc. 3rd Conference on Dimensioning, Budapest, 1968.

22. Bouwkamp, J.G., "Structural Behaviour of Tubular Joints with Wing Plates", Structures and Materials Research Report No. 67-32, Civil Engineering, University of California, Berkeley, December 1967.

23. Bouwkamp, J.G., "Tubular Joints Under Static and Alternating Loads", Structures and Materials Research Report No. 66-15, Civil Engineering, University of California, Berkeley, June 1966.

24. Toprac, A.A., "Static and Fatigue Behaviour of Tubular Connections", S.F.R.L. Report No. P550-15, Civil Engg., University of Texas, Austin, Texas, April 1972.

25. Beale, L.A., Toprac, A.A. and Noel, J.S., "An Investigation of Stresses in Welded T-Joints", Report No. S.F.R.L. Technical Report, P550-3, University of Texas, Austin, Texas, 1973.

26. Toprac, A.A., Johnson, L.P. and Noel, J., "Welded Tubular Connections: An Investigation of Stresses in T-Joints", Welding Journal, Welding Research Council, January 1966.

27. Babiker, D.B., "The Fatigue Behaviour of Welded Joints Between Structural Hollow Sections", Ph.D. Thesis, University of Sheffield, Sheffield, England, December 1967.

28. Blockley, D.I., "Joints Between Structural Hollow Sections in Plane Frameworks", Ph.D. Thesis, University of Sheffield, June 1967.

29. Kwan, C.T., "Analysis of Tubular T-Connections by Finite Element Method: Comparison with Experiments", Ph.D. Thesis, University of Houston, Houston, Texas, December 1971.

30. Miller, C.D. and Hugh Trammell, J., "An Analytical and Experimental Study of Stiffened Tubular Joints with Multiple Branches", Offshore Tech. Conf., Paper OTC 2101, Houston, Texas, May 1974.

31. Eastwood, W., Wardle, S., Osgorby, C., Wood, A.A. and Shinbuda, M.R., "Analysis of Tubular Joints Consisting of Two Web Members and a Boom Member in a Plane Framework", The University of Sheffield, Sheffield, England, February 1968.

32. Eastwood, W., Osgerby, C., Wood, A.A. and Blockley, D.I., "A Theoretical Investigation into the Elastic Behaviour of Joints Between Structural Hollow Sections", University of Sheffield, Sheffield, England, November 1967.

33. Natarajan, M. and Toprac, A.A., "The Fatigue Strength of Tubular T-Joints", S.F.R.L. Report, University of Texas, Austin, Texas, November 1968.

34. Kurubane, Y., Natarajan, M. and Toprac, A.A., "Fatigue Tests of Tubular T-Joints", S.F.R.L., University of Texas, Austin, Texas, April 1967.

35. Bryant, J.E., "Circular Tubular Joint Design", Unpublished M.Sc. Thesis, Tulane University, 1962.

36. Hans, D., Visser, W. and Zunderdorp, H., "The Stress Analysis of Tubular Joints for Offshore Structures", Paper SPE 4342, Second Annual European Meeting of the Society of Petroleum Engineers of AIME, London, April 1973.

37. Kurobane, Y., Makino, Y. and Sagawa, M., "Low-Cycle Fatigue Research on Tubular K-Joints", IWW Doc. XX-291-70, Vol. XXI, No. 2, May 1970.

38. MEE, B.L., "The Structural Behaviour of Joints in Rectangular Hollow Sections", Thesis at University of Sheffield, Sheffield, England, September 1969.

39. Dasgupta, A., "The Behaviour of Joints in Rectangular Hollow Sections", Ph.D. Thesis, University of Sheffield, Sheffield, England, November 1970.

40. Shihouda, M.R., "Stiffened Tubular Joints", Ph.D. Thesis, University of Sheffield, Sheffield, England, June 1967.

41. Mall, G. and Zirn, R., "The Load Carrying Capacity of Pipe Joints Under Static and Dynamic Loadings", Translation from: Schweissen and Schneiden, Vol. 21, 1969.

42. Maeda, T., Uchino, K. and Sakurai, H., "Experimental Study on the Fatigue Strength of Welded Tubular K-Joints", International Institute of Welding, Doc. No. XV-269-69, July 1969.

43. Eastwood, W., Wood, A.A. and Shinouda, M.R., "An Investigation of the Strength of Ordinary and Stiffened Joints in Tubular Frameworks", University of Sheffield, Sheffield, England, September 1970.

44. Dover, W.D., Holdbrook, M.S.J., Hibberd, R.D., and Charlesworth, F.D.W., "Fatigue Crack Growth in T-Joints: Out-of-Plane Bending", Offshore Technology Conference, Paper OTC 3252, Houston, Texas, May 1978.

45. Delesques, R., Valbert, G. and Sfintesco, D., "Research on the Behaviour of Joints in Tubular Lattice Girders", CIDECT Programme 5B, CIDECT Issue 702/E, October 1966.

46. Martin, M., "Investigation into the Stress Distribution and Fatigue Strength of a Welded Tubular T-Joint", Offshore Tech. Conf., Paper OTc 2856, Houston, Texas, May 1977.

47. Wordsworth, A.C., "Experimental Determination of Stresses at Unstiffened Tubular T and X Joints", Paper No. 1, Australian Welding and Testing Conference, Perth, October 1977.

48. Hlavacek, V., "Strength of Welded Tubular Joints in Lattice Girders", Building Research Institute, Technical University, Prague.

49. Sammet, H., "The Strength of Tubular Joints Without Gusset Plates in Steel Constructions", Translation from German: CIDECT Issue 70/10/E, November 1963.

50. Hauk, V., "Tests of R.H.S. Joints Carried Out in the Mannesmann Research Institute in 1968", Mannesmannviohren-Werke, Dusseldorf, June 1972.

51. Anderson, G.W., "Circumferential Stresses in a Joint Between Structural Tubes", Special Report No. 22, Commonwealth Experimental Building Station, Australia, Sydney, May 1961.

52. Melworm, R.F. and Berman, I., "Welded Attachments to Tubes - Experimentation, Analysis and Design", Welding Research Council Supplement, October, 1966.

53. Gibstein, M.G., "Static Strength of Tubular Joints", Det Norske Veritas, Report No. 73-86-C, 1973.

54. Satake, S., Jujishima, K., Ishida, M., Kajimoto, K., Minami, N. and Hirozane, T., "Study of Brittle Fracture Characteristics of Tubular Joints Used in Offshore Structures", Mitsubishi Heavy Industries Technical Review, February 1977.

55. Pan, R.B., Plummer, F.B. and Kuang, J.G., "Ultimate Strength of Tubular Joints", Offshore Technology Conference, Paper OTC 2644, Houston, Texas, 1976.

56. "Structural Tube Joint Tests", Research Project No. 642, Research and Development Division, The Austin Company, September 1962.

57. "Local Loading of Tubes", International Commitee for Study of Tubular Structures, Report UK/10/1953.

58. "Load Transmission in Cruciform Joints", Translation from French: Article in Construction Mettalique 2/1972, CIDECT Program 5D, Issue 72/29/E, 1972.

59. "Tests on Welded Steel Tube Node Joints", Otto Graf Institute of the Stuttgart College of Technology, CIDECT Research Note, April 1967.

60. Eastwood, W., Osgerby, C., Wood, A.A. and Mee, B., "An Experimental Investigation of Joints in Rectangular Hollow Sections", The University of Sheffield, Sheffield, England, February 1970.

61. Eastwood, W. and Wood, A.A., "Welded Joints in Tubular Structures Involving Rectangular Sections", University of Sheffield, Sheffield, England, July 1970.

62. Eastwood, W., Osgerby, C., Wood, A.a. and Babiker, D.B., "The Fatigue Behaviour of Welded Joints Between Structural Hollow Sections", University of Sheffield, Sheffield, England, July 1968.

63. Grigory, S.C., "A Study to Develop a Design Procedure for Analysis of Plastic Fatigue Life of Tubular Joints on Offshore Structures", Final SWRI Report No. 03-1882, Southwest Research Institute, San Antonio, Texas, May 1969.

64. Pease, F.T., "Experimental Stress Analysis of a Structural Pipe T-Joint", M.S. Thesis, University of Houston, Texas, August 1960.

65. Smedley, G.P., "The Avoidance of Fatigue Failures in Offshore Steel Structures", Public Session and Metals Technology Conference, Sydney, Australia, 1976.

66. Mang, I.F., "Fatigue Strength of Welded HSS Joints", International Symposium on Hollow Structural Sections", Toronto, May 1977.

67. Dutta, D., "Recommendations on the Design of Welded Simple Joints of Circular Hollow Sections Under Static Load", International Institute of Welding, Doc. XV-373-75, June 1975.

68. Kwan, C.T., "Fatigue Analysis for Lattice Legs of Jack-up Drilling Platforms", Energy Technology Conference and Exhibit, Houston, Texas, September 1977.

69. Washio, K., Togo, T. and Mitsui, Y., "Experimental Study of Local Failure of Chords in Tubular Truss Joints", Technology Reports, Osaka University, Vol. 18, No. 850, 1968.

70. Kurobane, Y. and Konomi, M., "Fatigue Strength of Tubular K-Joints: S-N Relationships Proposed as Tentative Design Criteria", International Institute of Welding, Doc. XV-340-73, February 1973.

71. Maddox, S.J., "A Fracture Mechanics Approach to Service Load Fatigue in Welded Structures", Welding Institute Report E/45/71, Welding Research International, Vol. 4, No. 2, 1974.

72. Graff, W.J., "Design Correlation of Elastic Behaviour and Static Strength of Zero Eccentricity T, Y, and K Tubular Joints", Offshore Technology Conference, Paper OTC 1310, Houston, Texas, May 1970.

73. Brink, F.I.A. and Van der Krogt, A.H., "Stress Analysis of a Tubular Cross-Joint Without Internal Stiffening for Offshore Structures", International Conference on Welding in Offshore Constructions, Vol. 1, Newcastle, February 1974.

74. Holliday, G.H., "A Three-Dimensional Photoelastic Study of Welded Tubular T-Connections", Ph.D. Thesis, University of Houston, Texas, August 1970.

75. Holliday, G.H., Graff, W.J., "Three-Dimensional Photoelastic Analysis of Welded T-Connections", Offshore Technology Conference, Paper OTC 1441, Houston, Texas, April 1971.

76. Dikjstra, O.D. and deBack, J., "Fatigue Strength of Tubular X and T-Joints", Paper No. 8.4 International Conference: Steel in Marine Structures, Paris, October 1981.

77. Hicks, J.G., "Material and Structural Problems in Offshore Installations", International Conference on Welding in Offshore Constructures, Newcastle, February 1974.

78. Gibstein, M.B., "Fatigue Strength of Welded Tubular Joints at Det Norske Veritas Laboratories", Paper 8.5 International Conference - Steel in Marine Structures, Paris, 1981.

79. Walker, E.F., "Effect of Marine Environment", Paper PS4, International Conference Steel in Marine Structures, Paris, 1981.

80. Schutz, W., "Procedures for the Prediction of Fatigue Life of Tubular Joints", Paper PS5, International Conference - Steel in Marine Structures, Paris, 1981.

81. Vosikovski, O., "Fatigue Crack Growth in an X-65 Line-Pipe Steel at Low Cycle Frequencies in Aqueous Environments", Journal of Engineering Materials Technology, Transactions of the ASME, October 1975.

82. Haagensen, P.J., "Improvement on Fatigue Strength of Welded Joints", Paper PS6, International Conference - Steel in Marine Structures, Paris, 1981.

83. Mullen, C.L. and Merwin, J.E., "Fatigue Life Improvement Factors Obtained by Weld Reinforcement and Toe Grinding", Paper OTC 4240, Offshore Technology Conference, Houston, Texas, 1982.

84. Morgan, H.G., "The Effects of Plate Thickness on the Fatigue Performance of Simple Welded Joints", U.K. Department of Energy, to be published.

85. Zwaans, M.H., Jonkers, P.A.M. and Overbeeke, J.L., "The Endurance of a Welded Joint Under Two Types of Random Loading in Air and Sea Water", Paper 7.3, International Conference - Steel in Marine Structures, Paris, 1981.

86. API Recommended Practice for "Planning, Designing and Constructing Fixed Offshore Platforms", American Petroleum Institute, Washington, U.S.A., 1982.

87. "Structural Welding Code", AWS D1.1 - Rev. 2-77, American Welding Society, 1977.

88. U.K. Department of Energy, Fixed Offshore Structures", Draft for Development DD55, 1978.

89. Det Norske Veritas - "Rules for the Design Construction and Inspection of Offshore Structures", Appendix C, Norway, 1977.

90. Irvine, N.M., Fessler, H.G. and Wordsworth, A.C., "Physical Model Stress Analysis of Steel Tubular Connections", Offshore Structures - The Use of Physical Models in Their Design, The Construction Press, London, 1981.

91. Walker, A.C., "Some Uses of Small-Scale Modelling in the Design of Steel Offshore Structures", Offshore Structues - The Use of Physical Models in their Design, The Construction Press, London, 1981.

92. Wardenier, J., Hollow Section Joints, Delft University Press, 1982.

93. Visser, W., "On the Structural Design of Tubular Joints", OTC 2117, Proceedings Offshore Technology Conference, Houston, Texas, May 1974.

94. Wordsworth, A.C. and Smedley, G.P., "Stress Concentrations at Unstiffened Tubular Joints", Paper 35, Cambridge, 1978.

95. Gibstein, M.B., "Parametrical Stress Analysis of T-Joints", Paper 26, Cambridge, 1978.

96. Reber, J.B. Jr., "Ultimate Strength Design of Tubular Joints", Paper OTC 1664, Offshore Technology Conference, Houston, Texas, May 1972.

97. Tomkins, B., "Fatigue Design Rules for Steel Welded Joints in Offshore Structures", Paper OTC 4403, Offshore Technology Conference, Houston, Texas, May 1982.

98. Offshore Installations: Guidance of Design and Construction, Department of Energy, U.K., June 1981.

99. Marshall, P.W., "A Review of Stress Concentration Factors in Tubular Connections", CE-32 Report, Shell Oil Company, April 1978.

100. Radenkovic, D., "Stress Analysis in Tubular Joints", Paper PS1, International Conference Steel in Marine Structures, Paris, 1981.

101. Dover, W.D., Hibberd, R.D. and Holdbrook, S., "Fatigue Crack Growth in Tubulr Welded Joints", Conference on the Aplications of Fracture Mechanics in Industrial Problems, Sheffield, U.K., September 1976.

102. Timmins, P.F., "Fracture Mechanics for Engineers", Oil and Gas Journal, April, 1982.

103. Collins, J.A., "Failure of Materials in Mechanical Design", John Wiley and Sons, New York, 1981.

104. Pan, R.B., Maddox, N.R. and Plummer, F.B., "Fatigue Analysis of Offshore Structures", Ocean Engineering, November 1975.

105. Pook, L.P. and Smith, R.A., "Theoretical Background to Elastic Fracture Mechancis", Cambridge University, 1976.

106. "Rules for the Design and Inspection of Offshore Structures", Det Norske Veritas, Norway, 1977.

107. Hibberal, R.D. and Dover, W.D., "Random Load Fatigue Crack Growth in T-Joints", Offshore Technology Conference, Paper OTC 2853, Houston, Texas, 1977.

108. Becker, J.M., Gerberich, W.W. and Bouwkamp, J.G., "Fatigue Failure of Welded Tubular Joints", Journal of the Structural Division, ASCE, No. ST1, January 1972.

109. Parker, A.P., "The Mechanics of Fracture and Fatigue - An Introduction", E.Y.F.N. Spon. Ltd., London, 1981.

110. Paris, P.C., "The Fracture Mechanics Approach to Fatigue - An Interdisciplinary Approach", Proceedings of the Tenth Sagamore Army Materials Research Conference, Syracuse University Press, 1964.

111. Gurney, T.R., "Fatigue of Welded Structures", Cambridge University Bress, London, 1979.

112. Dover, W.D., - Private Communications.

113. Iwasaki, T., Kawahara, M. and Asano, K., "Fatigue Crack Growth Behaviour in Welded Tubular Joints in T, TY and K", Paper OTC 3423, Offshore Technology Conference, Houston, Texas, May 1979.

114. "Standard Test Method for Constant-Load-Amplitude Fatigue Crack Growth Rates above 10^{-8} m/cycle", ASTM E647-81, 1981.

115. Tsai, A.W., "The Evaluation of Fatigue Crack Growth in a Nuclear Pressure Vessel Steel", Ph.D. Thesis, University of Missouri, Columbia, 1977.

116. MSC/NASTRAN User's Manual, Analysts Guide, The Macneal-Schwendler Corporation, 1980.

117. Schaeffer, H.G., "MSC/NASTRAN Primar-Static and Normal Mode Analysis", Schaeffer Analysis, Inc., New Hampshire, 1979.

118. Photoelastic Inc. - Vishay Intertechnology Inc., Bulletin, No. TL-201A, 1977.

119. Intertechnology Ltd., Bulletin - "Protective Coating for Strain Gauge Applications", Don Mills, Ontario, 1980.

120. B & K Manual for Strain Indicator Type 1526, Denmark, 1974.

121. Van Leeuwen, J.L., de Back, J. and Vaessen, G.H.G., "Constant Amplitude Fatigue Tests on Welded Steel Joints Performed in Air and Seawater", Paper 2.1, International Conference - Steel in Marine Structures, Paris, 1981.

122. Irvine, N.M., "Comparison of Tubular Joint Stress Analysis Methods in the Near Weld Region", Paper 1.2, International Conference - Steel in Marine Structures, Paris, 1981.

123. Wylde, J.G. and McDonald, A., "The Influence of Joint Dimensions on the Fatigue Strength of Welded Tubular Joints", International Journal of Fatigue, January, 1980.

124. de Back, J., "Strength of Tubular Joints", PS7, International Conference - Steel in Marine Structures, Paris, 1981.

125. Iwasaki, T. and Wylde, J.G., "Recent Research on the Fatigue Performance of Welded Tubular Joints", Paper 44, Second International Conference on Offshore Welded Structures, The Welding Institute, Cambridge, November, 1982.

126. "Filler Metal Specifications", American Welding Society (AWS A5.1-69), 1973.

127. Lewis, E.L. and Perkin, R.G., "Salinity - Its Definition and Calculation", Institute of Ocean Sciences, Patricia Bay, Victoria, B.C., Report 76-28, December 1976.

128. American Optical Bulletin (Instruction Manual, 1978).

129. Thome, O., Abrahamsen, E., Eliassen, S., Helgeland, O. and Jensen, F., "Corrosion and Protection of Offshore Steel Structures", Norges Teknisk - Naturvitenskapelige Forskningsrad (NTNF), Oslo, 1978.

130. HACH Chemical Co. Bulletin, 1971.

131. Hossdorf, H. and Van Amerongen, C., "Model Analysis of Structures", Van Nostrand Reinhold Co., Toronto, 1974.

132. Sellars, F.H. and Loukakis, T.A., "The Analysis and Modelling of Irregular Waves", Report No. 66-5, Department of Naval Architecture and Marine Engineering, M.I.T., Cambridge, Massachusetts, July 1969.

133. Technical Manual - MTS Model 431.12, MTS Systems Corporation, Minneapolis, Minnesota.

134. Paris, P.C., Bucci, R.J. and Little, C.D., "Fatigue Crack Propagation of D6ac Steel in Air and Distilled Water", Proceedings of the 1971 National Symposium on Fracture Mechanics, Part I, ASTM STP 513, 1972.

135. "Standard Test Method for Constant Amplitude Fatigue Crack Growth Rates Above 10^{-8} m/cycle", ASTM E647-81, 1981.

136. Dover, W.D. and Dharmavasan, S., "Fatigue Fracture Mechanics Analyais of T and Y Joints", Offshore Technology Conference, Paper OTC 4404, Houston, Texas, May 1982.

137. Reddy, D.V., Arockiasamy, M. and S.S. Gowda, "Corrosion Fatigue of Tubular Joits in Seawater for Offshore Monopod Structures", Report Submitted to CANMET, EMR, Ottawa, Contract No. 20 SU. 23440-1-9090, December 1982.

138. James, L.A., "The Effect of Frequency Upon the Fatigue Crack Growth of Type 304 Stainless Steel at 1000F", Proceedings of the 1971 National Symposium on Fracture Mechanics, Part I, ASTM STP 513, 1972.

139. Dijkstra, O.D. and de Back, J., "Fatigue Strength of Tubular T and X-Joints", Paper OTC 3696, Offshore Tech. Conf., Houston, Texas, May 1980.

140. Pozzolini, P.F., "Tests on Tubular Joints", Proc. Int. Conf., Special and Plenary Sessions, Paris, France, pp. 97-146, October 1981.

TABLE 1: Monopod Tubular Joint Parameters (mm)

Steel ASTM	Chord D	Brace d	Chord T	Brace t	α= 2L/D	β= d/D	γ= D/2T	τ= t/T
A36 and A53	318.75	133	9.4	6.5	11.47	0.43	16.38	0.70

Table 2(a): Validity Limits of Different Parametric Formulae

Parameter	Exxon (Kuang et al) (19)	Lloyds (Wordsworth and Smedley) (94)	DNV (Gibstein) (95)	Beale & Toprac (1)
α	6.67 - 40	8 - 40	6 - 40	7.7 - 15.4
β	0.30 - 0.80	0.13 - 1.00	0.225 - 0.90	0.17 - 1.0
γ	8.33 - 33.30	12 - 32	10 - 30	12.3 - 31.5
τ	0.20 - 0.80	0.25 - 1.00	0.40 - 1.00	0.40 - 1.0
θ	0° - 90°	15° - 90°	0° - 90°	0° - 90°

TABLE 2(b): Stress Concentration Factors (SCF) by Parametric Equations - Main Chord

Source	Exxon (19)	DNV (95)	Lloyds (94)	Visser (93)	Beale & Toprac (1)	Remarks
Eqn. No. in Text	7-9	14	10-13	6	5	
SCF	4.120	3.285	2.483	4.04	4.864	T or Y Joint Equation
	2.270	2.603	2.555	4.04	4.864	K Joint Equation

( ) Number in parenthesis refer to references.

TABLE 3: Mechanical Properties of Steel

Steel Grade	Yield Stress N/mm^2	Tensile Strength N/mm^2	Percentage Elongation %
ASTM A36	248	414	40
ASTM A53	372	483	36

TABLE 4: Chemical Composition of Steel (Weight Percentage)

Steel Grade	C	Mn	P	S	Si
ASTM A36	0.26	0.8	0.04	0.05	0.03
ASTM A53	0.09	1.11	0.002	0.016	0.05

TABLE 5: Mechanical Properties of Electrodes (Ref. 48)

Electrode Type	AWS-ASTM E6011	AWS-ASTM E7018
Yield Strength, σ_y N/mm^2	330 - 420	400 - 483
Tensile Strength, σ_u N/mm^2	413 - 510	483 - 586
Elongation in 50 mm, %	20 - 30	22 - 30
Reduction in Area, %	35 - 60	55 - 75

TABLE 6: Welding Details (Fig. 34, Ref. 126)

Electrode Type	Electrode Size (mm)	Current (Amperes)	Weld Speed (mm/min.)	Applicable Joint Detail		
				Detail	Range of Dihedral Angle	Location
E6011 and E7018	3.2 - 3.97	90 - 140 130-220	100 - 150	AA BB CC DD	180° - 135° 150° - 50° 75° - 30° 40° - 15°	Toe Zone Side Zone Transient Zone Heel Zone

TABLE 7: Strain Gauge Properties

Gauge Type	Designation	Resistance Ω	Gauge Factor	Gauge Length	Grid Width	Overall Length	Overall Width	Fatigue Life Cycles	Gauge Pattern
			Millimeters						
Single Element	EA-XX-125 AD	120	2.02	3.18	3.18	6.35	3.18		
Biaxial Element 90°	EA-XX-125 TM	120	2.02	3.18	3.81	5.46	8.51	10^6	
Rossette 45°	EA-XX-125 RA	120	2.02	3.18	1.57	6.99	11		

E-Open faced, polyimide backing, A-Constantan alloy, XX-Self Temperature Compensated

TABLE 8 Range of Sea Water Parameters

Parameter	Range
Chlorinity	16 - 22 g/litre
Salinity	36‰ - 38‰
HCO_3^- ion concentration	0.06 - 0.26 g/litre
pH	7.25 - 7.55
Dissolved Oxygen Concentration	10 mg/l - 12 mg/litre
Temperature	-1° C - +1.5° C

TABLE 9: Testing and Loading Details of Joints

Specimen No.	Environment	Weld Condition	Type of Loading	Test Frequency Hz	$\frac{P_{max}}{P_{min}}$ R	Load Levels	
						Horizontal ± kN	Vertical kN
Dry 1**	Air	Toe Ground	V A	Variable	-1	62	178
Dry 2**	Air	Toe Ground	C A	0.25	-1	66	22
Dry 3*	Air	As-Welded	C A	0.20	-1	53	133
Corr. 1	Seawater	As-Welded	C A	0.20	-1	53	133
Corr. 2	Seawater	Toe Ground	V A	Variable	-1	62	178
Corr. 3	Seawater	Toe Ground	C A	0.20	-1	80	178
Corr. 4	Seawater	As-Welded	C A	0.20	-1	58	133

* Ring Stiffened Joint, VA-Variable Amplitude, CA-Constant Amplitude
** Excess Weld Removal (Fig. 39, Section B)

TABLE 10: Static Strain Readings for Joint Dry 1
(Vertical 62 kN; Horizontal ± 178 kN)

Gauge No.	Strains (Microstrains) Horizontal Load		Gauge No.	Strains (Microstrains) Horizontal Load	
	-67 kN	+ 67 kN		- 67 kN	+ 67 kN
1	539	-426	31	206	-168
2	402	-400	32	86	-149
3	-133	160	33	228	-180
4	-454	674	34	118	- 95
5	-121	146	35	-175	148
6	94	-236	36	- 92	69
7	0	- 44	37	- 67	86
8	382	-519	38	15	- 55
9	482	-709	39	-414	261
10	348	-541	40	-584	333
11	511	-660	41	-310	213
12	318	-424	42	124	-158
13	215	-295	43	198	-326
14	292	-363	44	422	-442
15	362	-433	45	180	-308
16	332	-402	46	410	-354
17	268	-312	47	420	-238
18	567	-749	48	31	-174
19	825	-1022	49	-337	93
20	290	-331	50	37	-179
21	595	-654	51	-390	175
22	714	-847	52	191	-159
23	306	-466	53	-278	104
24	540	-669	54	94	- 46
25	518	-515	55	8	- 27
26	126	-291	56	10	110
27	10	- 60	57	- 36	32
28	-255	325	58	220	-405
29	-115	10			
30	12	- 92			

TABLE 11: Static Strain Readings for Joint Dry 2
(Vertical 22 kN; Horizontal ± 66 kN)

Gauge No.	Strains (Microstrains) Horizontal Load.		Gauge No.	Strains (Microstrains) Horizontal Load	
	-62 kN	+ 62 kN		- 62 kN	+ 62 kN
1	41	- 51	31	-148	107
2	8	- 57	32	-376	291
3	364	-356	33	-445	373
4	90	-111	34	-160	102
5	368	-562	35	-362	246
6	250	-473	36	-526	404
7	147	-240	37	10	- 28
8	252	-248	38	- 15	0
9	234	-353	39	-196	167
10	216	-389	40	-294	234
11	344	-418	41	-315	207
12	328	-412	42	- 68	-74
13	260	-332	43	278	-202
14	238	-306	44	548	-446
15	422	-516	45	451	-382
16	775	-850	46	-155	128
17	446	-633	47	-333	275
18	300	-450	48	-147	111
19	206	-252	49	-291	201
20	249	-248	50	-227	194
21	300	-366	51	170	-149
22	304	-412	52	- 28	0
23	- 53	21	53	- 96	118
24	- 20	40	54	232	-198
25	- 70	61	55	51	- 43
26	- 61	30	56	- 93	111
27	- 44	14	57	- 28	29
28	15	- 98	58	361	-449
29	-208	174	59	30	-225
			60	265	- 45
30	133	- 85	61	265	-45

TABLE 12: Static Strain Readings for Joint Dry 3
(Vertical 133 kN; Horizontal ± 53 kN)

Gauge No.	Strains (Microstrains) Horizontal Load.		Gauge No.	Strains (Microstrains) Horizontal Load	
	-62 kN	+ 62 kN		- 62 kN	+ 62 kN
			29	-120	40
1	280	-180	30	-260	100
2	260	-260	31	-380	100
3	160	-220	32	-160	0
4	-120	- 60	33	-	-
5	- 40	- 60	34	- 0	80
6	140	-140	35	- 40	20
7	360	-520	36	- 80	0
8	520	-780	37	-120	60
9	320	-500	38	-360	160
10	260	-460	39	0	20
11	320	-480	40	- 20	40
12	380	-560	41	120	-120
13	420	-640	42	- 20	20
14	200	- 80	43	-	-
15	240	-340	44	-340	160
16	380	-380	45	-280	100
17	240	-300	46	20	240
18	120	- 40	47	-260	60
19	-	-	48	-160	80
20	140	-280	49	-	-
21	20	- 80	50	20	100
22	- 20	-420	51	80	-180
23	20	- 40	52	160	-260
24	0	60	53	240	-360
25	10	0	54		
26	- 20	40	55		
27	60	20			
28	- 60	60			

TABLE 13: Static Strain Readings for Joint One (Corr. 1)
(Vertical 133 kN; Horizontal ∓ 53 kN)

Gauge No.	Strains (Microstrains) Horizontal Load.		Gauge No.	Strains (Microstrains) Horizontal Load	
	-53 kN	+ 53 kN		- 53 kN	+ 53 kN
1	150	-130	28	70	-60
2	240	-220	29	80	-120
3	150	-160	30	30	-40
4	340	-280	31	-	-
5	360	-480	32	-	-
6	560	-780	33	-	-
7	340	-460	34	-10	50
8	560	-400	35	-60	45
9	640	-520	36	-	-
10	340	-300	37	-170	40
11	290	-340	38	-60	+20
12	300	-320	39	-200	380
13	180	-280	40	-210	250
14	125	-200	41	-360	170
15	-	-	42	-370	170
16	-	-	43	-	-
17	-	-	44	-280	130
18	-	-	45	-180	160
19	-60	- 70	46	-155	130
20	-495	-390	47	30	+60
21	-350	-210	48	-200	70
22	-100	- 60	49	30	+60
23	-	-	50	-250	160
24	-75	- 20	51	-180	140
25	-103	-185	52	-	-
26	-20	-130	53	-	-
27	-20	-			

TABLE 14: Static Strain Readings for Joint Two (Corr. 2)
(Vertical 178 kN; Horizontal ±62 kN)

Gauge No.	Strains (Microstrains) Horizontal Load		Gauge No.	Strains (Microstrains) Horizontal Load	
	-62 kN	+62 kN		-62 kN	+62 kN
1	220	-280	20	80	60
2	420	-300	21	80	0
3	340	-560	22	240	-40
4	520	-920	23	200	-20
5	320	-540	24	-320	+160
6	240	-420	25	-520	+240
7	240	-540	26	-500	+160
8	260	-320	27	-160	+100
9	460	-200	28	-340	+200
10	320	-200	29	-280	+320
11	180	-120	30	-160	+180
12	320	-40	31	-100	+200
13	160	0	32	-140	+280
14	100	100	33	- 40	+200
15	60	40	34	100	-80
16	120	0	35	140	-180
17	280	-80	36	280	-120
18	300	-120	37	400	-240
19	220	20			

TABLE 15: Static Strain Readings for Joint Three (Corr. 3)
(Vertical 178 kN; Horizontal ∓ 80 kN)

Gauge No.	Strains (Microstrains) Horizontal Load		Gauge No.	Strains (Microstrains) Horizontal Load	
	-80 kN	+80 kN		-80 kN	+80 kN
1	640	-320	19	+180	200
2	520	-400	20	260	-100
3	640	-340	21	140	-200
4	520	-720	22	-80	600
5	840	-1140	23	-140	780
6	500	-680	24	-280	580
7	200	-80	25	-160	+300
8	340	-180	26	- 20	+460
9	40	-15	27	- 40	+440
10	200	-80	28	-120	+420
11	100	-60	29	-220	+120
12	100	-20	30	-100	+120
13	940	-640	31	-100	320
14	800	-740	32	-260	+280
15	840	-440	33	-180	400
16	60	-20	34	360	-340
17	320	-100	35	-120	140
18	40	-10			

TABLE 16: Static Strain Readings for Joint Four (Corr. 4)
(Vertical 133 kN; Horizontal ∓ 58 kN)

Gauge No.	Strains (Microstrains) Horizontal Load		Gauge No.	Strains (Microstrains) Horizontal Load.	
	-58 kN	+58 kN		-58 kN	+58 kN
1	+260	-240	17	280	-320
2	200	-200	18	220	-180
3	100	-100	19	80	-60
4	+380	-300	20	240	-160
5	+500	-400	21	60	-40
6	+840	-640	22	+ 60	-40
7	+480	-380	23	100	-20
8	+660	-500	24	+100	-40
9	+360	-240	25	- 60	60
10	+240	-140	26	-200	440
11	+160	- 40	27	- 80	120
12	80	- 30	28	- 80	80
13	600	-440	29	-140	+300
14	700	-560	30	- 80	+260
15	360	-320	31	- 60	+220
16	460	-380	32	- 20	+160

TABLE 17(a): Hot Spot Strain Range and Strain Concentration Factor (SNCF) - Main Chord

Specimen No.	Nominal Strain Range (μs)	Hot Spot Strain Range (μs)			SNCF		
		Measured	Extrapolated	FEM	Measured	Extrapolated	FEM
Dry 1 (TG)**	84	684	713	815	8.12	8.49	9.70
Dry 2 (TG)**	200	1625	1675	1957	8.13	8.38	9.78
Dry 3 (AW)	160	1202	1285	-	7.51	8.03	-
Corr. 1 (AW)	160	1340	1365	1549	8.38	8.53	9.68
Corr. 2 (TG)	84	684	713	815	8.12	8.49	9.69
Corr. 3 (TG)	240	1980	2070	2327	8.25	8.63	9.70
Corr. 4 (AW)	173	1480	1550	1680	8.56	8.96	9.71

TG = Toe Ground, AW = As Welded; ** Excess Weld Removal (Fig. 39, Section B)

TABLE 17(b): Hot Spot Strain Range and Strain Concentration Factor (SNCF) – Branch Tube

Specimen No.	Nominal Strain Range (μs)	Hot Spot Strain Range (μs)			SNCF		
		Measured	Extrapolated	FEM	Measured	Extrapolated	FEM
Dry 1 (TG)**	84	333	378	553	3.96	4.50	6.59
Dry 2 (TG)**	200	817	985	1318	4.06	4.93	6.59
Dry 3 (AS)	160	218	–	–	1.36	–	–
Corr. 1 (AW)	160	640	735	1052	4.00	4.56	6.58
Corr. 2 (TG)	84	333	378	553	3.96	4.50	6.59
Corr. 3 (TG)	240	940	1100	1578	3.92	4.58	6.58
Corr. 4 (AW)	173	700	790	1138	4.05	4.57	6.58

TG = Toe Ground, AW = As Welded, ** Excess Weld Removal (Fig. 39, Section B)

TABLE 18: Hot Spot Stress Range and Stress Concentration Factor (SCF) - Main Chord

Specimen No.	Nominal Stress Range (N/mm^2)	Hot Spot Stress Range (N/mm^2)				SCF				
		Measured	FEM	Marshall (99)	Radenkovic (100)	Measured	FEM	Marshall (99)	Radenkovic (100)	Parametric Equations (1,19,95)
Dry 1** (TG)	16.76	152.24	198.34	136.77	156.54	9.09	11.83	8.16	9.34	
Dry 2** (TG)	39.90	400.39	472.42	324.93	367.88	10.01	11.84	8.14	9.22	
Dry 3 (AW)	31.92	283.52	-	240.35	281.85	8.88	-	7.53	8.83	4.86
Corr. 1 (AW)	31.92	314.22	377.17	267.94	299.41	9.84	11.82	8.39	9.38	
Corr. 2 (TG)	16.76	152.24	198.34	136.77	156.54	9.09	11.83	8.16	9.34	
Corr. 3 (TG)	47.89	464.07	566.47	395.91	454.48	9.69	11.83	8.26	9.49	4.86
Corr. 4 (AW)	34.58	343.66	408.96	295.93	340.96	9.94	11.83	8.56	9.86	

( ) Numbers in parenthesis refer to references, AW = As Welded, TG = Toe Ground
** Excess Weld Removal (Fig. 39, Section B)

TABLE 19: Fatigue Test Results

Specimen No.	Number of cycles for (in 10^4)					Ratio of Fatigue Lives		
	15% Strain Drop N_1	First Visible Crack		Crack Through Chord Wall N_3	End of Test N_4	$\frac{N_1}{N_4}$	$\frac{N_2}{N_4}$	$\frac{N_3}{N_4}$
		N_2	Length mm					
Dry 1	15.35	23.80	10.0	81.15	95.0	0.162	0.251	0.854
Dry 2	2.65	3.90	11.5	4.94	13.4	0.198	0.291	0.369
Dry 3	11.02	13.95	5.0	16.37	33.2	0.332	0.420	0.493
Corr. 1	6.53	8.90	2.5	11.68	23.3	0.280	0.382	0.501
Corr. 2	41.7	61.00	9.0	82.86	95.0	0.439	0.642	0.872
Corr. 3	1.26	-	-	1.52	3.3	0.382	-	0.461
Corr. 4	7.20	8.20	6.0	11.20	20.6	0.350	0.398	0.544

TABLE 20: Comparison of Fatigue Lives with Fracture Mechanics Approach

Joint Number	Constants From					Crack Lengths mm		Stress Range N/mm^2	Fatigue Lives to Wall Penetration N_3 Cycles	
	C.T.S. Specimen Data		Tubular Joint S-N Data							
	C	m	n	m	y	Initial	Final		Experimental	Fracture Mechanics
Corr. 1					0.352			314.22	116800	108610
	3.96×10^{-13}	3.6	0.3001	3.33		0.10	9.525			
Corr. 4					0.325			343.66	112000	105350

TABLE 21: Summary of Crack Growth Data (Fig. 63) - Right of Centre Line

Test Specimen: Joint Dry-1

Load Range = 125 kN
Frequency = Variable
N_4 = 95x10⁴ cycles

Main Crack Length = 210 mm
Secondary Crack Length = 4 mm
Total Crack Length = 417 mm

Location of crack tip	Increase in cycles in 10^4 units	Total number of cycles in 10^4 units (N)	$\frac{N}{N_4}$	Increase in crack length (mm)	Crack growth rate (10^{-4} mm/cycle)	Crack length (mm)
0	23.80	23.80	0.25	5	0.21	5
A	3.77	27.57	0.29	6	1.59	11
B	0.57	28.14	0.29	10	17.54	21
C	0.30	28.44	0.30	6	20.00	27
D	7.36	35.80	0.38	15	2.04	42
E	8.54	44.34	0.47	9	1.05	51
F	6.42	70.76	0.75	10	1.56	61
G	4.12	74.88	0.79	8	1.94	68
H	3.78	78.66	0.83	9	2.38	77
I	4.27	82.93	0.87	25	5.86	102
J	2.10	85.03	0.89	24	11.43	126
K	1.17	86.20	0.91	14	11.96	140
L	2.30	88.50	0.93	33	14.35	173
M	1.10	89.60	0.94	10	9.09	183
N	3.71	92.31	0.97	21	5.66	204
P	2.69	95.00	1.00	6	2.23	210

TABLE 22:. Summary of Crack Growth Data (Fig. 64) - Right of Centre Line

Test Specimen: Joint Dry-2

Load Range = 132 kN
Frequency = 0.25 Hz
N_4 = 13.4 x 10^4 cycles

Main Crack Length - 156 mm
Total Crack Length = 317 mm

Location of crack tip	Increase in cycles in 10^4 units dN	Total number of cycles in 10^4 units (N) N	$\frac{N}{N_4}$	Increase in crack length (mm) (da) mm	Crack growth rate (10^{-4} mm/cycle) da/dN	Crack length (mm)
A	3.91	3.91	0.29	16	4.09	16
B	0.13	4.04	0.30	15	115.38	31
C	0.50	4.54	0.34	15	30.00	46
D	0.40	4.94	0.37	12	30.00	58
E	0.57	5.51	0.41	15	26.32	73
F	0.94	6.45	0.48	10	10.64	83
G	0.71	7.16	0.53	8	11.27	91
H	0.73	7.89	0.59	11	15.07	102
I	0.64	8.53	0.64	5	7.81	107
J	0.47	9.00	0.67	5	10.64	112
K	0.55	9.55	0.71	6	10.91	118
L	0.96	10.51	0.78	8	8.33	126
M	0.49	11.00	0.82	5	10.20	131
N	1.50	12.50	0.93	13	8.67	144
	0.90	13.40	1.00	12	13.33	156

TABLE 23: Summary of Crack Growth Data (Fig. 65) - Right of Centre Line

Test Specimen: Joint Dry-3

Load Range = 106 kN
Frequency = 0.20 Hz
$N_4 = 33.3 \times 10^4$ cycles

Total Crack Length = 364 mm
Main Crack Length = 185 mm

Location of crack tip	Increase in cycles in 10^4 units dN	Total number of cycles in 10^4 units (N) N	$\frac{N}{N_4}$	Increase in crack length (mm) (da) mm	Crack growth rate (10^{-4} mm/cycle) da/dN	Crack length (mm)
A	14.87	14.87	0.45	5	0.34	5
B	0.13	15.00	0.45	4	30.77	9
C	0.75	15.75	0.47	8	10.67	17
D	0.49	16.24	0.48	17	34.69	34
E	0.13	16.37	0.49	8	61.54	42
F	1.43	17.80	0.53	20	13.99	62
G	1.7	19.50	0.58	27	15.88	89
H	2.10	21.60	0.65	16	7.62	105
I	1.63	23.23	0.69	11	6.75	116
J	3.07	26.30	0.79	16	5.21	132
K	1.40	27.70	0.83	22	15.74	154
L	3.80	31.50	0.96	15	5.53	169
M	1.80	33.30	1.00	16	8.89	185

Table 24: Summary of Crack Growth Data (Fig. 66) - Right of Centre Line

Test Specimen: Joint Corr. 1

Load Range = 106 kN
Frequency = 0.20 Hz
N_4 = 23.3x10^4 cycles

Main Crack Length = 164 mm
Secondary Crack Length = 23 mm
Total Crack Length = 430 mm

Location of crack tip	Increase in cycles in 10^4 units	Total number of cycles in 10^4 units (N)	$\frac{N}{N_4}$	Increase in crack length (mm)	Crack growth rate (10^{-4} mm/cycle)	Crack length (mm)
0	8.90	8.90	6.38	2.5	0.28	2.5
A	0.45	9.35	0.40	5.5	12.22	8
B	0.59	9.94	0.42	3	5.08	11
C	0.66	10.60	0.46	12	18.18	23
D	1.29	11.89	0.51	11	8.53	34
E	0.68	12.57	0.54	-	-	
	0.53	13.10	0.56	14	26.42	48
F	0.90	14.00	0.60	23	25.55	71
	0.50	14.50	0.62	16	32.00	87
G	0.98	15.48	0.66	23	23.47	110
H	0.67	16.15	0.69	13	19.40	123
	1.24	17.39	0.75	10	8.07	133
I	0.66	18.05	0.77	7	10.61	140
	1.00	19.05	0.82	9	9.00	149
	1.11	20.16	0.86	9	8.11	158
	1.39	21.55	0.93	-	-	-
J	1.75	23.30	1.00	6	3.43	164

Table 25: Summary of Crack Growth Data (Fig. 67) - Right of Centre Line

Test Specimen: Joint Corr. 2

Load Range = 125 kN
Frequency = Variable
N_4 = 95x10⁴ cycles

Main Crack Length = 214 mm
Secondary Crack Length = 93 mm
Total Crack Length = 552 mm

Location of crack tip	Increase in cycles in 10^4 units	Total number of cycles in 10^4 units (N)	$\frac{N}{N_4}$	Increase in crack length (mm)	Crack growth rate (10^{-4} mm/cycle)	Crack length (mm)
0	61.00	61.00	0.64	9	0.15	9
A	3.05	64.00	0.67	15	5.00	24
B	1.9	65.90	0.69	26	13.68	50
C	3.93	69.83	0.74	18	4.58	68
D	0.82	70.65	0.74	10	12.49	78
–	–	–	–	–	–	–
E	2.73	73.38	0.77	13	4.76	91
F	1.92	75.30	0.79	10	5.21	101
–	–	–	–	–	–	–
G	9.60	84.90	0.89	37	3.85	138
H	1.45	86.35	0.91	17	11.72	155
I	1.43	87.78	0.92	16	11.19	171
J	2.42	90.20	0.95	14	5.78	185
K	2.37	92.57	0.97	6	2.53	191
L	2.26	94.83	0.99	7	3.10	198
M	2.43	95.00	1.00	16	6.58	214

Table 26: Summary of Crack Growth Data (Fig. 68) - Right of Centre Line

Test Specimen: Joint Corr. 3

Load Range = 160 kN
Frequency = 0.20 Hz
N_4 = 3.3×10^4 cycles

Main Crack Length = 229 mm
Secondary Crack Length = 116 mm
Total Crack Length = 717 mm

Location of crack tip	Increase in cycles in 10^4 units	Total number of cycles in 10^4 units (N)	$\frac{N}{N_4}$	Increase in crack length (mm)	Crack growth rate (10^{-4} mm/cycle)	Crack length (mm)
A	1.53	1.53	0.46	83	54.25	83
B	0.17	1.70	0.52	27	158.82	110
	0.26	1.96	0.59	29	111.54	139
C	0.09	2.05	0.62	13	144.44	152
D	0.15	2.20	0.67	16	106.67	168
E	0.16	2.36	0.72	10	62.50	178
F	0.23	2.59	0.79	20	86.96	198
	0.24	2.83	0.86	16	66.67	214
	0.28	3.11	0.94	8	28.57	222
G	0.19	3.30	1.00	7	36.84	229

Table 27: Summary of Crack Growth Data (Fig. 69) - Right of Centre Line

Test Specimen: Joint Corr. 4

Load Range = 116 kN
Frequency = 0.20 Hz
N_4 = 20.6×10^4 cycles

Main Crack Length = 263 mm
Secondary Crack Length = 41 mm
Total Crack Length = 509 mm

Location of crack tip	Increase in cycles in 10^4 units	Total number of cycles in 10^4 units (N)	$\frac{N}{N_4}$	Increase in crack length (mm)	Crack growth rate (10^{-4} mm/cycle)	Crack length (mm)
A	0.85	9.05	0.44	14	16.47	14
B	0.47	9.52	0.46	11	23.40	24
C	1.07	10.59	0.51	66	61.68	91
D	0.47	11.06	0.54	34	72.34	125
E	1.34	12.40	0.60	4	2.98	129
F	0.65	13.05	0.63	5	7.69	134
G	1.25	14.30	0.69	39	31.20	173
H	0.95	15.25	0.74	18	18.95	191
I	0.92	16.17	0.78	19	20.65	210
J	0.73	16.90	0.82	12	16.44	222
K	0.86	17.76	0.86	28	32.56	250
L	1.48	19.24	0.93	10	6.77	260
M	1.36	20.60	1.00	3	2.21	263

Table 28: Summary of Crack Growth Data (Fig. 63) - Left of Centre Line

Test Specimen: Joint Dry-1

Load Range = 125 kN
Frequency = Variable
N_4 = 95.0x10⁴ cycles

Main Crack Length = 198 mm
Secondary Crack Length = 5 mm
Total Crack Length = 417 mm

Location of crack tip	Increase in cycles in 10^4 units	Total number of cycles in 10^4 units (N)	$\frac{N}{N_4}$	Increase in crack length (mm)	Crack growth rate (10^{-4} mm/cycle)	Crack length (mm)
A'	27.57	27.57	0.29	11	0.39	11
B'	3.77	28.44	0.30	6	1.59	17
C'-C"	1.76	30.20	0.30	8	4.54	25
D'	1.74	31.94	0.34	8	4.59	33
E'	12.40	44.34		15		48
B"	12.40	44.34	0.47	5	1.61	53
F' and F"	26.42	70.76	0.75	15	0.57	68
F"-E'	3.99	74.75	0.79	9	2.26	77
H'	3.91	78.66	0.83	13	3.33	90
I'	4.27	82.93	0.87	10	2.34	100
J'	2.10	85.03	0.89	25	11.91	125
K'	1.17	86.20	0.91	11	9.40	136
L'	2.30	88.50	0.93	26	11.31	162
M'	1.10	89.60	0.94	13	11.82	175
N'	2.71	92.31	0.97	17	6.27	192
P'	2.69	95.00	1.00	6	2.23	198

Table 29: Summary of Crack Growth Data (Fig. 64) - Left of Centre Line

Test Specimen: Joint Dry-2

Load Range = 132 kN
Frequency = 0.25 Hz
N_4 = 13.4 x 10^4 cycles

Total Crack Length = 317 mm
Main Crack Length = 161 mm

Location of crack tip	Increase in cycles in 10^4 units ΔN	Total number of cycles in 10^4 units N	$\frac{N}{N_4}$	Increase in crack length mm	Crack growth rate in 10^{-11} mm/cycles	Total Crack length mm
A'	3.91	3.91	0.29	19	4.87	19
B'	0.13	4.04	0.30	13	100.00	32
C'	0.50	4.54	0.34	20	40.00	52
D'	0.40	4.94	0.37	18	45.00	70
E'	0.57	5.51	0.41	20	35.09	90
F'	0.94	6.45	0.48	15	15.96	105
G'	0.71	7.16	0.53	6	8.45	111
H'	0.73	7.89	0.59	5	6.85	116
I'	0.64	8.53	0.64	4	6.25	120
J'	0.47	9.00	0.67	6	12.77	126
K'	0.55	9.55	0.71	7	12.73	133
L'	0.96	10.51	0.78	4	4.17	137
M'	0.49	11.00	0.82	5	10.20	142
N'	1.50	12.50	0.93	6	4.00	148
O'	0.90	13.40	1.00	13	14.44	161

Table 30: Summary of Crack Growth Data (Fig. 65) - Left of Centre Line

Test Specimen: Joint Dry-3

Load Range = 106 kN
Frequency = 0.20 Hz
$N_4 = 33.4 \times 10^4$ cycles

Total Crack Length = 364 mm
Main Crack Length = 179 mm

Location of crack tip	Increase in cycles in 10^4 units dN	Total number of cycles in 10^4 units N	$\frac{N}{N_4}$	Increase in crack length mm da	Crack growth rate in 10^{-11} mm/cycles	Total Crack length
O'	13.95	13.95	0.42	6	0.43	6
A'A'	0.18	14.13	0.42	13	72.22	19
B'B'	0.13	14.15	0.43	14	107.69	33
A'	0.07	14.02	0.42	5	71.43	38
B'	0.18	14.13	0.42	12	66.67	50
C"	0.74	14.87	0.45	6	8.11	56
D'	0.88	15.75	0.47	8	9.09	64
E'	0.62	16.37	0.49	13	20.97	76
F'	1.43	17.80	0.53	7	4.90	84
G'	1.70	19.50	0.58	10	5.88	94
H'	2.10	21.60	0.65	14	6.67	108
I'	1.63	23.23	0.70	16	9.82	124
J'	3.07	26.30	0.79	12	3.91	136
K'	1.40	27.70	0.83	20	14.29	156
L'	3.80	31.50	0.95	8	2.11	164
M'	1.80	33.30	1.00	15	8.33	179

Table 31: Summary of Crack Growth Data (Fig. 66) - Left of Centre Line

Test Specimen: Joint Corr. 1

Load Range = 106 kN
Frequency = 0.20 Hz
N_4 = 23.2x10^4 cycles

Main Crack Length = 217 mm
Secondary Crack Length = 26 mm
Total Crack Length = 430 mm

Location of crack tip	Increase in cycles in 10^4 units	Total number of cycles in 10^4 units (N)	$\frac{N}{N_4}$	Increase in crack length (mm)	Crack growth rate (10^{-4} mm/cycle)	Crack length (mm)
A'	9.35	9.35	0.40	9	0.96	9
-	0.59	9.94	0.43	11	18.64	20
-	0.66	10.60	0.46	20	30.30	40
B'	1.29	11.89	0.51	40	31.01	80
C'	0.68	12.57	0.54	12	17.65	92
D'	0.53	13.10	0.56	17	32.08	109
E'	0.90	14.00	0.60	16	17.78	125
-	0.50	14.50	0.62	19	38.00	144
F'	0.98	15.48	0.66	15	15.31	159
-	0.67	16.15	0.69	9	13.43	168
G'	1.24	17.39	0.75	9	7.26	177
H'	0.66	18.05	0.78	8	12.12	185
I'	1.00	19.05	0.81	7	7.00	192
-	1.11	20.16	0.86	11	9.91	203
J'	1.39	21.55	0.92	8	5.76	211
K'	1.75	23.30	1.00	6	3.43	217

Table 32: Summary of Crack Growth Data (Fig. 67) - Left of Centre Line

Test Specimen: Joint Corr. 2

Load Range = 125 kN
Frequency = Variable
N_4 = 95×10^4 cycles

Main Crack Length = 143 mm
Secondary Crack Length = 109 mm
Total Crack Length = 552 mm

Location of crack tip	Increase in cycles in 10^4 units	Total number of cycles in 10^4 units (N)	$\frac{N}{N_4}$	Increase in crack length (mm)	Crack growth rate (10^{-4} mm/cycle)	Crack length (mm)
A'	64.00	64.00	0.67	13	0.20	13
B'	1.90	65.90	0.69	10	5.26	23
C'	3.93	69.83	0.74	12	3.05	35
D'	0.82	70.65	0.75	15	18.29	50
F'	4.65	75.30	0.79	10	21.51	60
G'	9.60	84.90	0.89	7	0.73	67
H'	1.45	86.35	0.91	14	9.66	81
I'	1.43	87.78	0.92	17	11.89	98
J'	2.42	90.20	0.95	18	7.44	116
K'	2.37	92.57	0.97	7	2.93	123
L'	2.26	94.83	0.99	9	3.98	132
M'	2.43	95.00	1.00	11	4.53	143

Table 33: Summary of Crack Growth Data (Fig. 68) - Left of Centre Line.

Test Specimen: Joint Corr. 3

Load Range = 160 kN
Frequency = 0.20 Hz
N_4 = 3.3×10^4 cycles

Main Crack Length = 260 mm
Secondary Crack Length = 112 mm
Total Crack Length = 717 mm

Location of crack tip	Increase in cycles in 10^4 units	Total number of cycles in 10^4 units (N)	$\frac{N}{N_4}$	Increase in crack length (mm)	Crack growth rate (10^{-4} mm/cycle)	Crack length (mm)
C'	1.53	1.53	0.46	103	67.32	103
D'	0.17	1.70	0.52	16	94.12	119
	0.26	1.96	0.59	15	57.69	134
E'	0.09	2.05	0.62	21	233.33	155
F'	0.15	2.20	0.67	24	160.00	179
G'	0.16	2.36	0.72	29	181.25	208
H'	0.23	2.59	0.79	15	65.22	223
	0.24	2.83	0.86	19	79.17	242
	0.28	3.11	0.94	12	42.86	254
I'	0.19	3.30	1.00	6	31.58	260

Table 34: Summary of Crack Growth Data (Fig. 69) - Left of Centre Line

Test Specimen: Joint Corr. 4

Load Range = 116 kN
Frequency = 0.20 Hz
N_4 = 20.6×10^4 cycles

Main Crack Length = 173 mm
Secondary Crack Length = 32 mm
Total Crack Length = 509 mm

Location of crack tip	Increase in cycles in 10^4 units	Total number of cycles in 10^4 units (N)	$\frac{N}{N_4}$	Increase in crack length (mm)	Crack growth rate (10^{-4} mm/cycle)	Crack length (mm)
0	8.20	8.20	0.39	6	0.73	6
A'	0.85	9.05	0.44	16	18.82	22
B'	0.47	9.52	0.46	19	40.43	41
G'	0.78	14.30	0.69	25	5.23	66
H'	0.53	14.83	0.72	26	49.06	92
	0.17	15.00	0.73	13	76.47	105
	0.60	15.60	0.76	20	33.33	125
I'	0.57	16.17	0.79	6	10.53	131
J'	0.73	16.90	0.82	15	20.55	146
	0.60	17.50	0.85	9	15.00	155
K'	0.26	17.76	0.86	7	26.92	162
	0.74	18.50	0.89	5	6.76	167
M'	2.10	20.60	1.00	6	2.86	173

Table 35: Comparison of Fatigue Test Results with Relevant Published Data

	Specimen Dimensions (mm)				Type of Loading (IPB)	Hot Spot Stress+/ Strain Range* (N/mm^2)	Fatigue Life (cycles)	Remarks
	Chord		Brace					
	D	T	d	t				
Present Investigation	318	9.525	133	6.5	VA	152.24+/684*	9.5×10^5	Dry 1
					CA	400.39+/1625*	1.34×10^5	Dry 2
					CA	283.52+/1202*	3.33×10^5	Dry 3
					CA	314.22+/1340*	2.33×10^5	Corr. 1
					VA	152.24+/684*	9.50×10^5	Corr. 2
					CA	464.07+/1980*	3.30×10^4	Corr. 3
					CA	343.66+/1480*	2.06×10^5	Corr. 4
Available Literature	457	16	457	16	CA	271+	5.0×10^5	Ref. 98
	457	16	457	16	CA	401+	3.3×10^5	Ref. 98
	472	22	340	22	CA	242+	1.9×10^5	Ref. 98
	685	40	343	22	CA	146+	7.6×10^5	Ref. 98
	947	44	683	44	CA	126+	6.5×10^5	Ref. 98
	168	6.3	168	4.47	CA	2000*	2.65×10^5	Ref. 123
	168	6.3	168	3.15	CA	1285*	3.7×10^5	Ref. 76
	168	6.3	168	3.15	CA	1445*	4.8×10^5	Ref. 76

IPB - In-plane Bending, CA - Constant Amplitude, VA - Variable Amplitude

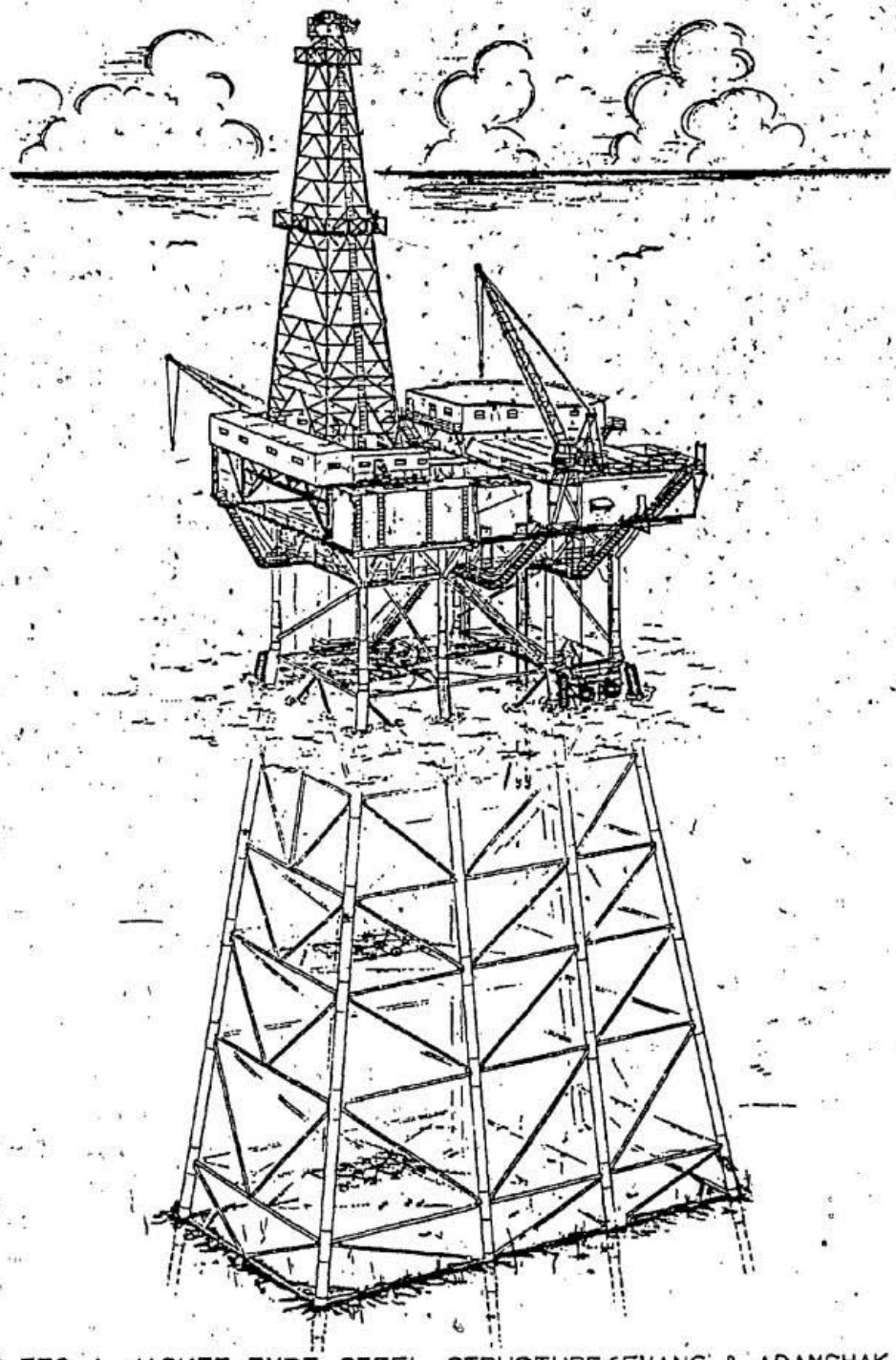

FIG. 1 JACKET-TYPE STEEL STRUCTURE (EVANS & ADAMCHAK, 1969)

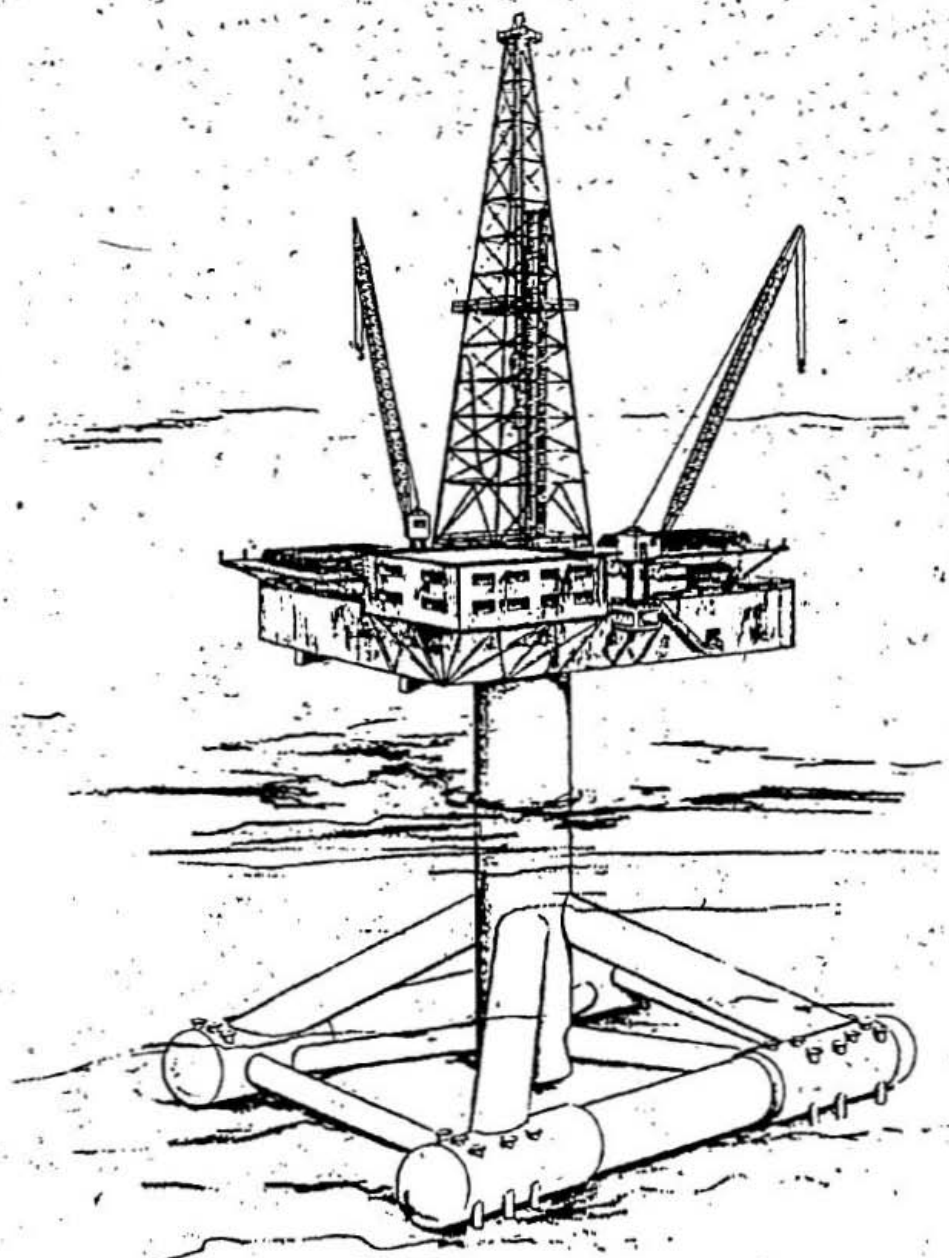

FIG.2 COOK-INLET ALASKA MONOPOD PLATFORM
(EVANS, & ADAMCHAK, 1969)

MONOCONE 135

MAXIMUM DESIGN WATER DEPTH = 135 FEET

ESTIMATED QUANTITIES

CONCRETE	38,900	C Y
REINFORCING STEEL	5,200	S.T
POST-TENSIONING	1,400	S.T
HULL & SHAFT	84,000	S.T
SUPERSTRUCTURE & EQUIPMENT	5,450	S.T
STEEL CONICAL COLLAR	6,600	S.T
LIGHTSHIP WEIGHT	96,000	S.T
LIGHTSHIP DRAFT	34.5	FT

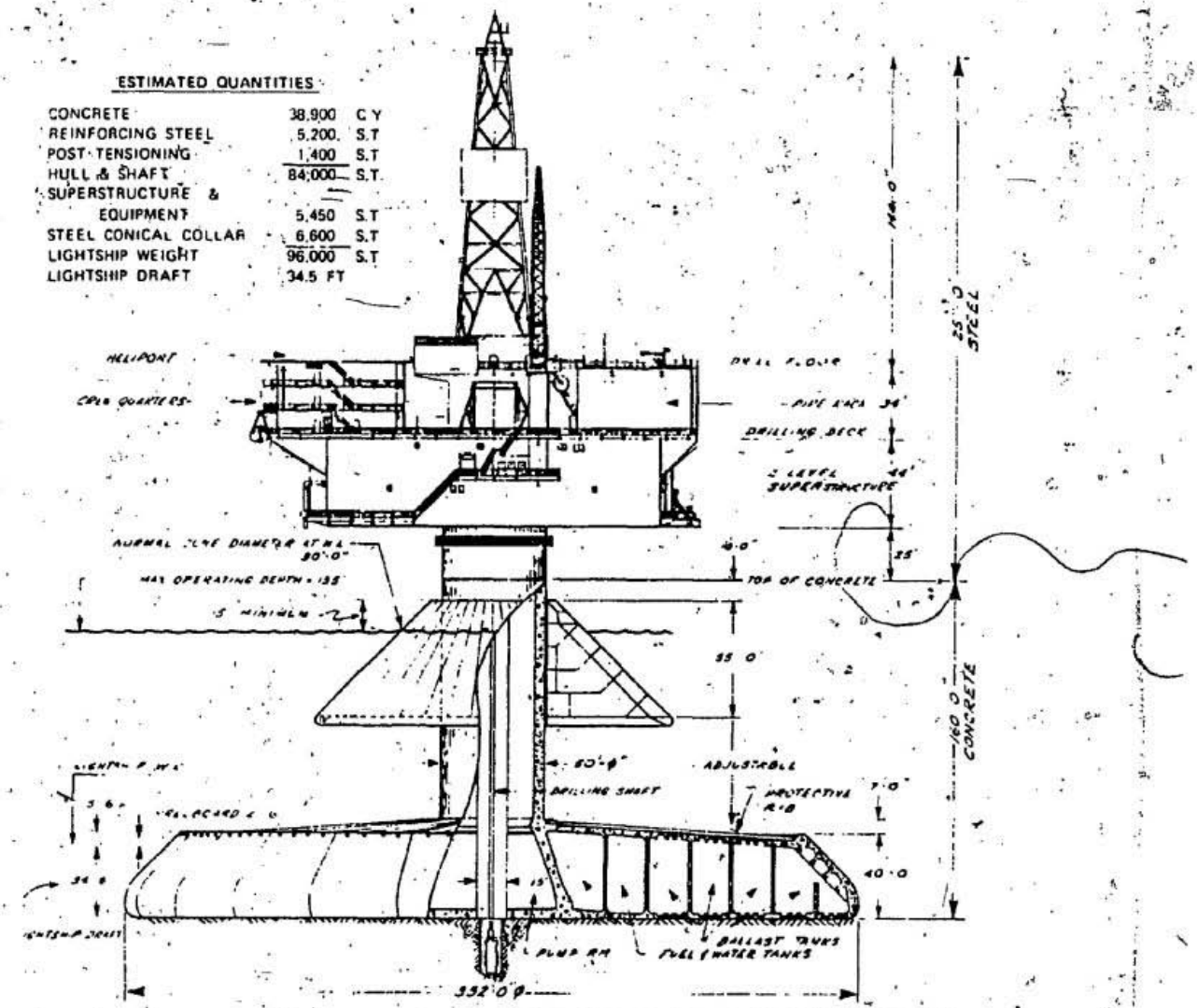

FIG.3 MONOCONE DRILLING UNIT(JAZRAWI & DAVIES, 1975)

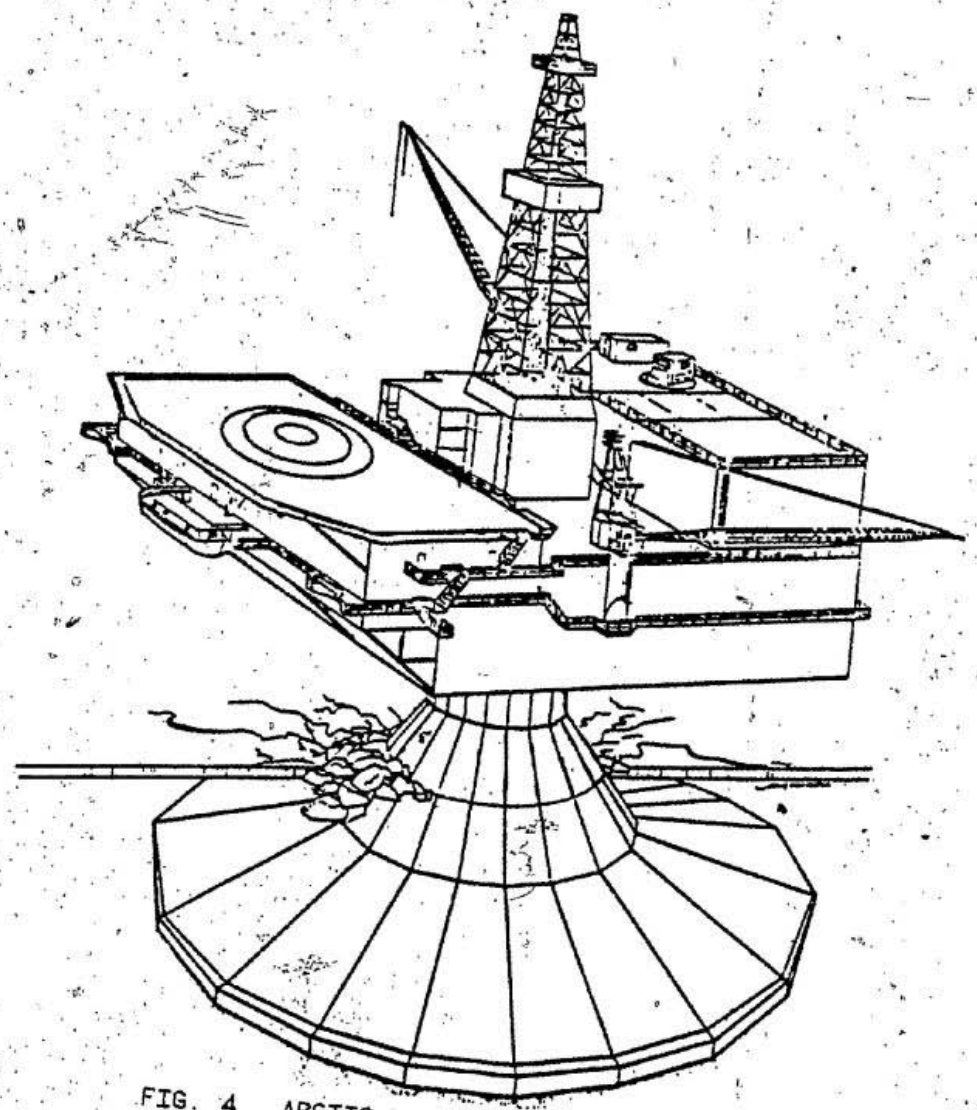

FIG. 4. ARCTIC MARINE DRILLING STRUCTURE
(OFFSHORE ENGINEER, 1979)

FIG 5 TRIPOD TOWER PLATFORM (MICHELSON & MEEK, 1982)

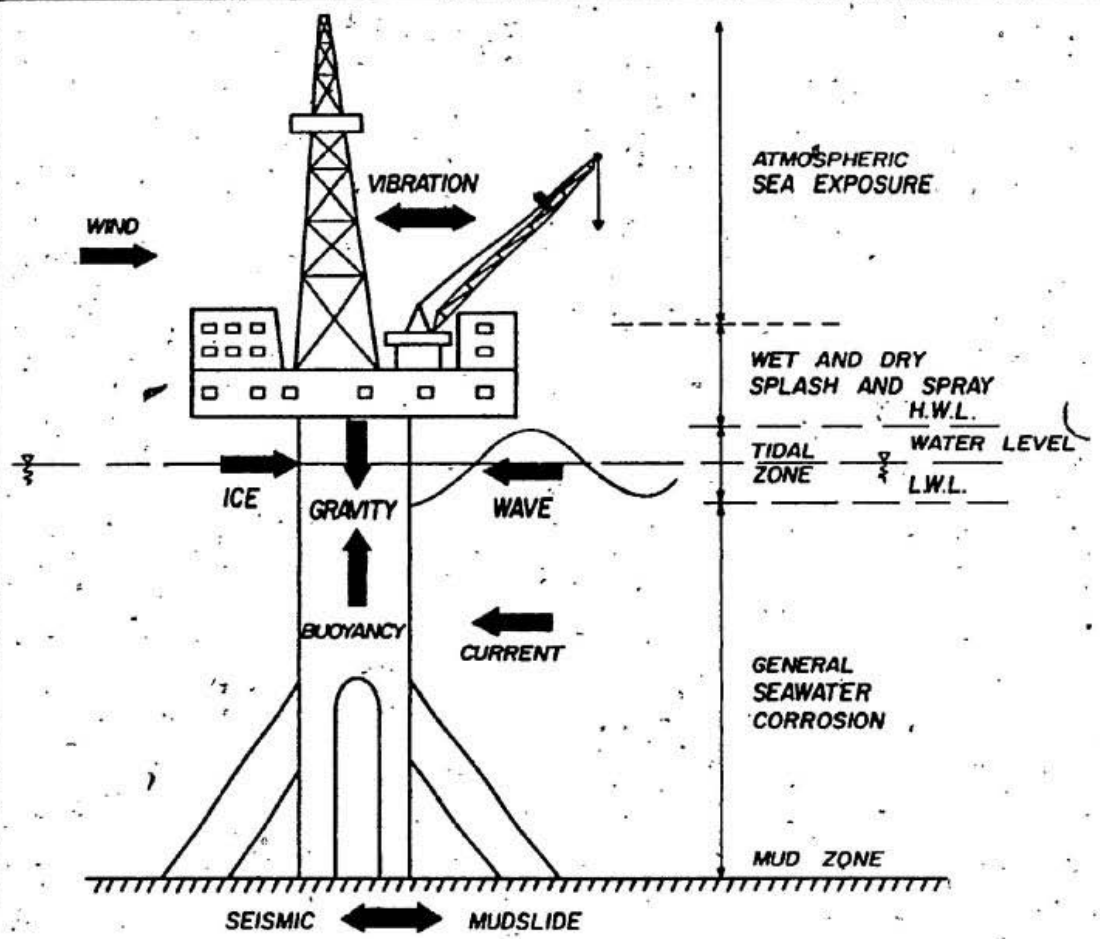

FIG.6 MAJOR PLATFORM LOADS AND CORROSION ZONES

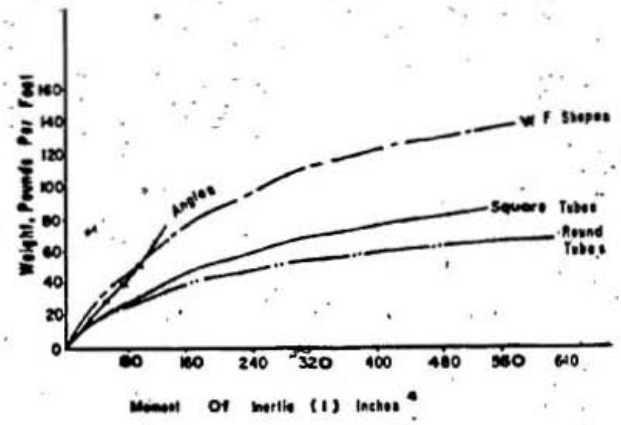

FIG. 7 WEIGHT - STRENGTH COMPARISON OF COMMON STRUCTURAL SHAPES (REF. 1)

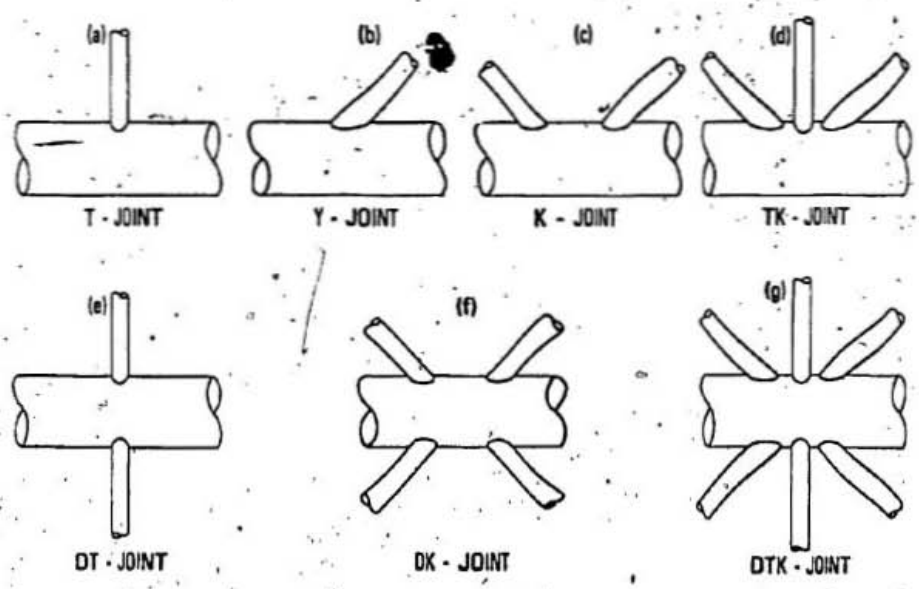

FIG. 8 TYPES OF SIMPLE PLANAR JOINTS (REF. 18)

A

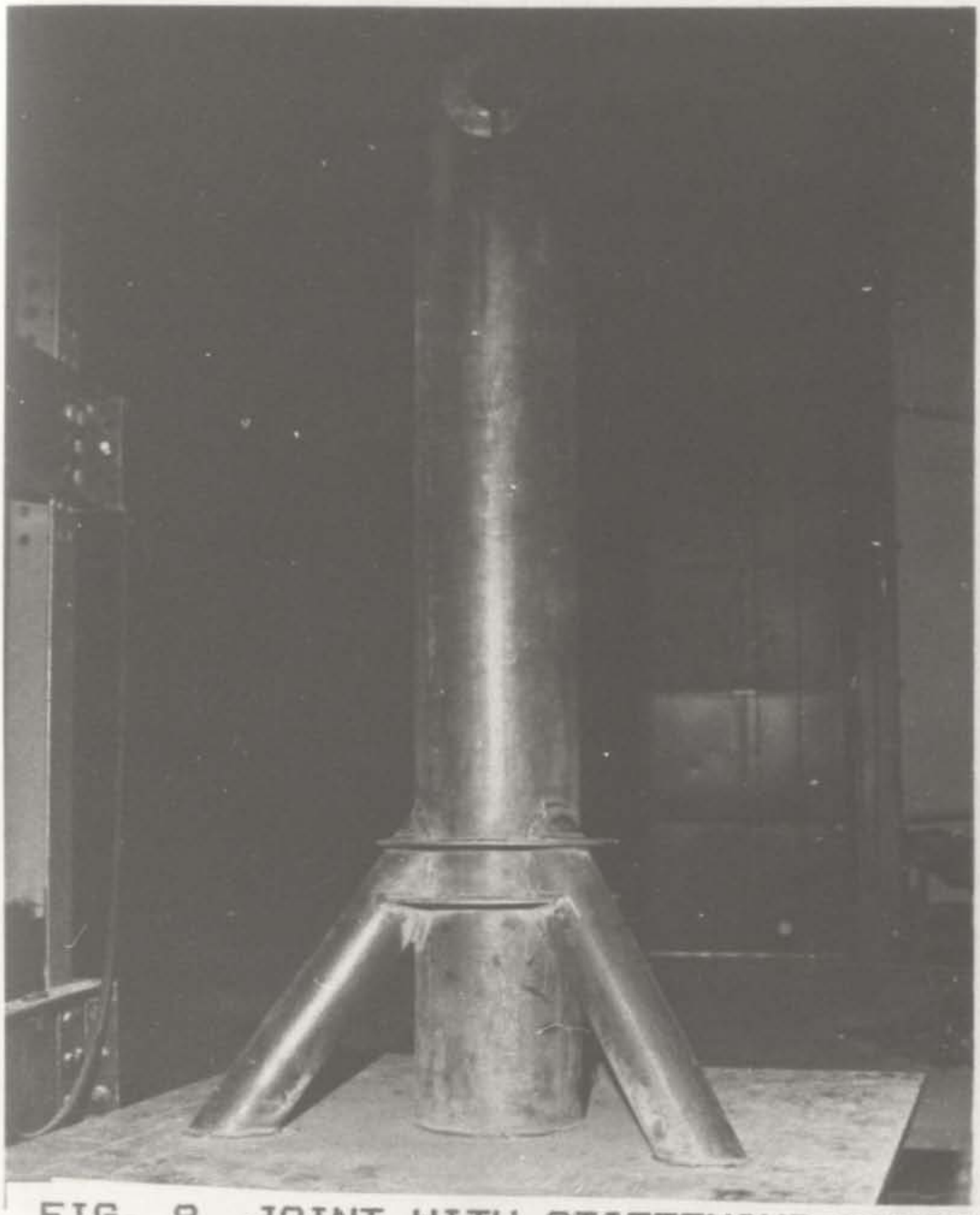

FIG. 9 JOINT WITH STIFFENING RINGS

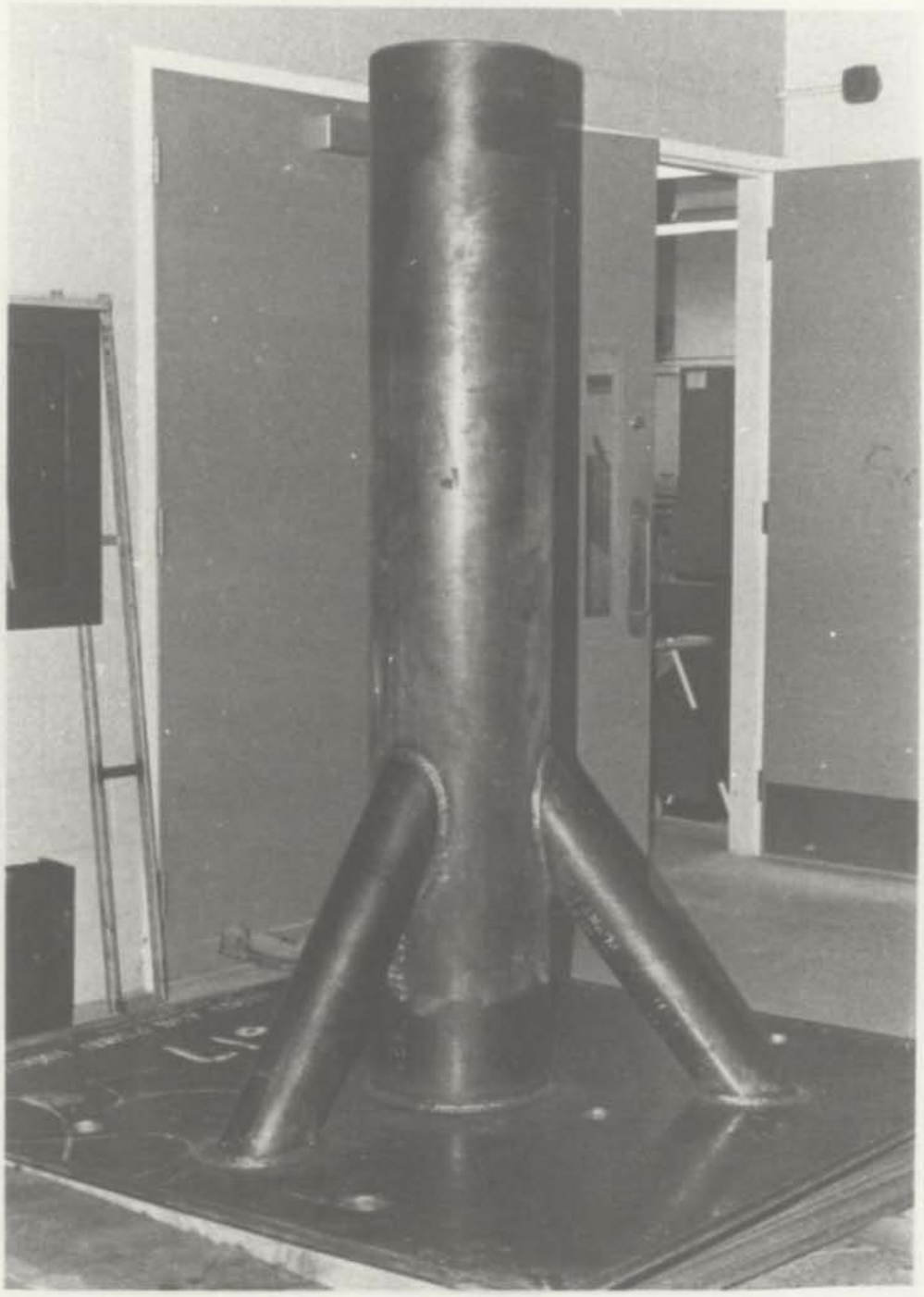

FIG. 10 JOINT WITHOUT STIFFENING RINGS

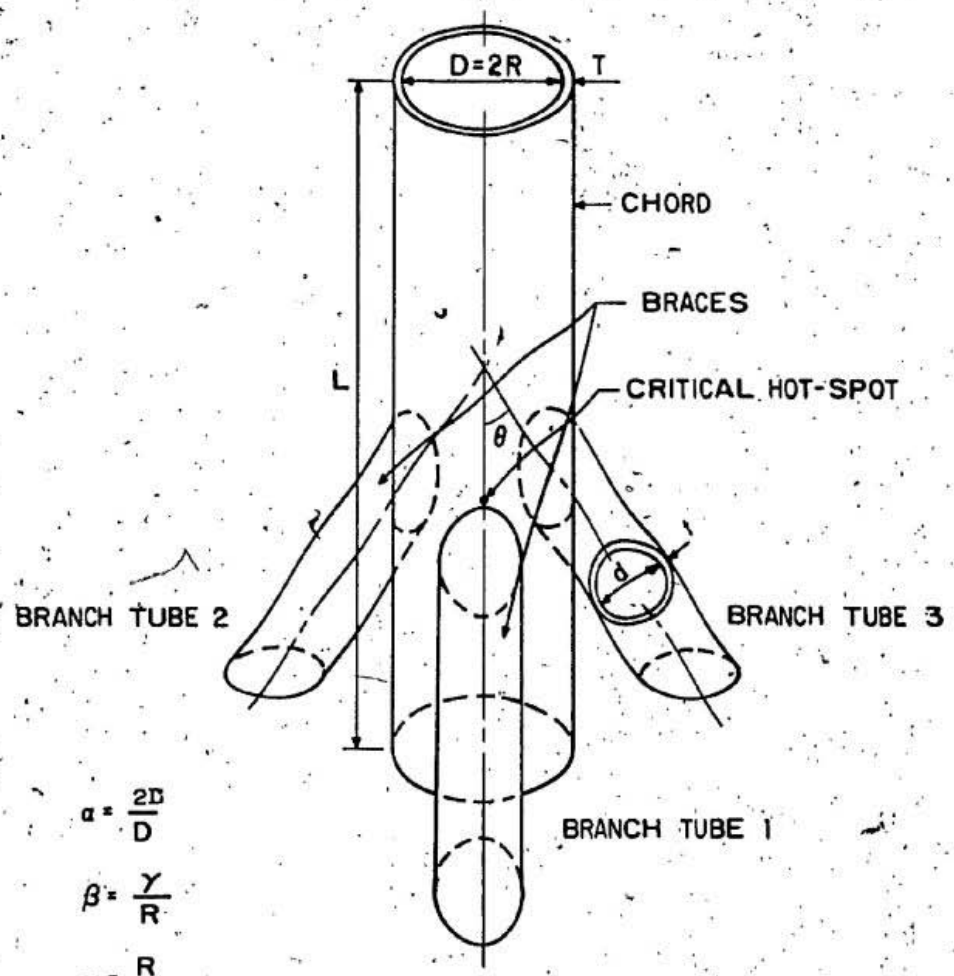

$\alpha = \frac{2D}{D}$

$\beta = \frac{\gamma}{R}$

$\gamma = \frac{R}{T}$

$\tau = \frac{t}{T}$

FIG. 11 MONOROD JOINT NOMENCLATURE

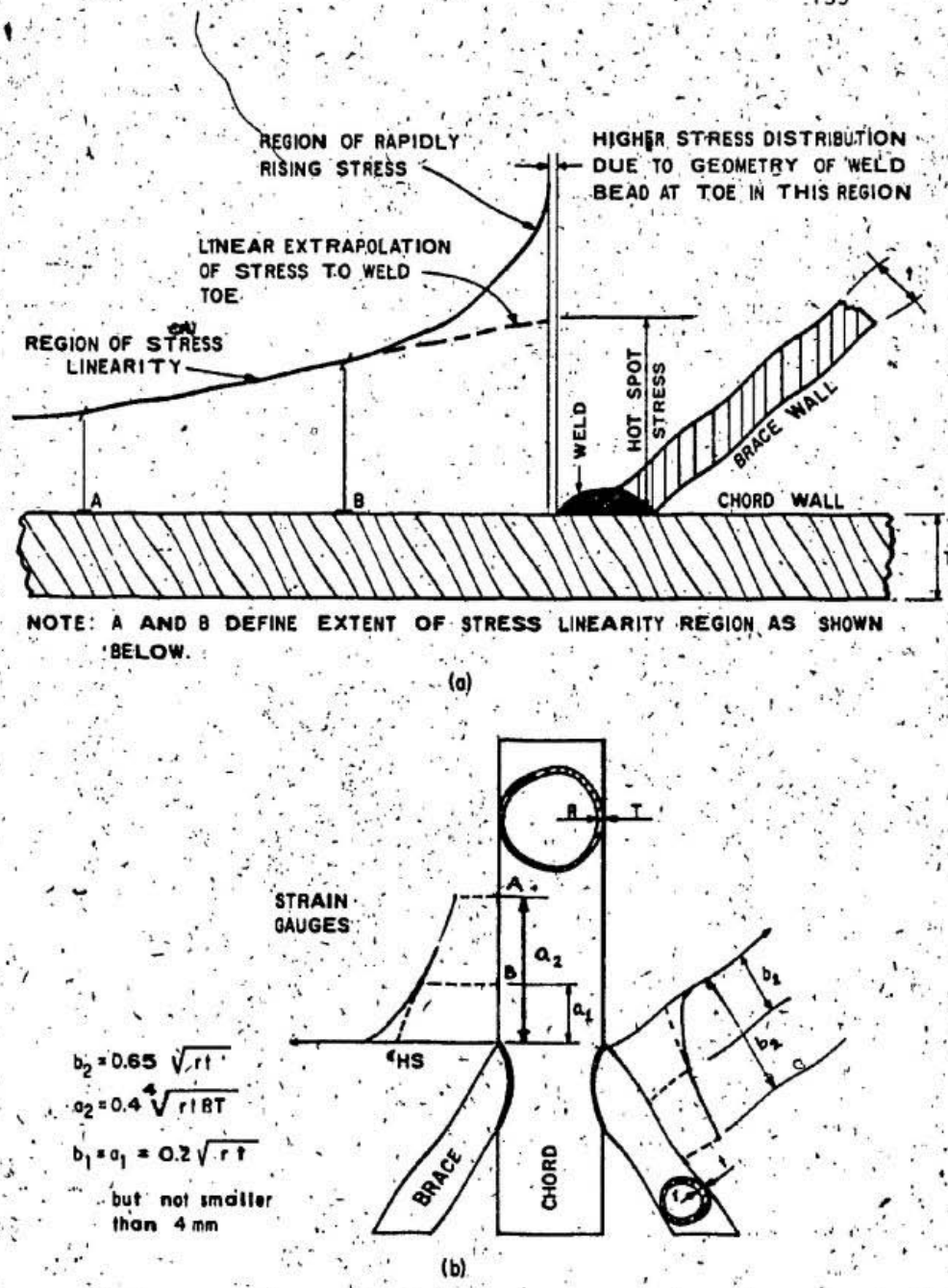

FIG. 12 DIAGRAMATIC REPRESENTATION DEFINING IDEALIZED HOT-SPOT STRESS

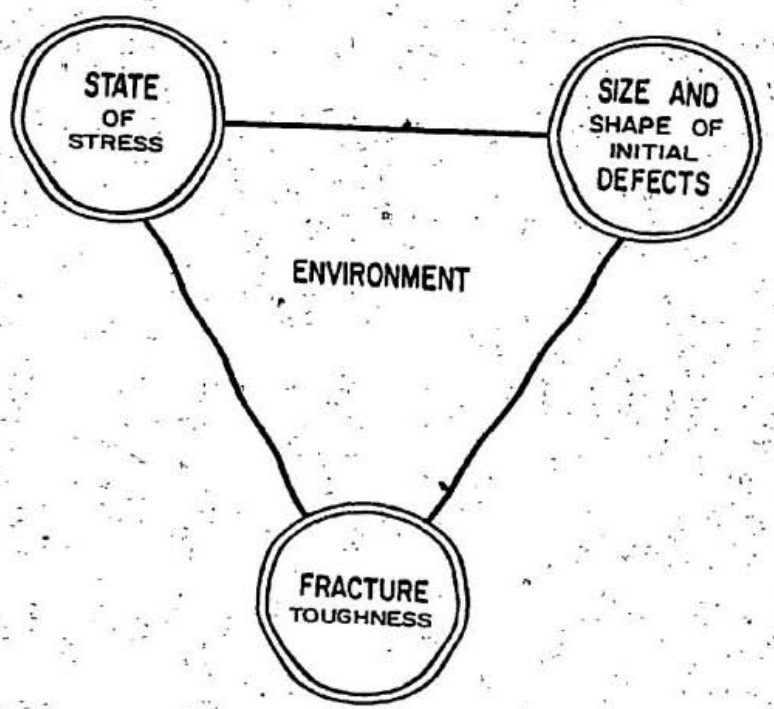

FIG. 13 STRUCTURAL INTEGRITY PARAMETERS

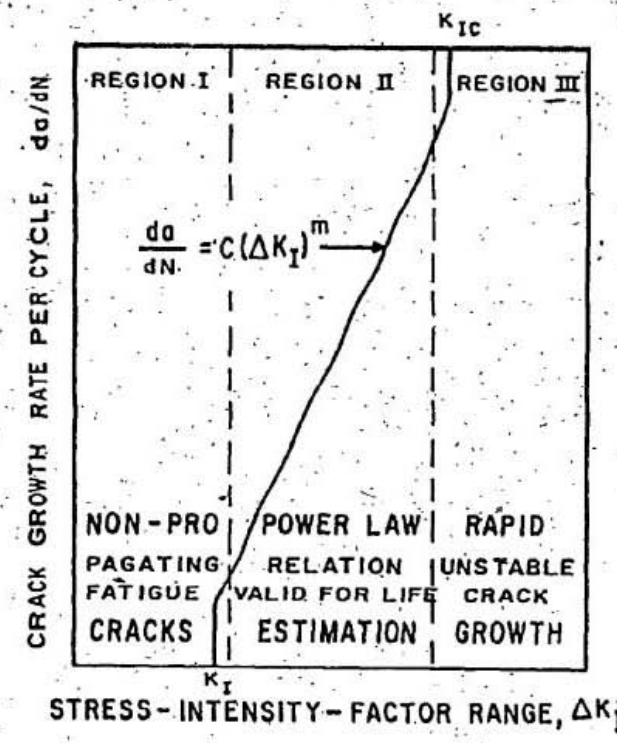

FIG. 14 SCHEMATIC REPRESENTATION OF FATIGUE CRACK GROWTH IN STEEL.

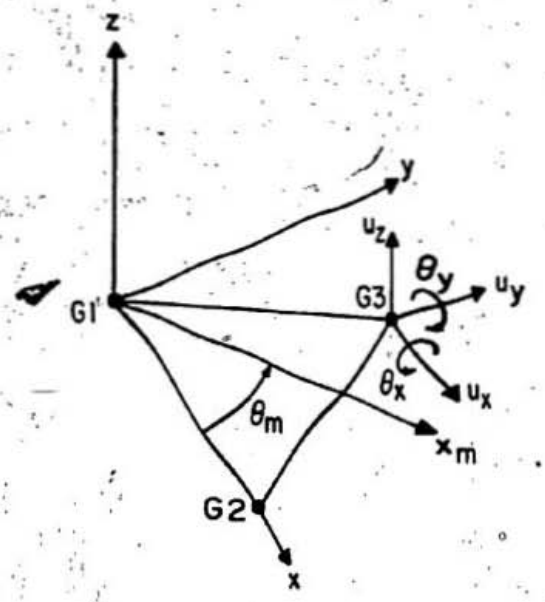

a) Triangular Element – TRIA3

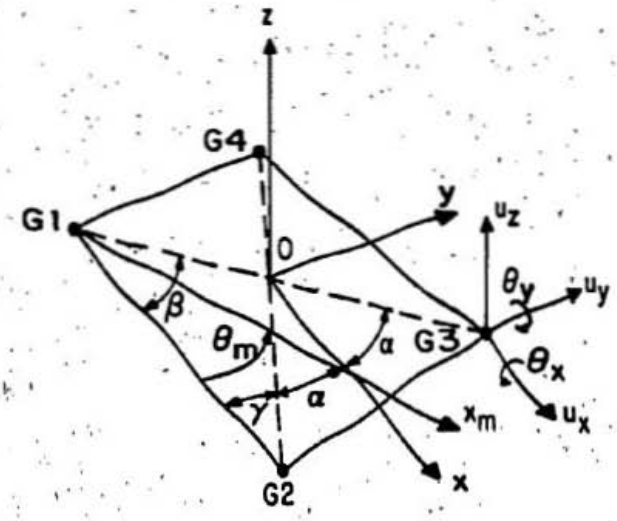

b) Quadrilateral Element – QUAD4

FIG. 15 FLAT SHELL ELEMENT COORDINATES

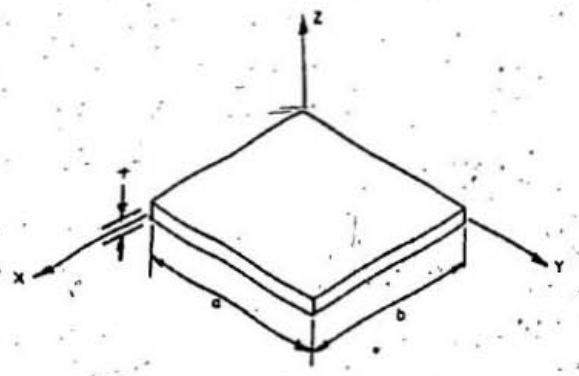

(a) Plate Configuration

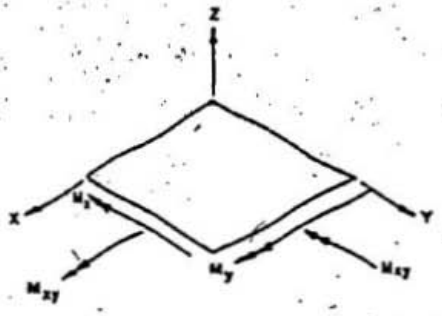

(b) Positive Moment Resultants

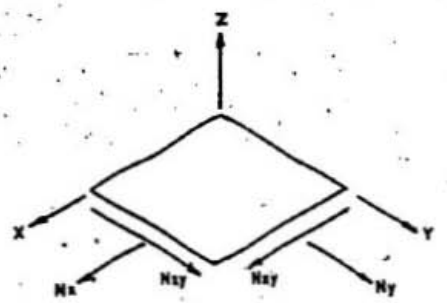

(c) Positive Force Resultants

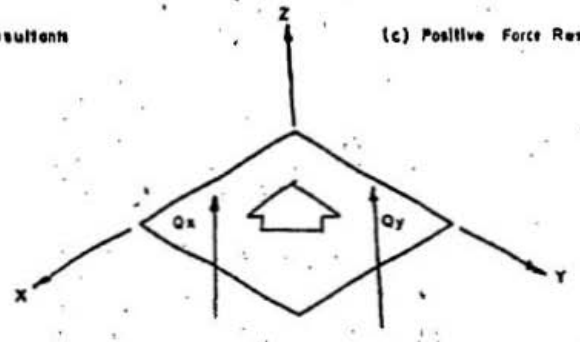

FIG. 16 FORCE AND MOMENT RESULTANTS

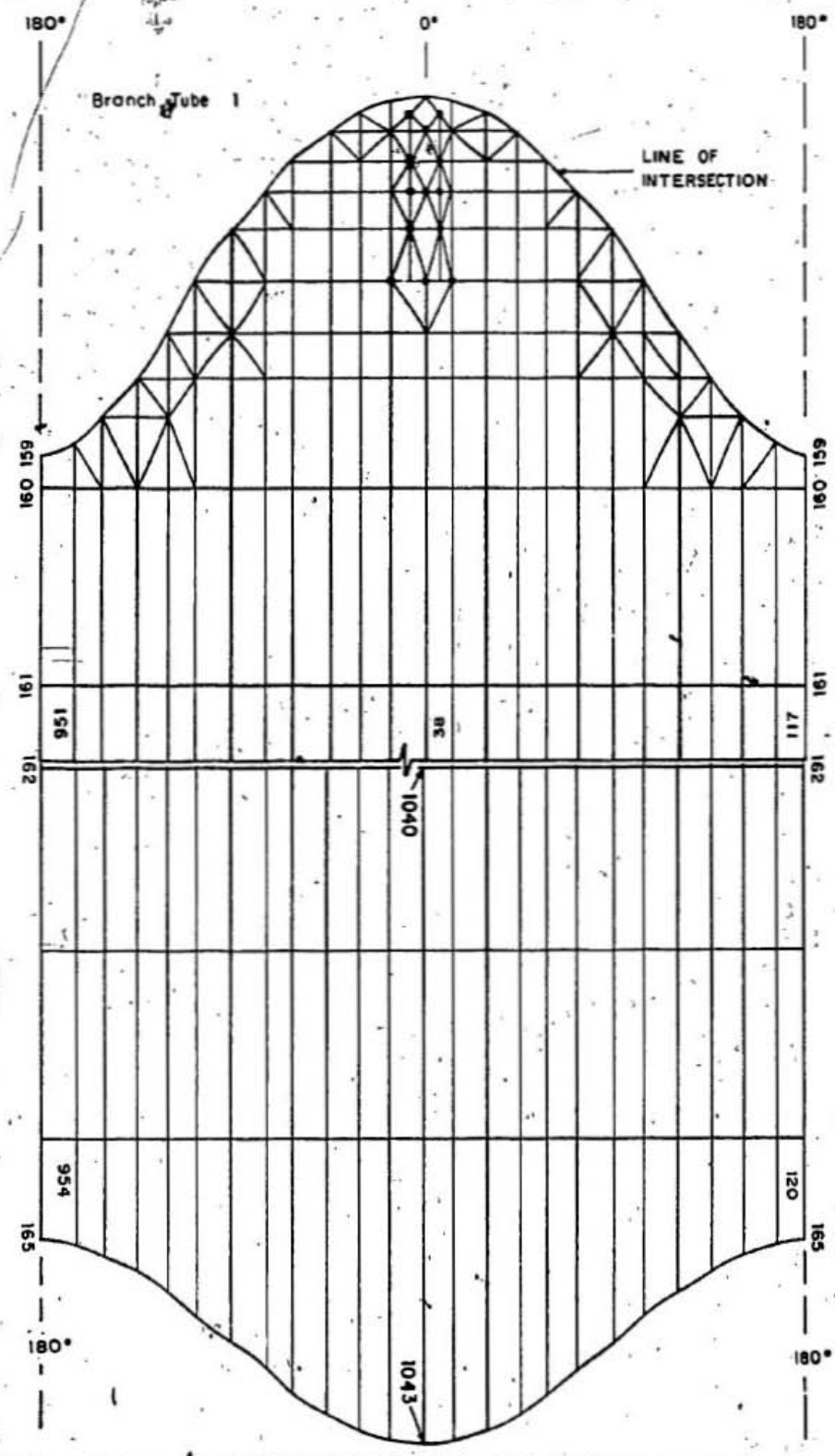

FIG. 17 DISCRETIZATION OF DEVELOPED SURFACE B.T. 1

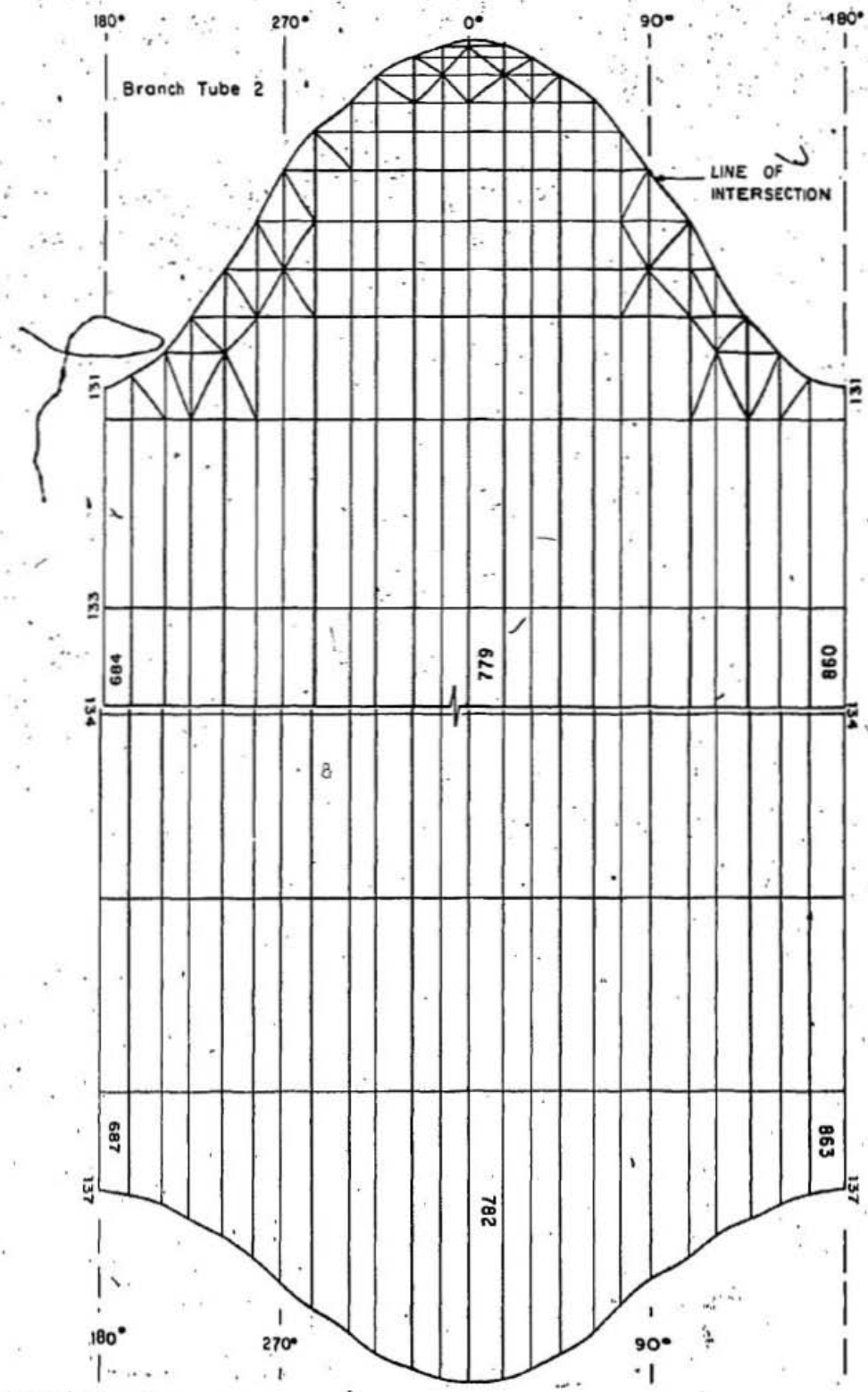

FIG. 18 DISCRETIZATION OF DEVELOPED SURFACE B.T. 2

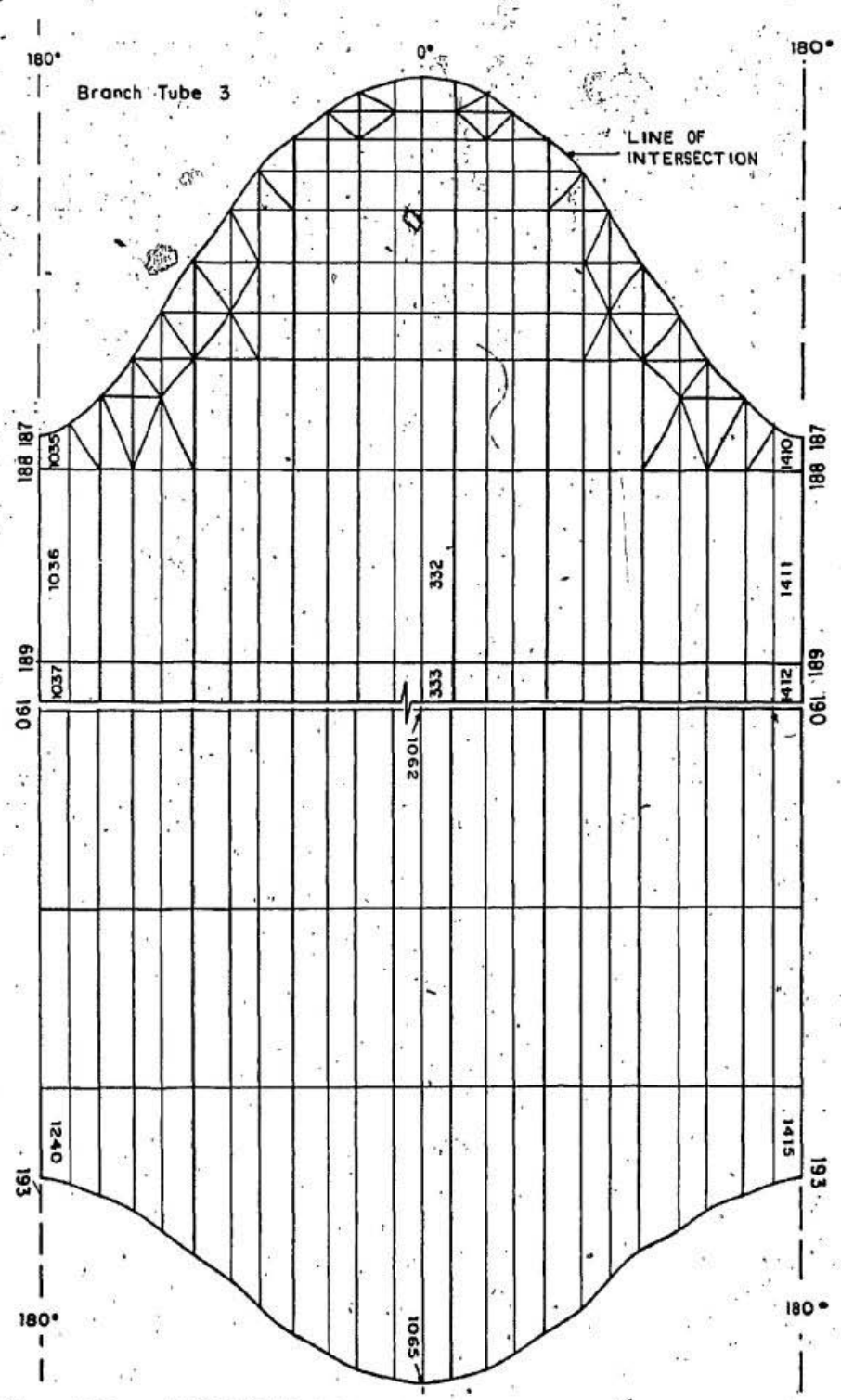

FIG. 19 DISCRETIZATION OF DEVELOPED SURFACE B.T. 3

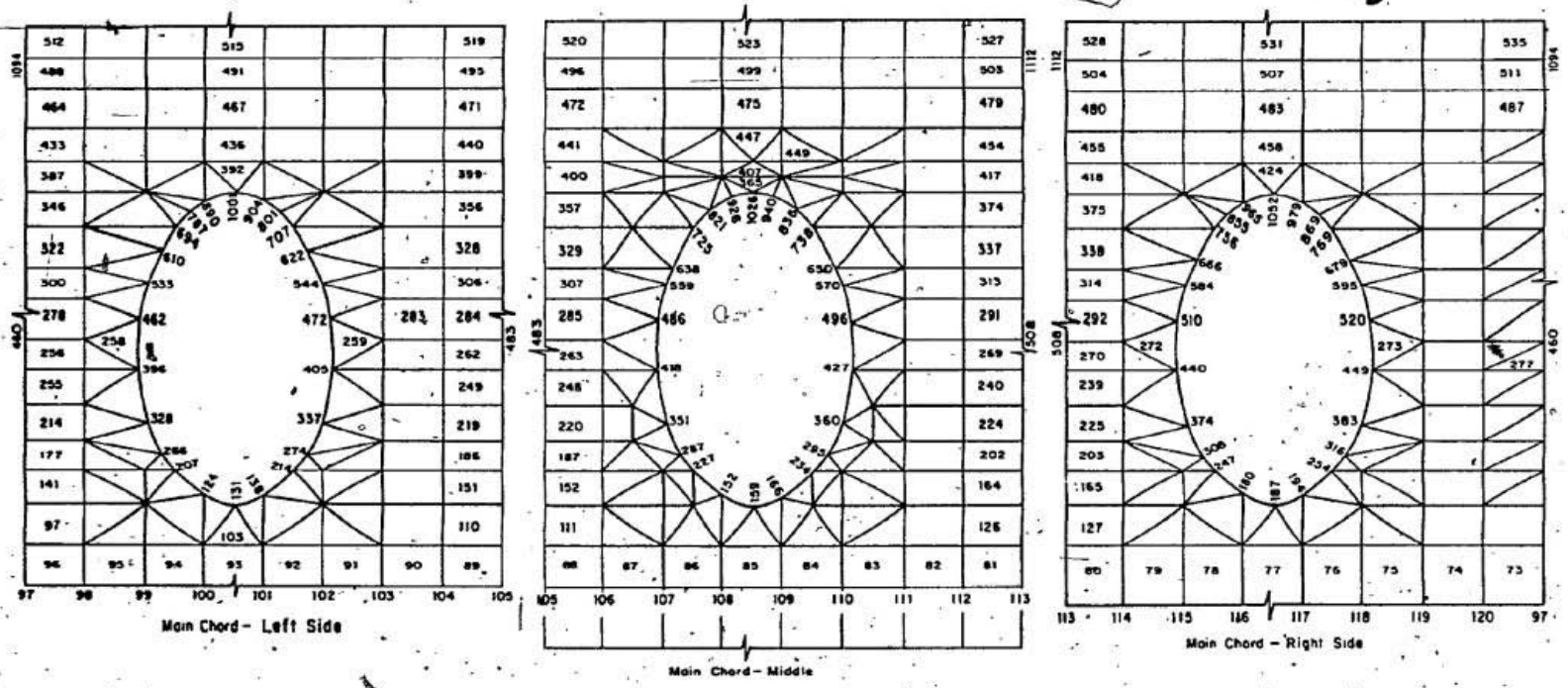

FIG. 20 DISCRETIZATION OF DEVELOPED SURFACE - MAIN TUBE

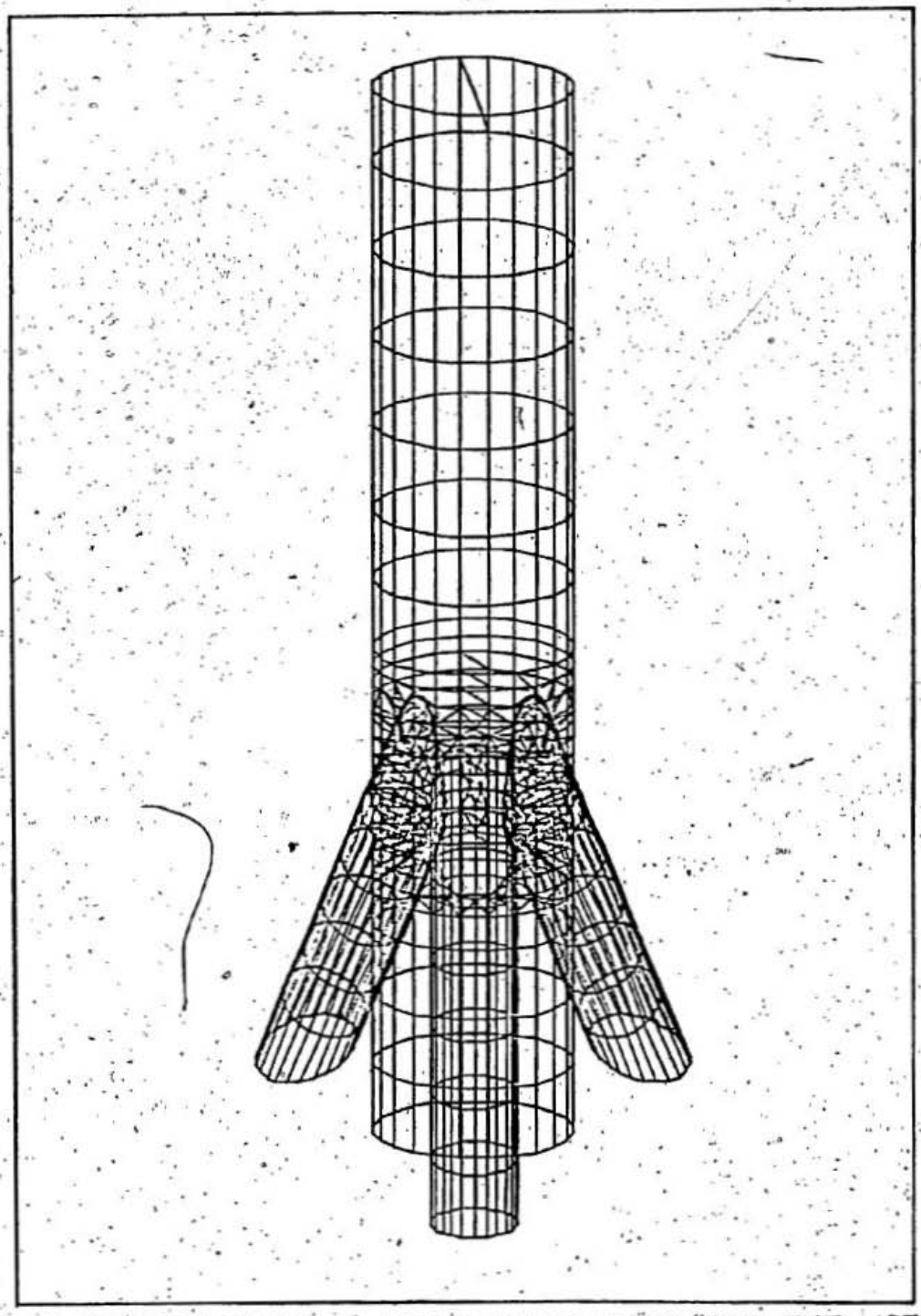

FIG.21 FINITE ELEMENT MESH GENERATION FOR THE JOINT

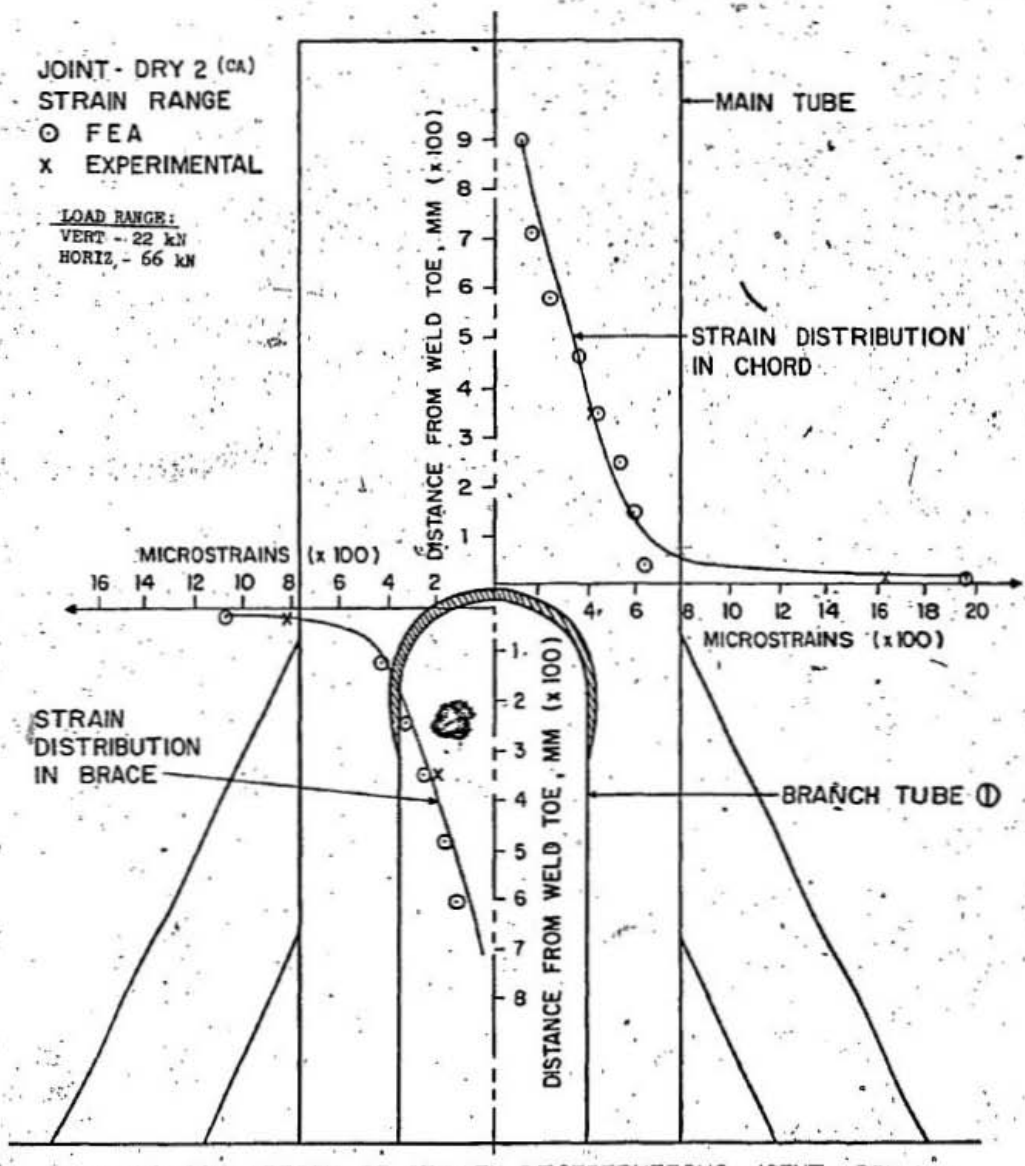

FIG. 22 COMPARISON OF STRAIN DISTRIBUTIONS: JOINT– DRY 2

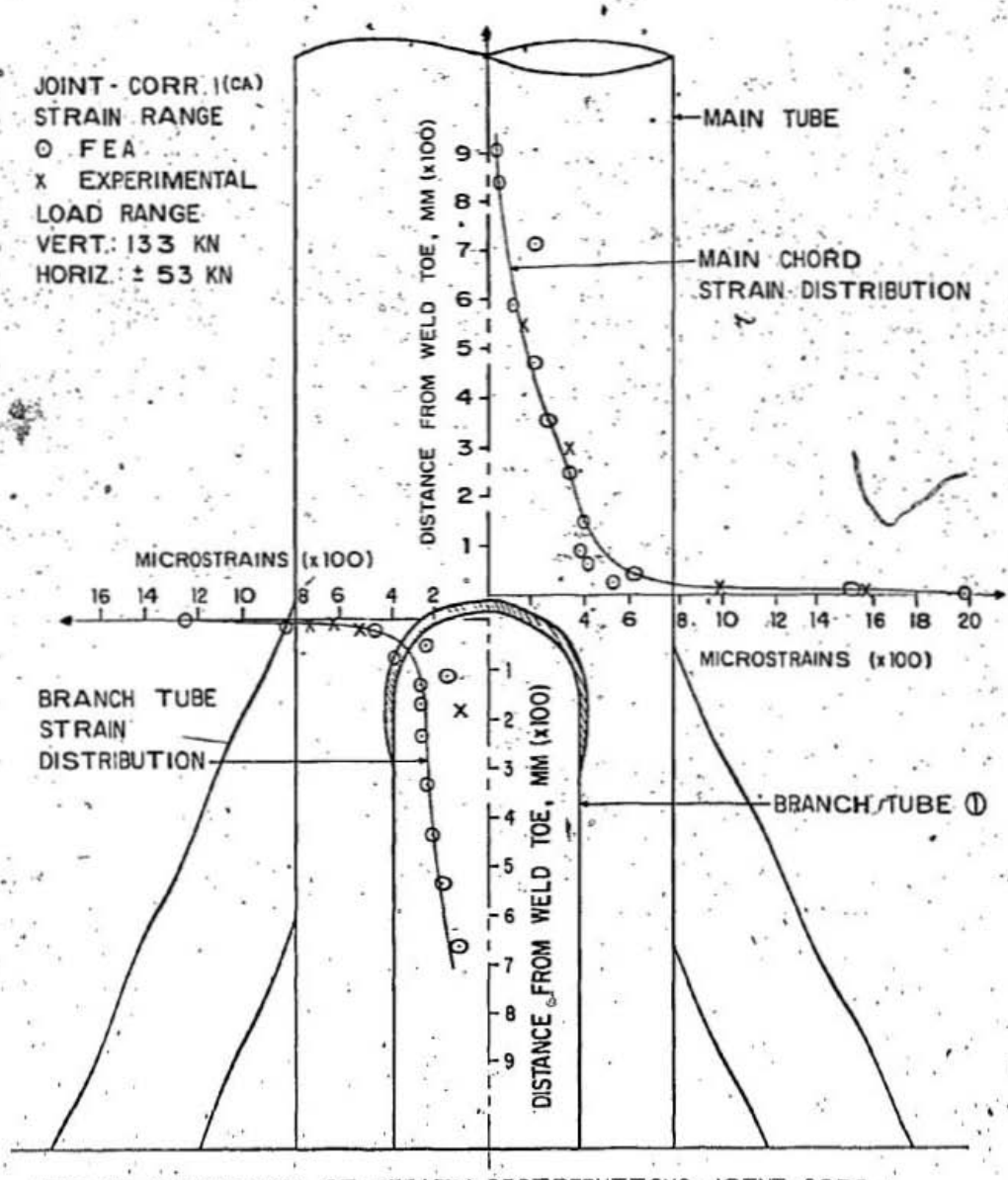

FIG.23 COMPARISON OF STRAIN DISTRIBUTIONS: JOINT-CORR.1

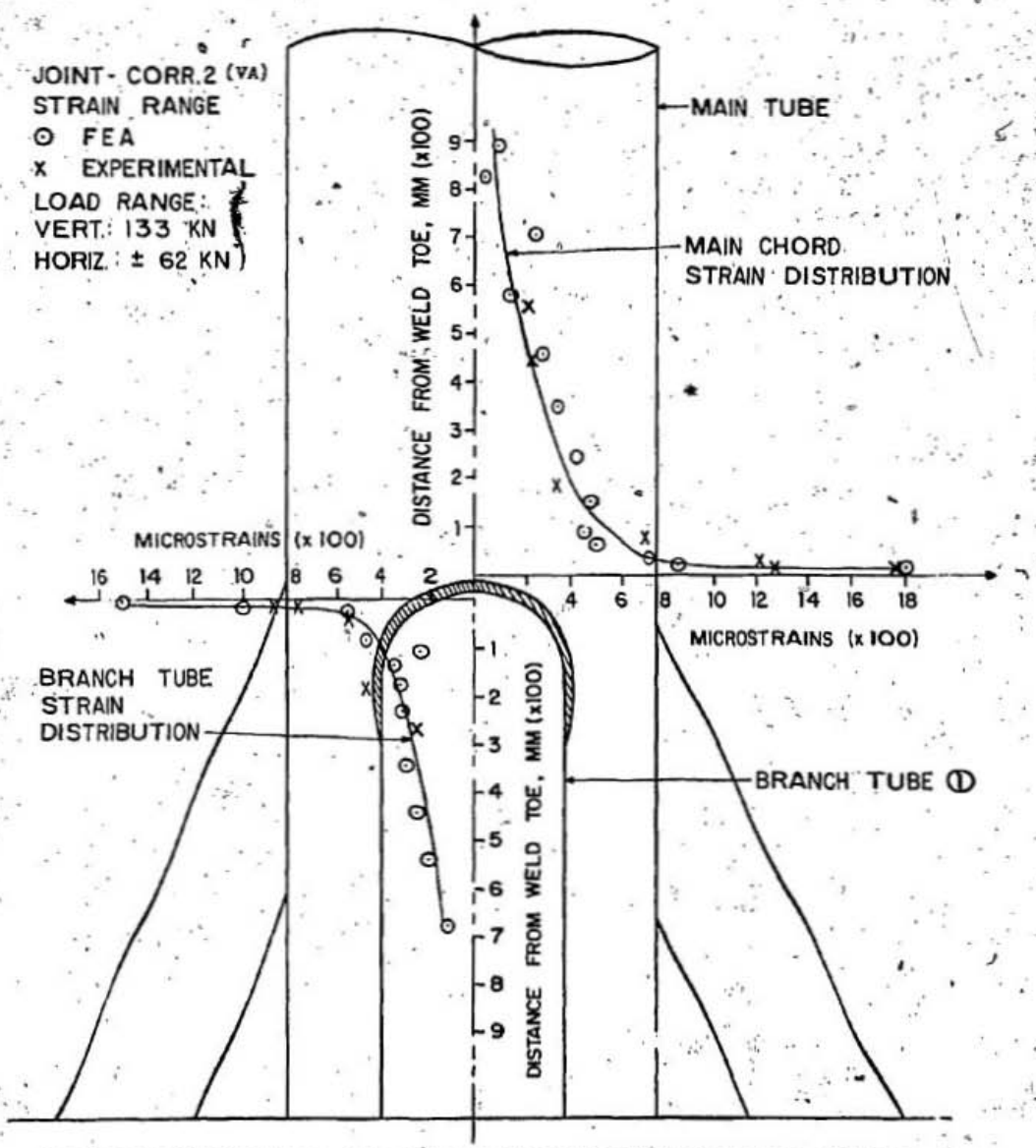

FIG.24 COMPARISON OF STRAIN DISTRIBUTIONS JOINT-CORR.2 AND DRY 1

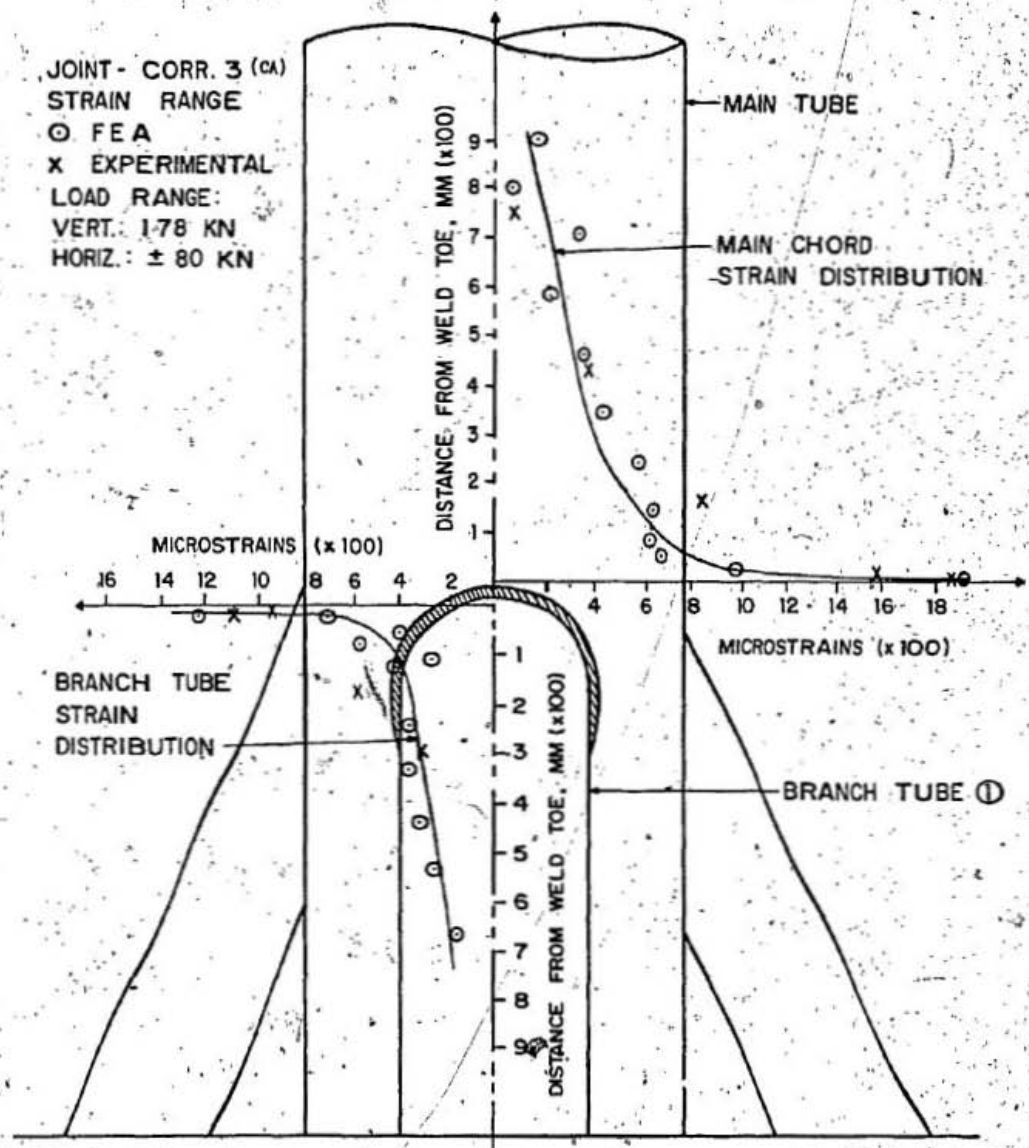

FIG. 25 COMPARISON OF STRAIN DISTRIBUTIONS: JOINT-CORR. 3

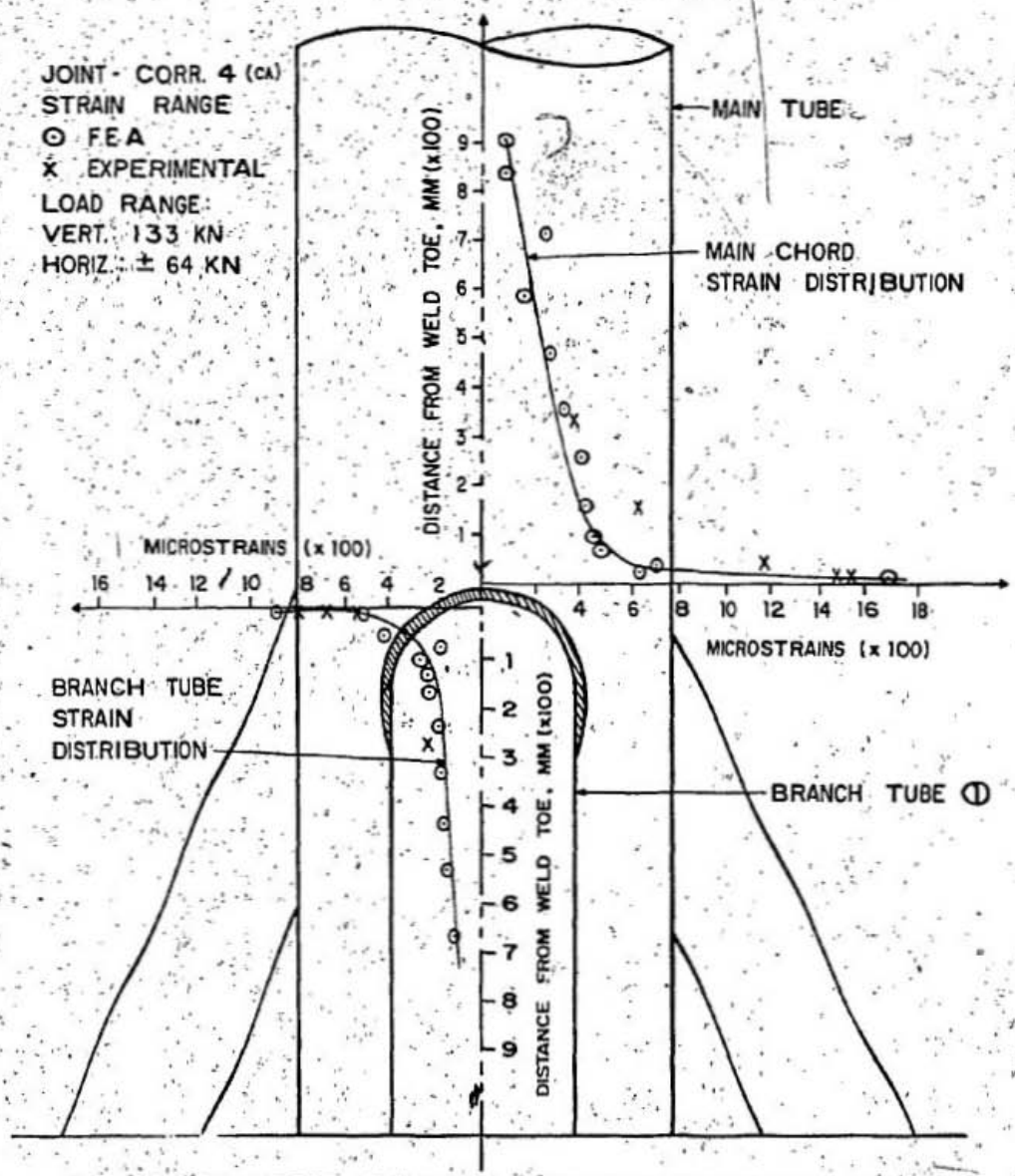

FIG. 26 COMPARISON OF STRAIN DISTRIBUTIONS JOINT-CORR. 4

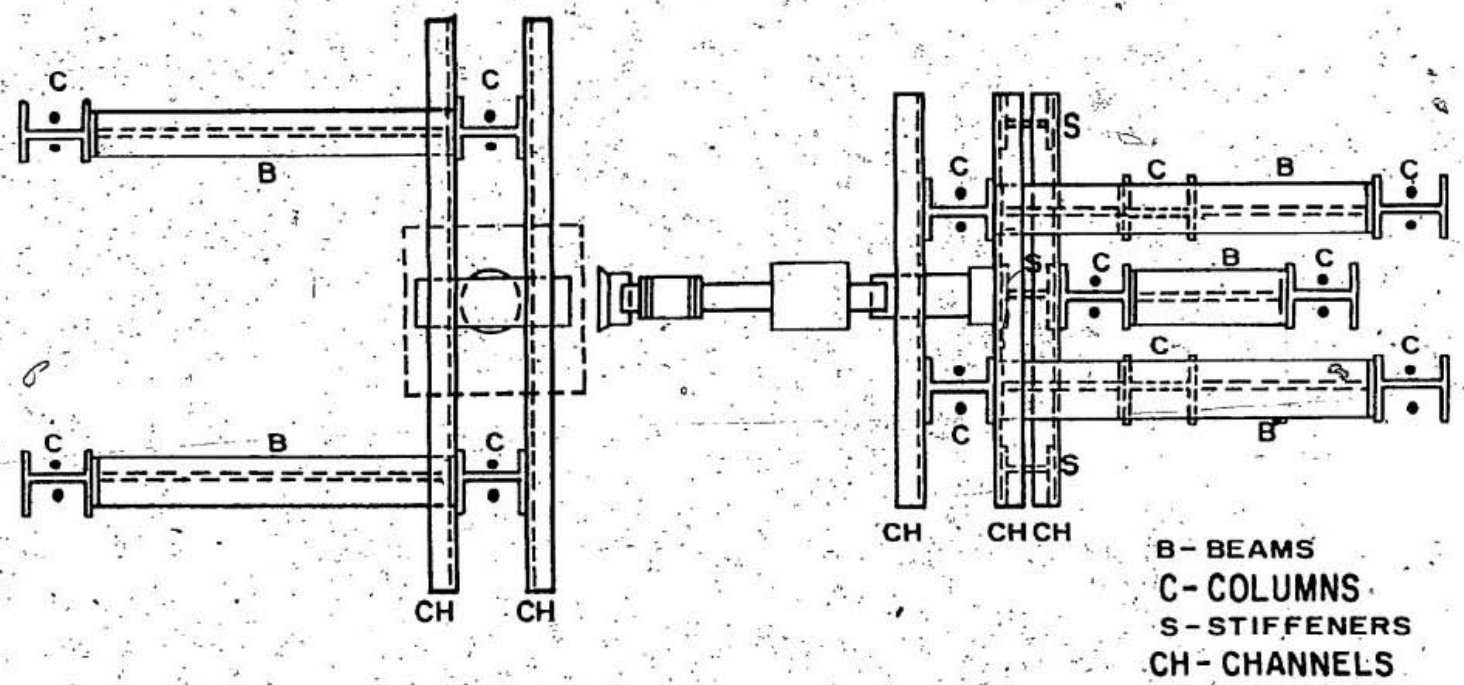

FIG. 27 PLAN OF TEST ASSEMBLY

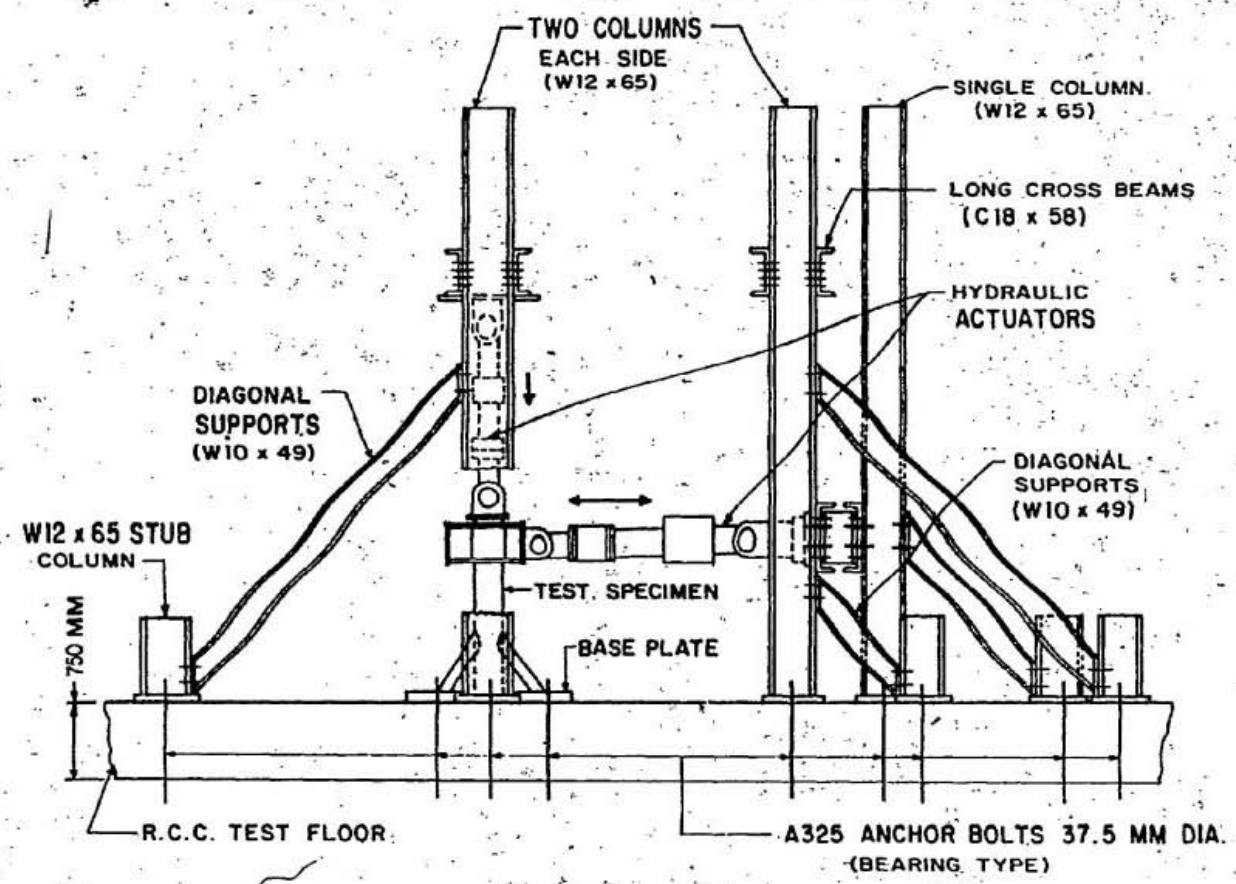

FIG.28 TEST ASSEMBLY FOR FATIGUE LOADING

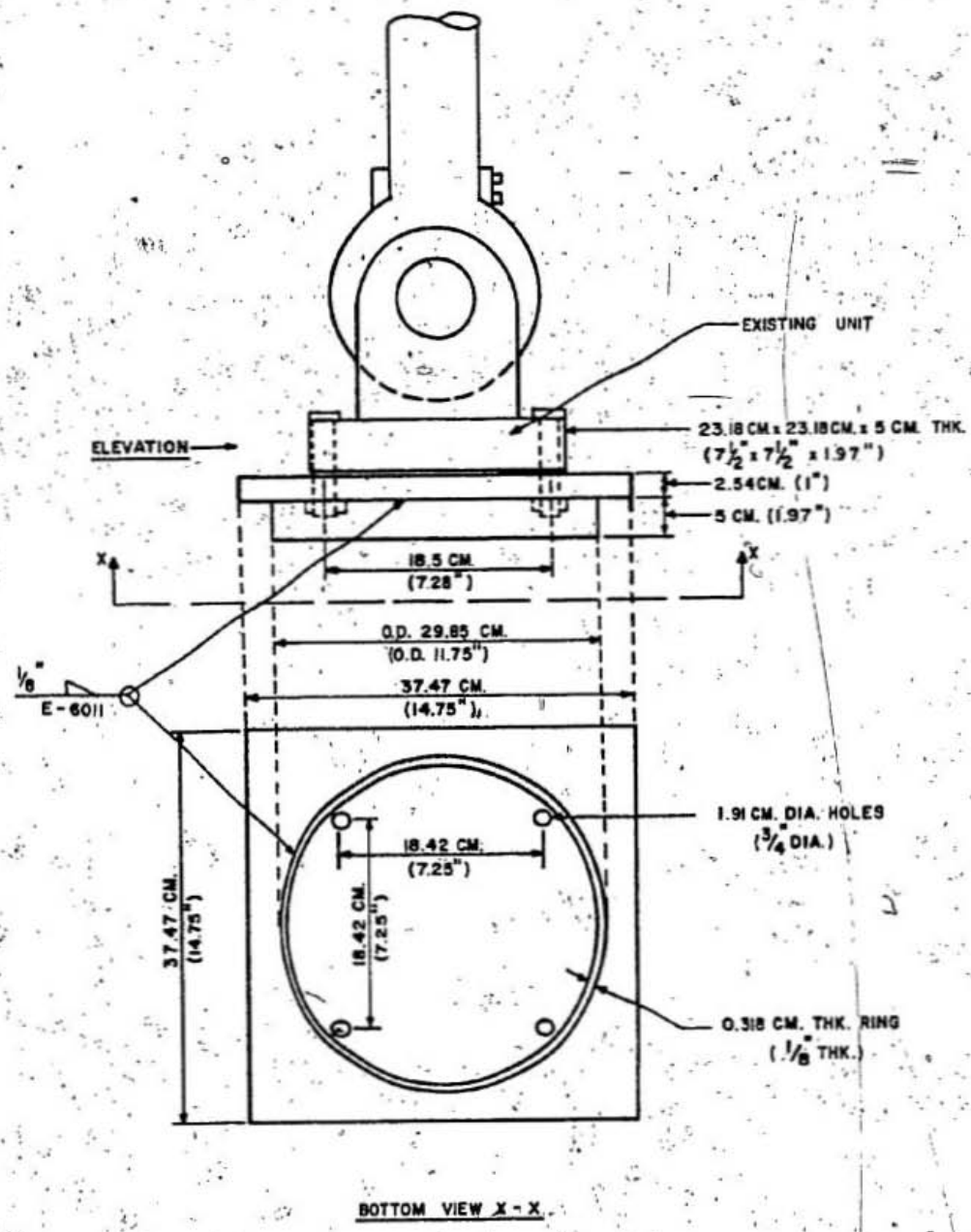

FIG. 29 CONNECTION UNIT FOR VERTICAL LOADING

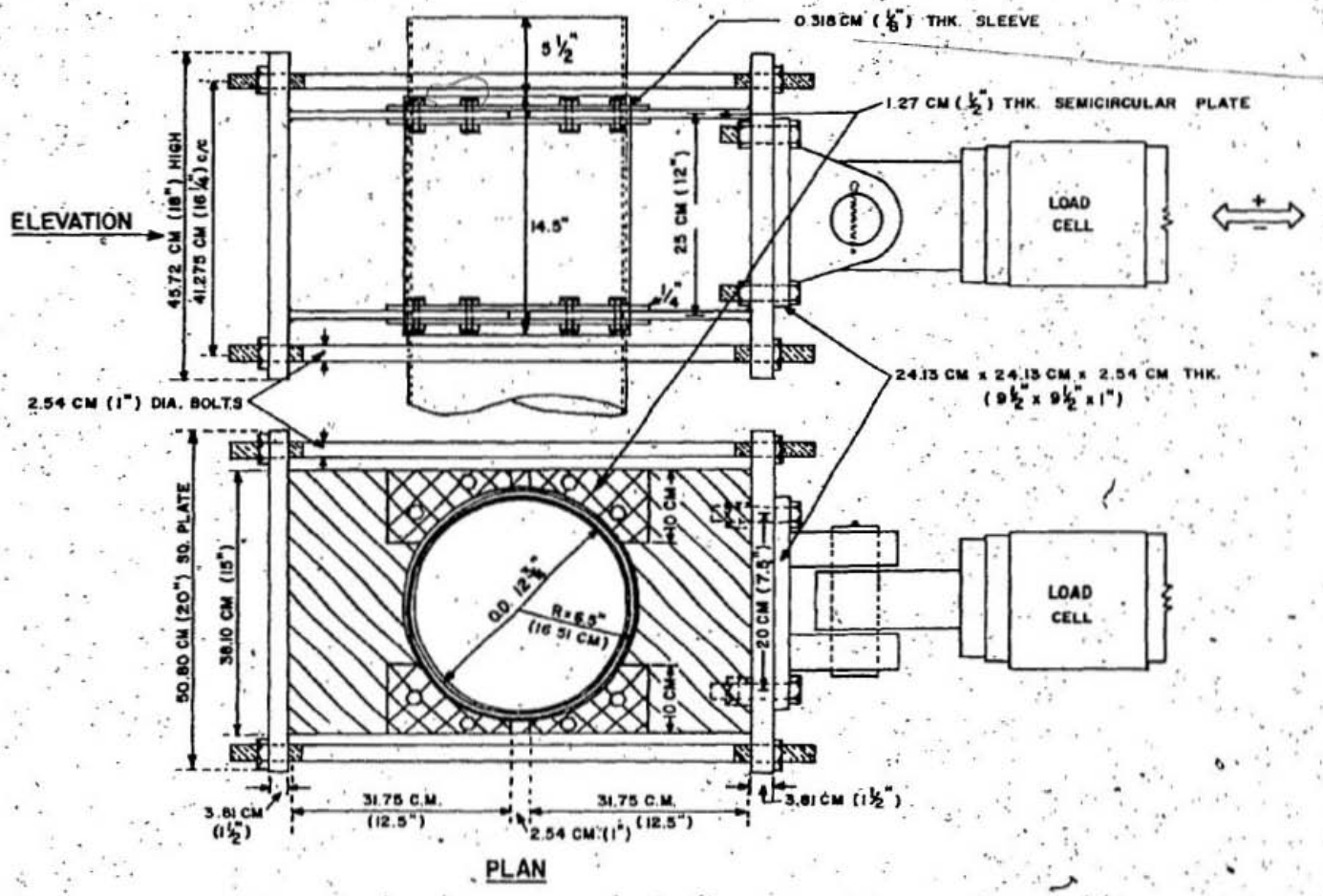

FIG. 30 CONNECTION UNIT FOR HORIZONTAL LOADING

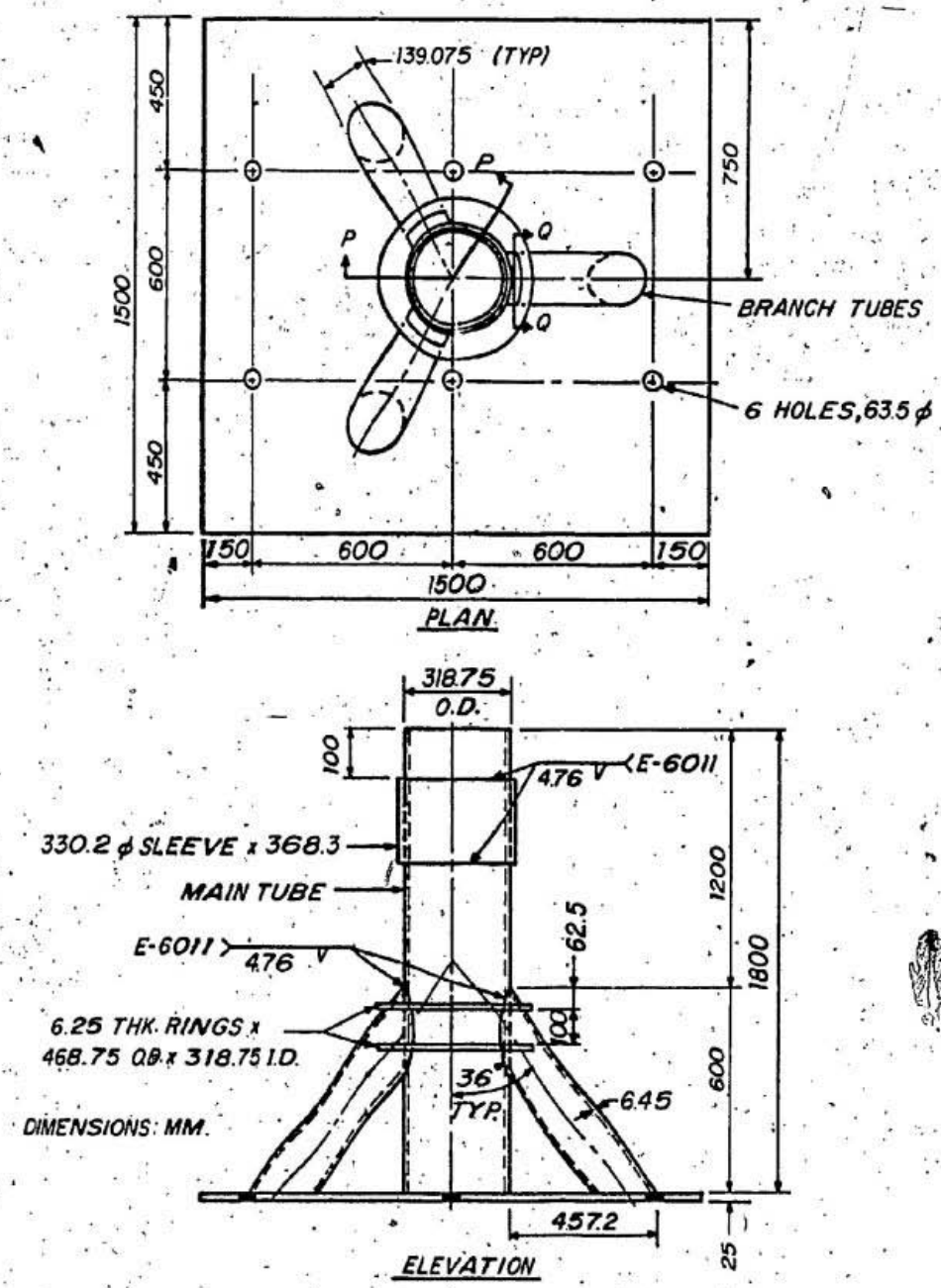

FIG.31 DETAILS OF MONOPOD JOINT WITH STIFFENING RINGS

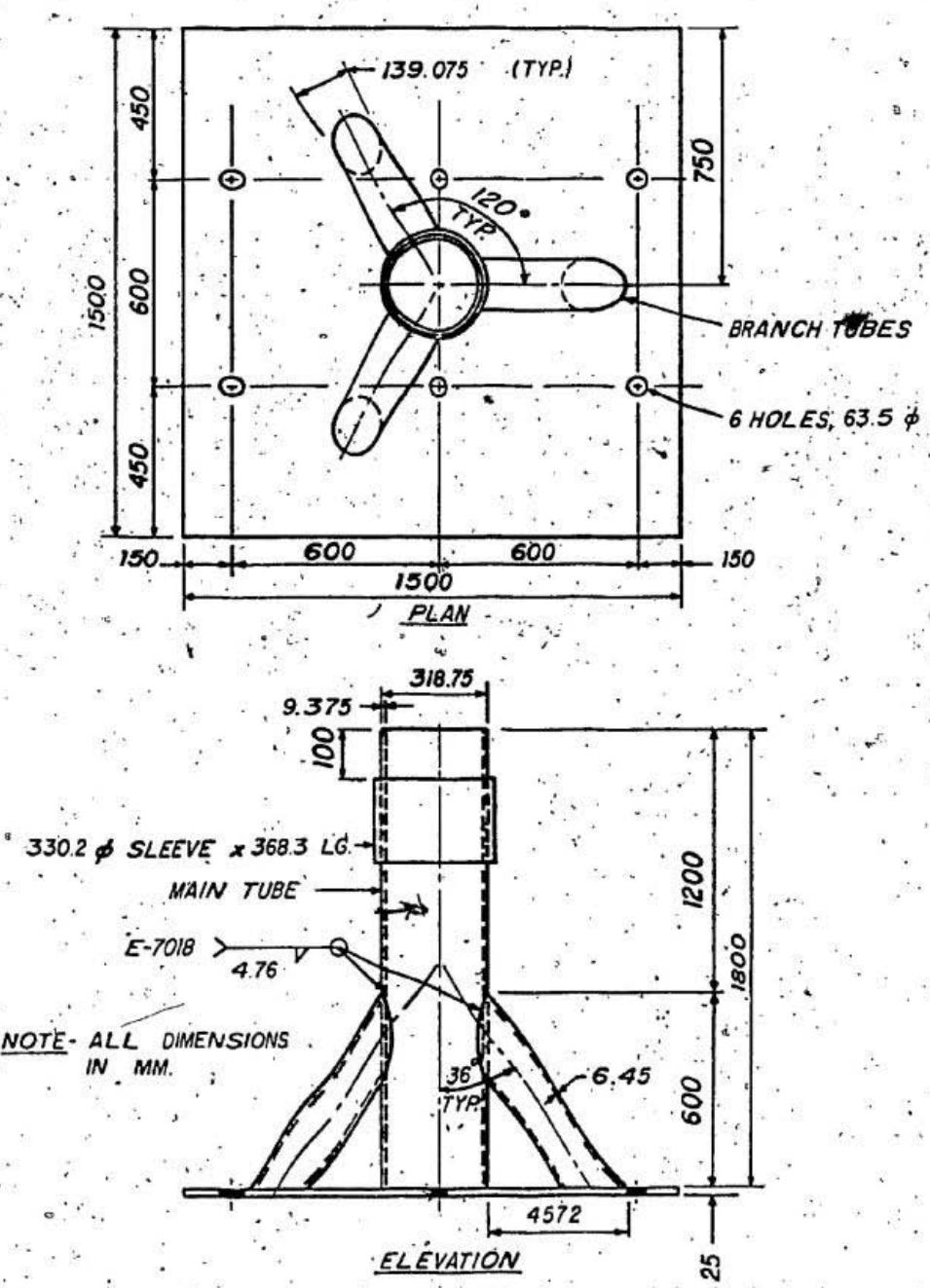

FIG.32 DETAILS OF MONOPOD JOINT WITHOUT STIFFENING RINGS

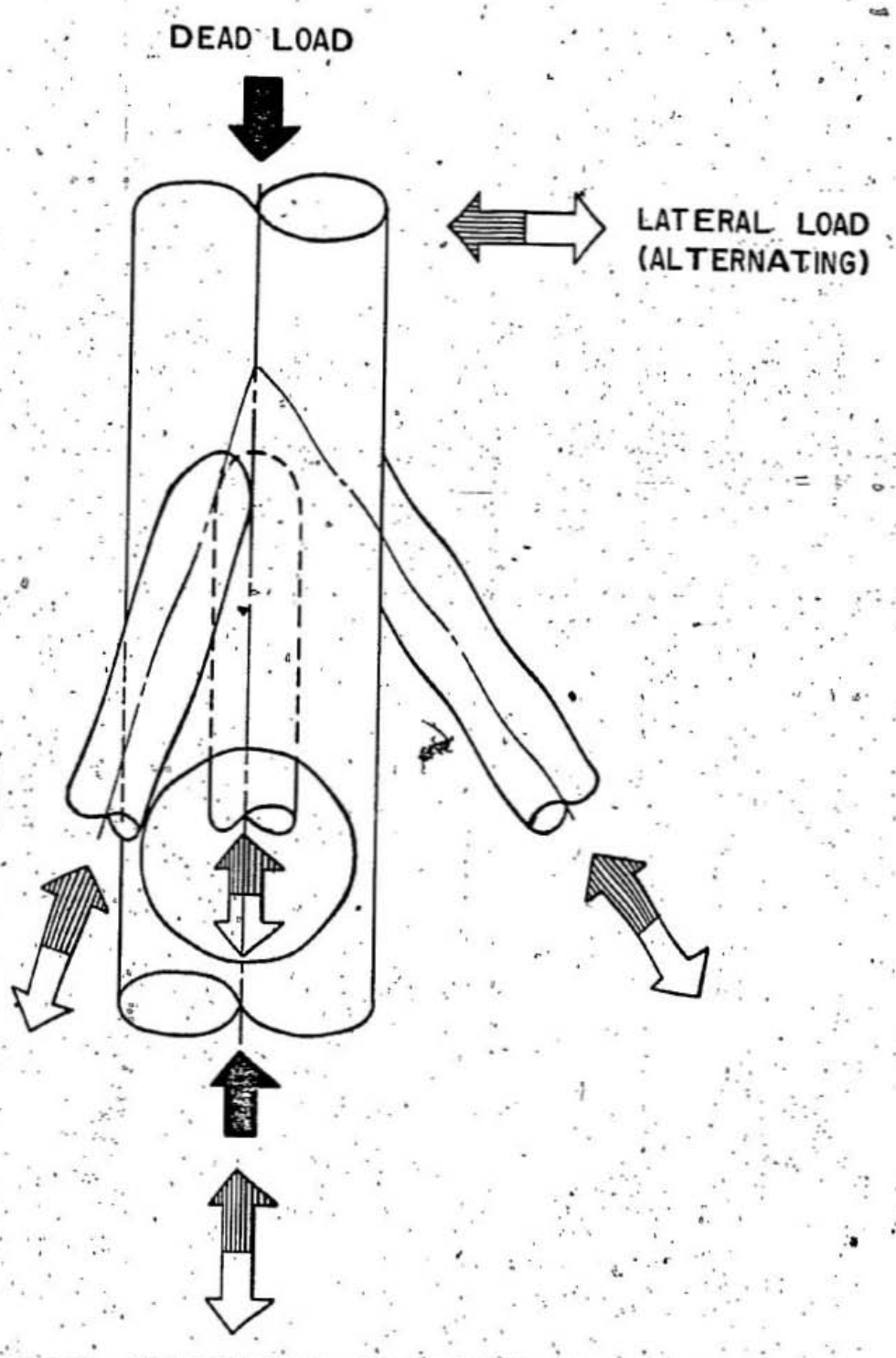

FIG.33 DIRECTIONS OF APPLIED LOADS AND REACTIVE FORCES

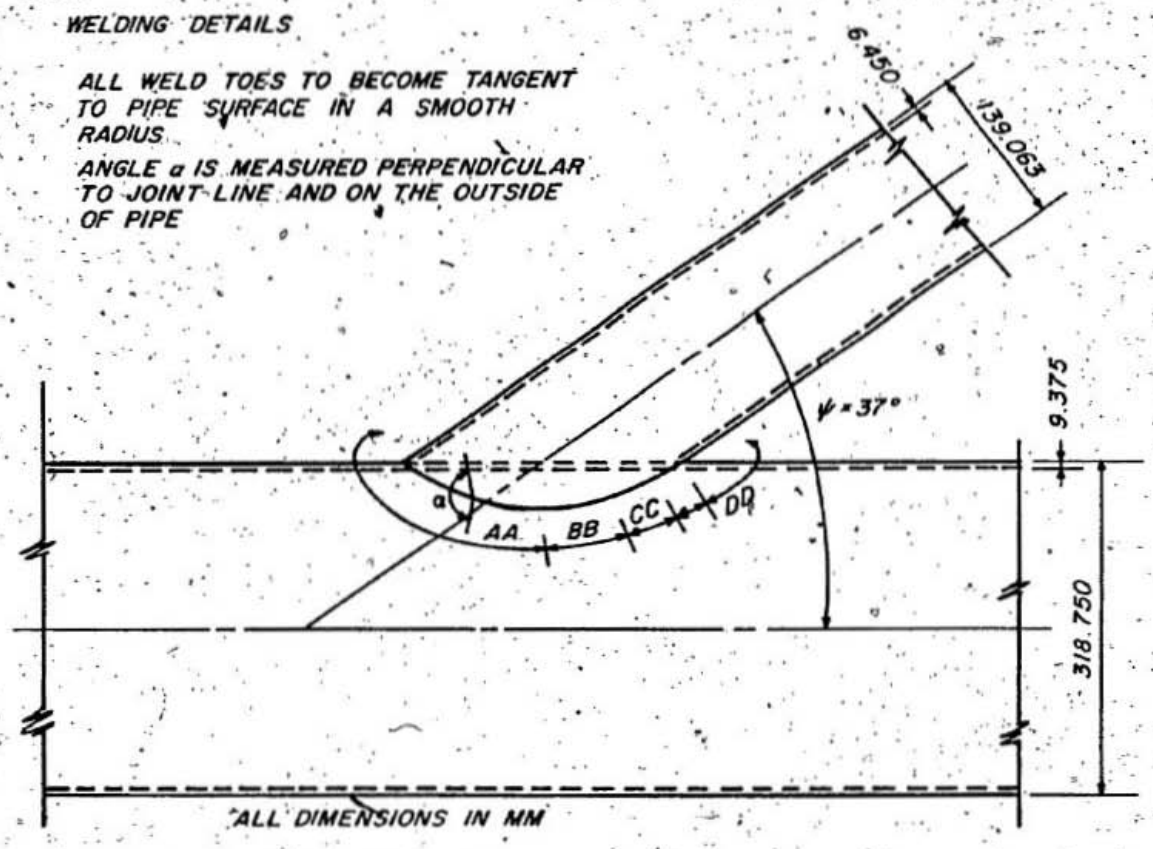

TYPICAL CONNECTION ELEVATION

FIG. 34 TUBE WELD CONNECTION ELEVATION

WELD DETAILS FROM ONE SIDE ONLY – TYPES I & II

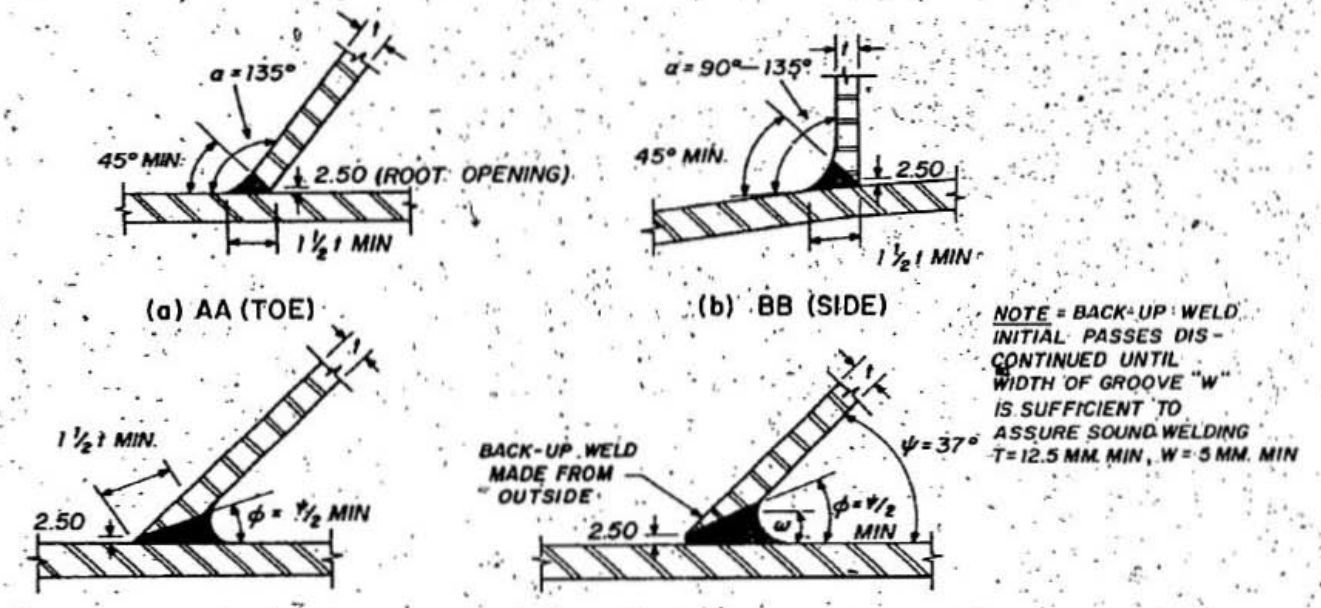

FIG. 35 WELDING DETAILS

DETAILS OF RING-TO-TUBE WELDS FOR JOINT TYPE-II.

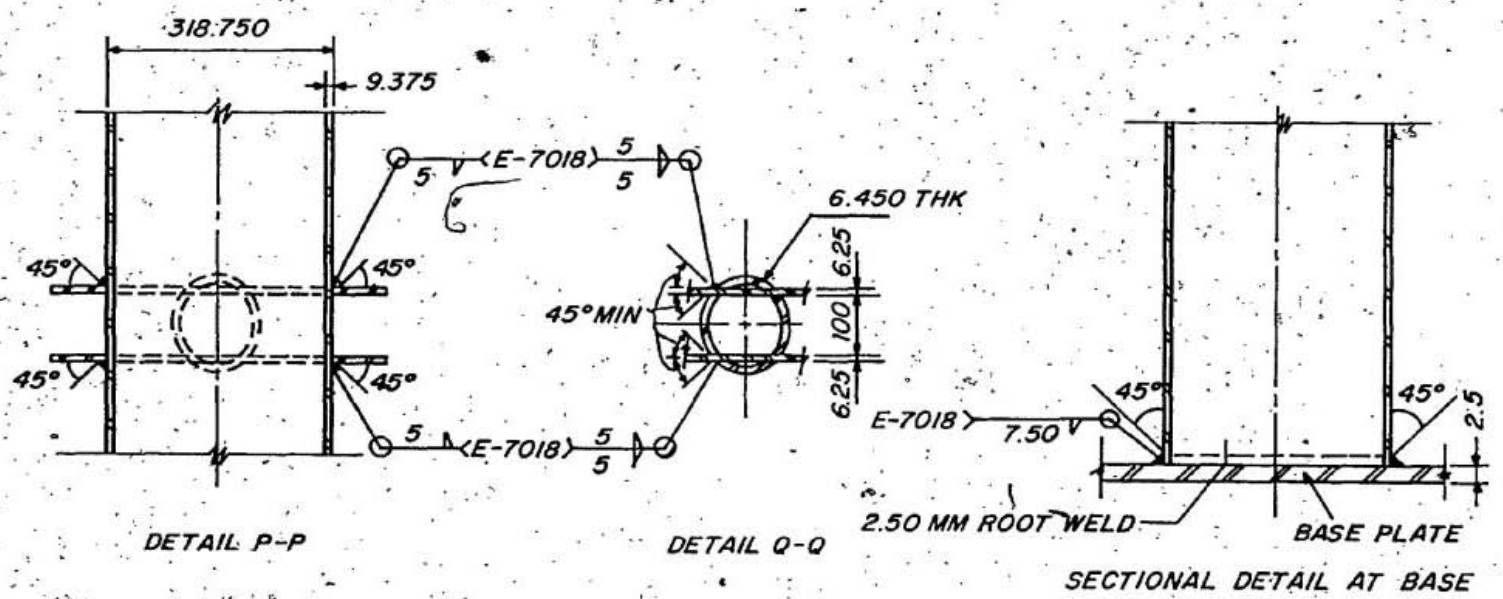

FIG.36 DETAILS OF RING-TO-TUBE WELDS FOR STIFFENED JOINT

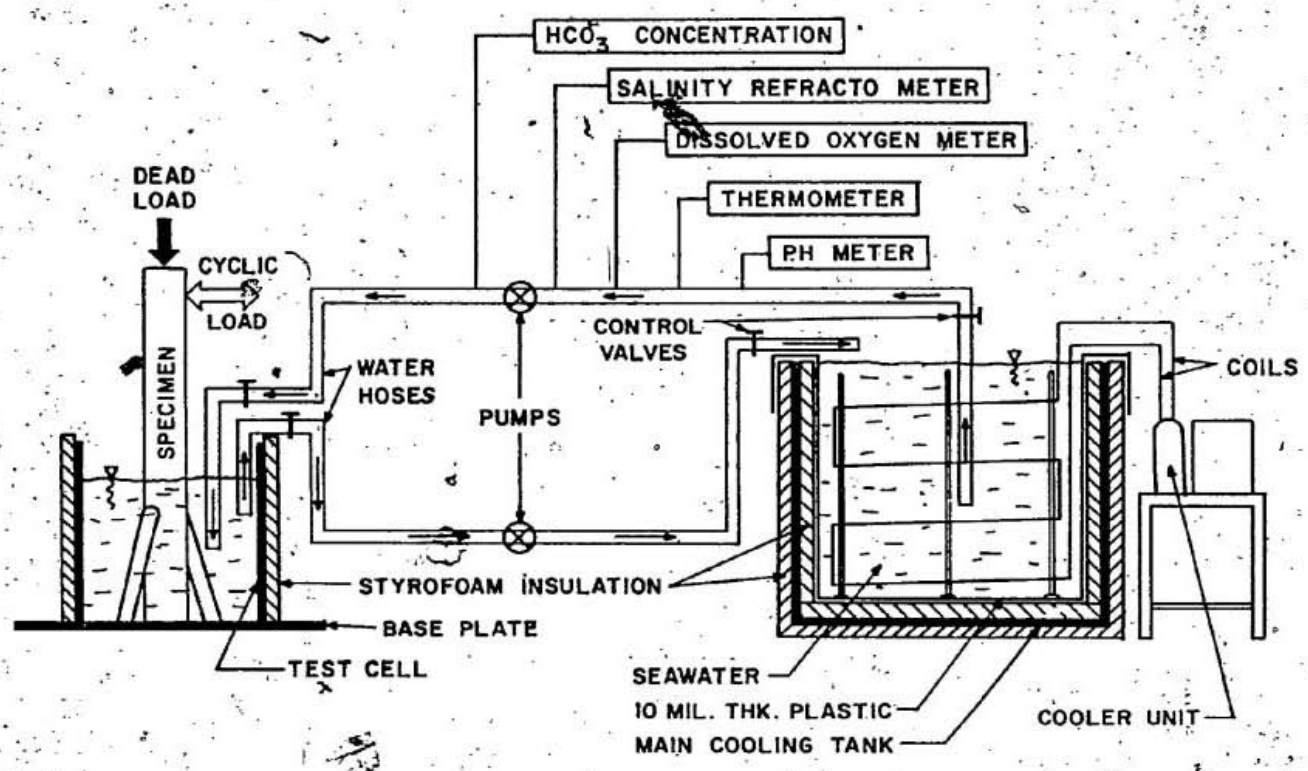

FIG. 37 SCHEMATIC OF SEAWATER COOLING AND CIRCULATION SYSTEMS

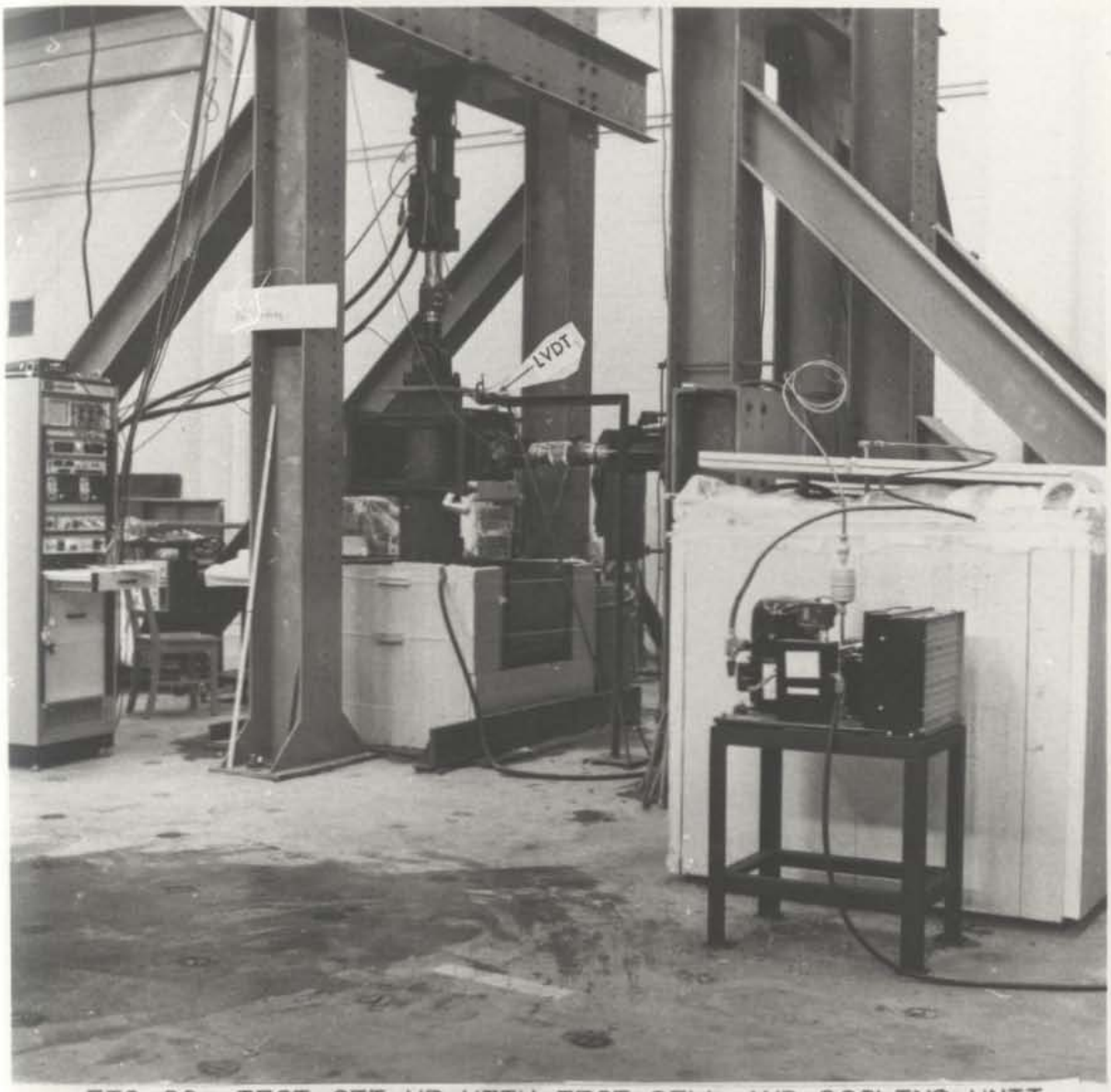

FIG.38 TEST SET-UP WITH TEST-CELL AND COOLING UNIT

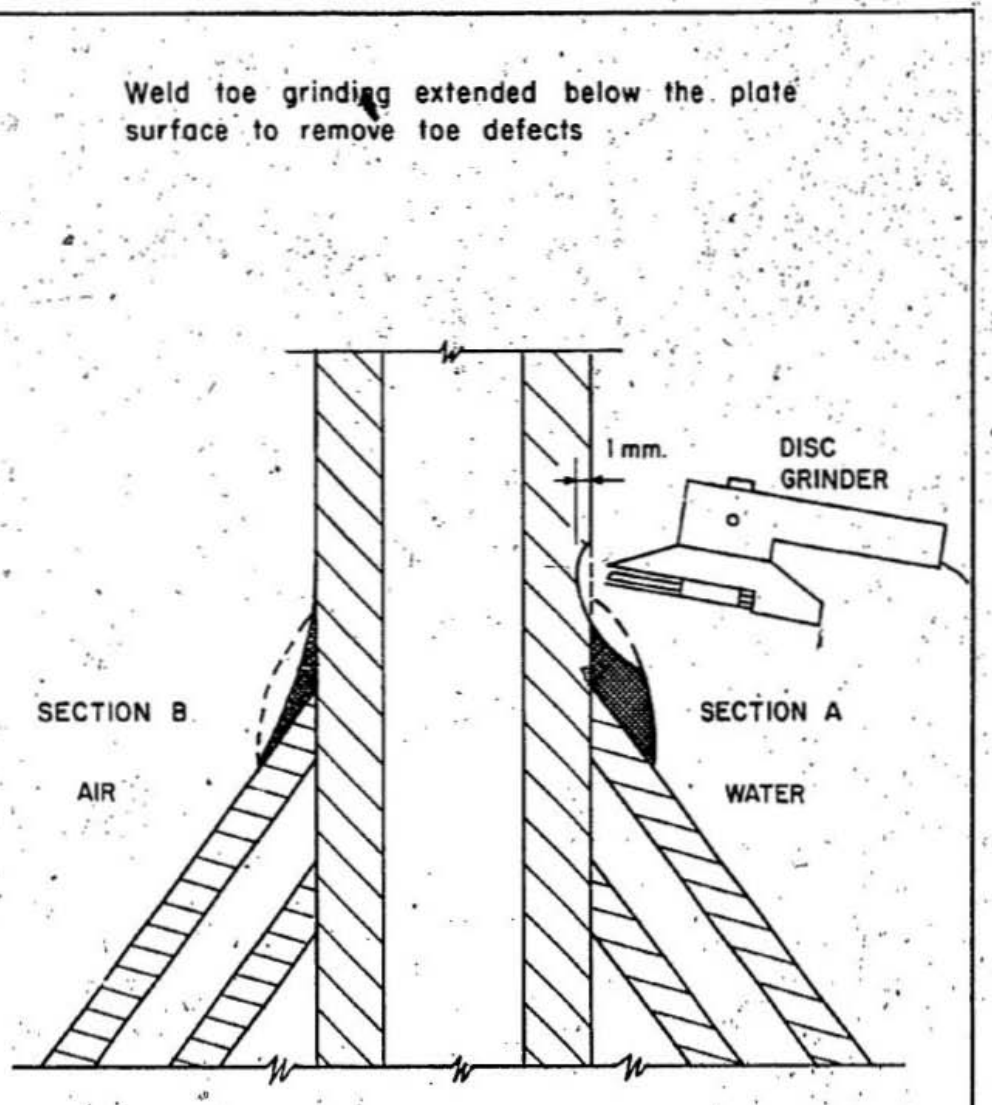

FIG.39 WELD TOE GRINDING PROFILE

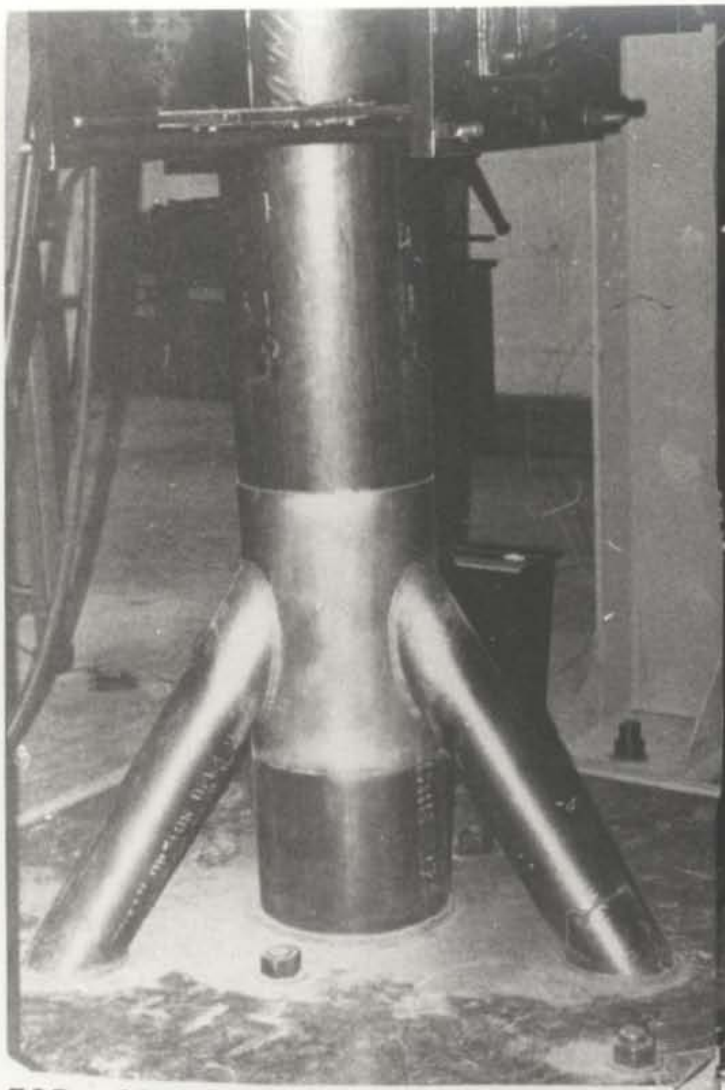

FIG. 40 BRITTLE LACQUER COATING FOR JOINT INTERSECTION

FIG. 41 BRITTLE LACQUER COATING FOR STIFFENED JOINT

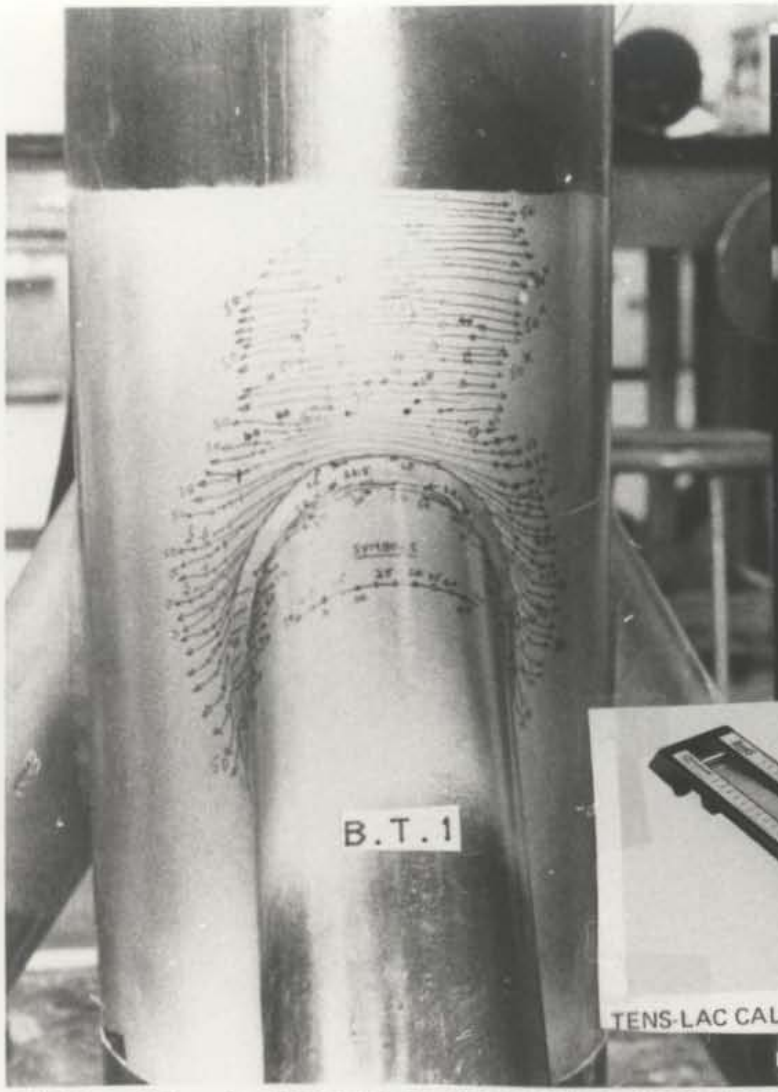

FIG. 42 a) BRITTLE COATING CRACKS DUE TO TENSILE LOAD

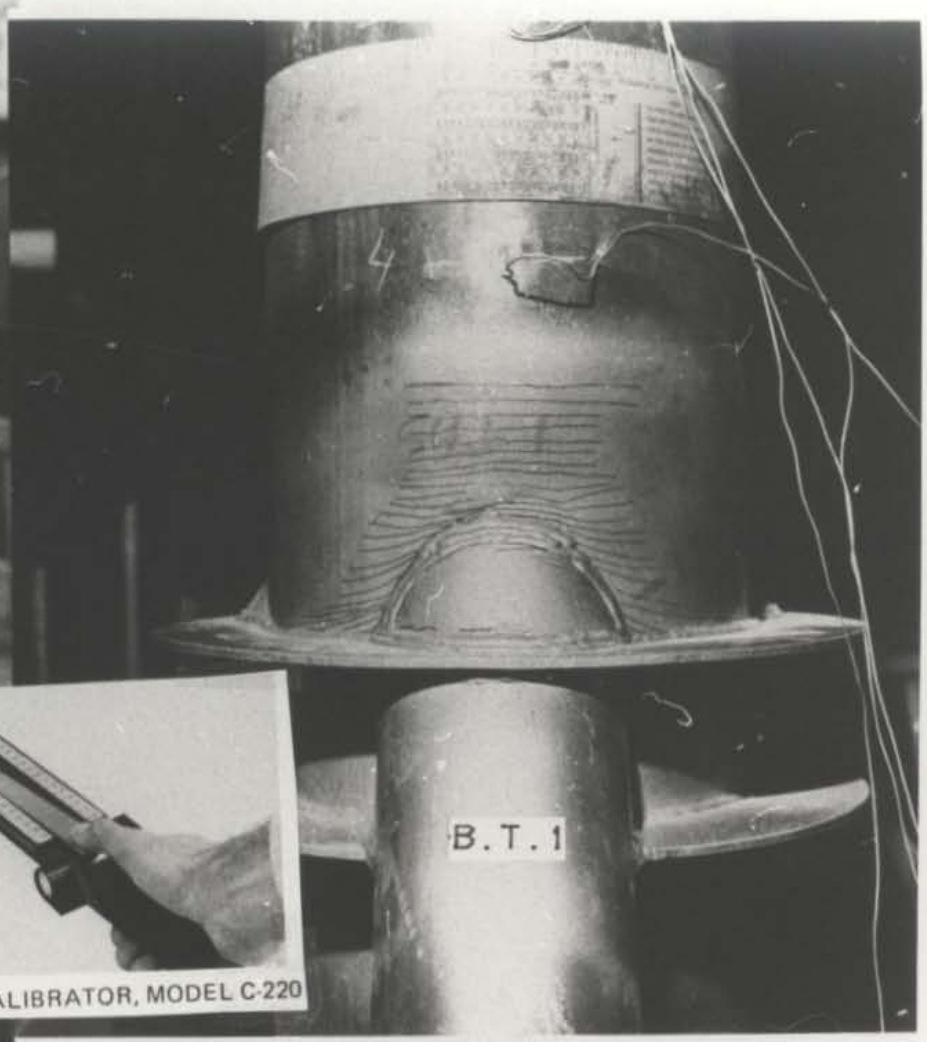

FIG. 42 b) BRITTLE COATING CRACKS DUE TO TENSILE LOAD

FIG. 43 a) BRITTLE COATING CRACKS DUE TO COMPRESSIVE LOAD (CRITICAL REGION - BRANCH TUBE 1)

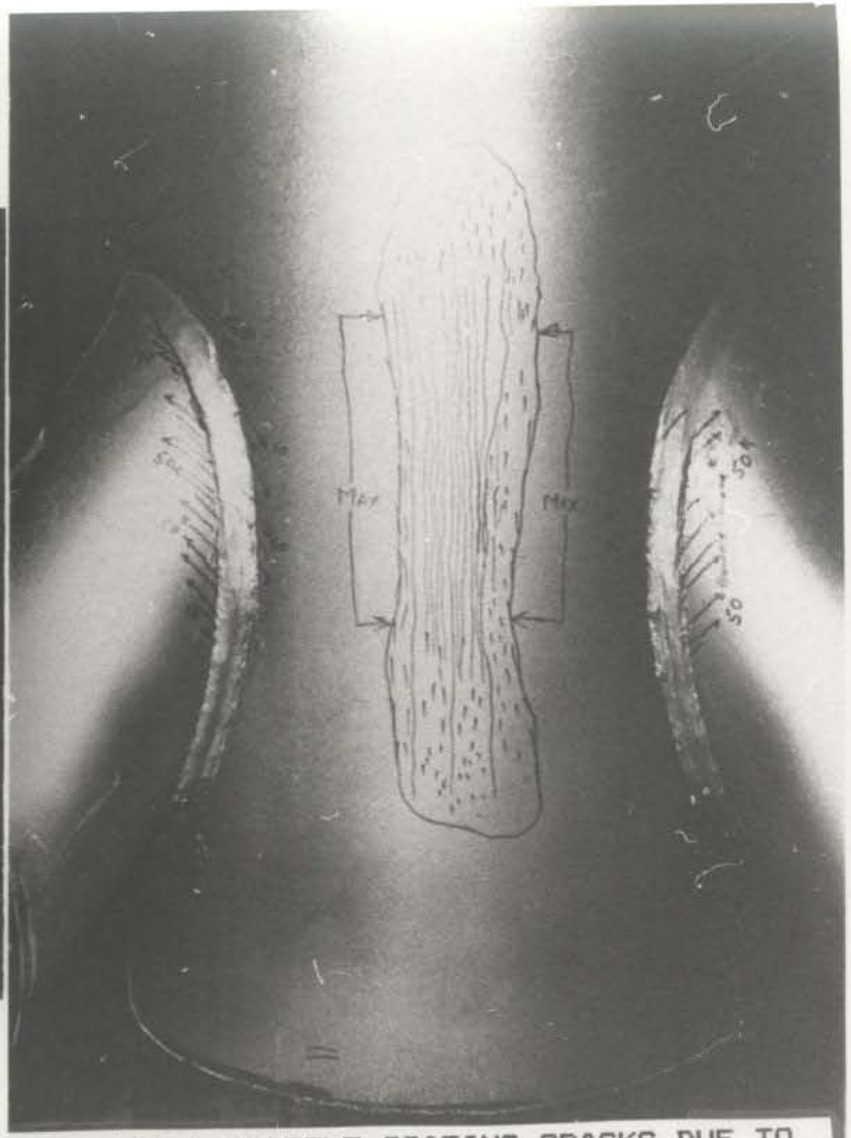

FIG. 43 b) BRITTLE COATING CRACKS DUE TO COMPRESSIVE LOAD (BRANCH TUBES 2 & 3)

FIG. 44 a) BRITTLE COATING CRACKS DUE TO TENSILE LOAD (BTRANCH TUBES 2 & 3)

FIG. 44 b) BRITTLE COATING CRACKS DUE TO TENSILE LOAD (BRANCH TUBE 2)

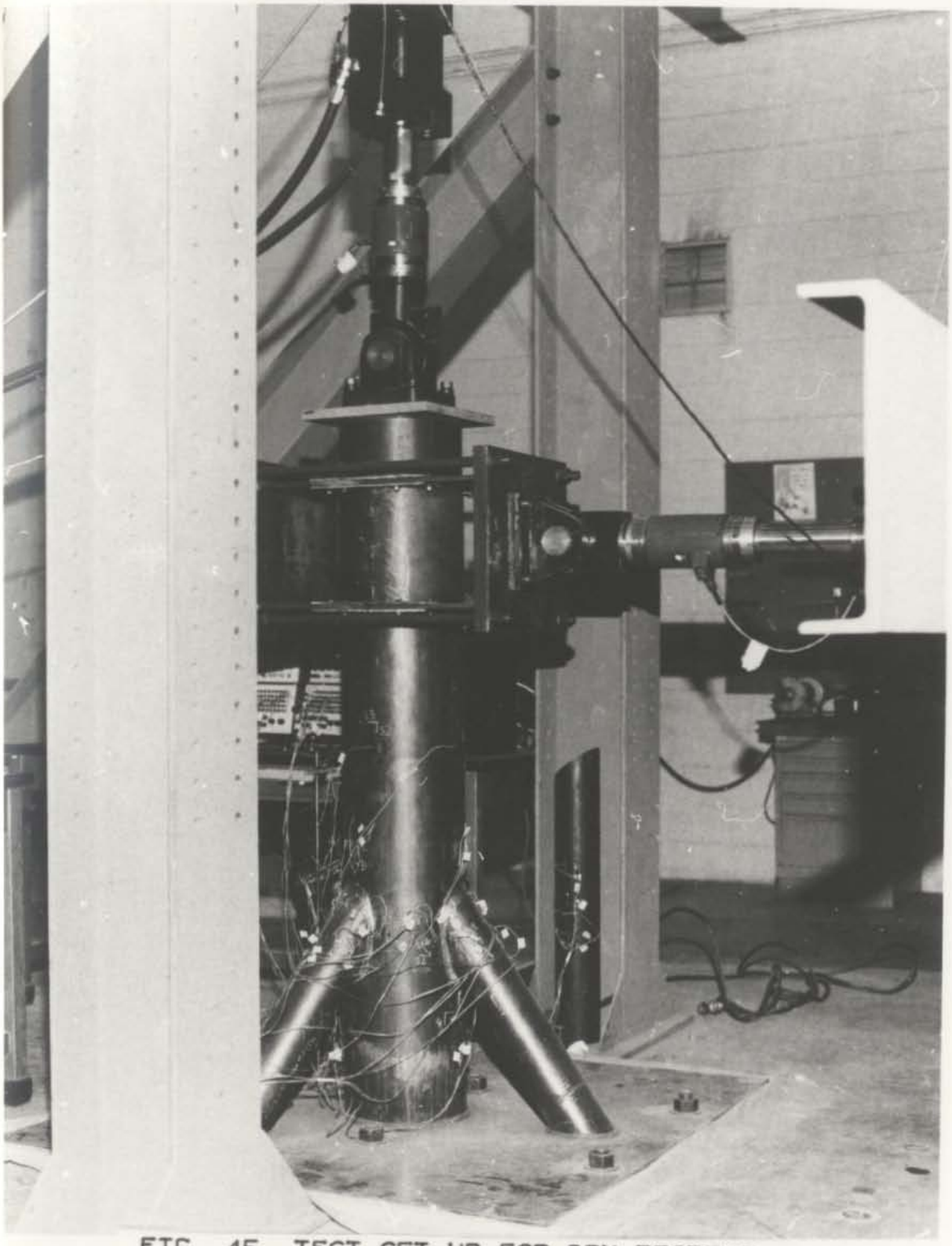

FIG. 45 TEST SET-UP FOR DRY TESTING

Protective Coatings for Strain Gage Applications.

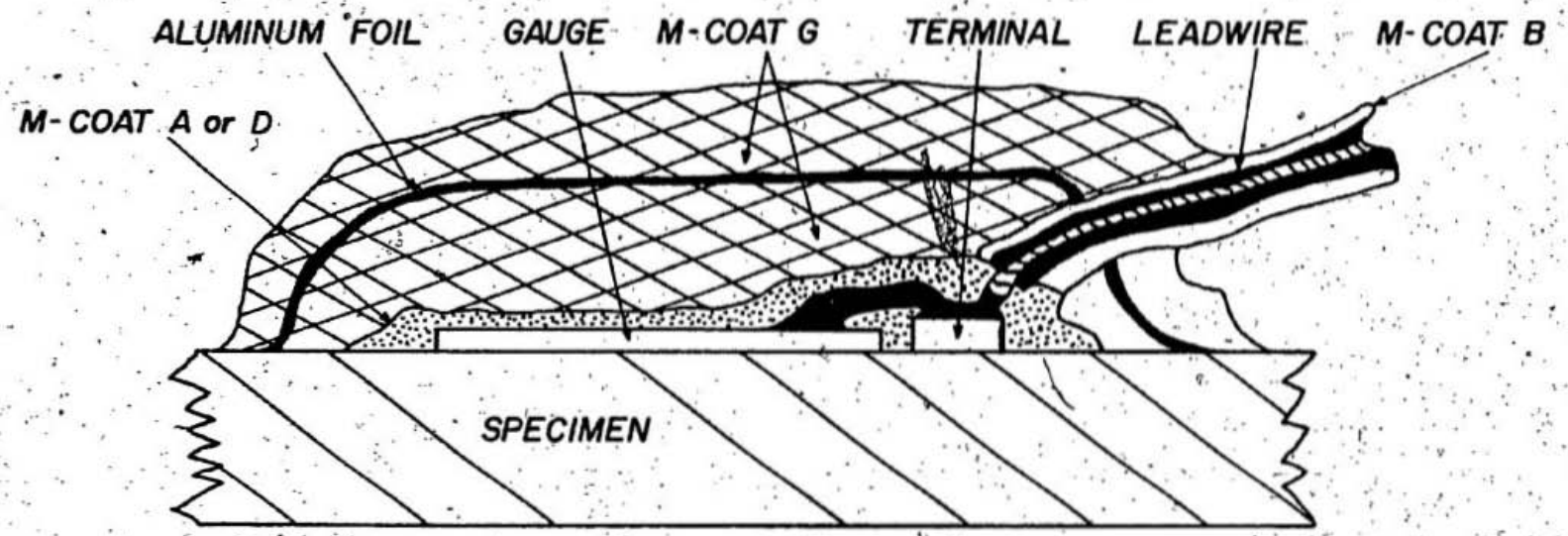

FIG. 46 CROSS-SECTIONAL VIEW OF PROTECTIVE COATINGS FOR STRAIN GAUGE INSTALLATIONS IN WATER

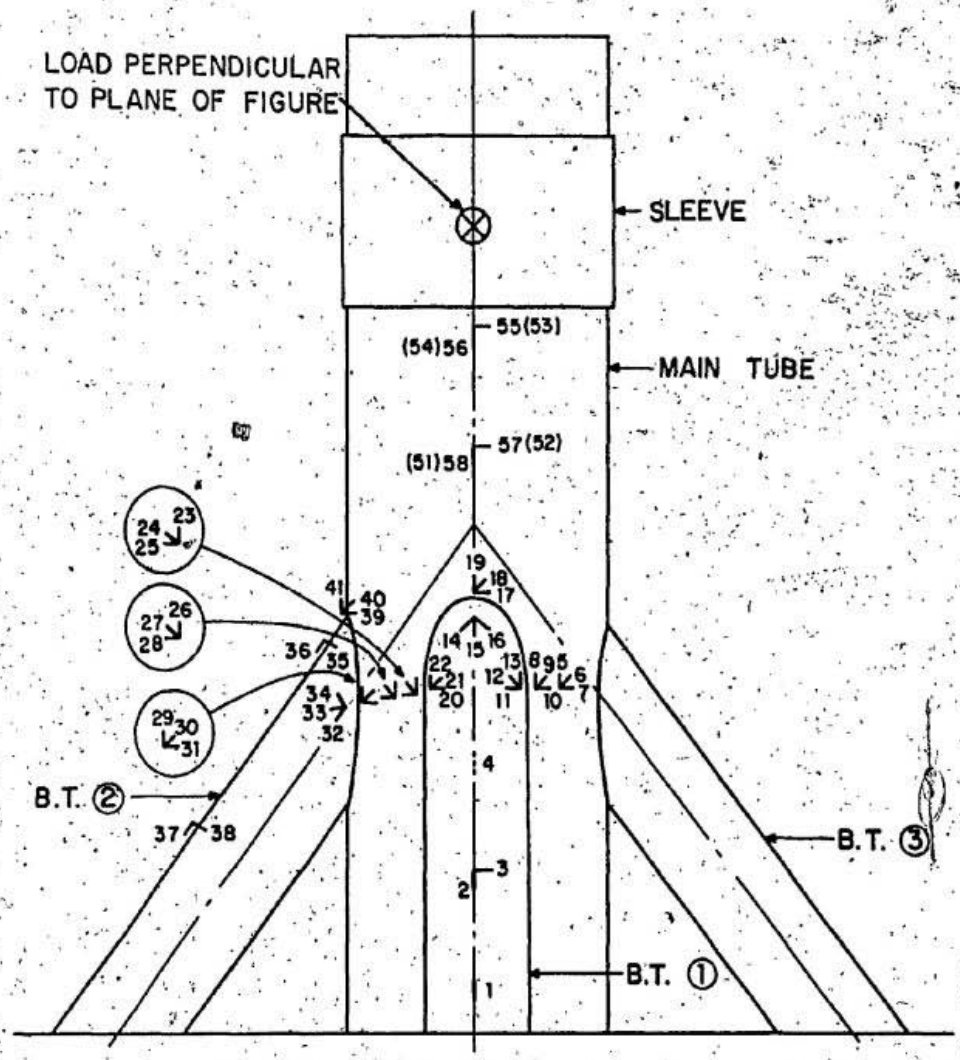

GAUGE NO. 4 ON MAIN TUBE
GAUGE NOS. 42 TO 54 ON REVERSE SIDE

FIG. 47 STRAIN GAUGE LOCATIONS FOR JOINT - DRY

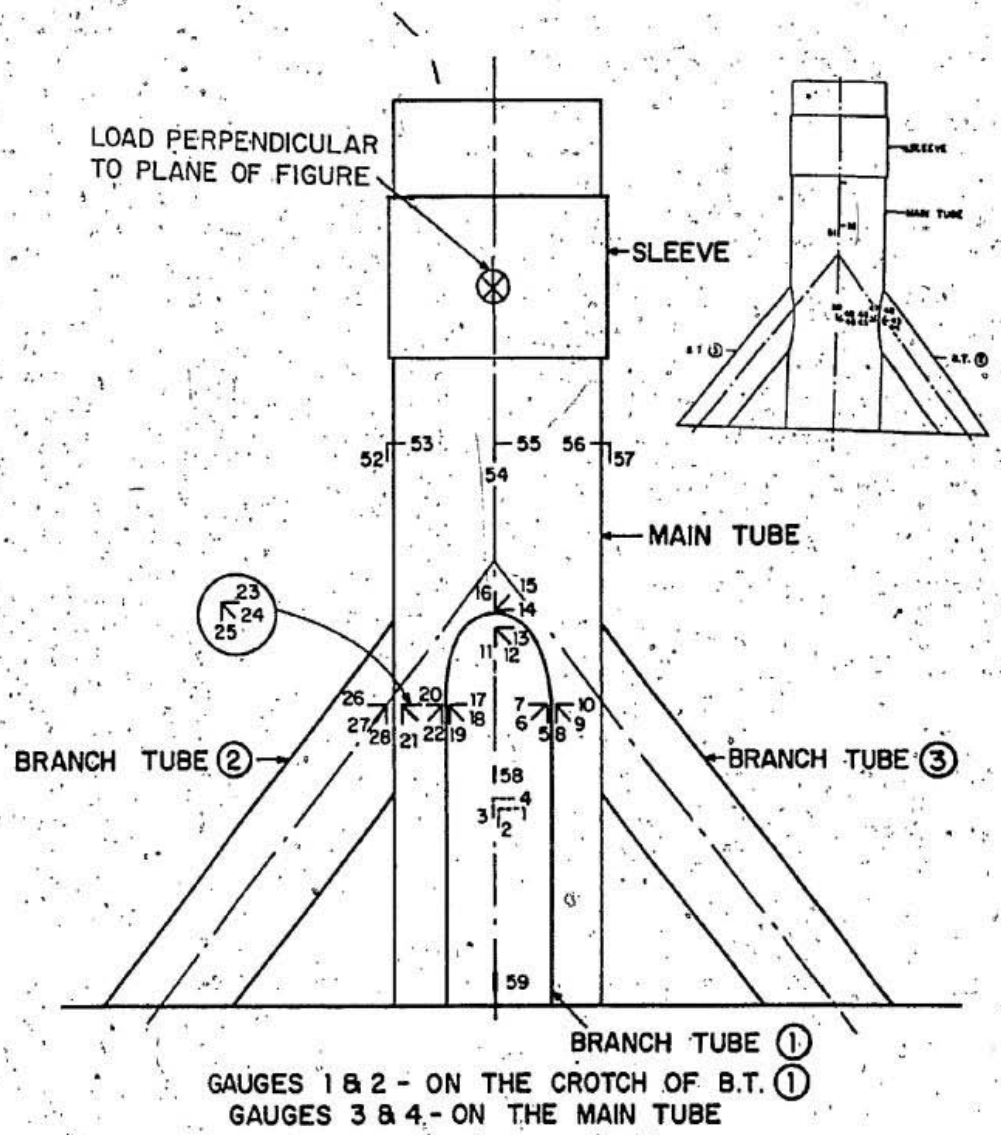

FIG. 48 STRAIN GAUGE LOCATIONS FOR JOINT - DRY 2

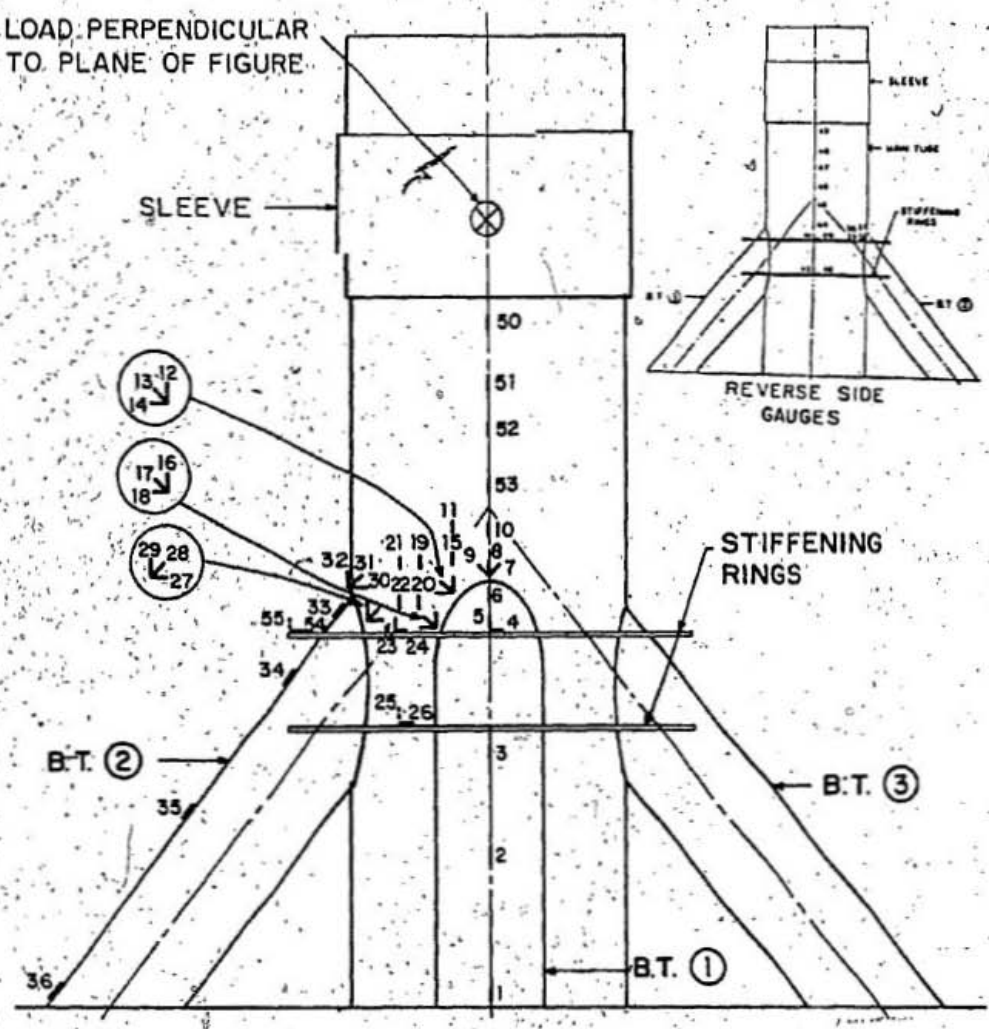

FIG. 49 STRAIN GAUGE LOCATIONS FOR JOINT - DRY 3

(JOINT NO. 3- WITH RINGS)

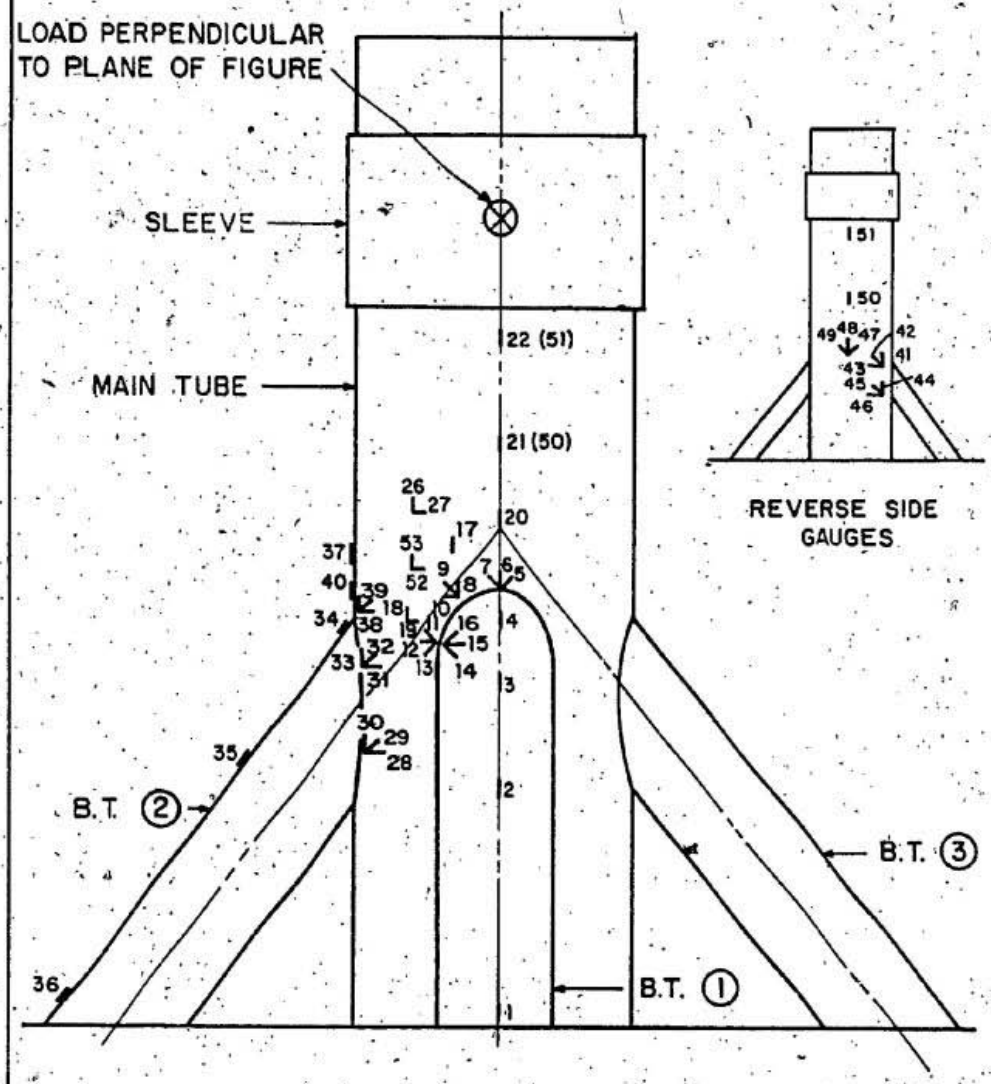

FIG.50 STRAIN GAUGE LOCATIONS FOR JOINT - CORR. 1

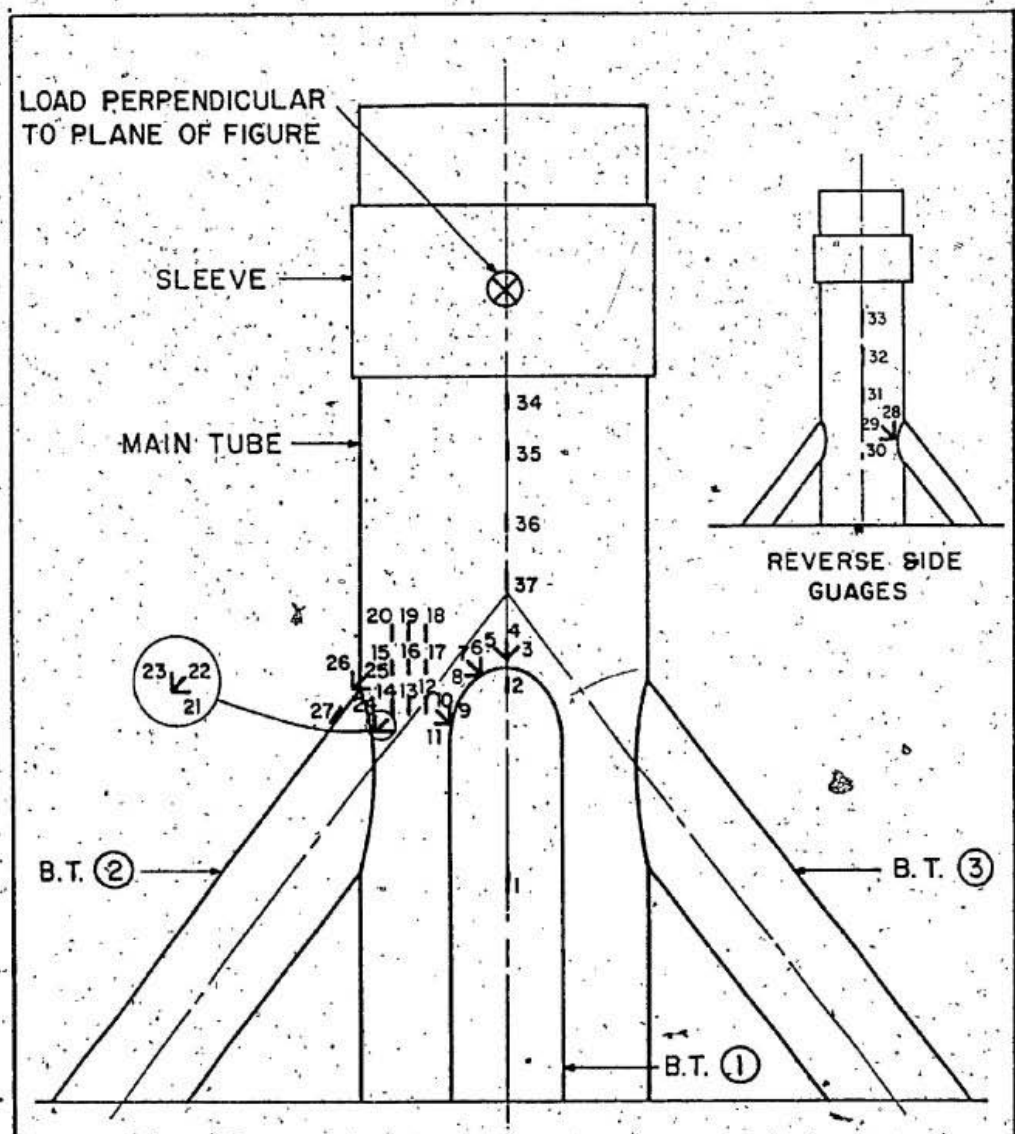

FIG. 51 STRAIN GAUGE LOCATIONS FOR JOINT - CORR. 2

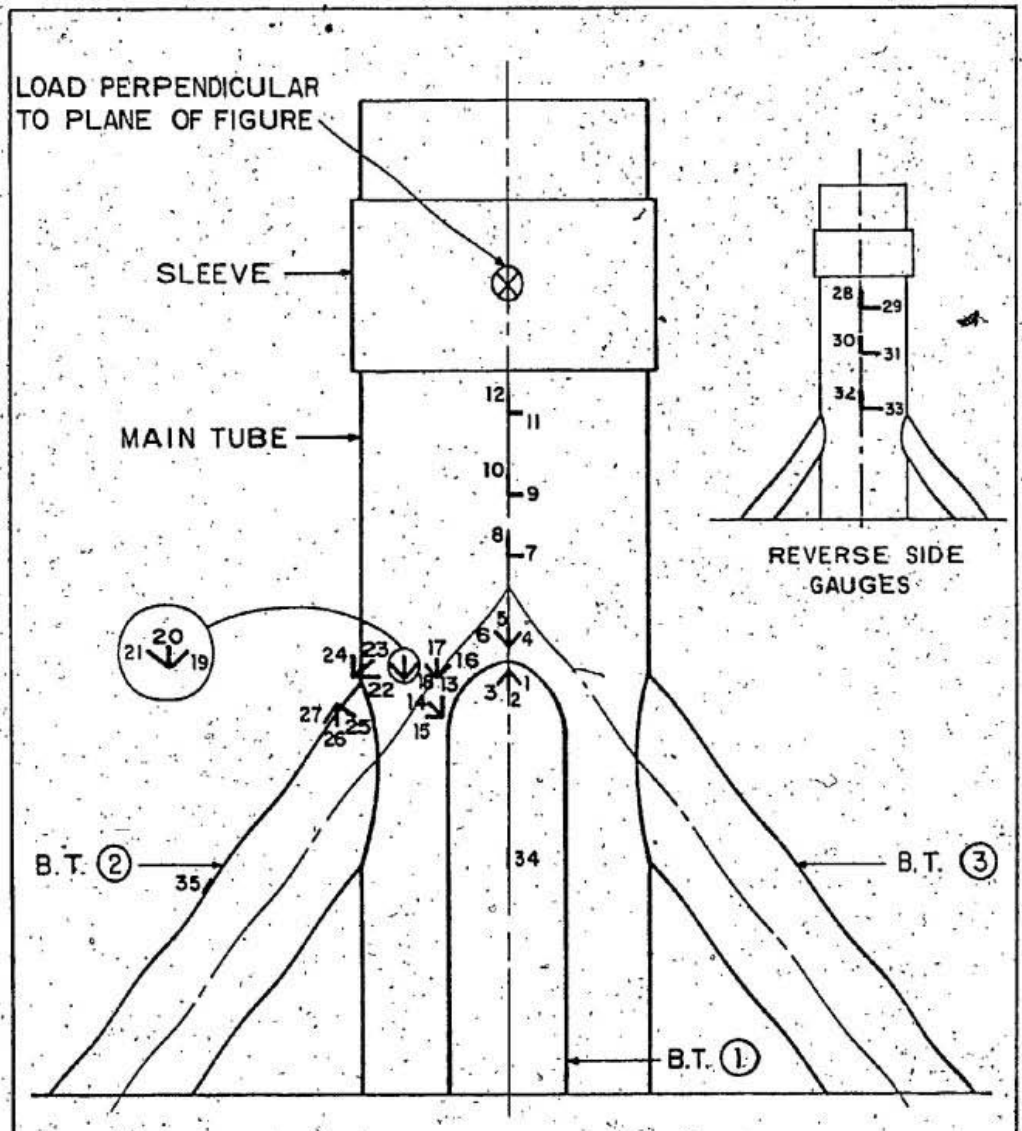

FIG. 52 STRAIN GAUGE LOCATIONS FOR JOINT - CORR. 3

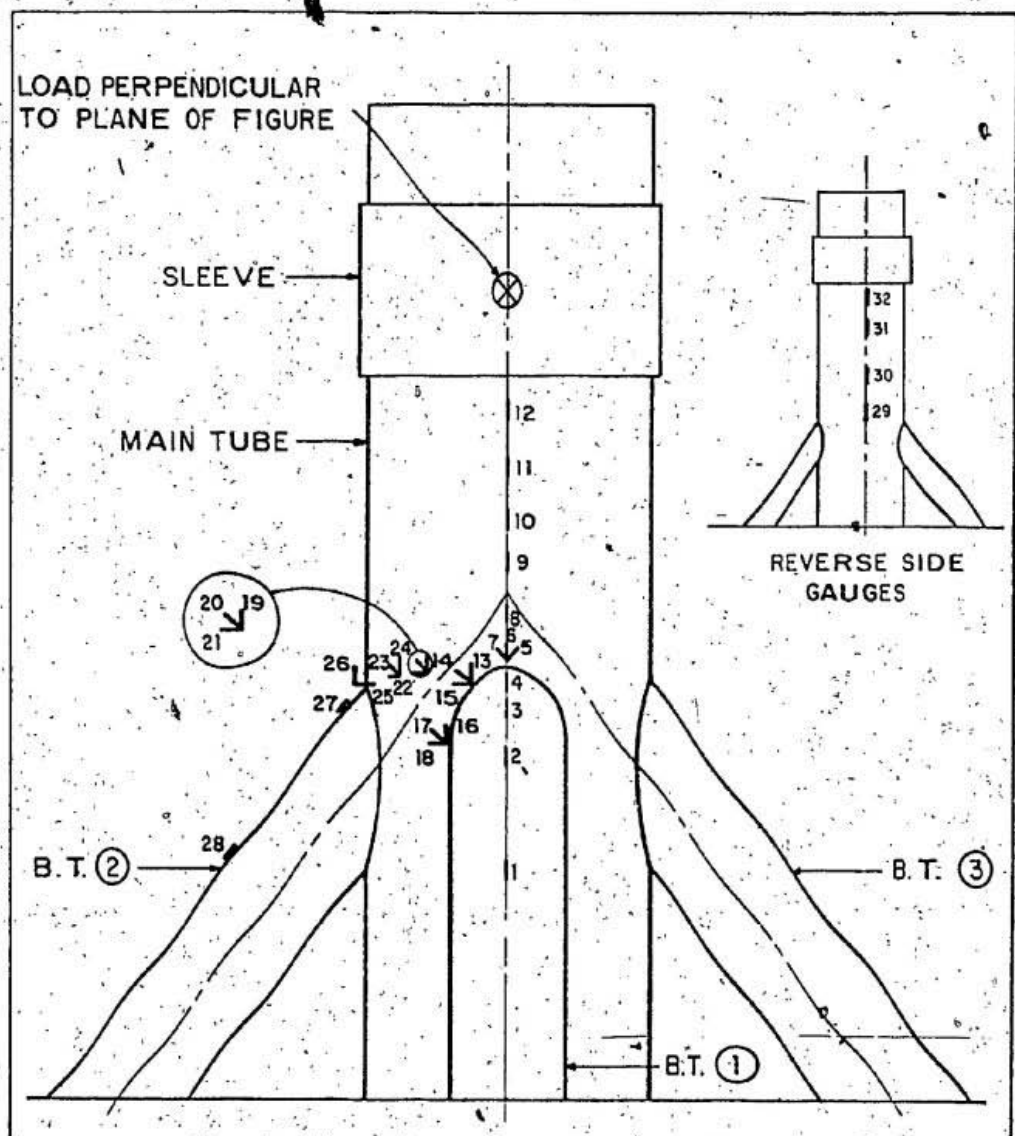

FIG 53 STRAIN GAUGE LOCATIONS FOR JOINT - CORR. 4

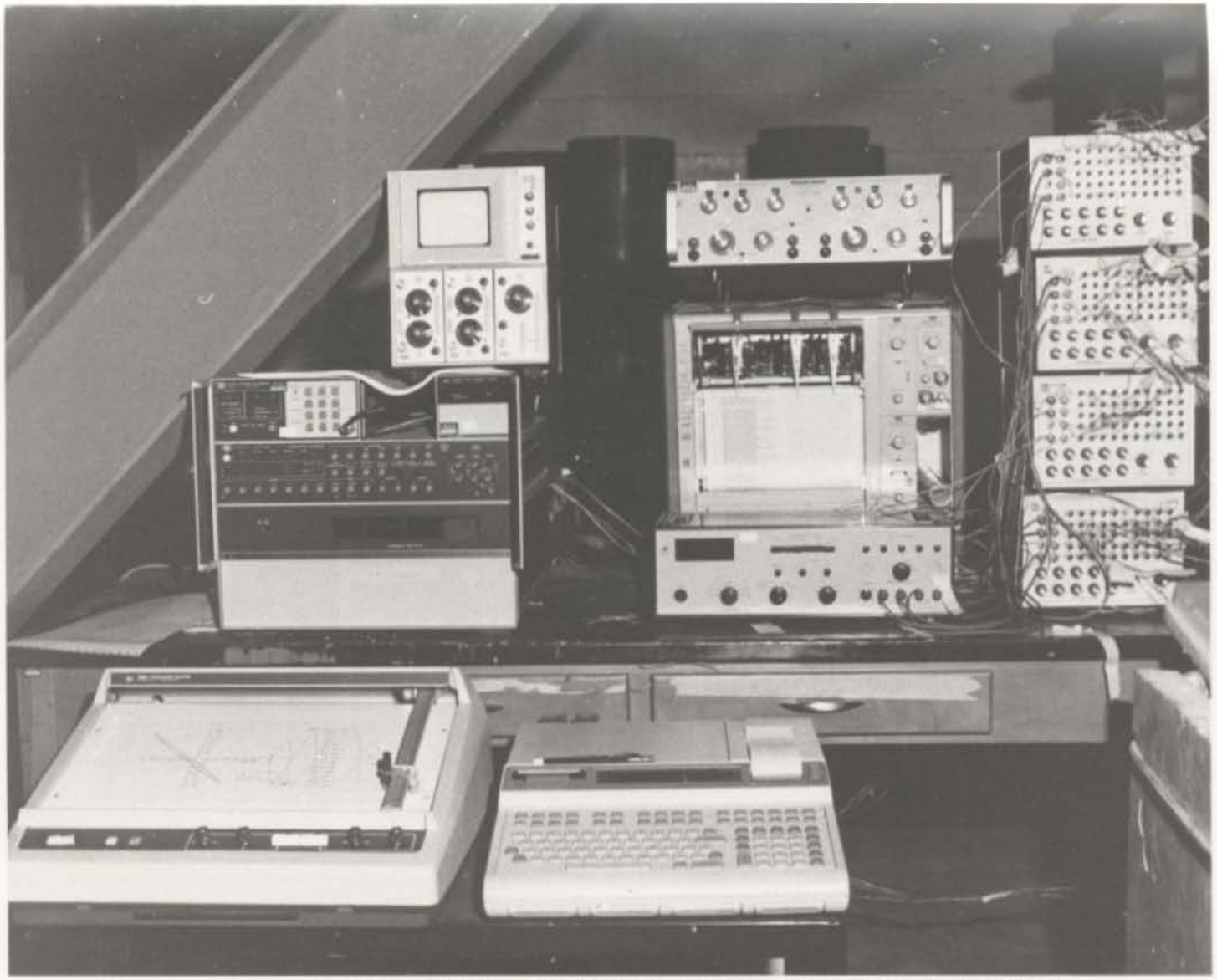

FIG.54 COMPUTER CONTROLLED AUTOMATIC DATA ACQUISITION SYSTEM

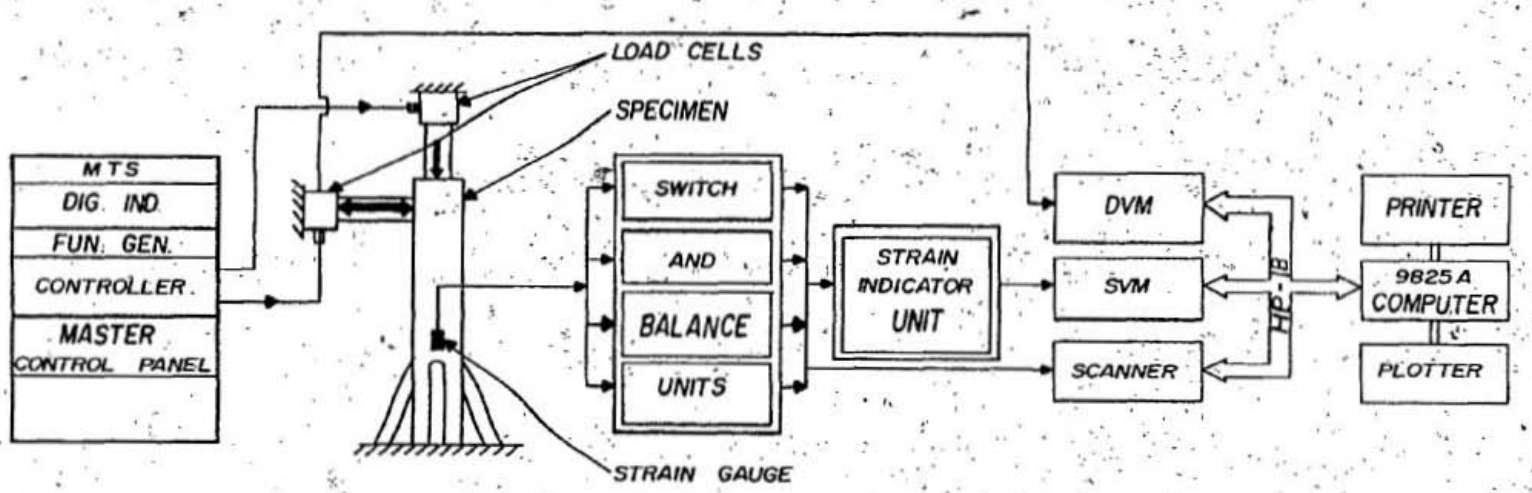

FIG. 55 BLOCK DIAGRAM OF DATA ACQUISITION SYSTEM

COMPACT TENSILE TEST COUPON

(ASTM STANDARD E-647-81)

ALL DIMENSIONS ARE IN MILLIMETRES

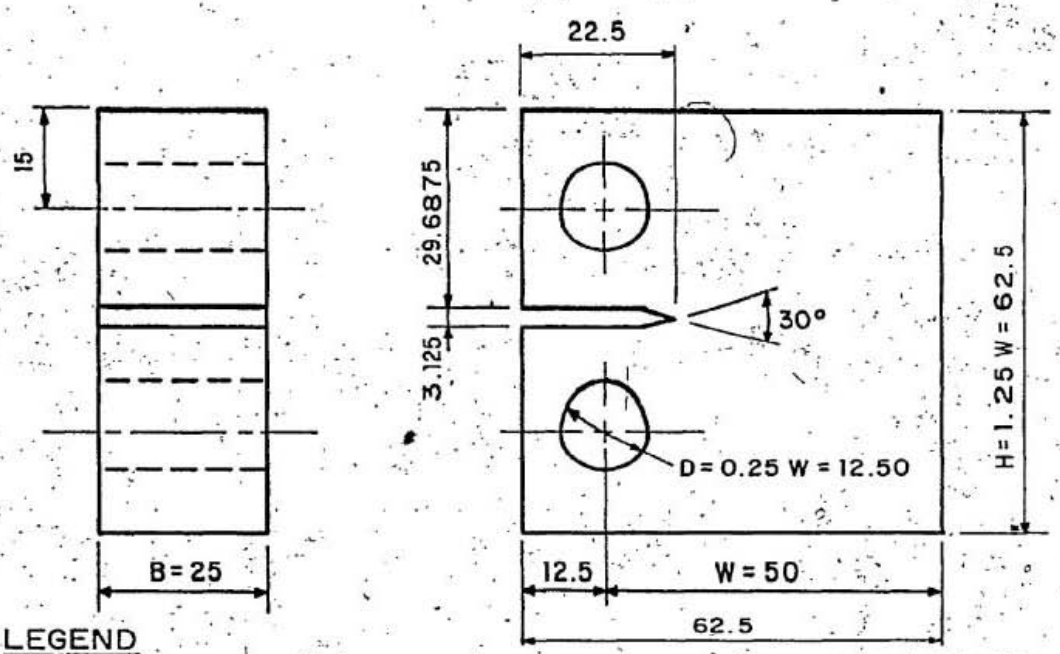

LEGEND

NET WIDTH = W = 50

THICKNESS $B = \frac{W}{2} = 25$

TOTAL WIDTH C = 1.25 W

HEIGHT H = 1.25 W

HOLE DIA. D = 0.25 W = 12.50

NOTCH WIDTH N = 0.065 W MAX.

EFFECTIVE NOTCH LENGTH M = 0.4 W

EFFECTIVE CRACK LENGTH a = 0.45 W

FIG. 56 a) STANDARD COMPACT TENSION SPECIMEN

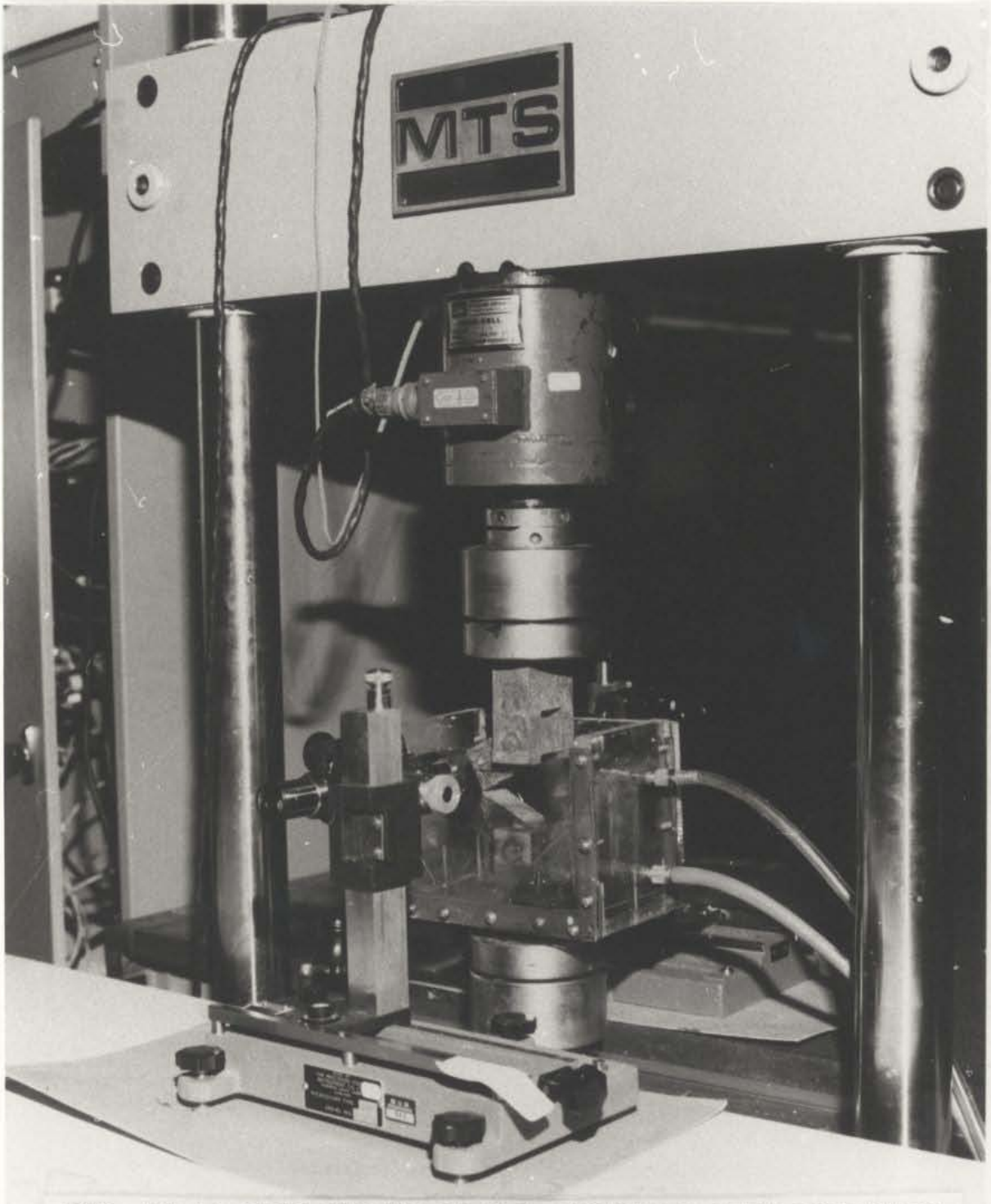

FIG. 56 b) TEST SET-UP OF C.T. SPECIMEN WITH CONTAINER

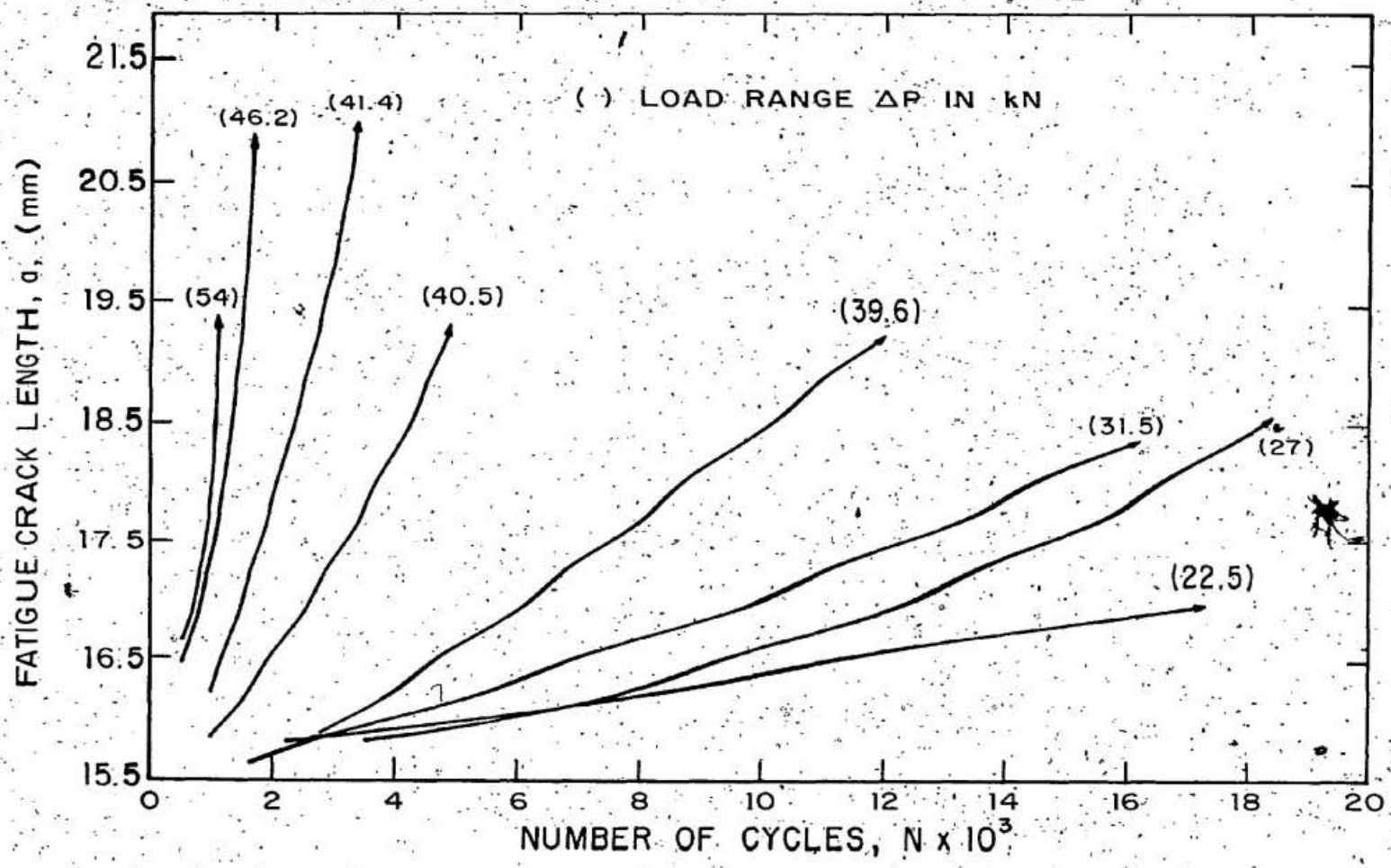

FIG. 56 CRACK GROWTH DATA OF COMPACT TENSION SPECIMENS

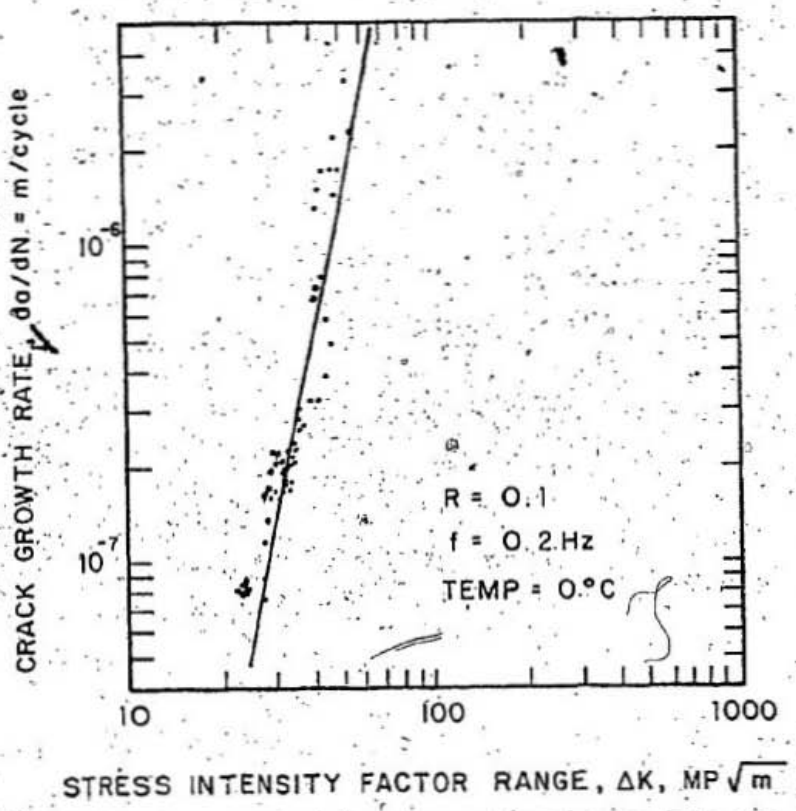

FIG. 57 SUMMARY OF FATIGUE CRACK GROWTH RATE DATA FOR A36 STEEL

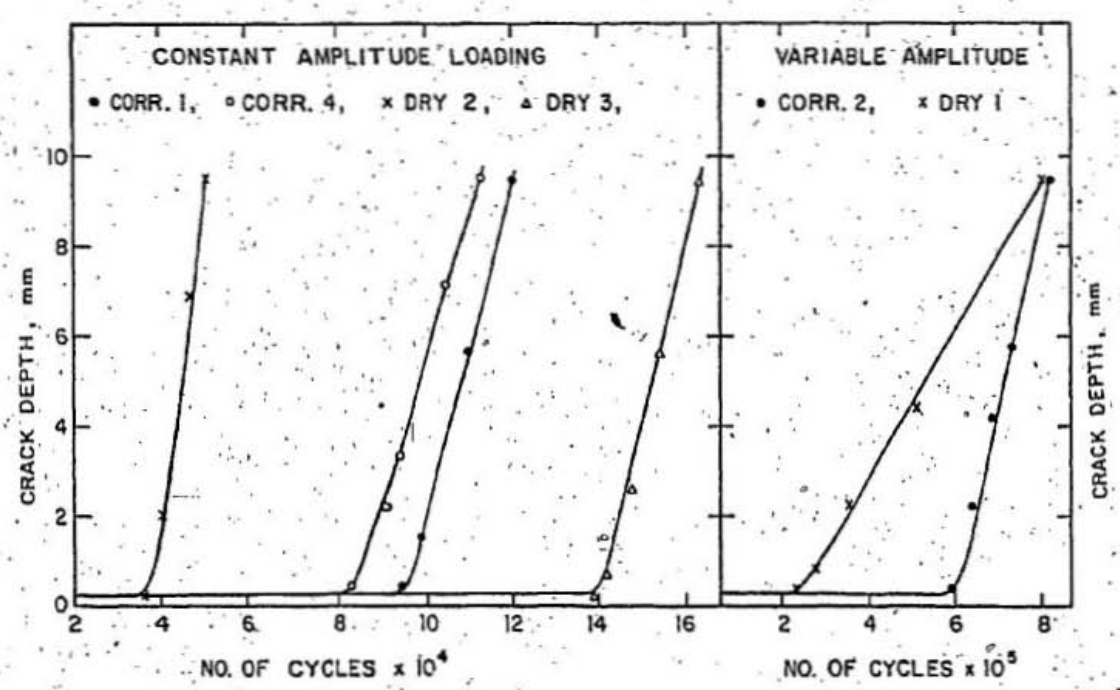

FIG. 58 FATIGUE CRACK GROWTH DATA FOR TUBULAR JOINTS

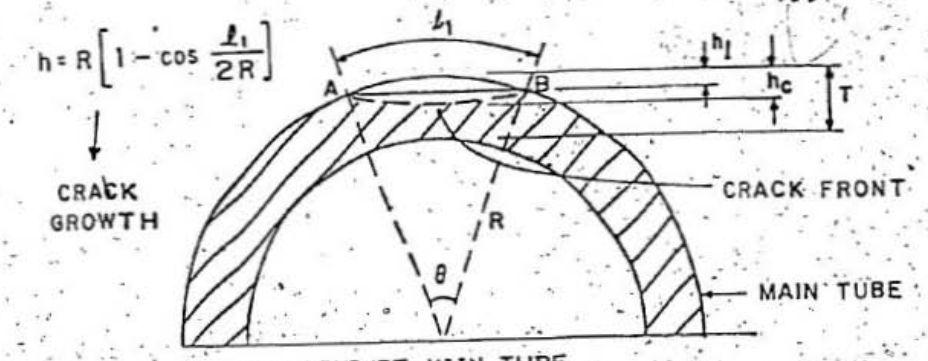

R = RADIUS OF MAIN TUBE
l1 = LENGTH OF CRACK AT N1 CYCLES
h1 = HEIGHT OF CHORD AB FOR LENGTH L1
h_c = HEIGHT OF CRACK FRONT AT N1 CYCLES ($h_c = 2h_1$)
T = THICKNESS OF MAIN TUBE

FIG. 59 ASSUMED GEOMETRY OF BOWED CRACK IN TUBULAR JOINTS

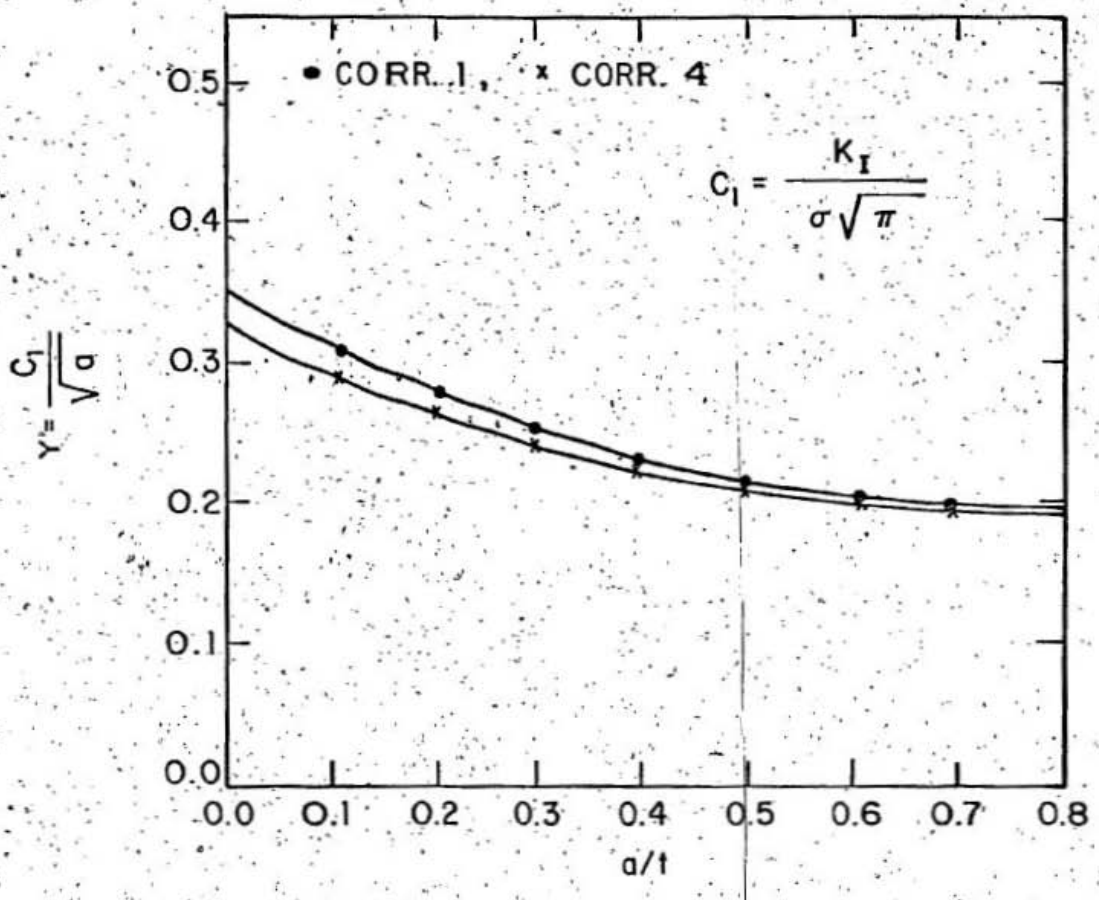

FIG. 60 VARIATION OF CORRECTION FACTOR Y WITH CRACK DEPTH FOR TUBULAR JOINTS.

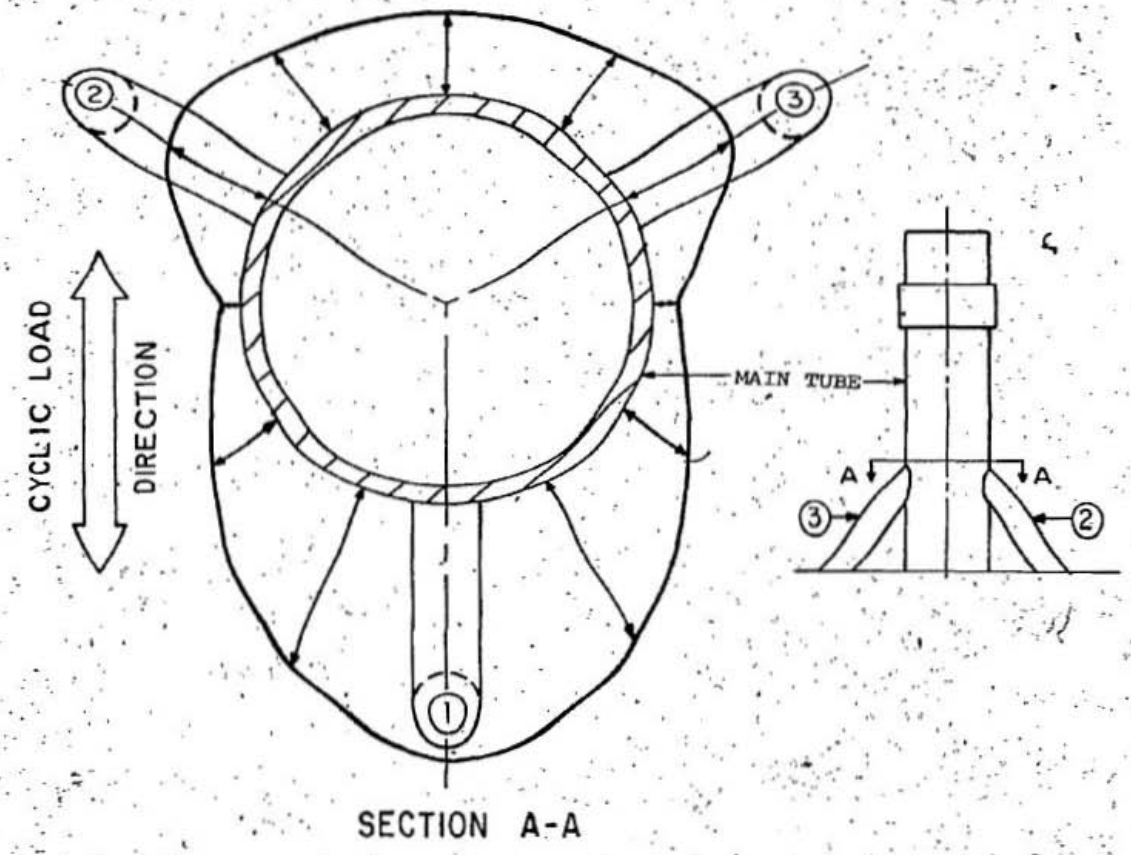

FIG. 61 SCHEMATIC OF CIRCUMFERENTIAL STRESS DISTRIBUTION ABOVE JOINT INTERSECTION

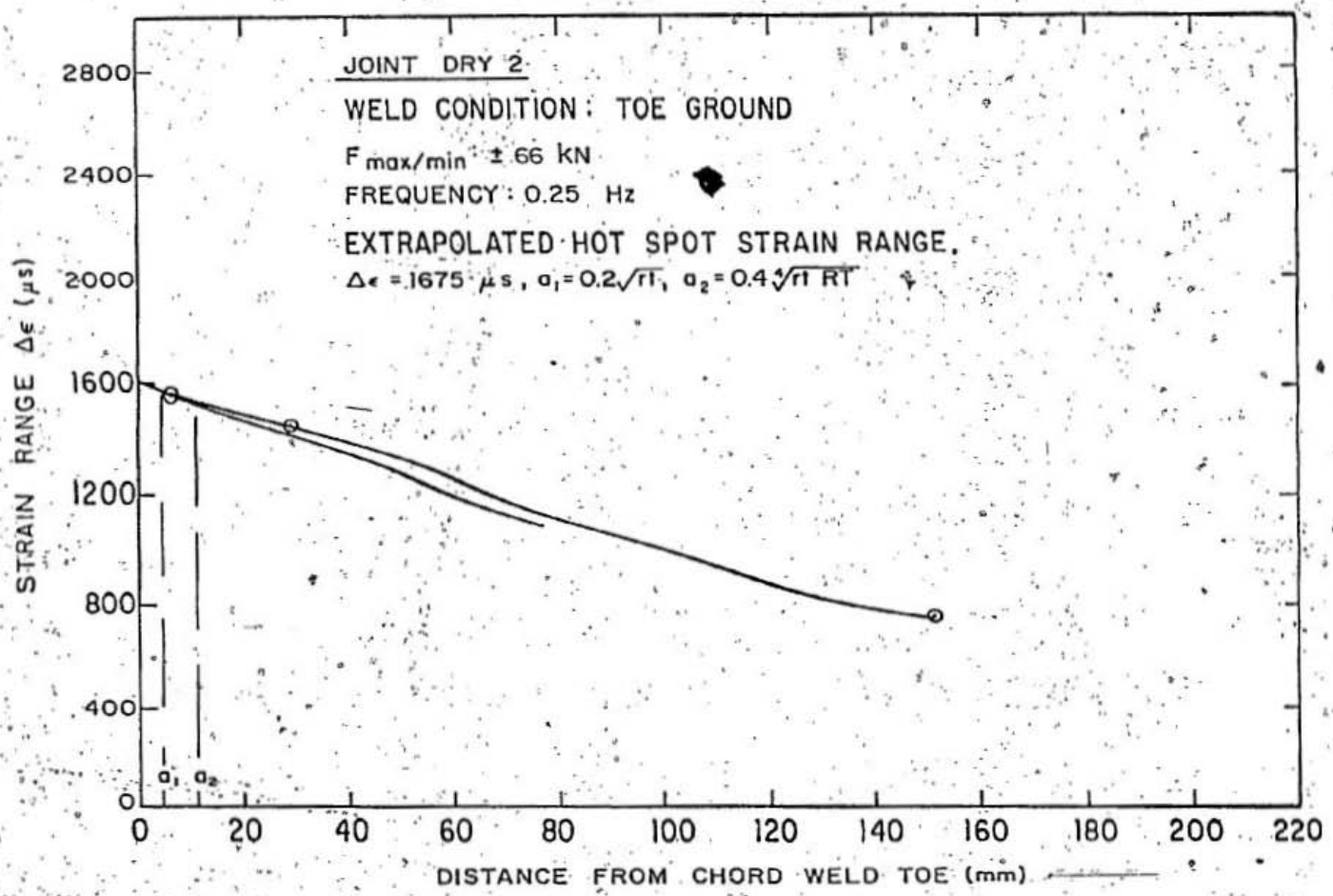

FIG. 62 a) STRAIN DISTRIBUTION NEAR WELD TOE: JOINT - DRY 2

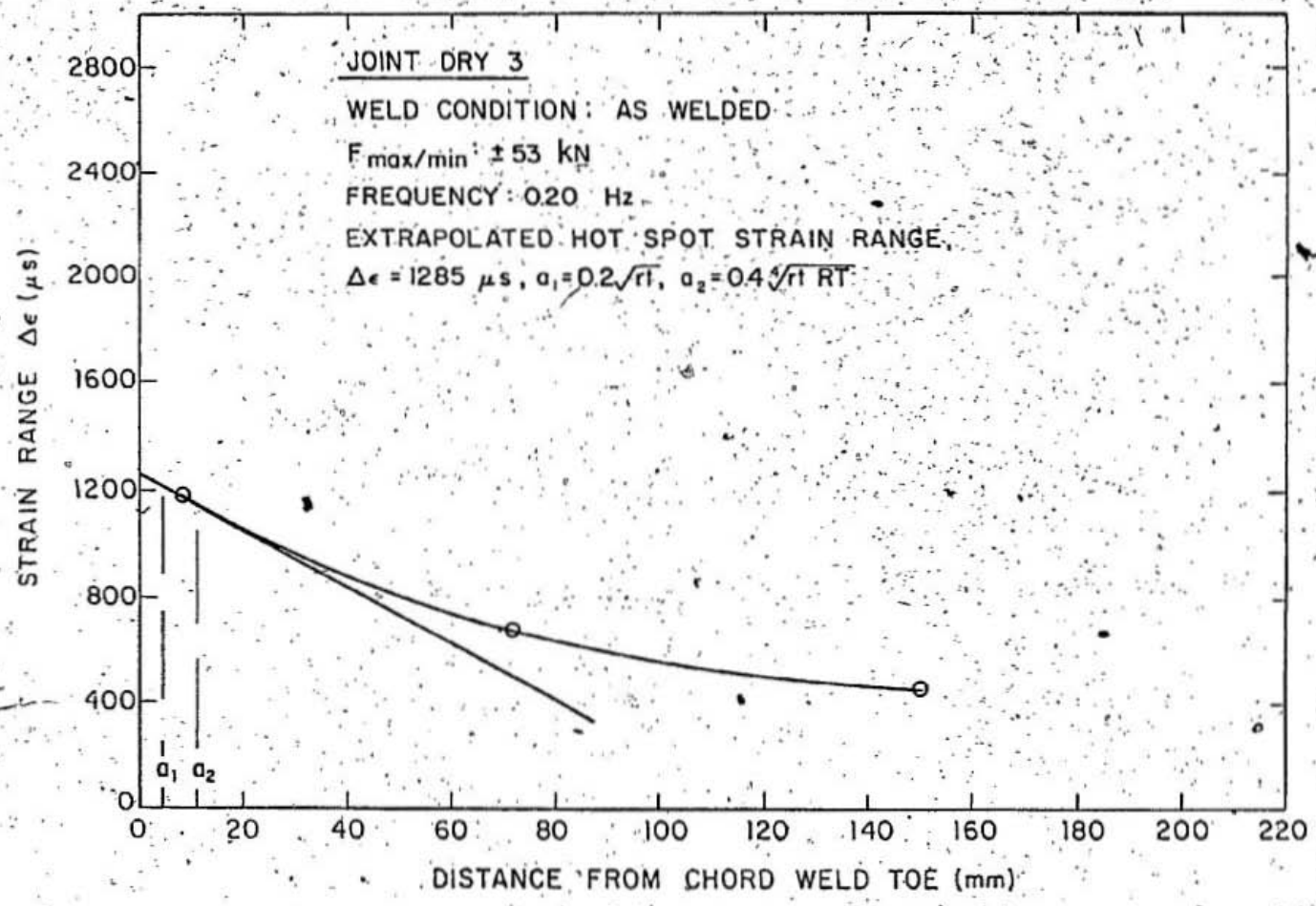

FIG. 62 b) STRAIN DISTRIBUTION NEAR WELD TOE: JOINT – DRY 3

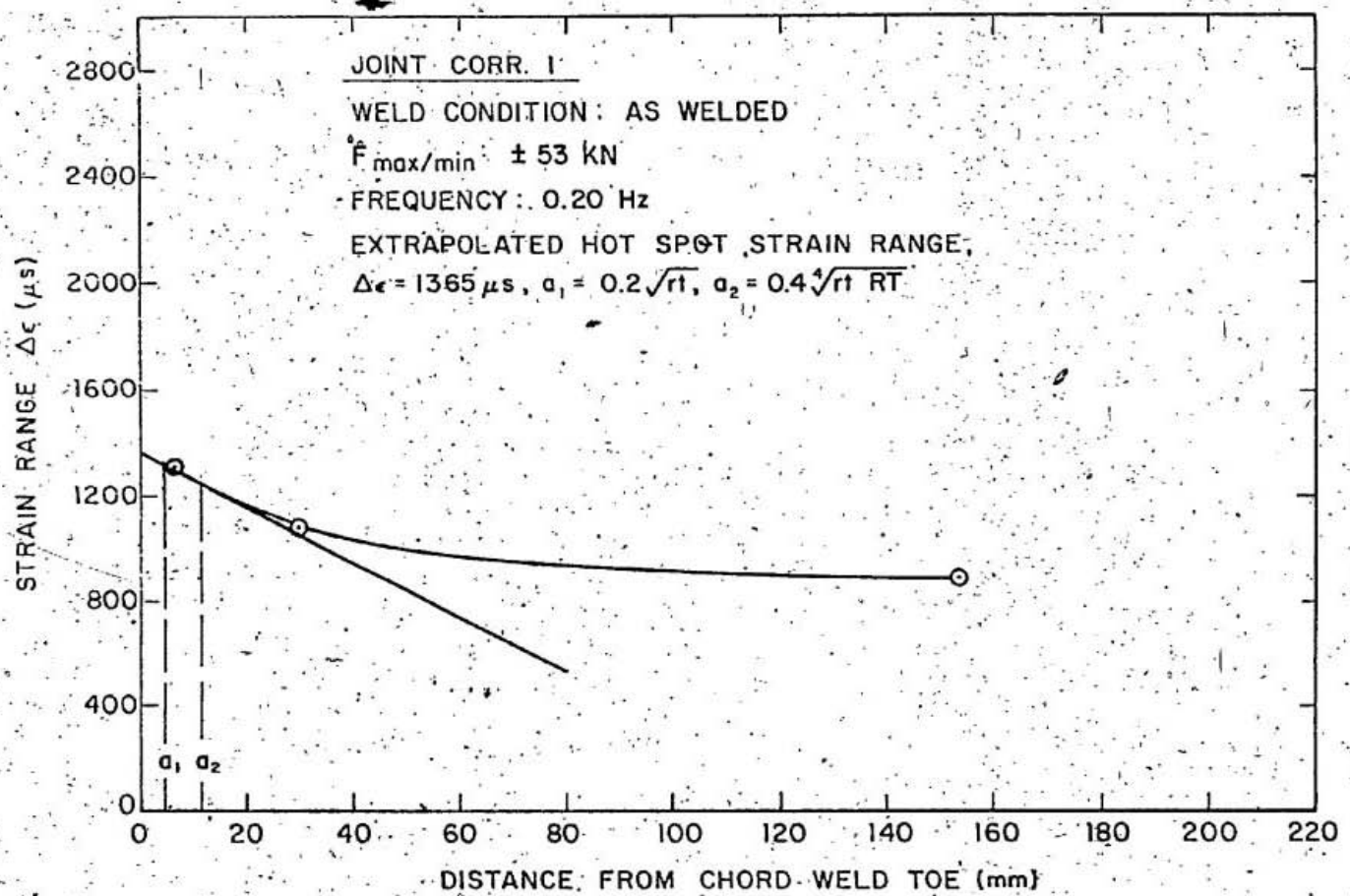

FIG; 62 a) STRAIN DISTRIBUTION NEAR WELD TOE: JOINT — CORR. 1

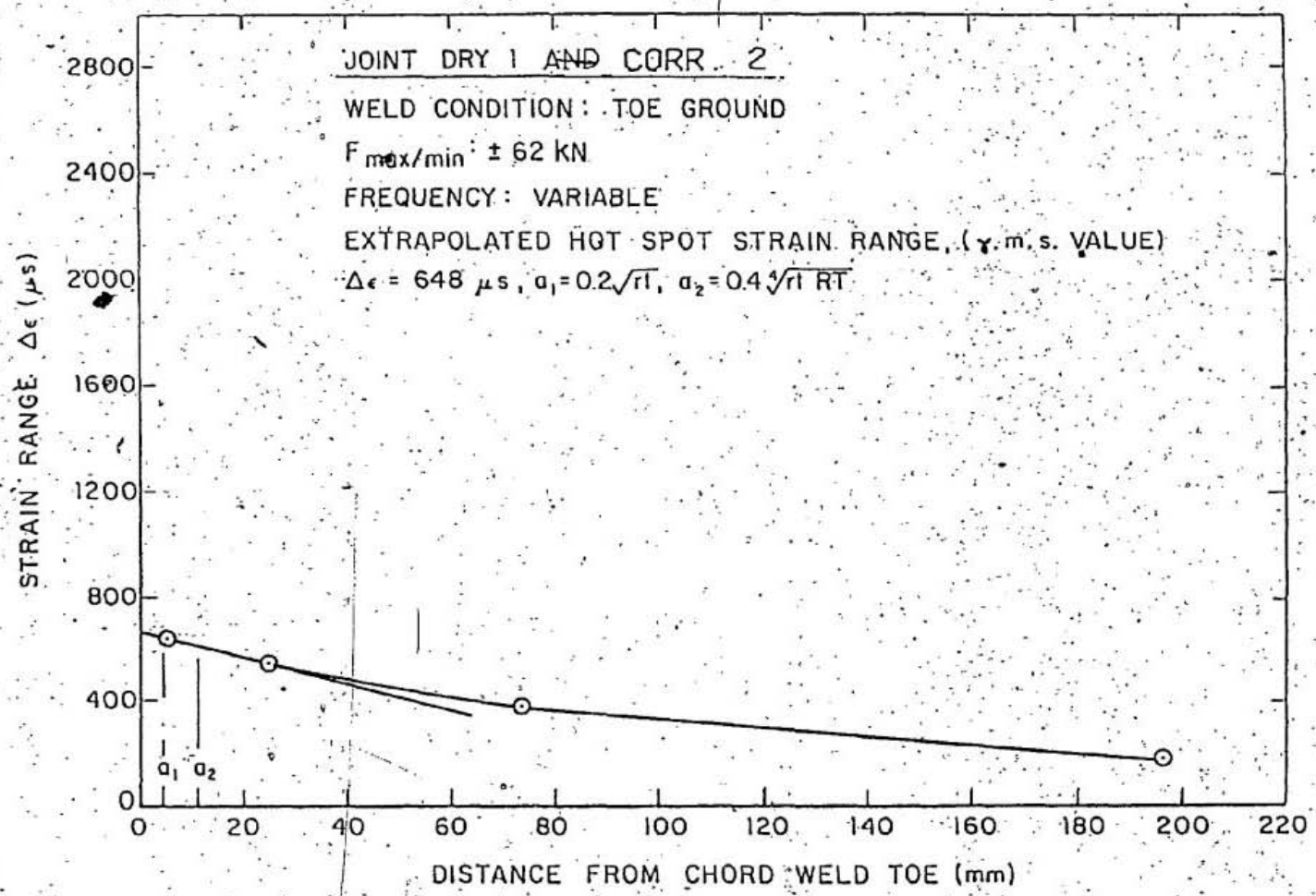

FIG. 62 d) STRAIN DISTRIBUTION NEAR WELD TOE: JOINT – CORR. 2 & DRY 1

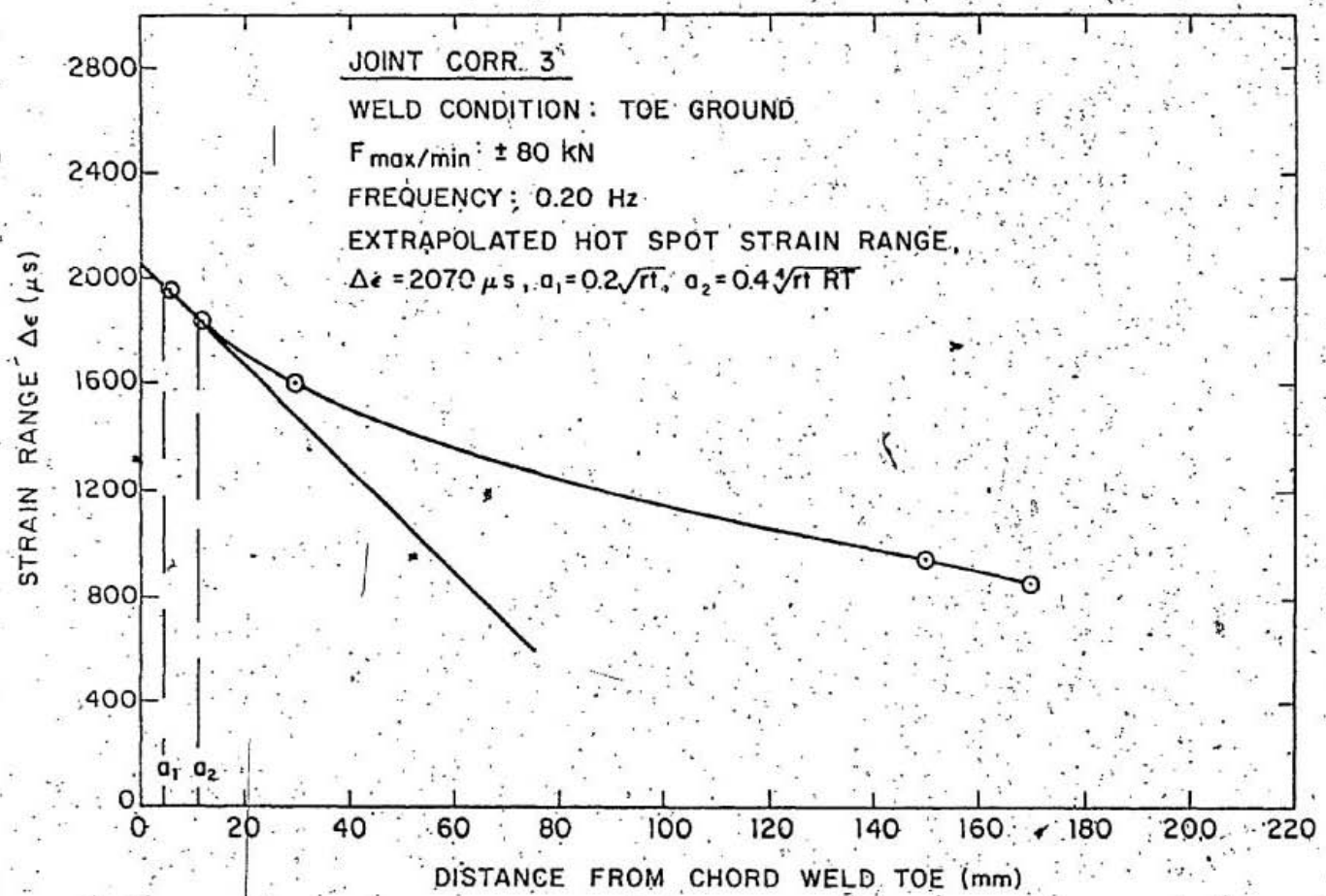

FIG. 62 e) STRAIN DISTRIBUTION NEAR WELD TOE: JOINT – CORR. 3

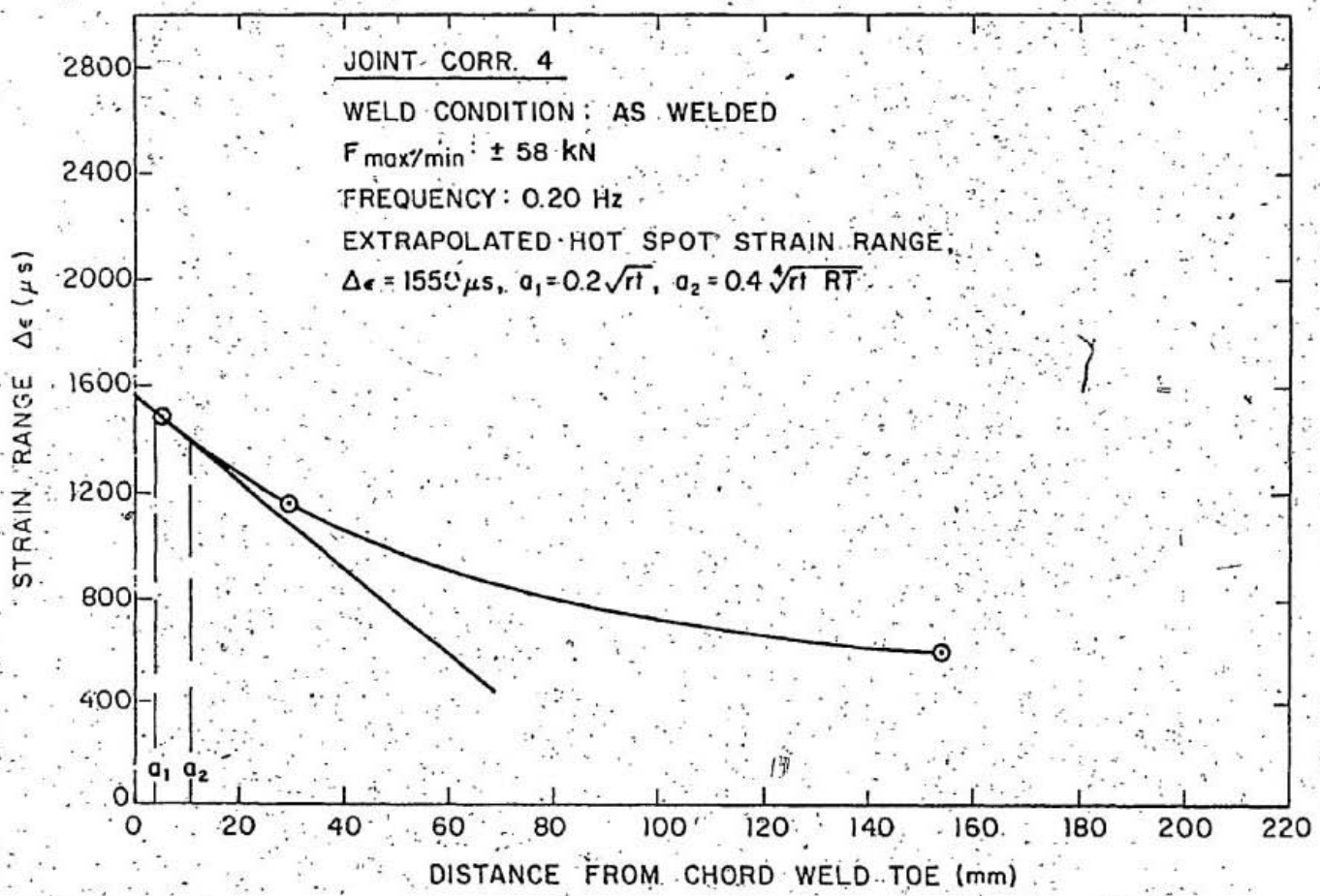

FIG. 62 f) STRAIN DISTRIBUTION NEAR WELD TOE: JOINT - CORR. 4

JOINT DRY 1

• POINT OF CRACK INITIATION

— N x 10^4 CYCLES

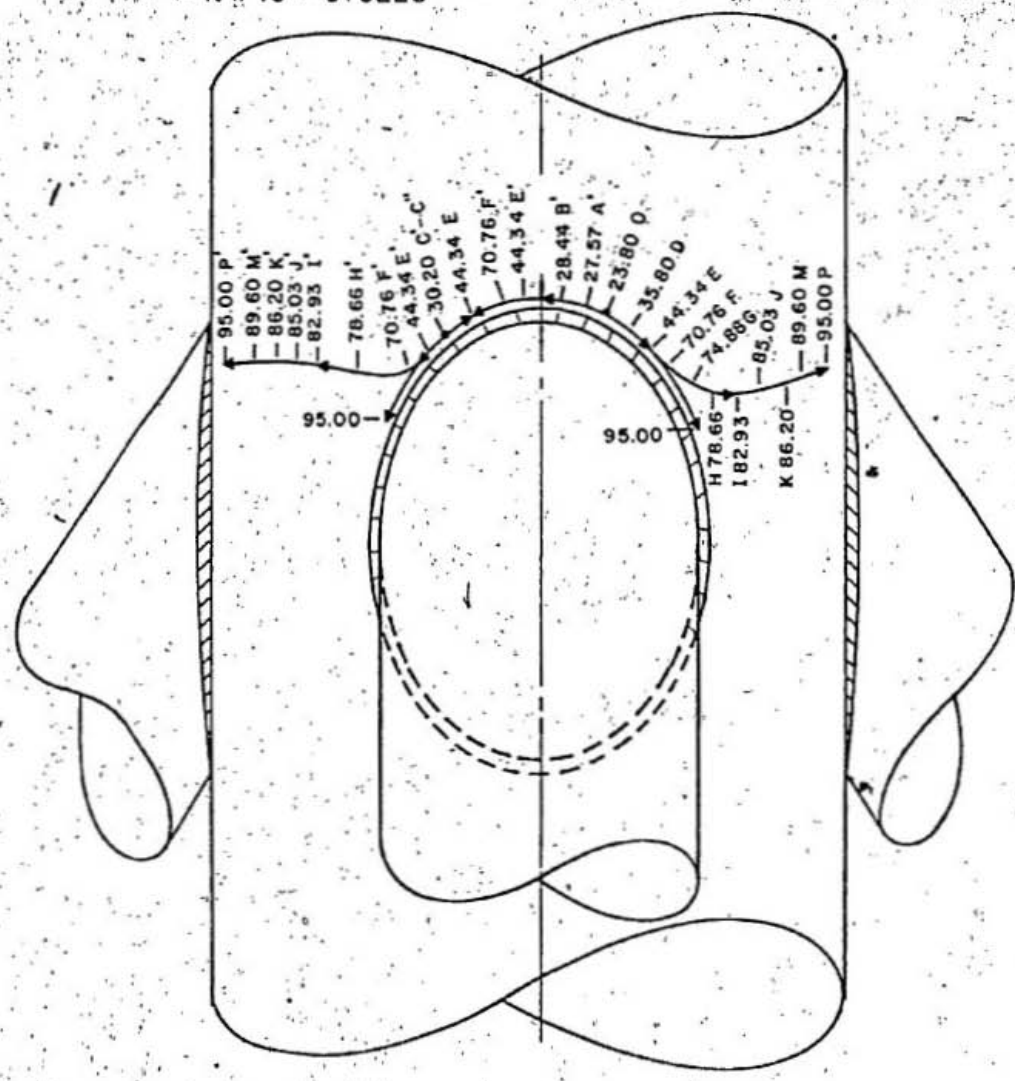

FIG. 63 SURFACE CRACK GROWTH DEVELOPMENT: JOINT – DRY 1

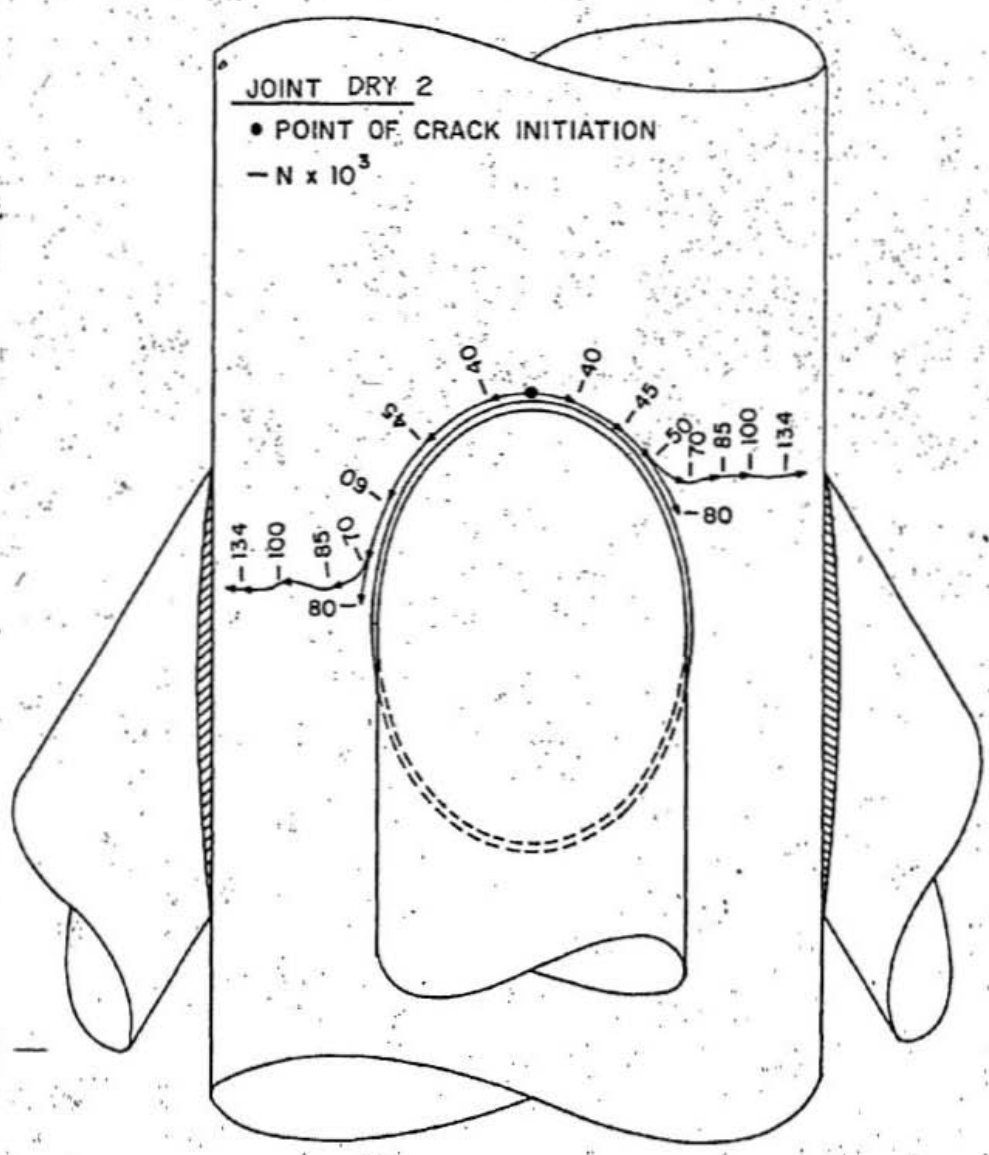

FIG. 64 SURFACE CRACK GROWTH DEVELOPMENT: JOINT – DRY 2

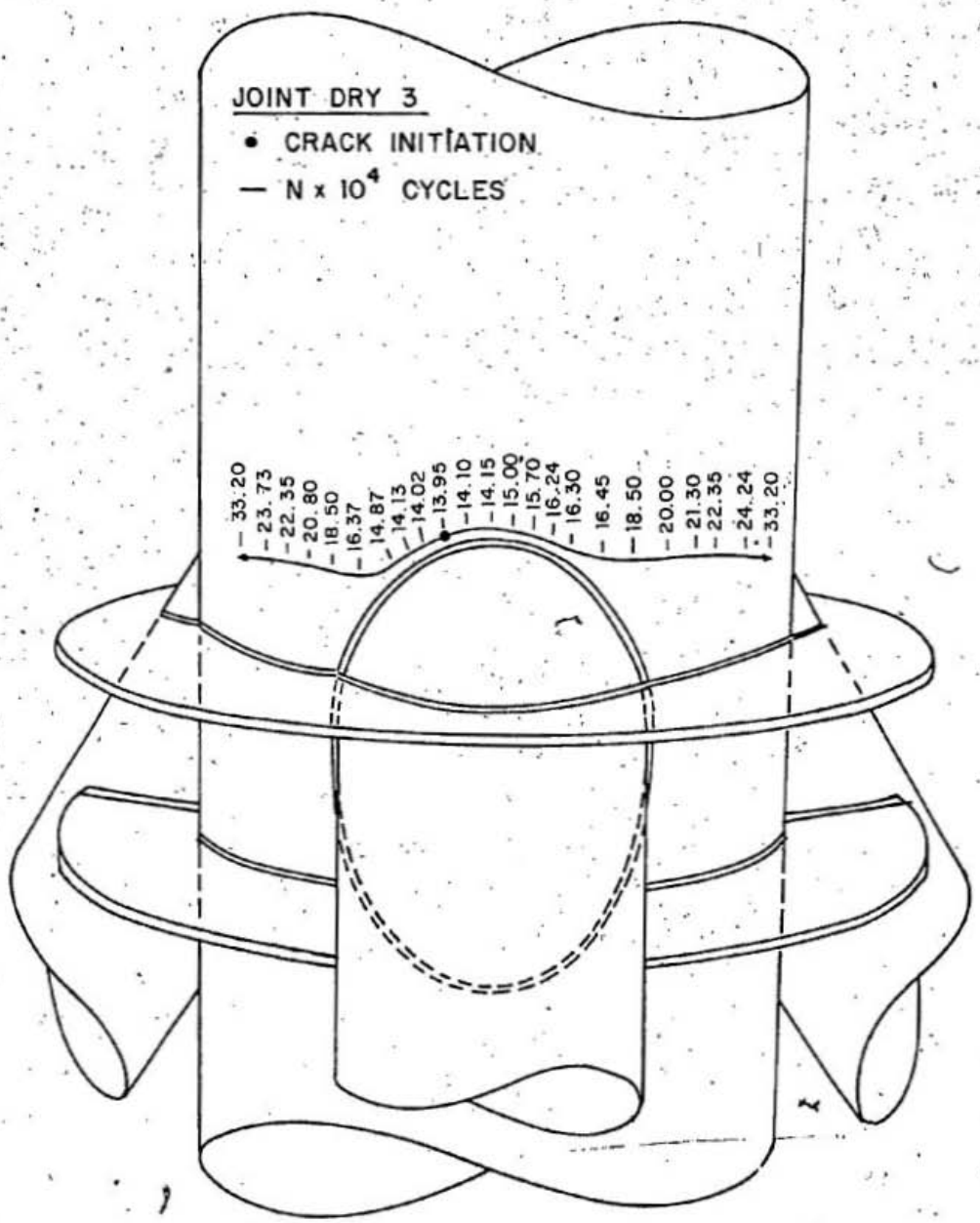

FIG.65 SURFACE CRACK GROWTH DEVELOPMENT: JOINT – DRY 3

JOINT CORR. 1

• POINT OF CRACK INITIATION

– N x 10^4 CYCLES

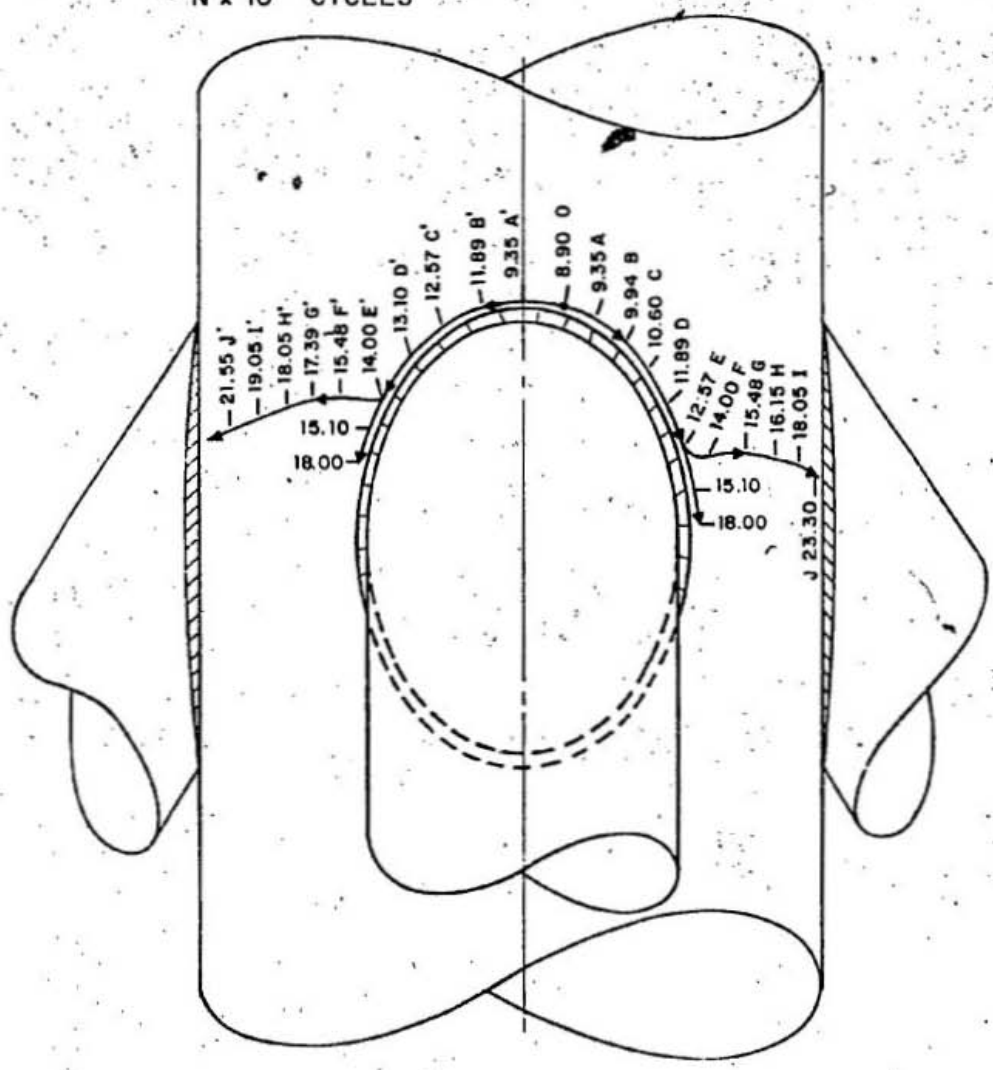

FIG. 66 SURFACE CRACK GROWTH DEVELOPMENT: JOINT – CORR. 1

JOINT - CORR. 2

• POINT OF CRACK INITIATION

– N x 10^4 CYCLES

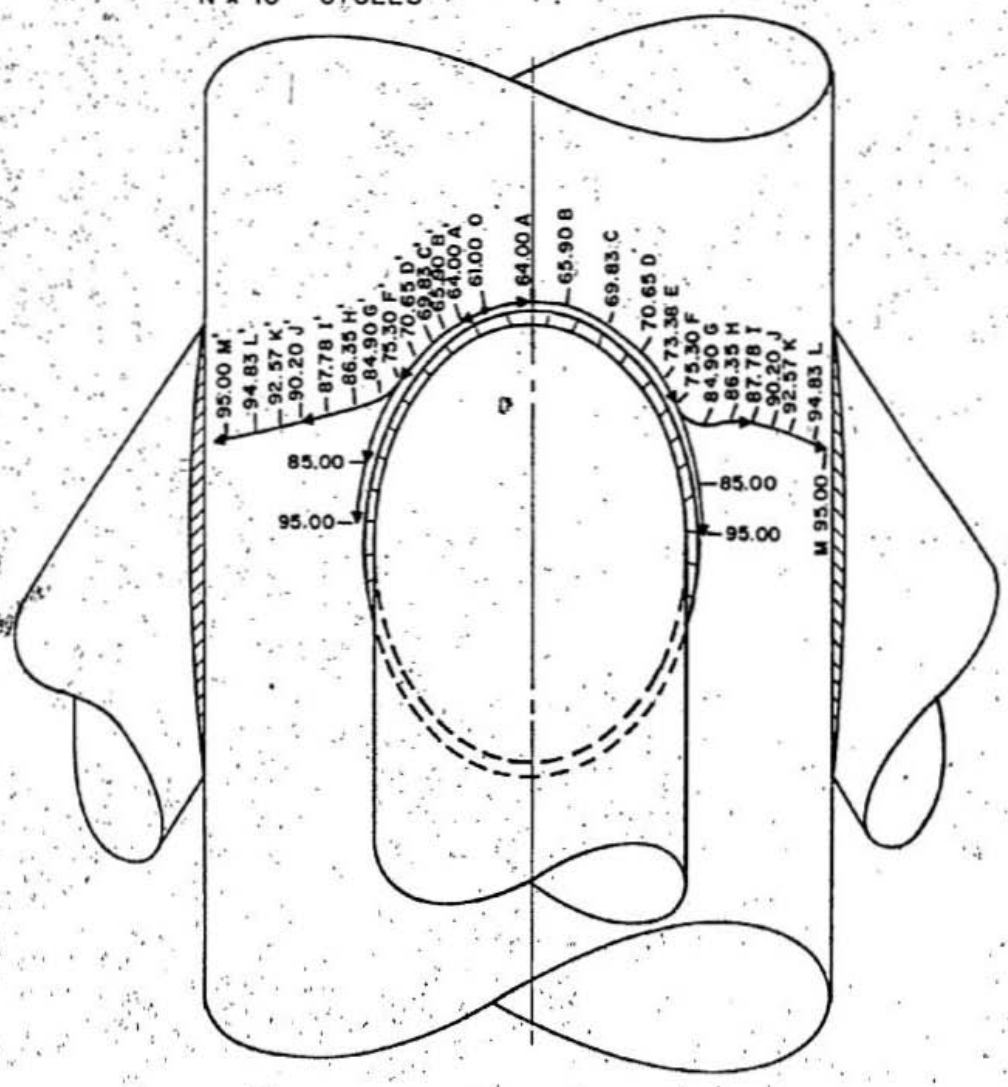

FIG. 67 SURFACE CRACK GROWTH DEVELOPMENT: JOINT - CORR. 2

JOINT CORR. 3

• POINT OF CRACK INITIATION

– N x 10^4 CYCLES

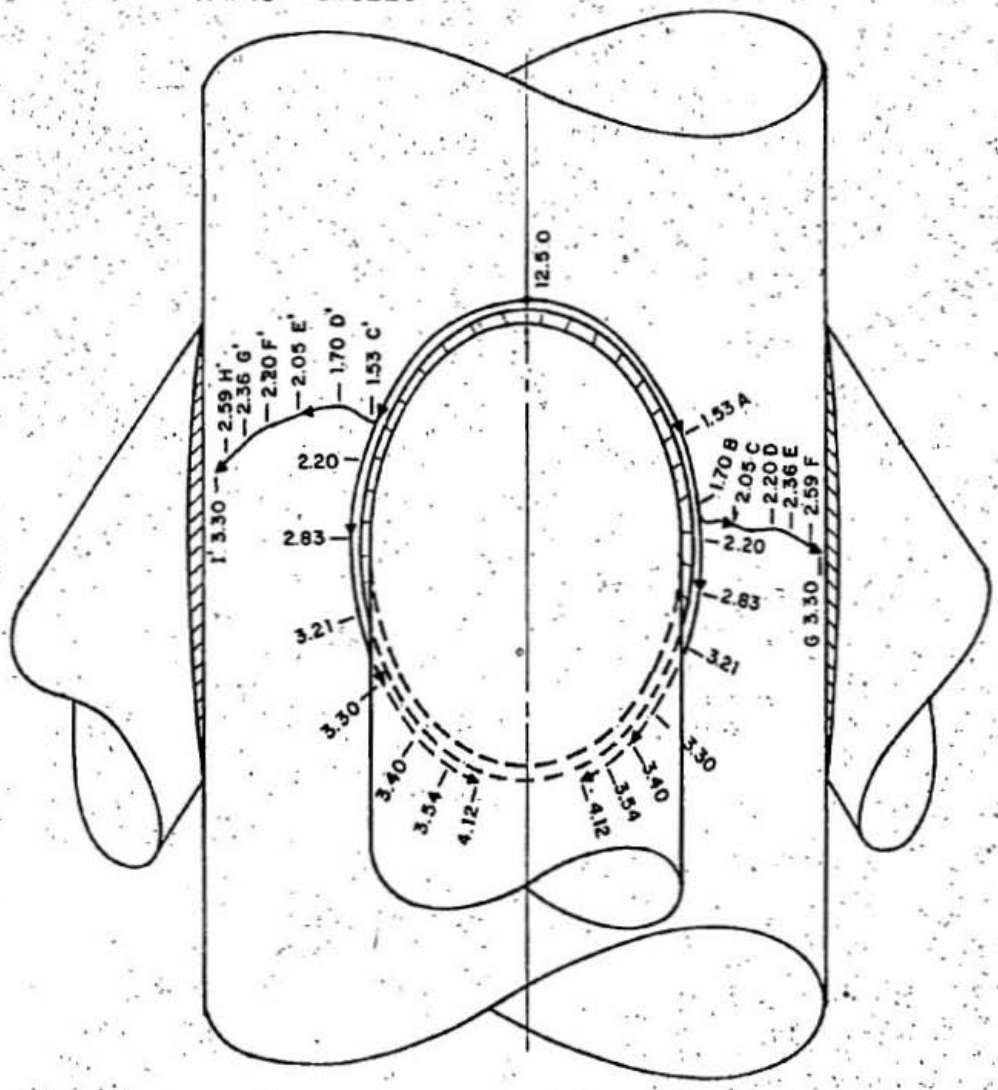

FIG. 68 SURFACE CRACK GROWTH DEVELOPMENT: JOINT – CORR. 3

JOINT CORR 4

• POINT OF CRACK INITIATION

– N x 10^4 CYCLES

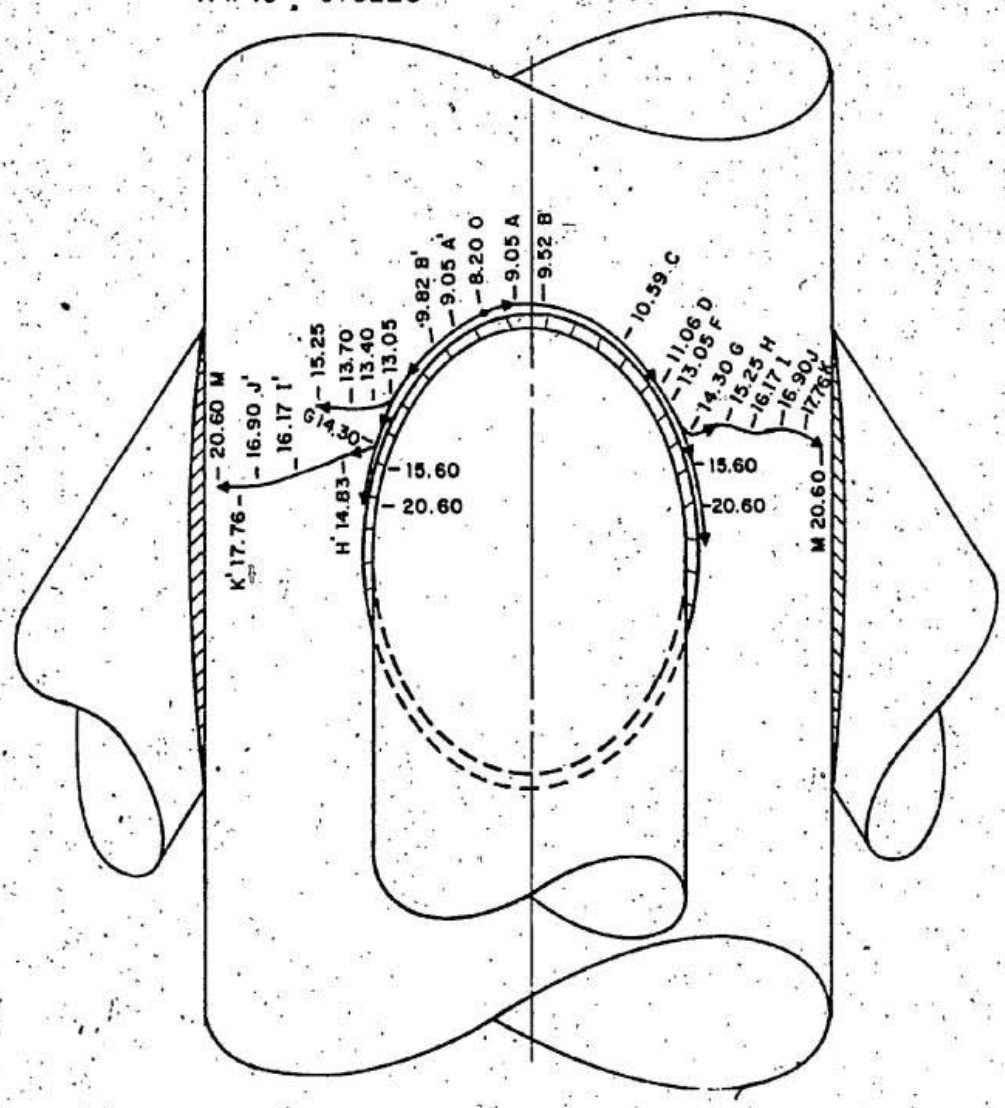

FIG.69 SURFACE CRACK GROWTH DEVELOPMENT: JOINT – CORR. 4

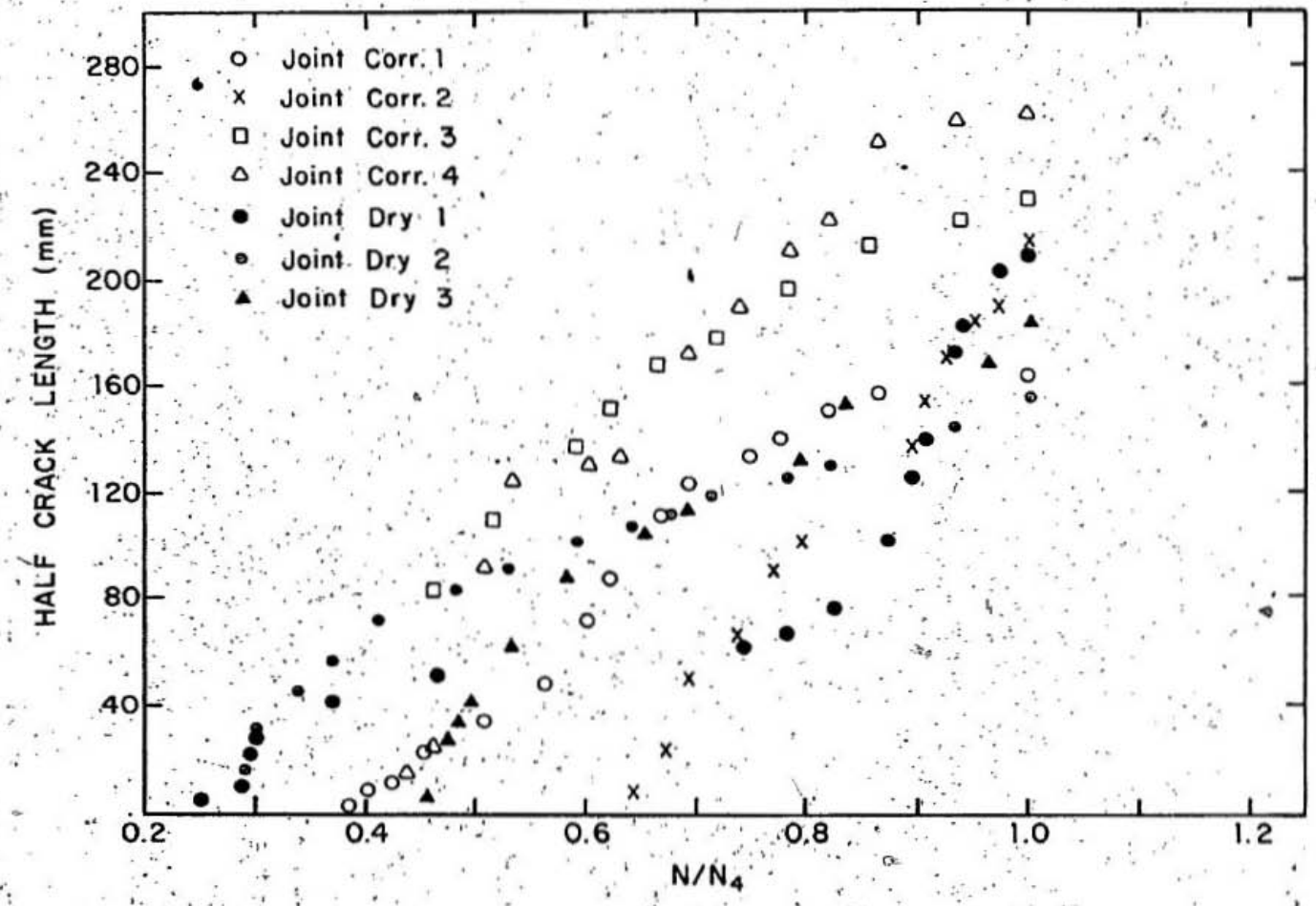

FIG.70 CRACK GROWTH CHARACTERISTICS OF JOINTS

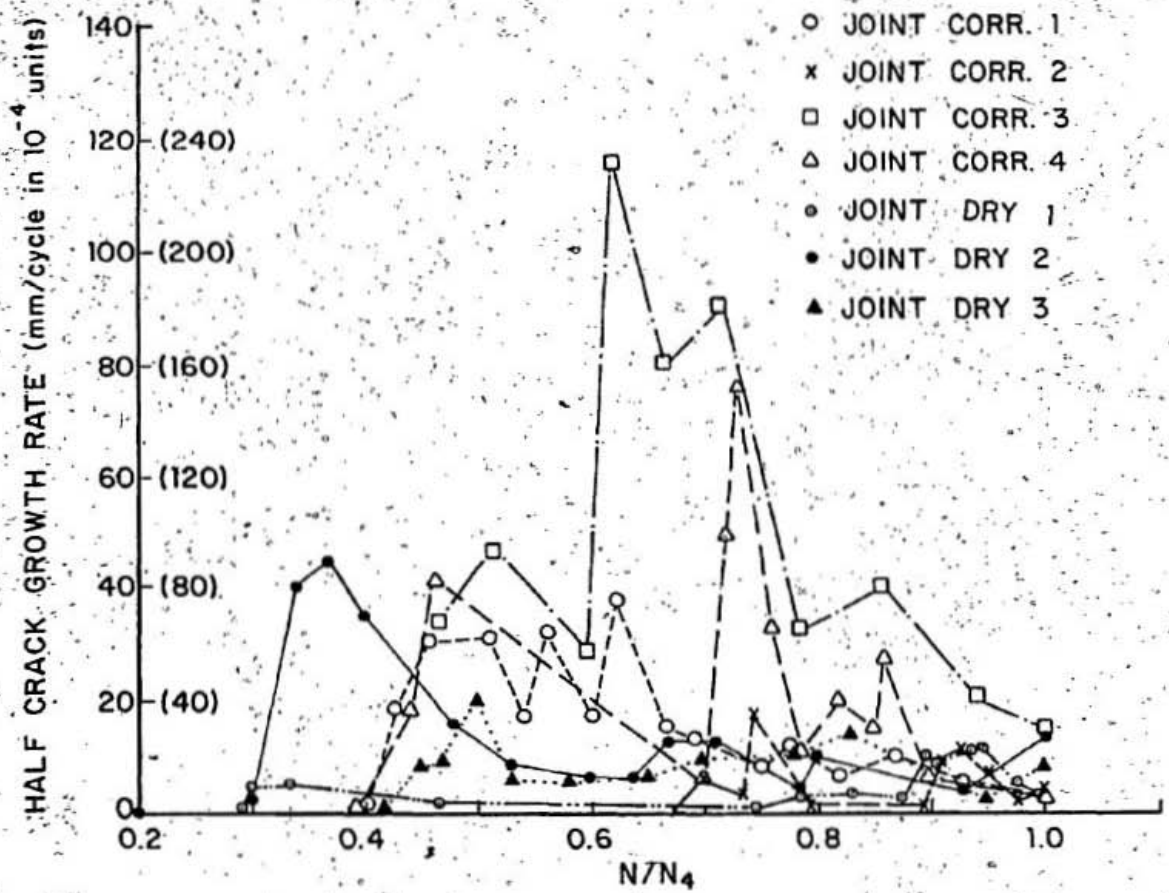

FIG. 71 OVERALL FATIGUE CRACK GROWTH OF JOINTS (LEFT OF CRACK INITIATION POINT)

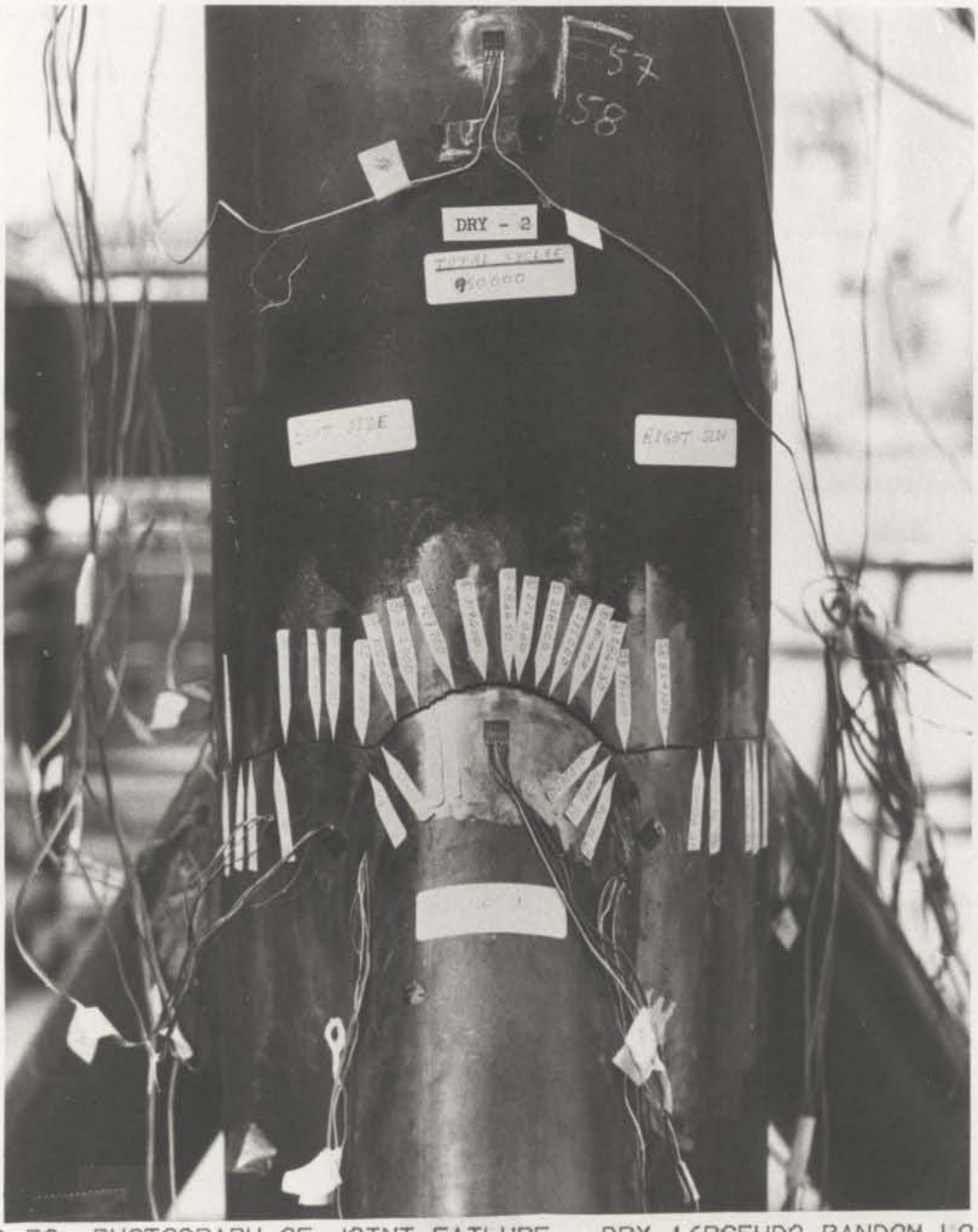

FIG.72 PHOTOGRAPH OF JOINT FAILURE - DRY 1(PSEUDO-RANDOM LOAD)

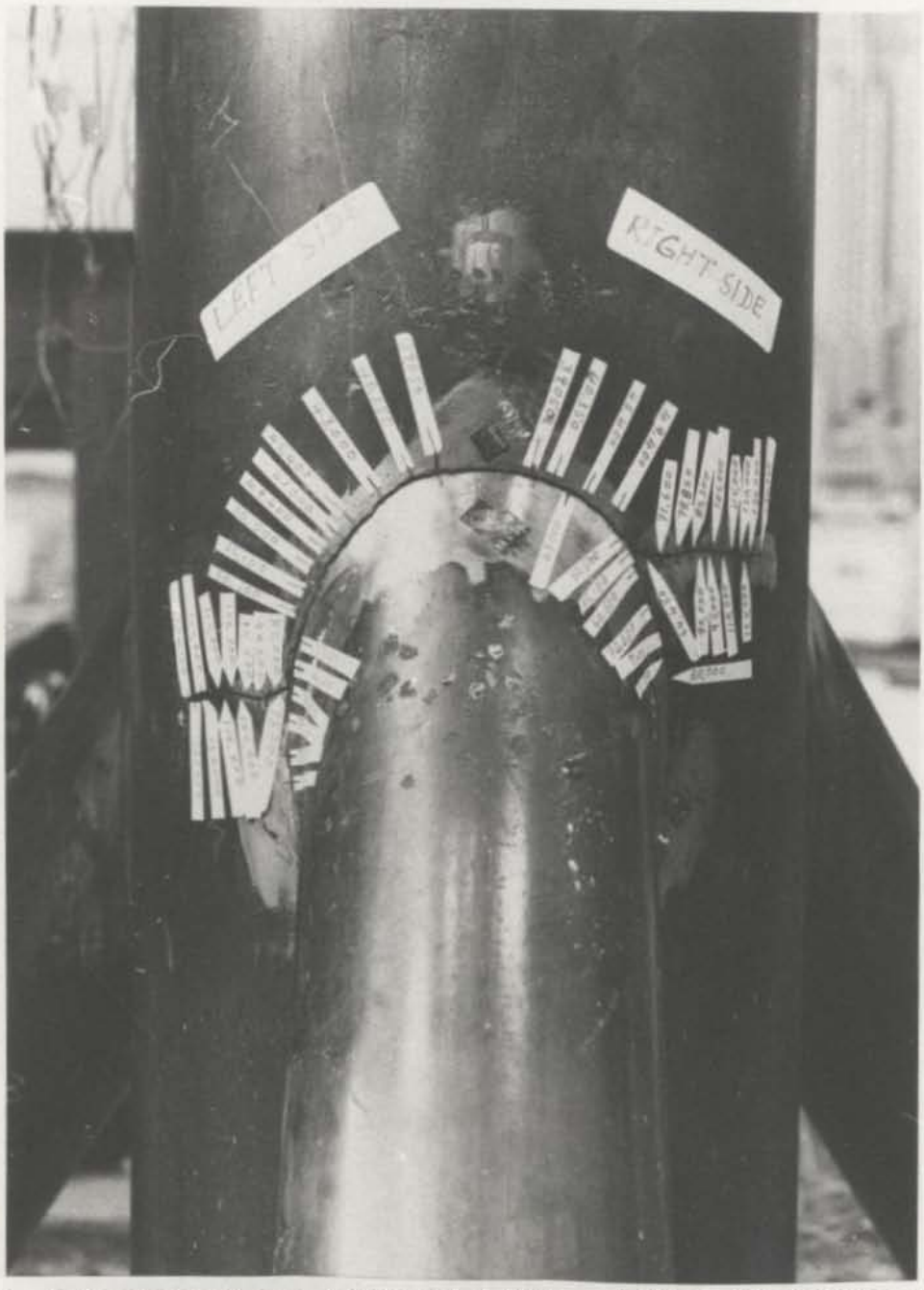

FIG.73 PHOTOGRAPH OF JOINT FAILURE - DRY 2 (HARMONIC LOAD)

FIG.74 PHOTOGRAPH OF JOINT FAILURE - DRY 3 (HARMONIC LOAD)

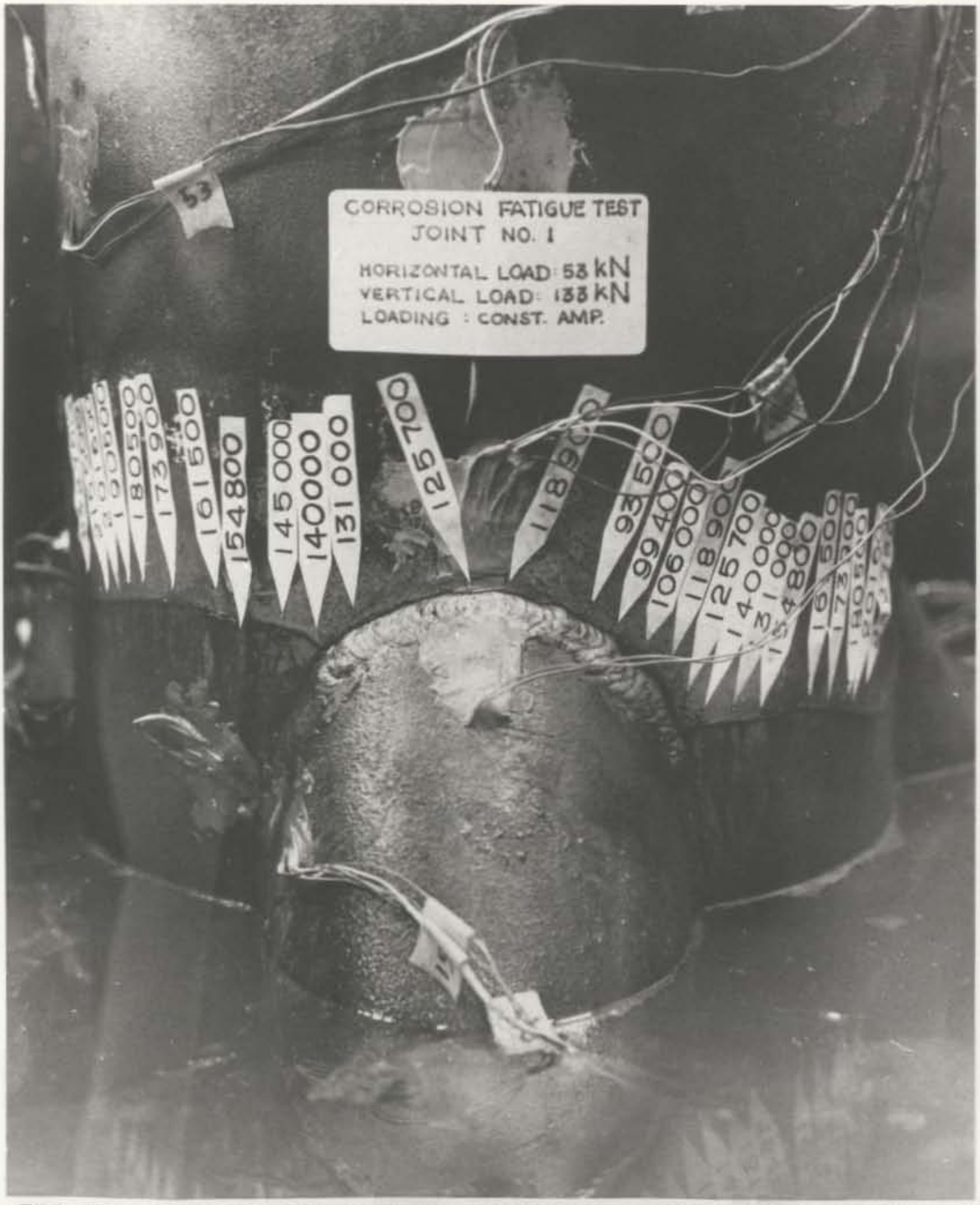

FIG.75 PHOTOGRAPH OF JOINT FAILURE - CORR.1 (HARMONIC LOAD)

FIG. 76 PHOTOGRAPH OF JOINT FAILURE - CORR. 2 (PSEUDO-RANDOM LOAD)

FIG.77 PHOTOGRAPH OF JOINT FAILURE – CORR.3 (HARMONIC LOAD)

FIG. 78 PHOTOGRAPH OF JOINT FAILURE - CORR. 4 (HARMONIC LOAD)

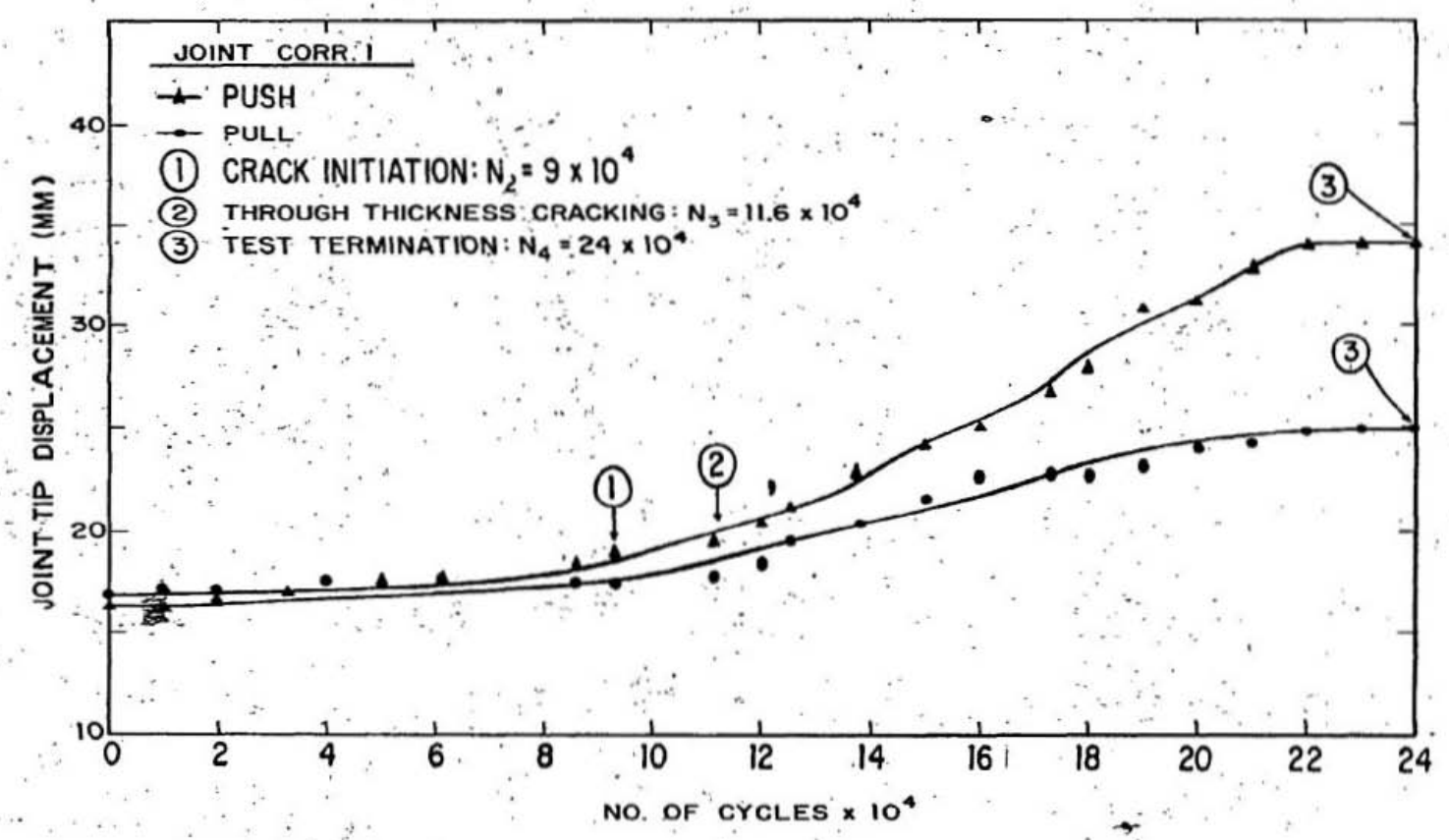

FIG.79 SPECIMEN TIP DISPLACEMENT: JOINT - CORR. 1

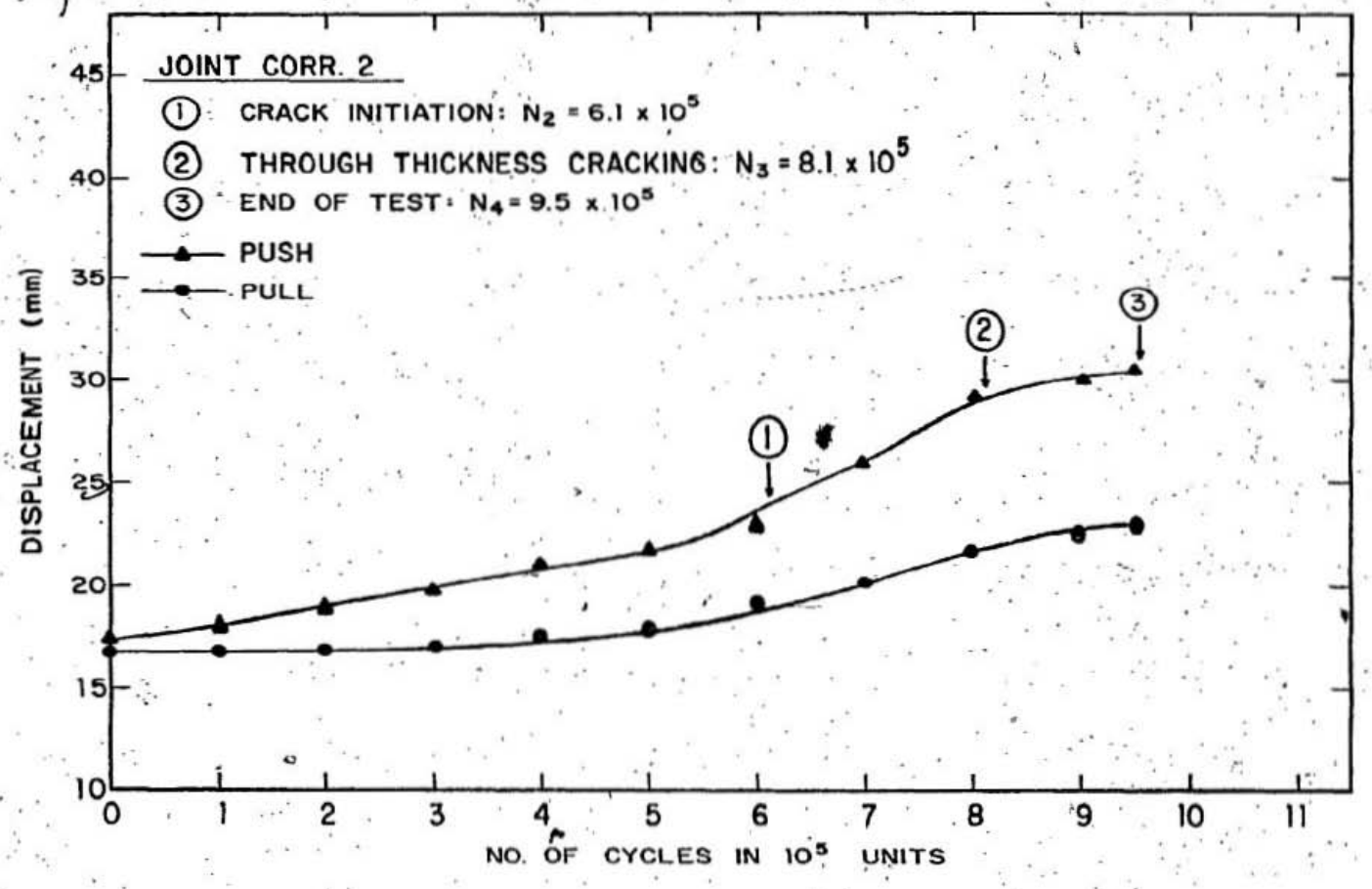

FIG. 80 SPECIMEN TIP DISPLACEMENT: JOINT - CORR. 2

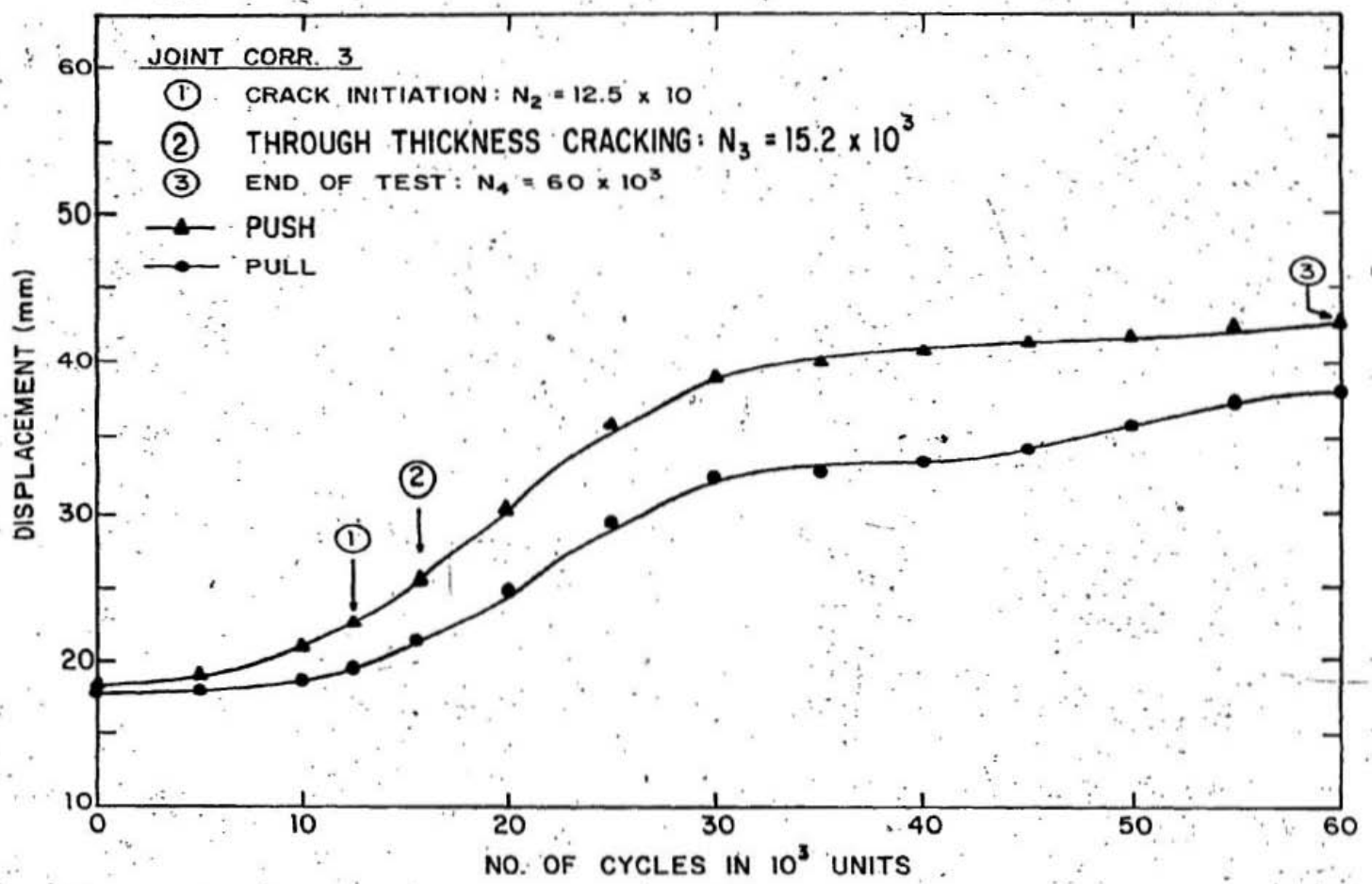

FIG. 81 SPECIMEN TIP DISPLACEMENT: JOINT – CORR. 3

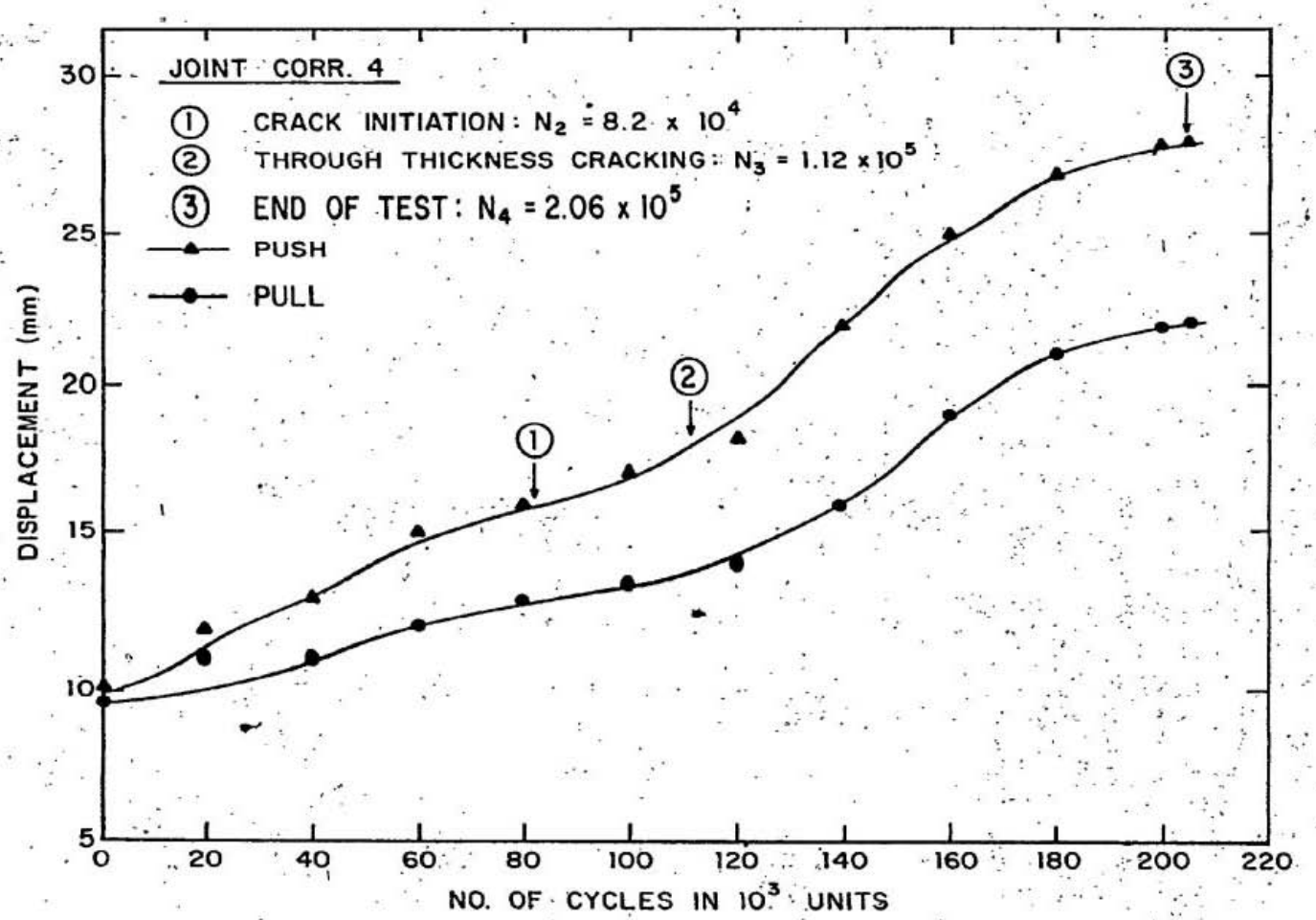

FIG. 82 SPECIMEN TIP DISPLACEMENT: JOINT - CORR. 4

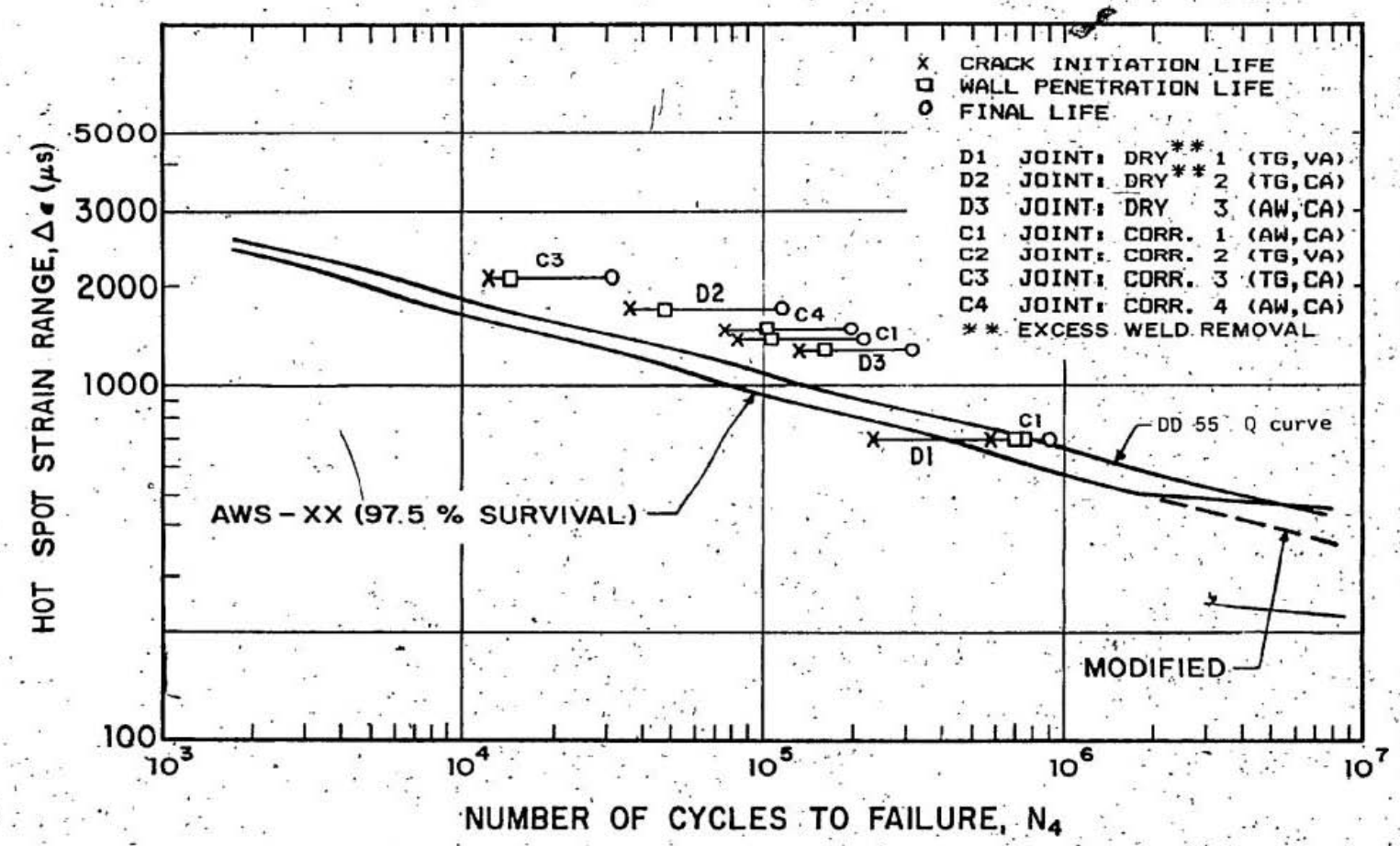

FIG. 83 COMPARISON OF FATIGUE TEST RESULTS

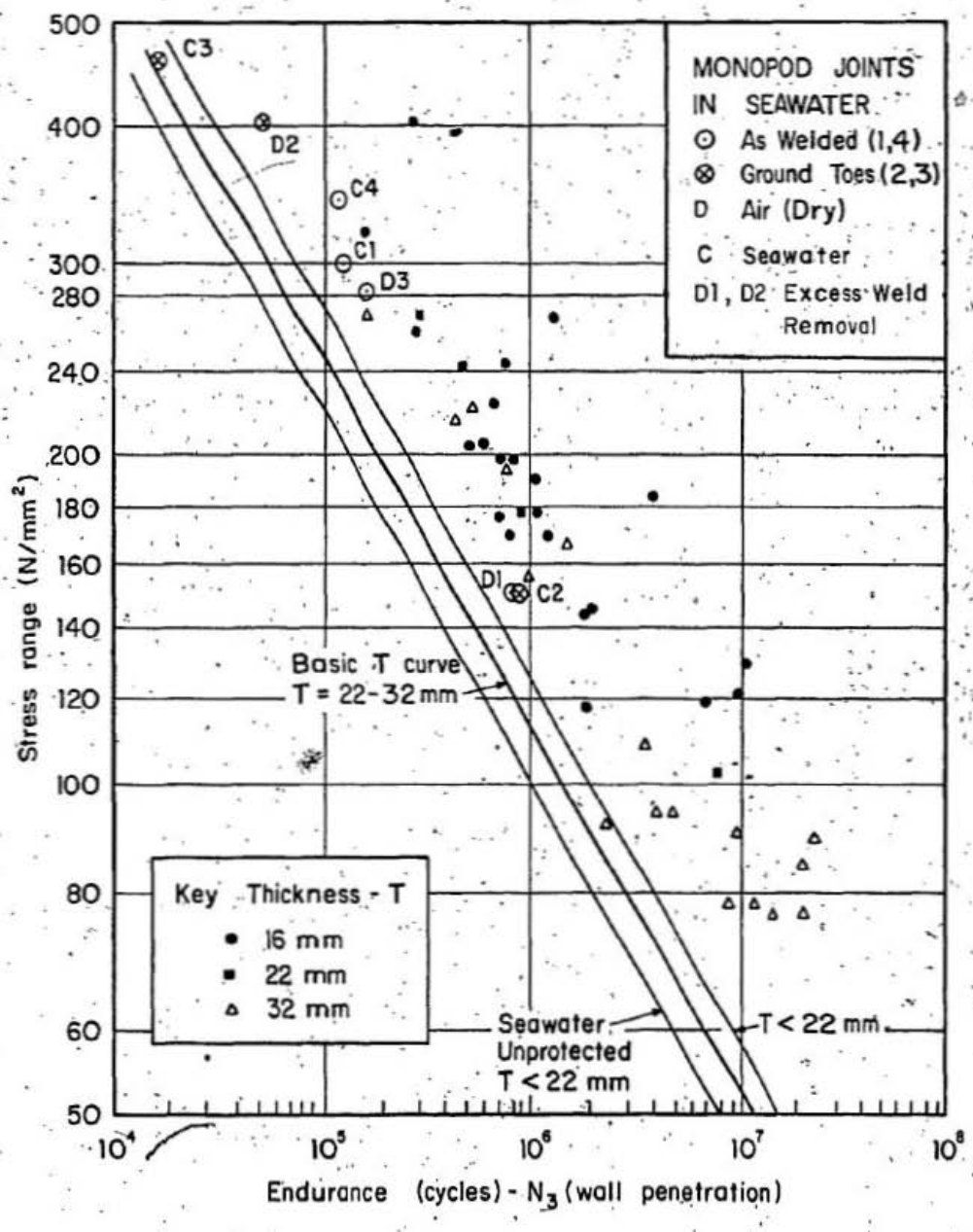

FIG. 84 BASIC S - N CURVES FOR TUBULAR JOINTS (REF. 98)

APPENDIX A

A. STRAIN GAUGE INSTALLATION

For the installation of the strain gauges at selected points around the specimen, a high speed grinder was used to sand the locations. The resulting surface was equivalent to that which would be obtained by using a medium grade emery paper. Scribe lines were marked for the gauge alignments. The gauge application in position was done in the following manner (127):

Step 1 - The gauging area was thoroughly degreased with a solvent, such as Chlorothene NU, using the aerosol cans.

Step 2 - Preliminary dry abrading with 220 or 320 grit silicon carbide paper was carried out. The final abrading was done by using 320 or 400 grit silicon carbide paper on the surfaces thoroughly wetted with M-PREP CONDITIONER A. This was followed by wiping dry with a gauge sponge. With a steel pointer, the alignment marks were done to the required position of the gauges. Finally all the residues and conditioner were again slowly wiped out with a gauge sponge.

Step 3 - A liberal amount of M-PREP NEUTRALIZER 5 was applied and scrubbed with a cotton tipped

applicator. The surface was carefully dried with a single, slow wiping motion of a gauge sponge.

Step 4 - The gauge was removed from the acetate envelope with the help of tweezers and placed on a chemically clean glass plate, with the bond side of the gauge down. With a cellotape of length 100 x 150 mm, pasted the tape over the gauge. Carefully the tape was lifted at a shallow angle, bringing the gauge up along the tape.

Step 5 - The gauge and tape assembly were positioned so that the triangle alignment marks on the gauge are over the layout lines on the specimen. By properly realigning the gauge was anchored down firmly with one end of the tape on the specimen.

Step 6 - The gauge end assembly was lifted at a shallow angle to the specimen surface until the gauge and terminal are free from the specimen surface and approximately 13 mm beyond the terminal. The loose end of the tape was tucked under and pressed to the specimen surface so that the gauge and terminal lay flat with the bending surface exposed.

Step 7 - M-BOND 200 Catalyst was then applied to the bond surface of the gauge and terminal. By setting the brush down on the gauge, swab the gauge backing and to the adjacent tape area also. The catalyst was

allowed to dry at least one minute under normal ambient conditions.

Step 8 - By lifting the tape end of the assembly, and holding in the same position, one or two drops of M-BOND 200 adhesive was applied at the fold formed by the junction of the tape and specimen surface. This adhesive application should be approximately 13 mm outside the actual gauge installation area. This will insure that local polymerization taking place when the adhesive comes in contact with the specimen surface will not cause unevenness in the gauge glue-line.

Step 9 - Immediately the tape was rotated to approximately 30° angle so that the gauge is bridged over the installation. While holding the tape slightly taut, with a piece of gauze slowly and firmly a single wiping stroke was made over the gauge and tape assembly bringing the gauge back down over the alignment marks on the specimen. Use of firm thumb pressure with the finger is sufficient when wiping over the gauge.

Step 10 - Upon completion of wipe-out of the adhesive, firm thumb pressure must be applied to the gauge and terminal area for one minute so that the thumb heat will help to speed adhesive polymerization.

Step 11 - The gauge and terminal strip are now solidly bonded in place. The tape was removed by pulling it back directly over itself, peeling it slowly and steadily off the surface. This technique will prevent possible lifting off the foil in open faced gauges or otherwise damaging the installation.

Step 12 - Finally with an appropriate solder, the lead-in wires were attached and the soldering checked for any open circuit.

APPENDIX-B

B. MEASUREMENT OF SEAWATER PROPERTIES

B.1 Salinity

The resistivity of the seawater changes with the salinity, thereby changing its electrical resistance, which is one of the major factors affecting the rate of corrosion. At 0°C the salinity of seawater is 35‰. Salinity is expressed as the amount of solid material in grams contained in one kilogram of seawater when all the carbonate has been converted to oxide, all the bromine and iodine replaced by chlorine, and all the organic material is oxidized (127). The salinity is related to chlorinity as

$$S‰ = 1.80655 \times \text{chlorinity} \qquad \text{(B-1)}$$

In the laboratory, the salinity was measured using a Salinity Refractometer (Fig. B1). The refractometer is a unique hermetically-sealed hollow-prism, filled with a stable liquid, changes index with temperature to compensate instantly and automatically for temperature changes of the sample. The scale provides two direct readings, one for refractive index and the other for salinity. The procedure to obtain salinity measurements is as follows (128):

(1) Hold the instrument in a horizontal position, and swing the coverplate over the body of the instrument.

(2) Pipette, not more than 0.02 ml (one drop) of sample to the measuring prism and close the cover plate over the measuring prism immediately.

(3) Keeping the cover plate in contact with the prism, point the instrument towards illuminating light source while taking readings.

(4) Bring the scale seen in the eyepiece into best focus by rotation of the eyepiece, and note the reading at the point where the dividing line between light and dark crosses, which gives the salinity level of the sample.

B.2 pH Value

pH indicates a measure of acidity and alkalinity of the solution caused by the hydrogen ion concentration. The pH value was measured during testing using a standard pH meter (Fig. B2), adapting the following procedure:

I. 1) Prepare a standard solution having 10^{-2}, 10^{-3}, 10^{-4} M, or 1000, 100 and 10 ppm.

2) Mix 50 ml of 10^{-3} M or 1000 ppm standard solution with 5 ml CO_2 buffer solution.

3) Place the electrode in standard solution and set function switch to REL MV.

4) Adjust calibration control to 0.0.

II. 1) Mix 50 ml of 10^{-4} M or 10 ppm standard with 5 ml CO_2 buffer solution.

2) Rinse the electrodes and place in the standard solution and note the reading after stabilizing.

III. Repeat the procedure, II, with 10^{-2} M standard, and read pH of the solution direct from the meter.

B.3 Dissolved Oxygen Content

Variation of oxygen content in seawater gives rise to formation of concentration cells, thereby increasing the rate of corrosion. The limiting current density for the reduction of oxygen can be used to estimate the rate of corrosion given by (129):

$$i_{cor} = \frac{4FD}{1000t} C_o \qquad \text{(B-2)}$$

where

i_{cor} = rate of corrosion (A/cm^2)

F = Faraday's constant

t = thickness of diffusion layer

D = diffusion constant (cm^2/sec)

C_o = oxygen concentration in seawater (mol/l)

This limiting current value will become larger if the dissolved oxygen content increases and the electrolyte undergoes velocity changes. Under free corrosion potential, the increased oxygen level accelerates the crack growth significantly.

The Winkler titration method was used to determine the change in the level of the dissolved oxygen in seawater and the following procedure is used (130):

1) A sample of seawater is collected in a 60-ml glass-stoppered standard bottle.
2) Add the contents of one Dissolved Oxygen I Powder Pillow and one Dissolved Oxygen II Powder Pillow (direct replacement reagents). Carefully replace the stopper so that no air is trapped in the bottle. Invert the bottle several times to ensure proper mixing. A flocculent precipitate will form which will be brownish-orange in color if oxygen is present.
3) Allow the sample to stand until the flocculent precipitate settles and leaves the top half of the solution clear. Again invert the bottle several times for mixing and let the sample stand until the upper half of the solution is clear.
4) Remove the stopper and add the contents of one Dissolved Oxygen III Powder Pillow (direct replacement reagent). Replace the stopper and invert the bottle several times to ensure mixing. The flocculent precipitate will dissolve and leave a yellow colour indicating the presence of oxygen.
5) Pipette 5.8 ml of the prepared solution into the 50 ml flask (about 10 drops).

6) While constantly swirling the flask, titrate the sample with PAO (Phenylarsine oxide) solution for dissolved oxygen until the yellow coloured solution becomes colourless.

7) The number of drops of PAO solution added for Dissolved Oxygen is equal to the mg/l Dissolved Oxygen (each drop is equal to 0.25 mg/l dissolved oxygen).

B.4 Concentration of HCO_3^-

The carbon dioxide exists as bicarbonate and carbonate, and depends on temperature and pH value. The velocity of the surrounding fluid removes the protective material thereby increasing corrosion. The procedure for determination of HCO_3^- concentration in the laboratory is as follows:

1) Prepare a standard dilute solution of HCl (0.01 M).

2) Using BROMOCRESOL GREEN as indicator, titrate a known volume (25 ml) of the seawater sample, against the standard HCl solution.

3) Note the change in the indicator color used from yellow to blue, which gives the end point.

4) Determine the amount of HCO_3^- ion in the sea water sample by volumetric measurements.

FIG. B1 SALINITY REFRACTOMETER

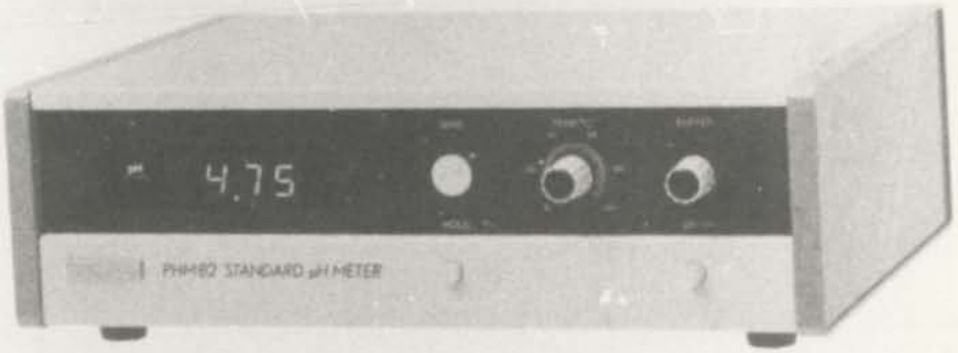

FIG. B2 STANDARD PH METER

APPENDIX C

C. CALCULATION OF MAXIMUM PRINCIPAL STRAINS AND STRESSES

From the measured values of the strains during testing, the magnitude and direction of maximum and minimum principal strains and stresses were calculated using Hook's law and the theory of elasticity. For a three-element rectangular 45° rosette, the maximum and minimum principal strains are given by (131):

Max. principal strain, ε_1,

$$\varepsilon_1 = \frac{1}{3}(\varepsilon_I + \varepsilon_{II} + \varepsilon_{III}) + \frac{\sqrt{2}}{3}\sqrt{(\varepsilon_I+\varepsilon_{II})^2 + (\varepsilon_{II}-\varepsilon_{III})^2 + (\varepsilon_I-\varepsilon_{III})^2} \qquad \text{(C-1)}$$

Min. principal strain, ε_2,

$$\varepsilon_2 = \frac{1}{3}(\varepsilon_I + \varepsilon_{II} + \varepsilon_{III}) - \frac{\sqrt{2}}{3}\sqrt{(\varepsilon_I+\varepsilon_{II})^2 + (\varepsilon_{II}-\varepsilon_{III})^2 + (\varepsilon_I-\varepsilon_{III})^2} \qquad \text{(C-2)}$$

$$\tan 2\alpha = \frac{\sqrt{3}\,(\varepsilon_{II}-\varepsilon_{III})}{(2\,\varepsilon_I-\varepsilon_{II}-\varepsilon_{III})} \qquad \text{(C-3)}$$

where,

ε_I, ε_{II} and ε_{III} are the measured strains at 0°, 45° and 90° angles.

The maximum principal stresses were calculated using the following equations:

For a uniaxial strain gauge, principal stress, σ is,

$$\sigma = E\ \varepsilon \tag{C-4}$$

where

E = Young's modulus of elasticity

ε = principal strain

For the biaxial (double) strain gauge, maximum and minimum principal stresses σ_1 and σ_2 respectively are,

$$\sigma_1 = \frac{\varepsilon}{1-\mu^2}\ (\varepsilon_I + \mu\ \varepsilon_{II}) \tag{C-5}$$

$$\sigma_2 = \frac{\varepsilon}{1-\mu^2}\ (\varepsilon_{II} + \mu\ \varepsilon_I) \tag{C-6}$$

For the rosette strain gauges,

$$\sigma_1 = \frac{E}{2}\ [\frac{\varepsilon_I+\varepsilon_{II}}{1-\mu} + \frac{1}{1-\mu}\ \sqrt{[2\ \varepsilon_{III} - (\varepsilon_I+\varepsilon_{II})]^2 + (\varepsilon_I-\varepsilon_{II})}] \tag{C-7}$$

$$\sigma_2 = \frac{E}{2}\ [\frac{\varepsilon_I+\varepsilon_{II}}{1-\mu} - \frac{1}{1-\mu}\ \sqrt{[2\ \varepsilon_{III} - (\varepsilon_I+\varepsilon_{II}]^2 + (\varepsilon_I-\varepsilon_{II})^2}] \tag{C-8}$$

$$\tan\ \phi = \frac{1}{2}\ [\frac{2\ \varepsilon_{III} - (\varepsilon_I+\varepsilon_{II})}{\varepsilon_I - \varepsilon_{II}}] \tag{C-9}$$

APPENDIX-D

D. GENERATION OF PSEUDO-RANDOM LOAD (132)

For the pseudo-random load application, a block of unimodal variable amplitude random sequence load signal was recorded on a magnetic tape and played repeatedly via a tape loop. The history of the random load signal is as follows: The "random" sea surface $\eta_o(t)$ with a specified power spectrum and a Gaussian probability distribution is generated by convolving a time series of Gaussian "white noise", $\varepsilon(t)$, with an appropriate filter function, $h(\tau)$ and given by

$$\eta_o(t) = \int_{-\infty}^{\infty} h_o(\tau)\ \varepsilon(t-\tau)d\tau \qquad \text{(D-1)}$$

The filter function, $h(\tau)$, is computed from the specified power spectrum of the sea surface on the assumption of zero phase shift in the filter. The wave power spectrum $\phi_{\eta\eta}(\omega)$, is related to the "white noise" power spectrum $\phi_{\varepsilon\varepsilon}(\omega)$ through the frequency function $H_o(\omega)$, which is the Fourier transform of the filter, $h_o(\tau)$ and given by

$$\phi_{\eta\eta}(\omega) = |H_o(\omega)|^2\ \phi_{\varepsilon\varepsilon}(\omega) \qquad \text{(D-2)}$$

The 'band limited white noise' is obtained by generating a series of uncorrelated Gaussian random numbers with zero mean and unit variance. The power spectrum corresponding to a digital time series with uniform time spacing, Δt, is

$$\phi_{\varepsilon\varepsilon}(\omega) = \begin{cases} \frac{1}{\Delta t} & -\frac{\pi}{\Delta t} < \omega < \frac{\pi}{\Delta t} \\ 0 & |\omega| > \frac{\pi}{\Delta t} \end{cases} \qquad \text{(D-3)}$$

The frequency functions (Eqns. D-3 and D-4) corresponding to wave velocities and accelerations at any location (X_i, Z_i), maintain the amplitude and phase relationships consistent with linear wave theory for waves travelling in the positive direction.

$$H_{\bar{u},\,i}(\omega) = H_o(\omega)\ \beta_i \omega e^{k(Z_i - Z_o)}\ e^{-kX_i} \qquad \text{(D-4)}$$

$$H_{\dot{u},\,i}(\omega) = i\omega\ H_{\bar{u},i}(\omega) \qquad \text{(D-5)}$$

The corresponding filter functions (eqns. D-5 and D-6) are obtained from the Fourier transform of the frequency functions.

$$h_{\bar{u},\,i}(\tau) = \frac{1}{2\pi} \int_{-\infty}^{\infty} H_{\bar{u},\,i}(\omega)\ e^{i\omega t}\ d\omega \qquad \text{(D-6)}$$

$$h_{\dot{u},\,i}(\tau) = \frac{1}{2\pi} \int_{-\infty}^{\infty} H_{\dot{u},\,i}(\omega)\ e^{i\omega\tau}\ d\omega \qquad \text{(D-7)}$$

The time series of the wave heights are then obtained based on the velocities and accelerations determined from the convolutions of filter functions with the "white noise" time series.

The pseudo-random load proposed in the present investigation is based on the modelling of the Pierson-Moskowitz spectrum (1:100) for a wind speed of 15 m/s. The drive signal for this particular spectrum was provided by an analog tape prepared at the Rivers and Harbours Laboratory, Norwegian Institute of Technology, Trondheim, Norway. This tape was generated by bandpass filtering of white noise.

A special loop attachment was used in a LYREC tape recorder, Fig. D1, and played continuously. The single block of the random sequence load pattern with 58 cycles and its power spectral density are shown in Figs. D2 and D3.

The random signal was filtered with a cut-off frequency of 20 Hz and fed to the controller unit of the MTS machine. This type of loading was applied to two joints - one in air and the other in water. The typical strain-time signal recorded at the hot spot and its power spectral density are shown in Figs. D-4 and D-5.

The remaining five joints were tested under constant amplitude loading, the frequency and sinusoidal wave-form signal were generated from the MTS machine.

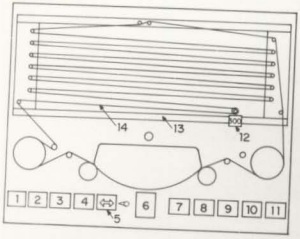

1. ERASE
2. RECORD
3. STOP
4. START
5. ⇐⇒ WINDING CONTROL
6. ADJUSTER
7. 0.6 IPS (INCH PER SECOND)
8. 6 IPS
9. 60 IPS
10. LOOP
11. MAINS
12. LOOP IDLER
13. LOOP ATTACHMENT
14. $\frac{1}{2}$" 1 MIL INSTRUMENTATION TAPE

FIG. D1 a) LYREC TAPE RECORDER

FIG. D1 b) PHOTOGRAPH OF LYREC TAPE RECORDER

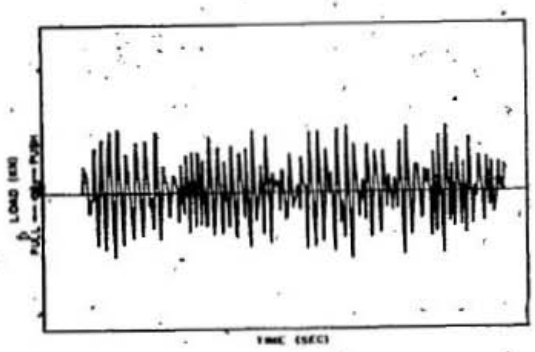

FIG. D2 RANDOM LOAD-TIME HISTORY

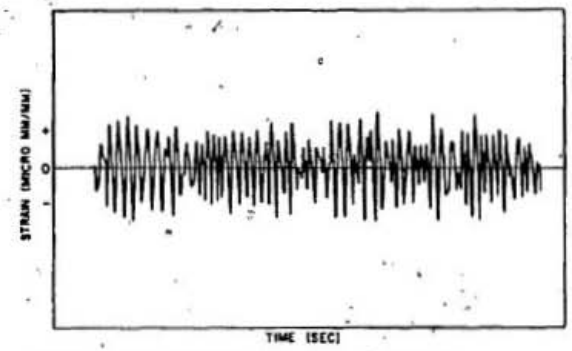

FIG. D4 HOT SPOT STRAIN-TIME HISTORY

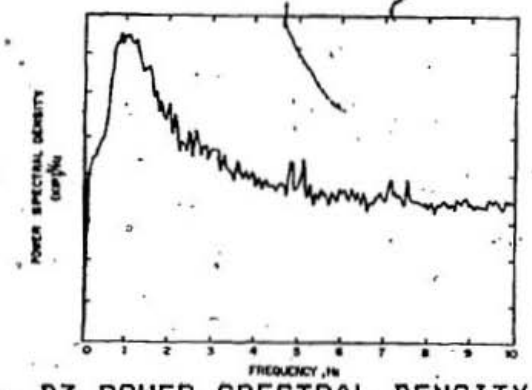

FIG. D3 POWER SPECTRAL DENSITY OF RANDOM LOAD SIGNAL

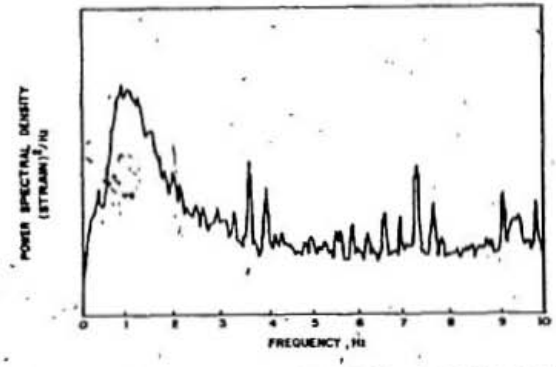

FIG. D5 POWER SPECTRAL DENSITY OF STRAIN SIGNAL

APPENDIX-E

E. FATIGUE TESTING MACHINE

The fatigue testing machine employed in the present experimental investigation was a closed loop MTS electro-hydraulic machine (Fig. E-1). The details of the system with different units are given in the following (133):

E1. Model 430.41 Digital Indicator

The Digital Indicator in the MTS System is a readout device used to monitor continuously and display in digital form the voltage on one of five operator selectable inputs. This operates in two Modes - DC or PEAK READ. The DC mode is selected for static or slowly changing inputs and the peak read mode is selected for cyclic inputs. In both operating modes, register and store the sign and magnitude of the maximum and minimum values of the selected input attained during the test, which can be recalled at any time. The Digital Indicator can be used as a dual range digital voltmeter.

E2. Model 430.31 Digital Function Generator (DFG)

The Digital Function Generator provides dynamic programming capabilities in MTS closed-loop electro-hydraulic testing system. The inputs for selection include normal and

inverted variable frequency sine, hoversine, and hoversquare and variable time signal and dual slope ramps.

Null pacing using the null or error detector is the Servo-Controller, and limit programming using a limit detector module for ramp function program control during the test is in progress.

E3. Model 406.11 Controller

The Controller is an electronic sub-system containing the principal servo-control, fail safe and readout functions for one channel in the MTS System. The System's hydraulic actuator applies a mechanical input to the specimen and transducer. Transducer Conditioner supplies AC excitation to its associated transducer and provides a DC output proportional to the mechanical input to the transducer. The full scale conditioner output is ± 10 VDC.

The Feedback Selector allows selection of either Transducer Conditioner or an external transducer conditioner signal as the feedback input to the Servo-Controller. The selected input is called the controlled variable and may be load, stroke, strian, etc. depending on transducer. The Servo Controller compares feedback with a command signal to develop a control signal that operates the servovalves. The Servo Controller has an Error Detector circuit that can open a system failsafe interlock to stop the test if error between

command and feedback exceeds a preset limit. The Limit Detector monitors the output of a selected Transducer Conditioner and indicates if its output exceeds preset upper and lower limits.

E4. Model 413.05 Control Panel

The Control Panel provides centralized manual and automatic control of the systems:
i) console power on/off; ii) hydraulic pressre on/off; iii) simultaneous starting, and iv) stopping of programmers and recorders. The panel also includes an interlock circuit which depends on normal/abnormal condition sensors, located throughout the system, to remain in a normal or reset condition. A reset push-button will light when the interlock is open and extinguish when the interlock is reset. In addition an end of count signal from the MTS Counter Panel will automatically stop all programmers and recorders.

FIG. E1 M.T.S. TESTING MACHINE